Universität Hamburg
DER FORSCHUNG | DER LEHRE | DER BILDUNG

# On the Matrix Product State Approach in Time-Dependent Ab Initio Quantum Chemistry

## Dissertation

zur Erlangung des Doktorgrades
an der Fakultät für Mathematik, Informatik
und Naturwissenschaften
Fachbereich Physik
der Universität Hamburg

vorgelegt von

## Lars-Hendrik Frahm

**Hamburg**
2019

| | |
|---|---|
| Gutachter/in der Dissertation: | Prof. Dr. Daniela Pfannkuche |
| | Prof. Dr. Robin Santra |
| | |
| Zusammensetzung der Prüfungskommission: | Prof. Dr. Jochen Küpper |
| | Prof. Dr. Daniela Pfannkuche |
| | Prof. Dr. Michael Potthoff |
| | Prof. Dr. Nina Rohringer |
| | Prof. Dr. Robin Santra |
| | |
| Vorsitzende/r der Prüffungskommission: | Prof. Dr. Michael Potthoff |
| | |
| Datum der Disputation: | 13. September 2019 |
| | |
| Vorsitzende/r des Fach-Promotionsausschusses Physik: | Prof. Dr. Michael Potthoff |
| | |
| Leiter des Fachbereichs Physik: | Prof. Dr. Wolfgang Hansen |
| | |
| Dekan der Fakultät für Mathematik, Informatik und Naturwissenschaften: | Prof. Dr. Heinrich Graener |

# Danksagung

Lars-Hendrik
Hamburg im September 2019

# Abstract

Motion of charges at the atomic level is the fundamental mechanism for all chemical and biological processes in nature. Processes such as the photoelectric effect, molecular dissociation, and photosynthesis, are initiated by the electrons and the nuclei moving on the time scale of attoseconds to femtoseconds. Learning to control and steer these ultrafast dynamics is the objective of femtochemistry, where we have the vision to design artificial reactions and to engineer compounds with exceptional physical, chemical, or biological properties. The theoretical description of molecular systems is challenging however, due to the large number of degrees of freedom and the intrinsic quantum nature of the problem. A full quantum description of the molecules is far from feasible using today's computational resources. We need approximated models to resolve the ultrafast dynamics in molecules theoretically. Here we show, matrix product states (MPS) are particularly suited to describe ultrafast electron dynamics in molecules. Using the Hamburg CheMPS2 program developed for this thesis, we demonstrate the massive reduction of degrees of freedom when representing the many-body state by time-dependent MPS. In the context of ultrafast electron dynamics in molecules, we compare reduced density matrices and Green's functions obtained from the MPS approach with those from a completely correlated state. We see a reduction of the effective number of degrees of freedom by several orders of magnitude, while the error of the one-body reduced density matrix can be controlled to stay below $10\%$ within a time frame of $3fs$. This feature is shown for correlated systems such as the 10 site hydrogen chain, the hydrogen fluoride molecule, the water molecule, the ammonia molecule, and the methane molecule. Additionally, for the ionized iodoacetylene molecule, we observe electron dynamics that is in quantitative agreement with experimental reports. We pinpoint the performance of the MPS approach in resolving electron migration and demonstrate the vital role of correlations in this process. We expect the computationally efficient MPS based time evolution to enable accurate description of many phenomena involving electron dynamics in molecules hidden before. Still, the method can be expanded to describe phenomena including nuclear motion and explicit ionization processes.

# Kurzzusammenfassung

Die Bewegung von Ladungen auf atomaren Skalen ist die grundlegende Ursache für alle chemischen und biologischen Prozesse. Der photoelektrische Effekt, Dissoziation von Molekülen und Photosynthese sind nur einige Prozesse, die von einer Bewegung der Elektronen auf der Zeitskala zwischen Attosekunden und Femtosekunden ausgelöst werden. Kontrolle über diese ultraschnelle Dynamik zu gewinnen ist das Ziel der Femtochemie. In der Lage zu sein, die ultraschnelle Elektronenbewegung in Molekülen zu steuern, würde es ermöglichen künstliche Reaktionen hervorzurufen und damit Verbindungen mit neuartigen Eigenschaften zu schaffen. Eine theoretische Beschreibung solcher Prozesse ist allerdings sehr aufwendig, da Moleküle viele Freiheitsgerade besitzen und sie intrinsisch quantenmechanisch sind. Eine komplett quantenmechanische Beschreibung würde unsere heutigen Rechenkapazitäten bei Weitem übersteigen. Daher brauchen wir Methoden, um dennoch Zeitabhängigkeit in Molekülen annäherungsweise zu beschreiben. In dieser Arbeit zeigen wir, dass eine solche Beschreibung mittels Matrixproduktzuständen (MPS) möglich ist. Mit dem eigens für diese Arbeit entwickelten Hamburg CheMPS2 Programm demonstrieren wir die immense Reduzierung der Freiheitsgrade, wenn der Vielteilchenzustand durch einen zeitabhängigen MPS repräsentiert wird. Im Kontext von ultraschneller Elektronendynamik in Molekülen, vergleichen wir reduzierte Dichtematritzen sowie Greensche Funktionen zwischen dem MPS-Ansatz und einer komplett korrelierten Rechnung. Wir sehen eine Reduktion der Anzahl von effektiven Freiheitsgraden um mehrere Größenordnungen, wobei der Fehler in der Einteilchen-Dichtematrix immer unter $10\%$ innerhalb der ersten $3fs$ gehalten werden kann. Diese Eigenschaft weisen wir für korrelierte Systeme, wie der Kette aus zehn Wasserstoffatomen, Fluorwasserstoff, das Wassermolekül, Ammoniak und Methan, nach. Zusätzlich wird Ladungsmigration in ionisiertem Iodoacetylene untersucht, wobei wir hier eine quantitative Übereinstimmung mit experimentellen Daten erreichen. Wir spezifizieren in diesem System den Einfluss von Elektronenkorrelation und zeigen explizit, dass der MPS-Ansatz in der Lage ist diese aufzulösen. Wir erwarten, dass der sehr effiziente MPS-Ansatz zukünftig genutzt werden kann, um Ladungsmigrationseffekte zu beschreiben, die zuvor verborgen waren. Auch lässt sich der MPS-Ansatz noch zusätzlich erweitern, um beispielsweise Kernbewegungen oder Ionisierungsprozesse zu berücksichtigen.

# Contents

# Introduction

Quantum mechanics has been fascinating physicists for more then a century. The conception that the laws of physics at the nanoscopic scale are fundamentally different from what we perceive in our daily lives has driven generations of physicists to explore the quantum world experimentally and theoretically. Today, we have a coherent and consistent mathematical formulation of quantum mechanics that is our fundamental theory for physics at the nanoscopic scale [1]. Significant domains of this theory remain hidden however, since they are either too challenging to study experimentally, our understanding of mathematics is insufficient for an analytical description, and our computational resources are incapable of a numerical description. Based on this issue, it is an ongoing challenge to advance our perception of quantum mechanics into unexplored fields and to search for novel, unexpected phenomena.

But the interest in quantum mechanics is not only driven by curiosity. Quickly after the description and observation of the first quantum effects, quantum based applications emerged. Today, about a hundred years later, quantum technology made it into the lives of almost every human on earth, ranging from telecommunication technology that we use to stay connected with each other, information technology that shapes how we make decisions, to medical imaging technology that saved thousands of lives. To continue the technology-driven development of our community, however, an even more versatile understanding of quantum mechanics is necessary. Still, many facets of quantum physics remain undiscovered, but in this unexplored territory lays the potential for further fantastic technologies. Ideas for future technologies have been developed, e.g. as steering molecular reaction paths or using quantum states for information storage, their implementation simply fails at the insufficient degree we are able to control and describe quantum systems.

A manifestation of quantum mechanics that is particularly interesting from an academic and technological perspective are molecular systems. As the formation of molecular bonds is mostly driven by the electrons in the molecule that move on an Ångstrom length scale ($10^{-10}m$) and an attosecond time scale ($10^{-18}s$) [2], every chemical reaction can be considered a result of quantum mechanics. In this picture, quantum mechanics is ubiquitous in chemistry [3]. The field of *ab initio quantum chemistry* strives to join our understanding of quantum physics and molecular mechanics to create a concise picture of the foundation of chemistry. Having such a
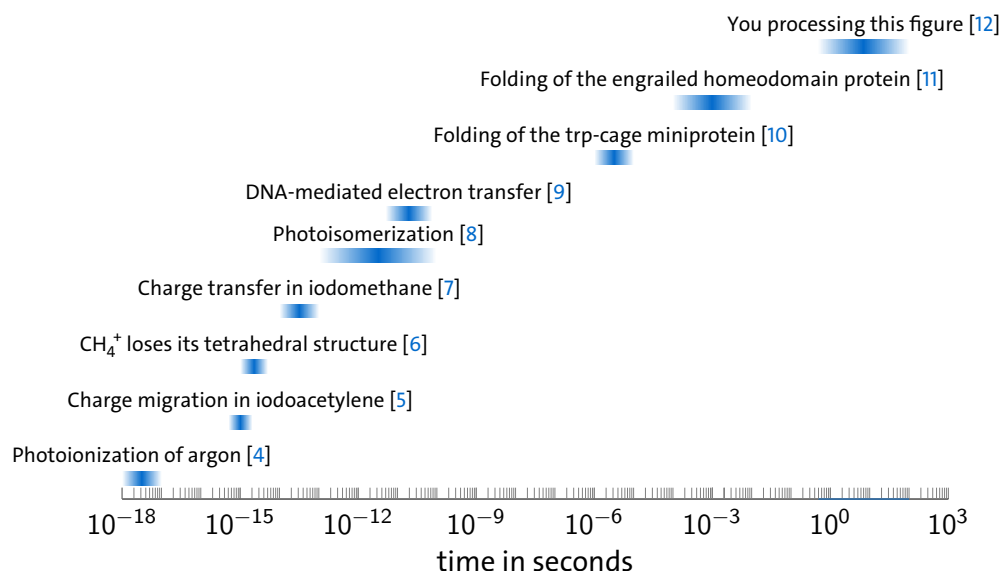
**Figure 1.1.:** Time scale of processes involving motion of electrons and nuclei in molecular systems.

precise description is fundamental to advance in physics and chemistry, where only cooperation between theory and experiment allows to interpret and validate any scientific result.

Most direct external access to the molecular systems occurs in terms of the interaction between the molecule and light. Photoinduced processes in molecules play a key role in experimental quantum chemistry, but are also the main driving force in numerous effects in physics [13], chemistry [14] and biology [15, 16]. For example, the transfer of charges in photovoltaic systems [17, 18], DNA damage triggered by ultraviolet light [19], and photosynthesis in plants and bacteria [20], are all results of an initial interaction of the compound and incoming light. Further, all these process have in common that they are triggered by an initial ultrafast motion of the electrons in the compound, that embodies the first response of the molecule with light. This ultrafast motion starts with a purely electronic part on the scale of attoseconds, coined *charge migration*, which is then the trigger of a slightly slower motion involving the nuclei as well on the scale of femtoseconds ($10^{-15}s$), coined *charge transfer* (see Figure 1.1). The community in quantum chemistry that aims to obtain control over the electrons in the molecule moving on the femtosecond scale and the subsequent molecular reaction is named *femtochemistry* [21]. Advances in shaping ultra short light pulses allows to resolve the time-dependent electron dynamics with a femtosecond and attosecond time resolution. Observing the electronic motion and the subsequent nuclear motion on the femtosecond time scale is the first step towards the vision of femtochemistry, in which we are able to steer the entire reaction path to form artificial compounds [22, 23].
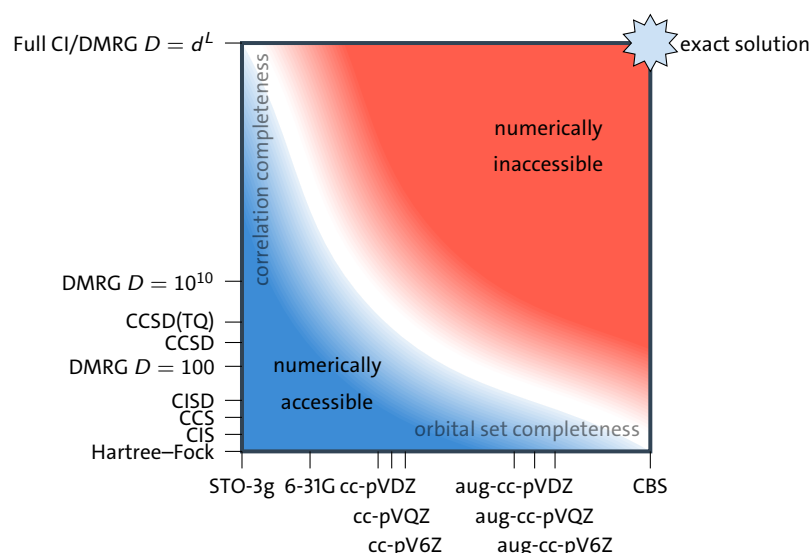
**Figure 1.2.:** Schematic illustration of the dimensions we need to consider when approaching the correct description of the molecular system. We need to consider orbital set completeness (x-axis) and correlation completeness (y-axis) independently, where only in the complete basis set limit (CBS) and in the full configuration interaction limit (full CI) we can find the exact solution. Example is for a small molecule with medium sized orbital set. Scales are not representative.

The theoretical description of the processes happening at the attosecond to femtosecond time scale is extremely challenging. The large number of degrees of freedom in combination with the intrinsic quantum mechanical effects, makes finding theoretical models for molecules a key subject of today's physical sciences. In fact, the accurate treatment of many-body systems is one of the greatest challenges in modern sciences [24]. Many different approaches have been developed to reduce the numbers of degrees of freedom, although still allowing for accurate representation of the essential mechanisms in the many-body system. In the context of molecular systems, a large family of methods have been proposed. These methods can be categorized into two types, first, methods based on *Hartree–Fock theory* [25, 26], where one describes the molecule with respect to molecular orbitals, and second, methods based on *density functional theory* [27, 28], where one drops the description of the molecule via quantum mechanical states but uses the charge density instead. Both methods have their own strengths and weaknesses [29] and for both methods exist large families of extensions [30–39].

In Hartree–Fock theory the approximation is two-fold. First, one assumes that the state of the electrons in the molecule can be described by a set of orbitals. The orbital basis set is then finite and is only able to represent the exact location in the *complete basis set limit* (CBS). Second, one assumes that correlations in the molecule are entirely absent and that the molecular state can be described by a single *Slater determinant* or *configuration* [40]. The single configuration approximation reduces the many-electron molecule to a set of coupled single-electron problems that are

then solved self-consistently. The resulting many-body state of the molecule is then a simple *product state* of *molecular orbitals*, which is easy to store even for large molecules.

The family of *post-Hartree–Fock methods* build upon the molecular orbitals and attempt to account for the electronic correlations by introducing more configurations. The post-Hartree–Fock methods are then distinguished by their approach to choose the included configurations. For example, in *configuration interaction* (CI) [30, 31] and *coupled cluster* (CC) [32–34] the configurations are chosen with respect to the number of electrons excited compared to the Hartree–Fock ground state (single excitations (CIS, CCS), double excitations, (CISD, CCSD), ...), in *complete active space self-consistent field theory* (CAS-SCF) the orbitals entering quantum mechanical superposition states remain separated from orbitals that are double occupied or empty, and in *full configuration interaction quantum Monte Carlo* the configurations are inserted or neglected stochastically based on the evolution of walkers [41]. Only if all configurations are included, i.e. *full configuration interaction* (full CI), the exact many-body state is represented and the electrons in the molecule can be arbitrarily correlated. However, already for medium sized orbital sets, such a description exceeds modern computational resources (see Figure 1.2).

The post-Hartree–Fock methods outlined above assume that the many-body state of the molecule can be described by a limited number of configurations. In contrast to this static approach, a method known from solid-state theory that describes quantum states using all configurations obtained large attention in quantum chemistry. The large success of the *density matrix renormalization group* [42, 43] method (DMRG) in quantum physics, motivated its extension to quantum chemical problems. Even if the number of configurations is too large for the post-Hartree–Fock methods mentioned above, DMRG can give full CI-like results and represent the many-body state accurately. For example, DMRG and its extensions revealed the large role of correlations in breaking nitrogen bonds [44–47] and allowed for calculation of avoided crossing in LiF, CsH, $Cr_2$ and $C_2$ [48–51]. In the representation of the many-body state in DMRG, no configurations are neglected, however, it is assumed that the entanglement entropy of the electrons in the system is limited. If this is the case, we can write the many-body state of the molecule in form of a *matrix product state* (MPS) [52]. The MPS approach at the heart of DMRG can be understood as generalization of the product state approach at the heart of Hartree–Fock theory.

Finding a general extension of the DMRG method and the underlying MPS approach to describe time-dependent problems appeared challenging however. In solid-state theory, various concepts have been developed that benefit from the locality of the interaction in solids [53–55]. An extension of the time-evolution methods for MPS to long-ranged problems was tedious and impractical due to complexity [56, 57].

For example, the *time-dependent variational principle* was benchmarked for various systems [58], however, it is prone to errors in case of systems with chaotic interaction. The contradicting convergence parameters time step size and number of MPS truncation steps have challenged scientists [59, 60]. Only a single study was reported applying dynamic DMRG in quantum chemistry [60] prior this work, successfully finding ionization potentials of the hydrogen chain and the water molecule.

**Outline**

In the following thesis, we extend the scope of the MPS approach to the context of ultrafast electron dynamics in molecules. We shine light on the features of the MPS approach that allow or limit its use in time-dependent quantum chemistry. Special focus is laid on the description of electron dynamics at the attosecond to few femtosecond time scales. Here, the dynamics are significantly quantum mechanical and the existing methods struggle most in finding appropriate many-body state representations without applying a priori truncations to the number of configurations. On the journey to a stable implementation of the time-dependent MPS approach in quantum chemistry, we reveal both, intrinsic properties of the MPS approach, as well as new manifestations of electronic correlations in molecules at ultrafast time scales. In the end, we will have a coherent understanding of the capabilities of the MPS approach when applied to time-dependent quantum chemistry problems, that is result of a profound comparison between the MPS approach and the full CI approach, as well as, from a comparison to a charge migration experiment.

In order to achieve this, we proceed coherently with only limited prior knowledge of quantum chemistry and the DMRG method necessary. We start in Chapter 2 with an introduction into the field of quantum chemistry. We introduce the reader to the *Born–Oppenheimer approximation* and the approximations related to the Hartree–Fock method. We explicitly introduce the orbital reference of the many-body state and its simplified Gaussian representation. We outline the Hartree–Fock method, its physical implications and relevance for the following thesis. Further, do we sketch two post-Hartree–Fock methods, namely CAS-SCF and CI-SCF, to sensitize the reader to common approaches in quantum chemistry and their inference in terms of configurations.

In the second half of Chapter 2, we introduce the MPS approach, which is the main subject of this study. We discuss its history in solid-state physics and quantum chemistry, its internal properties with respect to entanglement, and then formulate the MPS approach in terms of *tensor networks*. We introduce the concepts of tensor networks and its graphical representation to facilitate the following discussion of the

operations involving MPS. We continue by discussing variational handling of MPS, before turning to time evolution methods for MPS. Here, we outline two explicit time evolution methods that operate on the MPS globally, namely the *fourth-order Runge–Kutta*, and the *Krylov space time evolution* method. The Krylov space time evolution method is further examined with respect to orthogonal and non-orthogonal Krylov basis vectors.

In Chapter 3, we discuss the MPS approach more explicitly by means of symmetries and their implementation in the *Hamburg CheMPS2 extension*. We outline the computational advantage given by incorporating symmetries of the molecular system into the MPS approach. We discuss the particle number conservation of the molecular system, the points group symmetry of the molecular geometry, and the spin conservation of the molecular system, as well as how these symmetries can be incorporated into the MPS approach using spin-adapted MPS tensors. Further do we outline the Hamburg CheMPS2 program as an extension of the MPS implementation CheMPS2 by Wouters [51]. We lay down the adaptions necessary for time dependent studies and illustrate implementational details improving convergence of the MPS approach.

Chapter 4 marks the beginning of the analysis of the MPS approach in this thesis. We compare results from the MPS approach to results obtained from a completely correlated many-body state representation. We perform this comparison for two distinct types of molecules. First, we use the MPS approach to study electron dynamics in the hydrogen molecule and in a chain of 10 hydrogen atoms. For this system, we discuss the performance of the MPS approach to resolve the one-body reduced density matrix, the two-body reduced density matrix, as well as one-body Green's functions in time and frequency domain. All these results are compared to quasi exact results using a completely correlated representation of the many-body state. Second, for a profound analysis of the MPS approach, we also study *multi-dimensional molecules*, namely the hydrogen fluoride molecule, the water molecule, the ammonia molecule, as well as the methane molecule. Here we compare the ability of the MPS approach to find the correct one-body reduced density matrix within a period of 1fs after a sudden excitation. We discuss both, single and double excited initial states. Lastly in Chapter 4, we compare time-evolution methods for time-dependent MPS and propose an improvement for the Krylov space time evolution method, that makes it particularly well suited for time evolution of MPS. We demonstrate, that the improved time-evolution is able to further improve the accuracy of the MPS representation.

In Chapter 5, we then apply the MPS approach to a situation, where a completely correlated description is beyond today's computational resources, however, there are experimental results to compare to. We study the ultrafast charge migration in iodoacetylene $C_2HI$ that was recently measured by Kraus et al. [5]. We demonstrate that the MPS approach is able to describe the charge migration following sudden

ionization qualitatively and quantitatively, whereas a modelling based on Hartree–Fock and density functional theory fails. We pursue this circumstance to the electronic correlations governing the charge motion. Further, do we consider the effect of the nuclear motion in this process and preclude any nuclei induced dephasing.

To conclude, we summarize in Chapter 6 and propose avenues that can be approached based on the findings of this thesis and the developed Hamburg CheMPS2 extension.

# Electrons in Molecules

<div style="text-align: right; font-size: 3em;">2</div>

The theoretical investigation of processes in molecules is an elaborate task as it requires both, a proper description of the physics in molecules, as well as tailored concepts to give meaning to the results. As processes in molecules occur on the atomic time, the atomic energy, and the atomic length scale, we will need an adequate quantum mechanical description, taking into account all necessary degrees of freedom [61]. On the one hand, our quantum mechanical picture needs to be suitable to describe the molecule correctly, on the other hand has it to be optimized to allow for an efficient simulation using today's computational means. This chapter presents the necessary tools to accomplish this. We will introduce quantum mechanical methods, numerical frameworks and appropriate approximations to facilitate an efficient description of dynamic processes in molecules. The chapter starts from concepts of today's quantum chemistry theory and then focuses on an optimized representation of the many-body state using the matrix product state approach [52]. We further establish the time evolution algorithms to allow for simulation of time-dependent phenomena in molecules.

## 2.1 Ab Initio Quantum Chemistry

There are two very common approaches to describe molecules computationally: The first option is to use empirical or semi-empirical models [62–65] that are tailored to represent the physical situation in the molecule at an effective level. This usually requires the use of empirical parameters that are unknown a priori but can be accessed by experiments. The second option is to work in the concept of *ab initio quantum chemistry* [66], where only natural constants and interactions enter the model prior to the calculation. Here, no empirical data is required, which enables quantitative predictions on situations that are challenging to study experimentally. The ab initio methods are usually more complex and it is more difficult to extract the intrinsic mechanisms, however, the fundamental setting makes this the more natural approach in most quantum chemistry studies. For example, in this concept it is possible to predict molecular geometries [67, 68], photo emission spectra [69], and dissociation energies [70], without requiring any experimental input. The ab initio concept will also be the concept of choice in our study, as we aim to describe electron

dynamics in molecules quantitatively and to challenge our numerical method with experimental observations.

## 2.1.1  The Quantum Chemistry Problem

On a quantum mechanical level, the molecule is completely described by the *time-dependent Schrödinger equation* [1]

$$i\hbar\frac{\partial}{\partial t}\left|\Psi(t)\right\rangle = \hat{H}\left|\Psi(t)\right\rangle,$$
(2.1)

where $\hbar = 6.582119514 \cdot 10^{-16}\,eVs$ is the reduced Planck constant, $\left|\Psi(t)\right\rangle$ is the time-dependent many-body quantum state of the molecule, and $\hat{H}$ is the Hamiltonian of the system. The time-dependent Schrödinger equation is the key equation of motion of the molecule, although it neglects all relativistic effects. Relativistic effects are mostly absent for light elements, but they contribute for heavy elements such as caesium (atomic number 55) [71]. We need to be careful when working with heavy elements and either add relativistic corrections to Hamiltonian $\hat{H}$ [72, 73], or replace the Schrödinger equation by the *Dirac equation* [74]. For molecules formed from light elements (such as most molecules studied here) we can safely neglect relativistic effects and only rely on the time-dependent Schrödinger equation.

In case of static problems, we obtain the *time-independent Schrödinger equation* from Equation 2.1

$$\hat{H}\left|\Psi\right\rangle = E\left|\Psi\right\rangle,$$
(2.2)

which we can turn into an eigenvalue equation using linear algebra. We see, there is a set of states that solve Equation 2.2, called *eigenstates*, which do not evolve any dynamics, i.e. they are stationary states. A molecule in one of the eigenstates as defined by Equation 2.2 does not have any time-dependent observables. Finding the eigenstates of the Hamiltonian embodies a significant part of quantum chemistry, which is a challenging problem [75, 76]. Nevertheless, from the eigenstates we are able to predict molecular geometries, emission spectra and dissociation energies. There are numerous methods to find ground states of molecules and low lying excited states [77–79], which we will partly discuss in later chapters, however, the main focus of this thesis is on dynamics in molecules, therefore, the time-dependent Schrödinger equation in Equation 2.1 will be absolutely essential throughout this thesis.

For an isolated molecule, the Hamiltonian in Equation 2.1 and Equation 2.2 can be split into the parts [61]

$$\hat{H} = \hat{T}_{ele} + \hat{T}_{nuc} + \hat{V}_{nuc-ele} + \hat{V}_{ele-ele} + \hat{V}_{nuc-nuc}, \tag{2.3}$$

where the specific parts in position space are given by

$$\hat{T}_{ele} = -\sum_{i=1}^{N_e} \frac{\hbar^2}{2m_e} \frac{\partial^2}{\partial^2 \mathbf{r}_i}, \tag{2.4}$$

$$\hat{T}_{nuc} = -\sum_{I=1}^{N_n} \frac{\hbar^2}{2M_I} \frac{\partial^2}{\partial^2 \mathbf{R}_I}, \tag{2.5}$$

$$\hat{V}_{nuc-ele} = -\frac{1}{4\pi\epsilon_0} \sum_{i=1}^{N_e} \sum_{I=1}^{N_n} \frac{eZ_I}{|\mathbf{r}_i - \mathbf{R}_I|}, \tag{2.6}$$

$$\hat{V}_{ele-ele} = \frac{1}{4\pi\epsilon_0} \sum_{i>j}^{N_e} \frac{e^2}{|\mathbf{r}_i - \mathbf{r}_j|}, \tag{2.7}$$

$$\hat{V}_{nuc-nuc} = \frac{1}{4\pi\epsilon_0} \sum_{I>J}^{N_n} \frac{Z_I Z_J}{|\mathbf{R}_I - \mathbf{R}_J|}. \tag{2.8}$$

The operator $\hat{T}_{ele}$ represents the kinetic energy of the $N_e$ electrons in the molecule. The natural constant $m_e = 9.10938 \cdot 10^{-31} kg$ is the electron mass and $\mathbf{r}_i$ is the position of the electron $i$. The operator $\hat{T}_{nuc}$ represents the kinetic energy of the $N_N$ nuclei in the molecule, where $M_I$ is the nuclear mass of the nucleus $I$ and $\mathbf{R}_I$ is its position. The Coulomb interaction between electrons and nuclei is represented by $\hat{V}_{nuc-ele}$, with $\epsilon_0 = 8.85419 \cdot 10^{-12} \frac{F}{m}$ being the vacuum permittivity, $e = 1.60218 \cdot 10^{-19} C$ being the elementary charge and $Z_I$ being the nuclear charge of the nucleus $I$. Lastly, the Coulomb interaction between the electrons is represented in $\hat{V}_{ele-ele}$ and the Coulomb interaction between the nuclei is represented in $\hat{V}_{nuc-nuc}$ using the same symbols as described before [1].

## 2.1.2 Born–Oppenheimer Approximation

Now we want to outline one of the most essential approximations applied in the field of ab initio quantum chemistry, namely the *Born–Oppenheimer Approximation*. Within the Born–Oppenheimer Approximation, we separate the molecular Schrödinger equation into one equation for the electrons and one equation for the nuclei [61]. This simplification is based on the assumptions that electrons and nuclei move on different time scales, which is a consequence of the large nuclear to electron mass ratio. Where an electron has a mass of $9.10938 \cdot 10^{-31} kg$ even the lightest atom, the hydrogen atom has a mass of $1.67353 \cdot 10^{-27} kg$, therefore being 1837 times heavier than the electron. This makes electrons react to external perturbations much

faster than the nuclei. The Born–Oppenheimer Approximation is widely used in both, the investigation of static properties such as geometries, as well as, in the description of dynamical quantities such as ionization potentials. In situations we are interested in, i.e. the molecular response to excitation on femtosecond time scales, the nuclei will be entirely inactive and only the electrons exhibit dynamics.

May $|\Psi(t)\rangle$ be the many-body state of the isolated molecule as introduced in Equation 2.1 and Equation 2.2. We can then, based on the Born–Oppenheimer Approximation, separate it into

$$|\Psi(t)\rangle = |\Psi(t)\rangle_{nuc} \cdot |\Psi(t)\rangle_{ele}, \qquad (2.9)$$

where $|\Psi(t)\rangle_{nuc}$ is the nuclear part of the many-body state and $|\Psi(t)\rangle_{ele}$ is the electronic part of the many-body state. If the nuclei are frozen at fixed positions, the nuclear part of the many-body state does not experience any dynamics $|\Psi(t)\rangle_{nuc} = |\Psi\rangle_{nuc}$. Only the electronic part of the many-body state evolves dynamics according to the electronic time-dependent Schrödinger equation

$$i\hbar \frac{\partial}{\partial t} |\Psi(t)\rangle_{ele} = \hat{H}_{ele} |\Psi(t)\rangle_{ele}, \qquad (2.10)$$

where the operator $\hat{H}_{ele}$ is the electronic Hamiltonian derived from the Hamiltonian in Equation 2.3 in the Born–Oppenheimer Approximation.

If the nuclei are kept at fixed positions, we treat them classically and do not need to consider them in the quantum calculation. The nuclei do not require a description in terms of wave functions, but we can allocate them well defined coordinates

$$|\Psi(t)\rangle_{nuc} \rightarrow \{\mathbf{R}_1, \cdots, \mathbf{R}_{N_N}\}, \qquad (2.11)$$

with $\{\mathbf{R}_1, \cdots, \mathbf{R}_{N_N}\}$ being the set of coordinates specifying the positions of the $N_N$ nuclei in the molecule. Only the electrons act according to the laws of quantum mechanics, whereas the nuclei have classic positions in space.

The electronic Hamiltonian $\hat{H}_{ele}$ reads in the Born–Oppenheimer approximation

$$\hat{H}_{ele} = \hat{T}_{ele} + \hat{V}_{nuc-ele} + \hat{V}_{ele-ele} + E_{nuc}, \qquad (2.12)$$

which is similar to the Hamiltonian explained in Equation 2.3. Only the kinetic energy of the nuclei vanishes and the nuclear interaction turns into a constant energy $E_{nuc}$ that only depends on the nuclei positions. If the nuclei stay at fixed positions with no momentum, their kinetic energy is zero and $\hat{T}_{nuc}$ can be neglected. Further, the sum in the nuclear-nuclear interaction $\hat{V}_{ele-ele}$ (see Equation 2.8) can be performed explicitly using the nuclear coordinates $\{\mathbf{R}_1, \cdots, \mathbf{R}_{N_N}\}$. This gives the constant energy
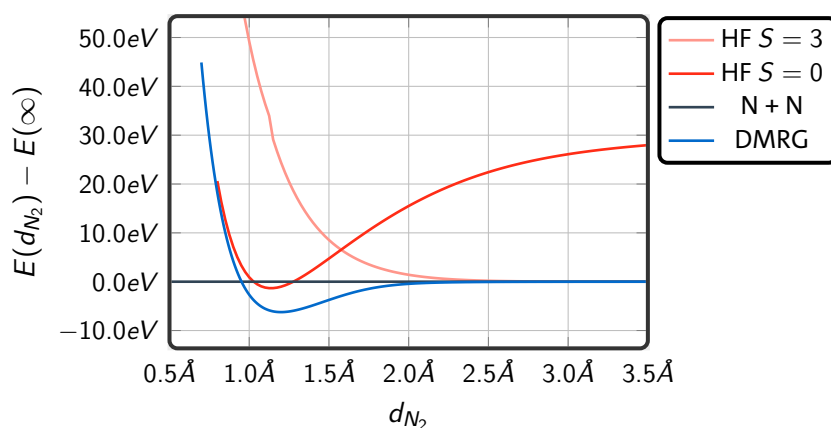
**Figure 2.1.:** Ground state potential energy surface of the nitrogen dimer ($N_2$), where the molecular energy $E(d_{N_2})$ depends on the distance between the two nitrogen atoms $d_{N_2}$. The energies are calculated using the Hartree–Fock implementation of the molpro program package [80] for two different spin states (HF $S = 0$ and HF $S = 3$), as well as, using the density matrix renormalization group (DMRG) implementation by Lau [67]. All calculations were performed in a minimal STO-6G Gaussian basis set [81].

$E_{nuc}$ shift that does not have any impact on the electronic part of the state. Solving Equation 2.10 is the main challenge of this thesis, as we are solely interested in the electronic dynamics and the nuclei rest on the time scales considered.

By solving the time-independent Schrödinger equation in the Born–Oppenheimer Approximation $\hat{H}_{ele} \left| \Psi(t) \right\rangle_{ele} = E \left| \Psi(t) \right\rangle_{ele}$ we can derive eigenstates and eigenenergies of the molecule within the Born–Oppenheimer Approximation. The eigenenergies depend on the chosen geometry of the molecule $\{\mathbf{R}1, \cdots, \mathbf{R}_{N_N}\}$, therefore, the energy is a function of the positions of the nuclei (see Figure 2.1 for the nitrogen dimer). These functions in the multi-dimensional space of all nuclei positions are called *potential energy surfaces*. The potential energy surface has a global minimum, which is referred to as the equilibrium geometry and there will be energy gaps between specific geometries that then allow to predict, for example, which energy is necessary to separate specific nuclei or parts of the molecule from the remaining part (dissociation). Further does the *Franck–Condon principle* [82] state that molecular excitations always occur vertically on potential energy surfaces, meaning that if excited, the molecule does not change its geometry instantly. A change of the molecular geometry is always a consequence of electronic excitation.

Of course, the Born–Oppenheimer approximation has very strict limitations. In our study, the Born–Oppenheimer approximation limits the time range we are able to describe. Already on the time scale of femtoseconds, light elements may start moving as a response to the electronic motion. However, the nascent nuclear motion (translations and vibrations) is completely neglected in Born–Oppenheimer approximation. This excludes a dynamic description of processes such as bond formation

and dissociation. In order to capture such effects, it is necessary to go beyond the Born–Oppenheimer approximation [83]. Further, work by Arnold et al. [84] has shown, that the width of the nuclear wave function in position space can lead to significant decoherence in the electronic motion and therefore damps the correlated electron motion. Although the nuclei are expected to keep their fixed positions, the assumptions of the classically described nuclei may not be appropriate (see Equation 2.11). This is in particular the case for light atoms such as hydrogen. As a consequence of these issues, our studies will be limited to a few femtoseconds time range and we will need to make sure that the results are stable with respect to small displacements of hydrogen atoms in the molecules we will be discussing (see Section 5.1.1).

## 2.2  The Electronic State

From now on, we completely focus on the electronic part of the many-body state for the reasons outlined above. We do not consider the nuclear part of the many-body state in what follows, but treat the nuclei purely classically. If we omit the subscript $|\cdot\rangle_{elec} \rightarrow |\cdot\rangle$, we symbolize the electronic many-body state in all following equations.

### 2.2.1  Single Electron Orbitals

Let us start with the single electron picture and then extend the single electron picture to the many electron picture by using the means of second quantization later in Section 2.2.2. We now search for an elegant choice to express the state of a single electron in the molecule in terms of *spatial orbitals*

$$\langle \mathbf{r}|\phi_i\rangle = \phi_i(\mathbf{r}). \tag{2.13}$$

The function $\phi_i(\mathbf{r})$ specifies the spatial distribution of an electron occupying orbital $i$. The set of orbitals the electrons enter $\{\phi_0(\mathbf{r}), \phi_1(\mathbf{r}), \cdots\}$ can be any collection of linear independent functions. For example, they can be eigenstate of the position operator $\hat{\mathbf{r}}|\mathbf{r}\rangle = \mathbf{r}|\mathbf{r}\rangle$ or the eigenfunctions to the (hydrogen-like) atomic Schrödinger equation $\hat{H}_{Atom}|\phi_i\rangle = E_i|\phi_i\rangle$ (see following discussion). If the set is complete, an arbitrary electron distribution $\varphi(\mathbf{r})$ can be resolved in the orbital basis set

$$\varphi(\mathbf{r}) = \sum_{i=0}^{\infty} c_i\phi_i(\mathbf{r}), \tag{2.14}$$

with expansion coefficients $c_i$. This is the so called *complete basis set limit*, where we are able to describe arbitrarily distributed electrons. Of course, such a description is numerically impractical and usually unnecessary to describe electrons that move

close to the center of mass of the molecule. We therefore use a *finite orbital basis set* $\{\phi_0(\mathbf{r}), \phi_1(\mathbf{r}), \cdots, \phi_L(\mathbf{r})\}$ that incorporates a limited number of basis set functions only. With the finite orbital basis set, the correct electron distribution can only be resolved approximately $\varphi(\mathbf{r}) \approx \sum_{i=0}^{L} \tilde{c}_i \phi_i(\mathbf{r})$, which introduces a *basis set truncation error*. However, we should be able to balance the basis set truncation error, as long as the electrons remain close to the molecule.

We want to make sure that the orbitals we use form an orthogonal basis. The overlap between the arbitrary orbitals $i$ and $j$ is given by

$$S_{ij} = \langle \phi_i | \phi_j \rangle = \int \phi_i^*(\mathbf{r})\phi_j(\mathbf{r})d\mathbf{r}, \tag{2.15}$$

which might be far from an identity matrix. Working with a non-orthogonal basis is disadvantageous for solving the molecular Schrödinger equation, as we need to adapt the Equation 2.1 to the non-orthogonality. We rather use a set of orthonormalized orbitals by bringing the orbitals in an orthonormal form. This can be done by diagonalizing the matrix $S$ and use the eigenstate as orbital basis set.

If we have decided on a set of orthonormal orbitals, we can write down the one-electron part of the Hamiltonian of the molecule. In the Born–Oppenheimer Approximation, the one-electron Hamiltonian $\hat{H}^{OE}(i)$ for the electron $i$ in the molecule constitutes of two addends, namely the kinetic energy of the electrons, as well as the static potential of the nuclei on the electrons (compare Equation 2.4 and Equation 2.6)

$$\hat{H}^{OE}(i) = -\frac{\hbar^2}{2m_e}\frac{\partial^2}{\partial^2 \mathbf{r}_i} - \frac{1}{4\pi\epsilon_0}\sum_{I=1}^{N_n}\frac{eZ_I}{|\mathbf{r}_i - \mathbf{R}_I|} = \hat{T}^{OE}(i) + \hat{V}^{OE}(i). \tag{2.16}$$

To express the molecular one-electron Hamiltonian in the chosen orbital basis we need two types of integrals:

- The orbital representation of the kinetic energy:

$$T_{ab} = \langle \phi_a | \hat{T}^{OE}(1) | \phi_b \rangle = -\frac{\hbar}{2m_e}\int_{-\infty}^{\infty}\phi_a^*(\mathbf{r}_1)\frac{\partial^2}{\partial^2 \mathbf{r}_1}\phi_b(\mathbf{r}_1)d\mathbf{r}_1 \tag{2.17}$$

This integral represents the kinetic energy of a single electron. The kinetic energy may cause an electron to be scattered from orbital $a$ to orbital $b$ (or vice versa).

- The orbital representation of the electron-nucleus interaction:

$$V_{ab} = \langle \phi_a | \hat{V}^{OE}(1) | \phi_b \rangle = -\frac{1}{4\pi\epsilon_0}\sum_{I=1}^{N_n}\int_{-\infty}^{\infty}\phi_a^*(\mathbf{r}_1)\frac{eZ_I}{|\mathbf{r}_1 - \mathbf{R}_I|}\phi_b(\mathbf{r}_1)d\mathbf{r}_1 \tag{2.18}$$

This integral represents the interaction of an electron with the $N_n$ nuclei of the molecule. The electron-nucleus interaction may cause an electron to be scattered from orbital $a$ to orbital $b$ (or vice versa).

As the electrons are indistinguishable, the integrals are independent of the electron index $i$ in Equation 2.16 ($\langle \phi_a | \hat{T}^{OE}(1) | \phi_b \rangle = \langle \phi_a | \hat{T}^{OE}(2) | \phi_b \rangle = \cdots$). The integrals then form the one-electron part of the molecular Hamiltonian in Equation 2.12. In this orbital basis, the one-electron part of the Hamiltonian is given by

$$t_{ab} = T_{ab} + V_{ab} \tag{2.19}$$

where we use $t_{ab}$ as the combined *one-electron integral*.

**Slater Type Orbitals**

To find a finite orbital basis set, a common option is to orient at bound states of the atoms in the molecule. This is especially advantageous in situations where the electrons stay close to the nuclei of the molecule. The analytic form of the bound orbitals are known for the hydrogen atom [85] only. For atoms with more than one electron, numerical methods need to be applied to find the approximated orbitals for atoms with more than one electron. The general procedure in quantum chemistry is to find approximated atomic orbitals numerically and then expand these orbitals in terms of *Slater type orbitals* or in terms of *Gaussian type orbitals* [3].

Slater type orbitals have the general form in spherical coordinates

$$\phi_S^{nlm_l}(r, \theta, \varphi) = \mathcal{N} r^{n-1} e^{-\mu r} Y_l^{m_l}(\theta, \varphi), \tag{2.20}$$

where $n$ and $\mu$ are the parameters fitted to the numerical solution of the many-electron atomic orbitals. $\mathcal{N}$ is a normalization constant and $Y_l^{m_l}(\theta, \varphi)$ is a spherical harmonic with $l$ being the angular momentum quantum number and $m_l$ being the magnetic quantum number. In case of the $1s$ orbital ($n = 1$, $l = 0$, $m_l = 0$) of the hydrogen atom located at $\mathbf{R}_I$, the Slater type orbital reads [61]

$$\phi_S^{H,1s}(\mathbf{r} - \mathbf{R}_I) = \frac{1}{\sqrt{\pi}} \left( \frac{1}{a_0} \right)^{\frac{3}{2}} e^{-\frac{|\mathbf{r} - \mathbf{R}_I|}{a_0}}, \tag{2.21}$$

where $a_0 = 0.52918\text{Å}$ is the *Bohr radius*. In case of the $1s$ orbital of hydrogen, the Slater type orbital matches the exact atomic orbital.

The atomic orbitals can be extended to all elements, although the orbitals cannot be determined exactly as soon as more than one electron surrounds the nucleus. But we

know from numerical calculations that their qualitative shape and the angular momentum representation remains the same if electron-electron interaction is present in the atom. The atomic orbitals have a decaying exponential $\mathbf{r}$-dependence, which is correctly resolved by the Slater type orbital [86]. Further, according to the Kato theorem [3], the orbitals have a cusp at the position of the nucleus, which is also correctly resolved by the Slater type orbitals. Therefore, correctly tuned Slater type orbitals allow for accurate representation of the atomic orbitals, even for atoms with many-electrons.

The single electron basis set for the molecule $\{\phi_0(\mathbf{r}), \phi_1(\mathbf{r}), \cdots, \phi_L(\mathbf{r})\}$ is then constructed from the atomic orbitals of the atoms in the molecule. For example, when describing the water molecule ($H_2O$) with an atomic basis set of $1s$ orbitals for the hydrogen atoms and $1s$, $2s$, and $2p$ orbitals for the oxygen atom, we have the basis set

$$
\begin{aligned}
\Phi_S^{H_2O} = \{ &\phi_S^{H,1s}(\mathbf{r} - \mathbf{R}_{H_1}), \phi_S^{H,1s}(\mathbf{r} - \mathbf{R}_{H_2}), \phi_S^{O,1s}(\mathbf{r} - \mathbf{R}_O), \phi_S^{O,2s}(\mathbf{r} - \mathbf{R}_O), \\
&\phi_S^{O,2p_x}(\mathbf{r} - \mathbf{R}_O), \phi_S^{O,2p_y}(\mathbf{r} - \mathbf{R}_O), \phi_S^{O,2p_z}(\mathbf{r} - \mathbf{R}_O) \},
\end{aligned}
\tag{2.22}
$$

where $\mathbf{R}_{H_1}$ is the location of the first hydrogen atom, $\mathbf{R}_{H_2}$ is the location of the second hydrogen atom, and $\mathbf{R}_O$ is the location of the oxygen atom. The orbital $\phi_S^{H,1s}$ is fitted to express the $1s$ atomic orbital of a hydrogen atom and the orbital $\phi_S^{O,1s}$ is fitted to express the $1s$ atomic orbital of a oxygen atom, the orbital $\phi_S^{O,2s}$ is fitted to express the $2s$ atomic orbital of a oxygen atom, ... . With this construction, we obtain a basis set of 7 atomic orbitals, which makes it a *minimal basis set*.

In atomic and molecular orbital theory, we distinguish between two types of basis sets: *minimal basis sets* and *extended basis sets* [61]. In minimal basis sets, the orbitals are limited to the shell that is occupied by at least one electron in the neutral atom. For example, hydrogen and helium will be considered using the $1s$ orbital; lithium to neon will be considered using the $1s$, $2s$, $2p_x$, $2p_y$, and the $2p_z$ orbital; and sodium to argon will be considered using the $1s$, $2s$, $2p_x$, $2p_y$, $2p_z$, $3s$, $3p_x$, $3p_y$, and the $3p_z$ orbital. In contrast to minimal basis sets, extended basis sets also include atomic orbitals with larger main quantum number $n$. In case of molecules, electrons might occupy such excited atomic orbitals as a result of the hybridization of the atomic orbitals. Here, using extended basis sets allows for more precise results, as the electrons can adapt their location more flexible to the molecular situation (compare Equation 2.14). By using extended basis sets, we reduce the basis set truncation error and resolve the spatial distribution of the electrons in the molecule more accurately.

## Gaussian Type Orbitals

We decided to use a basis of atomic orbitals as a first approach to resolve the spatial distribution of the electrons in the molecule. However, the Slater type orbitals as introduced in Equation 2.21 are difficult to operate with [61, 87]. To find the one-electron matrix elements for Hamiltonian in Equation 2.16 a large number of integrals as given in Equation 2.17 and Equation 2.18 needs to be evaluated. This problem further exaggerates when considering the electron-electron interaction in Equation 2.7. In fact, evaluating the integrals has been considered to be the biggest problem in quantum chemistry [3]. An efficient and precise method to find the integrals is therefore crucial for our studies, however, there is no method to achieve this for Slater type orbitals. In quantum chemistry, an alternative approach is much more common, which simplifies the computational demand to evaluate the integrals.

Instead of Slater type orbitals, we use *Gaussian type orbitals* [88, 89]. In cartesian coordinates, Gaussian type orbitals have the form

$$\phi_{G,\alpha}^{ijk}(\mathbf{r}) = \mathcal{N} x^i y^j z^k e^{-\alpha|\mathbf{r}|^2} \tag{2.23}$$

with the major adjustment compared to Slater type orbitals being the exponential dependence $\sim |\mathbf{r}|^2$. The width of the Gaussian $\alpha$ is the parameter fitted to the atomic orbital (compare to Slater type orbitals) and $i$, $j$, and $k$ are positive integers accounting for the angular part of the atomic orbital and $\mathcal{N}$ is again a normalization constant. For example, for the $1s$ ($i = j = k = 0$) orbital of hydrogen we use the Gaussian function

$$\phi_{G,\alpha}^{H,1s}(\mathbf{r} - \mathbf{R}_i) = \left(\frac{2\alpha}{\pi}\right)^{\frac{3}{4}} e^{-\alpha|\mathbf{r}-\mathbf{R}_i|^2}, \tag{2.24}$$

If we represent the atomic orbital in terms of Gaussian functions, the integrals in Equation 2.15, Equation 2.17, and Equation 2.18 are easy to evaluate analytically. For example, the overlap of an $1s$ orbital located at $\mathbf{R}_i$ with an $1s$ orbital located at $\mathbf{R}_j$ is given by [87]

$$S_{(1s,i,\alpha),(1s,j,\beta)} = \int \phi_{G,\alpha}^{H,1s}(\mathbf{r} - \mathbf{R}_i)\phi_{G,\beta}^{H,1s}(\mathbf{r} - \mathbf{R}_j)d\mathbf{r} = \left(\frac{\pi}{\alpha + \beta}\right)^{3/2} e^{-\frac{\alpha\beta}{\alpha+\beta}|\mathbf{R}_i-\mathbf{R}_j|^2} \tag{2.25}$$
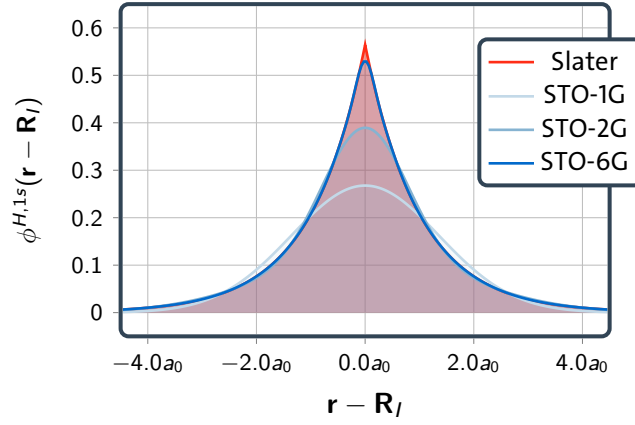
**Figure 2.2.:** Slater type orbital (Slater) and contracted Gaussian type orbitals (STO-nG) as the representation of the $1s$ orbital of the hydrogen atom.

and the integral for the kinetic energy is given by

$$T_{(1s,i,\alpha),(1s,j,\beta)} = -\frac{\hbar^2}{2m_e} \int \phi_{G,\alpha}^{H,1s}(\mathbf{r} - \mathbf{R}_i) \frac{\partial^2}{\partial^2 \mathbf{r}} \phi_{G,\beta}^{H,1s}(\mathbf{r} - \mathbf{R}_j) d\mathbf{r} \tag{2.26}$$

$$= \frac{\hbar^2}{2m_e} \frac{\alpha\beta}{\alpha+\beta} \left(6 - 4\frac{\alpha\beta}{\alpha+\beta}|\mathbf{R}_i - \mathbf{R}_j|^2\right) \left(\frac{\pi}{\alpha+\beta}\right)^{3/2} e^{-\frac{\alpha\beta}{\alpha+\beta}|\mathbf{R}_i-\mathbf{R}_j|^2}. \tag{2.27}$$

This allows for fast numerical evaluation of the integrals. All modern quantum chemistry software feature build-in integral evaluation and there are open source libraries to calculate the integrals [90]. In this work, we will use the integral evaluate program SEWARD of the molpro program package [80] and LIBINT [90] as part of the PySCF python package [91].

The Gaussian type orbitals are much easier to handle, however, in the current form, they do not represent the atomic orbitals correctly. The decaying slope is different and at the position of the nucleus $\mathbf{r} = \mathbf{R}_I$ atomic orbitals have a finite slope (Kato theorem), whereas, the slope of Gaussian type orbitals is zero (see Figure 2.2 for example of Slater type orbitals vs Gaussian type orbitals). We need to address these issues when utilizing Gaussian type orbitals for atomic orbitals. We do this in terms of *contracted Gaussian type orbitals*. For the example of the $1s$ orbital a contracted Gaussian type orbital reads

$$\phi_{CG}^{1s}(\mathbf{r} - \mathbf{R}_I) = \sum_{p=1}^{N_G} c_p \ \phi_{G,\alpha_p}^{1s}(\mathbf{r} - \mathbf{R}_I). \tag{2.28}$$

Instead of using a single (primitive) Gaussian type orbital, we mimic the atomic orbital by a linear combination (contraction) of Gaussian functions with different widths $\alpha_p$. The coefficients $c_p$ and $\alpha_p$ are fitted to give the best representation of the atomic orbital for a given number of Gaussian type orbitals $N_G$. The more

Gaussian type orbitals we use, the better this approximation gets (see Figure 2.2). The number of Gaussian type orbitals, the coefficients $c_p$ and $\alpha_p$ needed to represent a specific atomic orbital have been optimized for decades and are publicly available in databases such as the EMSL Basis Set Library [92]. Using contracted Gaussian type orbitals does not aggravate the integral evaluation, as the integrals can still be easily calculated analytically. The contraction just introduces additional sums including already evaluated integrals and the contraction coefficients $c_p$.

Although we focused on the $1s$ orbital in the shown examples, the discussion above translates directly to $p$ $(i + j + l = 1)$, $d$ $(i + j + l = 2)$, and $f$ $(i + j + l = 3)$ orbitals. Evaluation of the integrals remains simple when using Gaussian type orbitals in comparison to Slater type orbitals [89]. Attaching to the example above to find a minimal atomic basis set for the water molecule, we get using contracted Gaussian type orbitals

$$\Phi_{CG}^{\mathrm{H_2O}} = \{\phi_{CG}^{H,1s}(\mathbf{r} - \mathbf{R}_{H_1}), \phi_{CG}^{H,1s}(\mathbf{r} - \mathbf{R}_{H_2}), \phi_{CG}^{O,1s}(\mathbf{r} - \mathbf{R}_O), \phi_{CG}^{O,2s}(\mathbf{r} - \mathbf{R}_O),$$
$$\phi_{CG}^{O,2p_x}(\mathbf{r} - \mathbf{R}_O), \phi_{CG}^{O,2p_y}(\mathbf{r} - \mathbf{R}_O), \phi_{CG}^{O,2p_z}(\mathbf{r} - \mathbf{R}_O)\}, \tag{2.29}$$

where the orbital $\phi_{CG}^{X,z}$ is the contracted Gaussian type orbital to represent the $z$ atomic orbital of the atom $X$.

## 2.2.2 Electronic Many-Body State

Having decided about the single electron basis, we can use the means of second quantization to extend the Hilbert space to the many electron picture [61]. Suppose we have a set of $L$ orthonormal $(\langle \phi_i | \phi_j \rangle = \int \phi_i^*(\mathbf{r}) \phi_j(\mathbf{r}) d\mathbf{r} = \delta_{ij} \forall i, j)$ single electron orbitals

$$\Phi = \{\phi_0(\mathbf{r}), \phi_1(\mathbf{r}), \dots \phi_L(\mathbf{r})\}, \tag{2.30}$$

then we can define the operator $\hat{c}_{i\sigma}^\dagger$ creating an electron with spin $\sigma$ in the orbital labeled by $i$ and the operator $\hat{c}_{i\sigma}$ annihilating an electron with spin $\sigma$ in the orbital labeled by $i$. These operators are ladder operators between parts of the Fock space with different electron numbers, which take care of the fermionic many-body properties of the state.

Using the creation and annihilating operators, all possible states can be constructed from the vacuum state $|0\rangle$, the state were there is no electron in the system. A state with an electron with spin $\uparrow$ in orbital number 1 is constructed via

$$|n_{0\uparrow} = 0 \; n_{0\downarrow} = 0, \; n_{1\uparrow} = 1, \; n_{1\downarrow} = 0, \; \cdots n_{L\uparrow} = 0, \; n_{L\downarrow} = 0\rangle = \hat{c}_{1\uparrow}^\dagger |0\rangle. \tag{2.31}$$

The many-body basis state $|n_{1\uparrow}n_{1\downarrow}\cdots n_{L\uparrow}n_{L\downarrow}\rangle$ is then called a *configuration*, or a *Slater determinant*. The index $n_{i\sigma} \in \{0,1\}$ encodes the properties that only one electron can be in a given spin state. This basis of the many-body Hilbert space is called *occupation number basis*.

As electrons in molecules are indistinguishable particles in a quantum mechanical sense, the electronic many-body state needs to be conform to the permutation rules of fermions. This means, the many-body state must be anti-symmetric under particle exchange $-\hat{P}_{ij}|\Psi\rangle = |\Psi\rangle$, where $\hat{P}_{ij}$ is the permutation operator exchanging electron number $i$ and electron number $j$. The permutation properties for fermions are encoded in the commutation relations of the creation and annihilation operator $\hat{c}^\dagger_{\sigma i}$ and $\hat{c}_{\sigma i}$. These operators need to conform to the anti-commutation rules

$$\left[\hat{c}^\dagger_{\sigma i}, \hat{c}_{\tau j}\right]_+ = \delta_{ij}\delta_{\sigma\tau}, \tag{2.32}$$

$$\left[\hat{c}^\dagger_{\sigma i}, \hat{c}^\dagger_{\tau j}\right]_+ = 0, \tag{2.33}$$

$$\left[\hat{c}_{\sigma i}, \hat{c}_{\tau j}\right]_+ = 0, \tag{2.34}$$

where $[\cdot]_+$ is the anti-commutator. If the creation and annihilation operators obey these rules, the configurations $|n_{1\uparrow}n_{1\downarrow}\cdots n_{L\uparrow}n_{L\downarrow}\rangle$ constructed via Equation 2.31 automatically have the correct permutation relations.

The time-dependent many-body state of a molecule is completely specified by a linear combination of configurations. For a basis of $L$ orbitals the time-dependent many-body state reads

$$|\Psi(t)\rangle = \sum_{n_{1\uparrow}n_{1\downarrow}\cdots n_{L\uparrow}n_{L\downarrow}} c_{n_{1\uparrow}n_{1\downarrow}\cdots n_{L\uparrow}n_{L\downarrow}}(t)\,|n_{1\uparrow}n_{1\downarrow}\cdots n_{L\uparrow}n_{L\downarrow}\rangle, \tag{2.35}$$

where $n_{i\uparrow} \in \{0,1\}$ ($n_{i\downarrow} \in \{0,1\}$) is the number of up (down) electrons in the orbital $i$, and the coefficient tensor $c_{n_{1\uparrow}n_{1\downarrow}\cdots n_{L\uparrow}n_{L\downarrow}}(t)$ holds the time-dependent expansion coefficients. The many-body state representation in Equation 2.35 is considered *quasi exact*, as it describes the full quantum state and allows for any quantum mechanical superposition. Although, there is still the error due to the limited sized one-electron basis (only a limited number of orbitals are included in $\Phi$, see Equation 2.30 ). Depending on the situation, this error must be controlled by the form, the type, and the number of included single electron orbitals (see Section 2.2.1).

When writing down the Hamiltonian from Equation 2.12 using second quantization, it reads,

$$\hat{H} = \sum_{ij\sigma} t_{ij}\hat{c}^\dagger_{i\sigma}\hat{c}_{j\sigma} + \frac{1}{2}\sum_{ijkl\sigma\tau} V_{ijkl}\hat{c}^\dagger_{i\sigma}\hat{c}^\dagger_{j\tau}\hat{c}_{l\tau}\hat{c}_{k\sigma} + E_{nuc}, \tag{2.36}$$

where $t_{ij}$ represents the one-body part of the Hamiltonian, i.e. the kinetic energy and the static field from the nuclei (see Equation 2.16), and $V_{ijkl}$ represents two-body part of the Hamiltonian, i.e. the electron-electron interaction. When representing the Hamiltonian from Equation 2.10 in the single electron basis of orbitals, the two-body integrals read

$$V_{ijkl} = \frac{e^2}{4\pi\epsilon_0} \int_{-\infty}^{\infty} \int_{-\infty}^{\infty} \phi_i^*(\mathbf{r}_1)\phi_j^*(\mathbf{r}_2)\frac{1}{|\mathbf{r}_1 - \mathbf{r}_2|}\phi_k(\mathbf{r}_1)\phi_l(\mathbf{r}_2)d\mathbf{r}_1 d\mathbf{r}_2, \qquad (2.37)$$

that represents the interaction between two electrons in the orbitals $k$ and $l$, and the probability for them to be scattered in the orbitals $i$ and $j$ as a result of the interaction process. Using these integrals and the one-body integers $t_{ij}$ we have everything we need to specify the second quantized Hamiltonian in Equation 2.36.

## 2.3  Post-Hartree–Fock Methods

In Equation 2.35, we have seen the many-body state, which describes the electronic state of the molecule exactly up to errors due to the restricted basis set. However, the exponentially growing number of possible configurations in Equation 2.35,

$$\# \text{ configurations} = 4^L, \qquad (2.38)$$

makes working with $|\Psi(t)\rangle$ extremely challenging. We need to store the same number of coefficients as we consider configurations (the curse of dimensionality), which quickly exceeds the memory of today's computers. For example, if describing a molecule with an orbital space of 50 orbitals, we need $\approx 1.2675 \cdot 10^{30}$ coefficients (this number may reduce when using symmetries, see Section 3.1). It requires $1.014 \cdot 10^{14}$ terabytes of memory just to store the many-body state on a computer. Today, the limit for completely correlated ground state calculations are at system sizes of 22 orbitals holding 22 electrons, even with heavy use of high-performance and parallel computing [93]. To handle completely correlated time-dependent situations in a reasonable amount of time, the orbital basis sets must even be smaller. In the following Section 2.3 and in Section 2.4 we discuss concepts to reduce the number of configurations that are necessary to consider when describing the many-body state of medium sized orbital basis sets.

### 2.3.1  Hartree–Fock as a Starting Point

Most rigorous approximation is to reduce the many-body state to just a single configuration. Here, the single electron orbitals are optimized such that the chosen configuration is minimal in energy. This approach is known as the *Hartree–Fock*

*method* [61] and will be the starting point for most calculations in this thesis. It is the core of most approaches in quantum chemistry, therefore, we will briefly lay down the concepts related to this approximation to gain a picture of its physical implications.

Let us assume for a moment that the electrons in the molecule we want to describe are non-interacting, i.e. the two-electron part in the Hamiltonian in Equation 2.12 is absent. Then, the Hamiltonian can be written in the form

$$\hat{H} = \sum_{i=1}^{N_e} \hat{H}^{OE}(i),\qquad(2.39)$$

where $N_e$ is the number of electrons in the molecule and $\hat{H}^{OE}(i)$ is the one-electron Hamiltonian as given in Equation 2.16. If the Hamiltonian can be written as given in Equation 2.39, we can reformulate the many-body Schrödinger equation in Equation 2.2 into a set of $N_e$ one-body Schrödinger equations. The independent one-body Schrödinger equations can be solved

$$\hat{H}^{OE}(1)\phi_m^{OE}(\mathbf{r}_1) = E_m\phi_m^{OE}(\mathbf{r}_1),\qquad(2.40)$$

for each electron in the molecule (they are all similar due to the indistinguishably of fermions). For example, we could write down the Schrödinger equation in Equation 2.40 in the single electron basis of orthonormalized Gaussian type atomic orbitals as given above in Section 2.2.1. Then we have an $L$-dimensional eigenvalue problem, that is usually easy to solve. The resulting set of eigenfunctions $\Phi^{OE} = \{\phi_0^{OE}(\mathbf{r}), \phi_1^{OE}(\mathbf{r}), \dots \phi_L^{OE}(\mathbf{r})\}$ can be used as a new single-electron basis and the ground state configuration can be formed from a single Slater determinant (configuration). We obtain the ground state by distributing the $N_e$ electrons over the $N_e/2$ orbitals with the lowest energies (assuming an even number of electrons in the molecule)

$$|\Psi_{HF}\rangle_{OE} = |\underbrace{1}_{n_{1\uparrow}}\underbrace{1}_{n_{1\downarrow}}\underbrace{1}_{n_{2\uparrow}}\cdots\underbrace{1}_{n_{N_e/2\downarrow}}0\,0\cdots0\rangle,\qquad(2.41)$$

where the orbitals are ordered with respect to their energy $E_m$ from left to right. We solved the molecular Schrödinger equation in case of absent electron-electron interaction.

But the assumption of non-interacting electrons is unrealistic for most molecules. Usually, the long-ranged Coulomb interaction does form the orbitals and we need to consider electron-electron interaction to obtain realistic results. However, we still want to keep the description of the molecule on the one electron level. To do this, we add a *mean field* to the one electron Hamiltonian in Equation 2.39, that accounts for

the electrostatic field coming from the remaining electrons in the molecule. Therefore, the electrons are moving in both, the electrostatic field of the nuclei, as well as in the averaged field of the other electrons.

We add terms that represent the electron-electron interaction onto the one electron Hamiltonian, which makes it the *Fock operator*. It reads

$$\hat{F}(1) = \hat{H}^{OE}(1) + \sum_{n}^{occu} \left( \hat{J}_n(1) - \hat{K}_n(1) \right),$$ (2.42)

where $J_n(1)$ is the *Coulomb operator* and $K_n(1)$ is the *exchange operator*. We now solve the Schrödinger equation for the Fock operator

$$\hat{F}(1)\phi_m(\mathbf{r}_1) = E_m\phi_m(\mathbf{r}_1),$$ (2.43)

that gives us single-electron orbitals that also consider for the electron-electron interaction. The Coulomb operator

$$\hat{J}_n(1)\phi_m(\mathbf{r}_1) = \frac{e^2}{4\pi\epsilon_0} \int_{-\infty}^{\infty} \phi_n^*(\mathbf{r}_2) \frac{1}{|\mathbf{r}_1 - \mathbf{r}_2|} \phi_m(\mathbf{r}_1)\phi_n(\mathbf{r}_2)d\mathbf{r}_2,$$ (2.44)

accounts for the direct (classical) interaction of the electrons, and the exchange operator

$$\hat{K}_n(1)\phi_m(\mathbf{r}_1) = \frac{e^2}{4\pi\epsilon_0} \int_{-\infty}^{\infty} \phi_n^*(\mathbf{r}_2) \frac{1}{|\mathbf{r}_1 - \mathbf{r}_2|} \phi_n(\mathbf{r}_1)\phi_m(\mathbf{r}_2)d\mathbf{r}_2,$$ (2.45)

accounts for the exchange interaction that is a consequence of the indistinguishably of the electrons. Solving Equation 2.43 gives the optimal one electron orbitals, that minimize the energy if the many-body state is expressed using one configuration. The issue with Equation 2.43 is that the operators $J_n(1)$ and $K_n(1)$ themselves depend on the orbital basis set. Therefore, when optimizing the single-electron orbitals, the Coulomb operator and the exchange operator change. We need to solve Equation 2.43 *self-consistently*, i.e. to solve the eigenvalue problem in Equation 2.43 iteratively until the form of the operators has converged. For this reason, the Hartree–Fock method is often referred to as *self-consistent field theory*.

Electronic correlations are entirely absent in the Hartree–Fock description of the molecule. By describing the many-electron state of the molecule using a single configuration with an optimized orbital basis set, we neglect all correlations. Due to the neglected electronic correlations, the Hartree–Fock method is often called a quasi classic method, as the most prominent feature of quantum mechanics, the correlation of electrons in different orbitals, is absent. Everything that is necessary to

describe the system that goes beyond the Hartree–Fock method, is then understood as electronic correlations and quantum features.

The orbitals that solve Equation 2.43 to Equation 2.45 self-consistently are called *molecular orbitals*. These orbitals are now able to represent the electrons in the molecule optimally on the one-electron level. Whereas the atomic orbitals we started with were solely centered at the nuclei of the molecule, the molecular orbitals might now be delocalized. The electrons occupy these orbitals with integer occupation numbers. This uncorrelated approach is for closed shell molecules a good starting point, however, many situations also require to account for electron correlations. Especially when quantitative predictions of ground state energies and energy gaps is required, the energy reduction in the molecule as a result of electronic correlations needs to be considered (*correlation energy*). Further has the Hartree–Fock method problems to describe dissociation energies, in particular for open-shell fragments [3] (see for example Figure 2.1).

When introducing correlations in the next sections, we use the molecular orbitals obtained from the Hartree–Fock method, as they are the optimal orbitals on the one-electron level. Then we reintroduce correlations to the many-body state by extending the many-body space with more configurations. The resulting family of methods is called *post-Hartree–Fock methods*, as they go beyond Hartree–Fock, but still use the Hartree–Fock results significantly. Such methods are for example the *Complete Active Space Theory* and the *Configuration Interaction*, which will be explained in the following two Sections 2.3.2 and Section 2.3.3, and the *matrix product state approach* we will describe in detail in Section 2.4.

## 2.3.2 Complete Active Space Theory

One popular post-Hartree–Fock method is the *Complete Active Space Theory* (CAS) [76], which extends the semiclassical calculation by quantum corrections, allowing superpositional many-body states. Where in the Hartree–Fock method, at all times, only one configuration is considered, in the CAS method, some of the neglected configurations are reintroduced. This allows the system to be in superpositional states and thereby reintroduces electronic correlations to the many-body state representation.

We start with an orbital basis we obtained from a previous Hartree–Fock calculation. The molecular orbitals are categorized into three classes:

- The *core orbitals*, that remain doubly occupied throughout the entire calculation. These orbitals do not need to be considered in the quantum part of the calculation, since two electrons in a singlet state occupying an orbital cannot

contribute to any correlations. These orbitals and the occupying electrons are again considered on the Hartree–Fock level.

- The *active orbitals*, that are allowed to be occupied partly by electrons that enter correlated quantum states. These orbitals may contribute to superposition states and therefore they are treated on the full quantum mechanical level. For these orbitals, the additional configurations are added into the calculation.

- The *empty orbitals*, that remain empty throughout the entire calculation. Such orbitals are usually related to very high energies, therefore an occupation may be unlikely when doing ground state studies or studies involving time evolution introduced by small excitations. The empty orbitals are not considered in the quantum part of the calculation.

Using these different types of orbitals, the many-body Hilbert space state is extended by the corresponding configurations and therefore allows to consider quantum effects. We can write the many-body state in Equation 2.35 approximately as a product

$$|\Psi\rangle \approx |\Psi_{CAS}\rangle = |\Psi_C\rangle \otimes |\Psi_A\rangle \otimes |\Psi_E\rangle \,, \tag{2.46}$$

where $|\Psi_C\rangle$ is the part of the state describing electrons in core orbitals, $|\Psi_A\rangle$ is the part of the state describing electrons in active orbitals, and $|\Psi_E\rangle$ is the part of the state describing the empty orbitals. The correlation effects are only enabled in the active part of the many-body state ($|\Psi_A\rangle$), whereas the core orbitals and the empty orbitals are described on the Hartree–Fock level.

With some orbitals being active on the quantum mechanical level, we now can write down the Hamiltonian in the many-body basis, for which we can solve for the ground state or for which we can describe the time-dependence. For example, if we found the ground state $|\Psi^0_{CAS}\rangle$ of the many-body Hamiltonian, we will have a better representation of the physical ground state of the molecule compared to previous Hartree–Fock state in any case. However, this is not the best quantum representation we can find using a given number of active orbitals. We can start to optimize the molecular orbitals as we did in Hartree–Fock, but now based on the correlated calculation. If we calculate the *one body reduced density matrix* (OBRDM), which is given by

$$\gamma_{ij} = \sum_{\sigma} \langle \Psi^0_{CAS}| \, \hat{c}^\dagger_{i\sigma} \hat{c}_{j\sigma} \, |\Psi^0_{CAS}\rangle \,, \tag{2.47}$$

for $i$ and $j$ are indices of active orbitals, we will get a densely populated matrix in case the state is correlated. Diagonalizing the OBRDM lets us find new orbitals, that are now shaped based on the quantum mechanical calculation. These orbitals

are called *natural orbitals*. The natural orbitals are not the best possible orbitals on the one-electron level, as those are the orbitals obtained from the Hartree–Fock calculation, however, when considering superpositional many-body states and electronic correlations, the natural orbitals obtained from diagonalizing the OBRDM are advantageous.

The natural orbitals are a new set of single electron states, that we can use to expand our many-body state in. Further do they allow to quantify how entangled the electrons in the many-body state are. For uncorrelated states in Equation 2.47 the diagonal elements in $\gamma$ are integer and all non-diagonal elements are zero. This is a typical Hartree–Fock state, were all electrons are localized in specific orbitals. Now, in CAS, with the added correlations, also partly populated orbitals are possible and then the OBRDM obtains off-diagonal elements and the diagonal elements become fractional. The fractional occupation numbers of the natural orbitals are a measure for entanglement in the system [94].

The CAS method is a widely used method, especially in ground state theory, as it combines both, an inclusion of quantum features, as well as, optimization of the orbitals. Many benchmark calculations of ground states for molecules such as HNO [95], are done using the CAS. However, CAS is not that prominently featured in the area of dynamics. There are existing time-dependent CAS methods [96], but in most situations it is not the method of choice. Here, other methods are popular, for example approaches based on configuration interaction.

### 2.3.3 Configuration Interaction

One of the post-Hartree–Fock methods that is widely used in the description of time-dependent phenomena is the method named *configuration interaction* (CI) [77]. Again, we start from the Hartree–Fock ground state configuration and add new configurations to the reduced representation of the many-body state. But now in the CI approach, we choose the configurations in terms of electronic excitations.

Let $|\psi_0^{HF}\rangle$ be the Hartree–Fock ground state, with $N$ electrons occupying the $N/2$ lowest molecular orbitals and the remaining $L - N/2$ orbitals being unoccupied. Let us excite one electron from the initially occupied orbitals to one of the initially unoccupied orbitals. For example, we can form the state

$$|\psi_{i\sigma}^{j\sigma}\rangle = \hat{c}_{i\sigma}^{\dagger}\hat{c}_{j\sigma}|\psi_0^{HF}\rangle , \qquad (2.48)$$

i.e. the state where an electron with spin $\sigma$ has been annihilated from the orbital $j$ and promoted to one initially unoccupied orbital $i$. As we are working in the occupation

number basis, the resulting state $|\psi_{i\sigma}^{j\sigma}\rangle$ is again a basis state of the many-body basis. Of course, the orbital $i$ needs to be occupied in the Hartree–Fock ground state and the orbital $j$ needs to be unoccupied, as otherwise the result on the right hand side of Equation 2.48 is zero (see rules for second quantization operators). Using this type of excitations we can add more and more configurations to our reduced representation of the many-body state. Working with the CI representation of the many-body state will improve results compared to the Hartree–Fock representation of the many-body state (for both, representing eigenstates, as well as representing time-dependent states).

The most basic class to include are single particle-hole excitations, which are also called *configuration interaction singles* (CIS). Here we add all possible single excitations to the reduced many-body state. This means, we expand the many-body state as

$$|\psi(t)\rangle \approx |\psi_{CIS}(t)\rangle = c_0(t)\,|\psi_0^{HF}\rangle + \underbrace{\sum_{ij\sigma} c_{ij}(t)\hat{c}_{j\sigma}^\dagger \hat{c}_{i\sigma}\,|\psi_0^{HF}\rangle}_{\text{1h 1p}}. \quad (2.49)$$

The reduced many-body Hilbert space now includes the Hartree–Fock configuration and all possible (non-vanishing) single excitations $\hat{c}_{j\sigma}^\dagger \hat{c}_{i\sigma}\,|\psi_0^{HF}\rangle$. In case of a molecule including $N$ electrons and an orbital basis of $L$ orbitals, we have in total $2LN$ excited configurations and the Hartree–Fock ground state configuration. For the example outlined above of a molecule with 20 electrons and 50 orbitals, this reduces the number of configurations to 2001, which only requires 16 kilobytes to store in memory.

However, the many-body Hamiltonian does not mix the Hartree–Fock ground state and the newly added CIS configurations. This is a consequence of Brillouin's theorem [78], which states that all matrix elements of the Hamiltonian of the form $\langle \psi_{i\sigma}^{j\sigma}|\,H\,|\psi_0^{HF}\rangle = 0$ vanish. Therefore, we need to consider further classes of particle-hole excitations.

We can improve the results by including single and double particle-hole excitations (CISD)

$$|\psi(t)\rangle \approx |\psi_{CISD}(t)\rangle = |\psi_0^{HF}\rangle + |\psi_{CIS}(t)\rangle + \underbrace{\sum_{ijkl\sigma\tau} c_{ijkl}(t)\hat{c}_{j\sigma}^\dagger \hat{c}_{i\tau}^\dagger \hat{c}_{k\tau} \hat{c}_{l\sigma}\,|\psi_0^{HF}\rangle}_{\text{2h 2p}}, \quad (2.50)$$

in our reduced representation of the many-body state, where all configurations with up to two excited electrons form the many-body state. This class of states couples directly to the Hartree–Fock starting state [61].

The total number of configurations that belong to this class is

$$\text{\#CI Doubles} = 1/4(N-1)N(2L-N-1)(2L-N), \qquad (2.51)$$

which is substantially larger than what we have seen for CIS. But still, CISD calculations are easily possible with today's computational means. Returning to the example of a molecule with 20 electrons and 50 orbitals, we now need 601401 configurations to describe a many-body state within CISD, which requires 4.811 megabytes in memory. Such calculations are still easily manageable on desktop computers.

We can proceed like this and include more and more excitations, which will improve the quality of our many-body state representation. However, we already have seen the large jump in the number of excitation at the step from CIS to CISD. It continues like this, with more and more configurations coming with every CI class of excitation. The general formula to calculate the number of configurations in the class of $n$ excitations is

$$\text{\# configuration in class with } n \text{ excitations} = \binom{N}{n}\binom{2L-N}{n}, \qquad (2.52)$$

which shows the factorially growing number of possible configurations. When going to $n = N$ excitations, we obtain the complete many-body state in Equation 2.35. This demonstrates why the many-body state including all possible configurations is also called *full configuration interaction state* or full CI state. However, as explained above, going beyond CIS and CISD is in most situations computationally very challenging. Therefore most calculations focus on lower excitations classes, which is often justified by the increasing energy corresponding to high excitations.

The CI method has been applied to both, to ground state calculations [97], as well as, to time-dependent calculations [98]. Among the Hartree–Fock method, and the CAS method, most modern quantum chemistry codes feature a CI implementation [80, 91] that allows for arbitrary forms of excitations to be included in the quantum calculation.

When it comes to time-dependent studies, however, the CAS method and the CI method have a problem related to their choice of configurations. Both methods restrict the number of configurations artificially, which removes a large number of configurations from the considered many-body Hilbert space, although these configurations may become important within the dynamics. It is difficult to estimate the error coming with this restriction, especially if the underlying effects are unknown and the form of the configurations adapts time-dependently. Next we will outline a method that is more dynamic in the truncation of the many-body Hilbert space, which makes it in particular suited for time-dependent studies.

## 2.4 Matrix Product States

In the previous two chapters we have outlined three methods to simplify the representation of the many-body state in Equation 2.35. The three methods rely on the concept that a limited number of configurations is sufficient to represent the many-body state approximately. They choose a specific form of configurations and then perform the calculation within this reduced but fixed configurational space. This can be problematic for different reasons: On the one hand, choosing configurations gives the calculation a bias that propagates through the entire calculation. On the other hand, especially when calculating dynamic quantities, the configurations which represent the many-body state may change time-dependently. Then the many-body state is represented well in the initial state, however, after the system evolved dynamics for a couple of femtoseconds, the configurations involved may have changed [98]. It is very difficult to identify from the approaches outlined above, using statically chosen configurations, whether the many-body state is represented appropriately at all times.

To circumvent this behavior, we will introduce a more dynamic approach to represent the many-body states, which is able to simplify the many-body state without cutting any configurations (within the fixed orbital space). Instead of cutting configurations from the many-body Hilbert space, this approach directly tackles the electronic correlations [99]. Based on the assumption that not all electrons will be essentially correlated with each other, the approach dynamically cuts entanglement from the many-body state, however, the entanglement is able to reenter the many-body state dynamically if necessary [52]. With this dynamic inclusion of correlations and entanglement, the representation does not suffer from the static concept of the time-dependent Hartree–Fock method or the time-dependent configuration interaction singles and doubles. This form of representing the many-body state is called *matrix product state* (MPS) approach [100] and will be introduced in the following section. We will introduce it in the context of quantum chemistry, although, its origin is in condensed matter physics [42, 43]. Most of the following discussion can be directly translated to condensed matter physics [101] and other fields as well [102, 103].

### 2.4.1 Definition

To understand the idea behind MPS approach, it is good to start from the many-body state as given in Equation 2.35. The most crucial part in Equation 2.35 are the time-dependent expansion coefficients $c_{n_{1\uparrow}n_{1\downarrow}\cdots n_{L\uparrow}n_{L\downarrow}}(t)$ as they are too many to store on today's computers. We are now turning to the mathematical area of tensors, where

we understand the set of coefficients $c_{n_{1\uparrow}n_{1\downarrow}\cdots n_{L\uparrow}n_{L\downarrow}}(t)$ as a complex tensor of rank $2L$ that changes time-dependently. All possible coefficients forming the expansion of the many-body state are encoded in this large mathematical object. The idea is, originating from the idea of matrix decompositions [104], to decompose this large tensor into a sequence of low rank tensors. For example, in

$$c_{n_{1\uparrow}n_{1\downarrow}\cdots n_{L\uparrow}n_{L\downarrow}}(t) = \sum_{a_1 a_2 \cdots a_{L-1}} A_{a_1}^{n_{1\uparrow}n_{1\downarrow}}(t) A_{a_1 a_2}^{n_{2\uparrow}n_{2\downarrow}}(t) \cdots A_{a_{L-1}}^{n_{L\uparrow}n_{L\downarrow}}(t), \qquad (2.53)$$

$$= A^{n_{1\uparrow}n_{1\downarrow}}(t) A^{n_{2\uparrow}n_{2\downarrow}}(t) \cdots A^{n_{L\uparrow}n_{L\downarrow}}(t) \qquad (2.54)$$

with $A^{n_{1\uparrow}n_{1\downarrow}}(t)$ being a row vector (rank 1 tensor), $A^{n_{i\uparrow}n_{i\downarrow}}(t)$ being matrices (rank 2 tensors), and $A^{n_{L\uparrow}n_{L\downarrow}}(t)$ being a column vector (rank 1 tensor). This sequence of vector-matrix-…-vector products then exactly reproduces the original expansion coefficient $c_{n_{1\uparrow}n_{1\downarrow}\cdots n_{L\uparrow}n_{L\downarrow}}(t)$. Instead of storing all coefficients in a large tensor $c_{n_{1\uparrow}n_{1\downarrow}\cdots n_{L\uparrow}n_{L\downarrow}}(t)$, we store them factorized in $4L$ vectors and matrices.

There is no approximation behind this decomposition and such a decomposition is always possible by sequentially applying singular value decomposition on the coefficient tensor [104]. Schollwöck layed down this process very detailed in his seminal work [52]. The complete MPS representation of the many-body state is then written as

$$|\Psi(t)\rangle = |\Psi(t)\rangle_{MPS} \qquad (2.55)$$

$$= \sum_{n_{1\uparrow}n_{1\downarrow}\cdots n_{L\uparrow}n_{L\downarrow}} A^{n_{1\uparrow}n_{1\downarrow}}(t) A^{n_{2\uparrow}n_{2\downarrow}}(t) \cdots A^{n_{L\uparrow}n_{L\downarrow}}(t) |n_{1\uparrow}n_{1\downarrow}\cdots n_{L\uparrow}n_{L\downarrow}\rangle, \quad (2.56)$$

including all configurations $|n_{1\uparrow}n_{1\downarrow}\cdots n_{L\uparrow}n_{L\downarrow}\rangle$. At this point we did not cut any information from the representation of the many-body state.

## 2.4.2  Origin and Properties

Although MPS are commonly used in today's quantum chemistry [48, 51, 105–109], they originated in the field of condensed matter physics in a completely different shape. It was White [42, 43] who first came up with a new, size consistent extension of renormalization group in order to study the ground state energy of long one-dimensional chains of spins, which he described using the Heisenberg model. His method later became known as *density matrix renormalization group* (DMRG) [99]. White was able to calculate new benchmark level ground state energies, spin expectation values and the Haldane gap using DMRG for astonishingly long chains (up to $L = 300$).

DMRG is an efficient variational method to find ground states of many-body systems. It is able to reduce the effective degrees of freedom of a problem efficiently and only includes those that are necessary to represent the many-body ground state. Today, DMRG and many of its extensions are very popular in condensed matter physics [110–115], high-energy physics [116–118], and quantum information theory [119–122] and still allows for benchmark level results in many fields it is applied to.

Shortly after the DMRG has been introduced by White in 1992, Östlund and Rommer [123] noticed in 1995 the similarity of the DMRG approach with a variational concept known from information compression called *tensor trains* [124, 125] that commonly became known as MPS. Later, Noshino noticed [126] that an MPS-like ansatz was already used earlier by Kramers and Wannier in 1941 [127] and in 1986 by Baxter [128]. After understanding the mathematical origin of the DMRG method, a family of variational methods emerged quickly, ranging from ground and excited state evaluation [129–131], many different methods to describe time-dependence [55, 56, 132–134] and systems at finite-temperature [135–137], to pushing into (quantum) machine learning [103].

The keywords DMRG and MPS are sometimes used as synonyms in literature, although they are related to different subjects. Where MPS is the approach to represent the many-body state of a quantum system, DMRG is the method to obtain MPS variationally with respect to ground state energy for example. However, in the DMRG algorithm initially proposed by White, the MPS approach as given in Equation 2.56 is not directly apparent. For this historic reason, there are two types of DMRG implementation, one based on the algorithm by White, and one based directly on the MPS approach, although the two methods are mathematically equivalent. Older implementations [138–140] use the algorithm by White, whereas almost all new implementations rely on the more flexible MPS formulation [51, 107, 141, 142].

**Area Law**

The main benefit of the MPS approach is the mathematically proven advantage we have when studying gapped ground states of one-dimensional systems with short-ranged interaction. Here, the MPS approach has a mathematically proven feature to reduce the number of degrees of freedom to an amount that does not grow exponentially with system size (in contrast to Equation 2.35). The theorem behind this feature is the *area law* of condensed matter physics [143, 144]. The area law states that, for systems with short-ranged interaction and a gapped ground state, the entanglement entropy of the ground state $S(\rho) = -tr\left[\rho_0 log \rho_0\right]$ for any two subsystems $\mathcal{K}$ and $\mathcal{M}$ scales with the interface area $A_{\mathcal{K}\mathcal{M}}$ of these two systems (see

a)

subsystem $\mathcal{K}$     subsystem $\mathcal{M}$     subsystem $\mathcal{K}$

$A_{\mathcal{KM}}$     $A_{\mathcal{KM}}$

b)

subsystem $\mathcal{K}$

subsystem $\mathcal{M}$

$\rho_{\mathcal{M}} = tr_{\mathcal{K}}\{|\psi\rangle\langle\psi|\}$

surface $A_{\mathcal{KM}}$

$S(\rho_{\mathcal{M}}) \propto A_{\mathcal{KM}}$
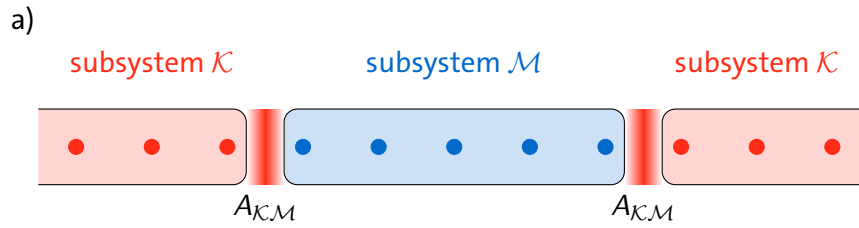
**Figure 2.3.:** a) Partition of a one-dimensional system in two parts, showing the constant area of interface $A_{\mathcal{KM}}$. The interface area between subsystem $\mathcal{K}$ and subsystem $\mathcal{M}$ does not grow with the size of subsystem $\mathcal{K}$ or with the size of subsystem $\mathcal{M}$. With the area law (see b) ), this means also the entanglement entropy of subsystem $\mathcal{K}$ is constant. b) Entanglement entropy of the bipartite system of subsystem $\mathcal{K}$ and subsystem $\mathcal{M}$. If the system has short-ranged interaction and a gapped ground state, the entangled entropy of any two subsystems scales as the area of the interface of these subsystems.
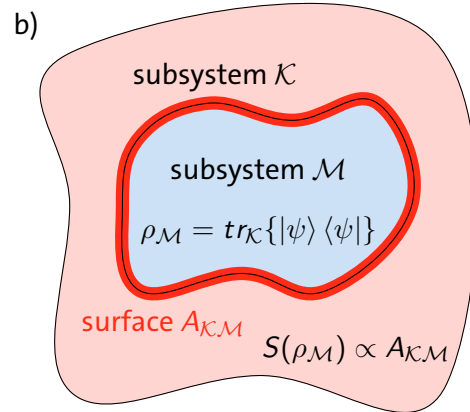
Figure 2.3 b) ). The entanglement entropy does not directly depend on the size of the two subsystems, only their intersection surface is crucial. However, if we pick a random state from the many-body Hilbert space, it will most likely violate the area law by having an entanglement entropy scaling with the size of the two subsystems. The entanglement entropy for different partitions of the random state will scale with the size of the partitions. For ground states we only want to consider states where the entanglement entropy is independent (up to finite size effects) of the subsystem sizes. By focusing on states conforming to the area law, i.e. the *area law states*, we can reduce the degrees of freedom for ground state calculations drastically.

For one-dimensional systems, the area of interface between two subsystems is constant due to geometry. On the one-dimensional line, there will be two points in each subsystem being closest to the other subsystem, which form the (one-dimensional) area of interface (see Figure 2.3 a) ). The area does not depend on the size of the subsystems, i.e. with the result from the area law, we know that the entanglement entropy is constant as well. One therefore wants to work in the manifold of the many-body Hilbert space that shows a constant entanglement entropy for any bipar-
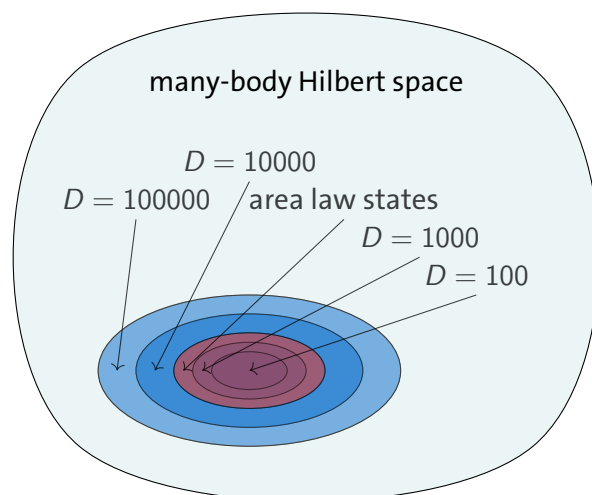
**Figure 2.4.:** Graphical illustration of the many-body Hilbert space and the MPS manifold for various exemplary MPS bond dimension $D$. The shown bond dimensions $D$ are examples and depend on the type of the system.

tition of the system. This manifold is often referred to by being the tiny *corner of the many-body Hilbert space* the ground states lives in [101, 145].

In Section 2.4.1 we introduced the MPS approach as sequential decomposition of the expansion coefficients of the complete many-body state in Equation 2.35, where we also highlighted that this can be done for any state without introducing a mathematical error. But when describing the gapped ground state of a one-dimensional, short-ranged system, we know from the area law that we can focus on states with constant entanglement entropy. We approach the states not conforming to the area law by limiting the matrix dimension $D$ of the matrices $A^{n_{i\uparrow} n_{i\downarrow}}(t)$ in the MPS approach (see Equation 2.56) to be constant (not depending on the system size). We will discuss in Section 2.4.5 the reason for this behavior. There exist a specific bond dimension where the MPS exactly represents the manifold of area law states, however this dimension is unknown a priori (see Figure 2.4). The necessary bond dimension need to be evaluated by convergence tests. With the limitation of the matrix dimension in the MPS we achieve two things: On the one hand, we neglect all states violating the area law, and on the other hand, we reduce the computational effort to handle the many-body state representation.

However, the area law is limited to gapped systems with short-ranged interaction and does not say anything about entanglement in case the interaction is long-ranged. The quantum chemical systems we are interested in encounter long-ranged interaction for two reasons: First, due to the long-ranged Coulomb interaction between electrons in different orbitals (see Equation 2.12), and second, due to the artificial one-dimensional lineup of the delocalized molecular orbitals to fit into the one-dimensional shape of

the sequence of matrix products in Equation 2.56. Both of these reasons forbid the application of the area law, therefore, there is no mathematical guarantee that MPS with limited bond dimension are a valid approach to represent the many-body state in quantum chemical systems.

Further is the area law limited to gapped ground states and it does not say anything about how the entanglement evolves with time. In time-dependent situations, it is possible that the many-body state leaves the area of the Hilbert space we are able to resolve efficiently using the MPS approach to represent the many-body state. This issue becomes even more problematic in long time studies. The more time evolves, the more the system may leave the area of the Hilbert space the MPS are able to resolve. This issue is called the *runaway error*. It is one of the reasons why, in this study, we will completely focus on the short-time behavior that takes place within a few femtoseconds after excitation. The idea is that the exact many-body state has not left the area of the Hilbert space in the time range we are looking at. There, the MPS approach is still able to describe the many-body state appropriately. Later in this thesis, we will outline a couple of concepts to reduce the runaway error, as it might be possible that the many-body state can be described by the MPS approach although the entanglement entropy has left the manifold of area law states.

Despite the bad news on long-ranged interaction and time-dependence, the MPS approach has shown striking performance for both, long-ranged systems, as well as in time-dependent situations. For many years, MPS are heavily used in quantum chemistry to predict ground states, excited states [48, 146–149], avoided crossings [48, 49, 150, 151], and spin-splittings [152–155] for many molecules regardless the system being long-ranged and high-dimensional. Of course, the guarantee of the area law does not apply here. However, this does not forbid the use of MPS as a valid approach to represent the many-body state. The same holds for time-dependent studies, also here MPS have proven to be a very efficient way in describing the time-dependent many-body state, ranging from spin dynamics [54, 156–159], transport properties[54, 160–163], to ionization potentials [60, 164].

## 2.4.3  Graphical Notation

Now we want to introduce some general concepts that will turn out to be helpful for the following discussions of the MPS approach. The MPS approach is a special case of the more general concept of *tensor networks* [101]. Tensor network theory includes the one-dimensional approach to represent the many-body state (the MPS as outlined above), but also covers higher dimensional decompositions of the many-body state such as *tree-tensor networks* [165–167], *multi-scale entanglement renormalization ansatz* (MERA) [168–170], and *projected entanglement pair states* (PEPS) [171–174].

|   a)   |   b)   |   c)   |   d)   |
|--------|--------|--------|--------|

a scalar     a vector     a matrix     a rank $n$ tensor
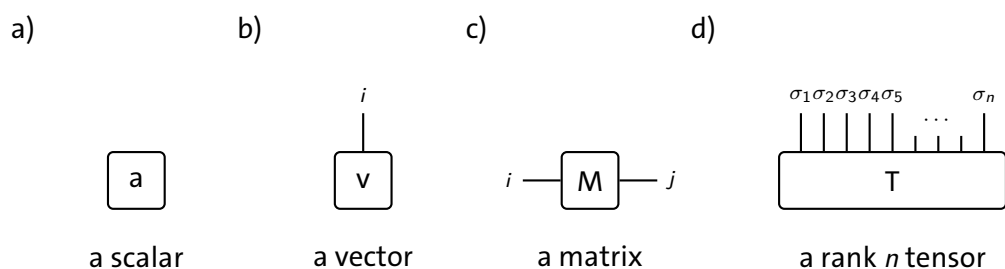
**Figure 2.5.:** Graphical representation of tensors with various ranks. a) a scalar is depicted using a box without any lines attached. b) a vector is depicted using a box with one line attached. c) a matrix is depicted using a box with two lines attached. d) a rank $n$ tensor is depicted using a box with $n$ lines attached.

Later in this section, will we explain the algorithms to perform operations on MPS in the language of tensor networks, therefore it will be beneficial to have a good understanding of the ideas behind the tensor network concept and its notation [101].

Tensor networks are (graphical) representations of linear algebra operations. To every tensor network we can either write down a formula specifying the operation or we can draw a graphic that represents the network much more comprehensively. The large number of indices and sums occurring in tensor networks usually obscures the operation from analytic formulas, however, the graphical representation makes it easy to understand it at first sight.

In these graphical representations, the tensors are described by different boxes that are connected by lines that we call *bonds* in the following. These bonds represent free indices of the tensor. For example, a scalar $a$ does not have any free indices, therefore, it is represented by a box without any lines attached (see Figure 2.5 a) ) . A vector **v** has one free index, therefore it is described by a box with one line attached to its graphical representation (see Figure 2.5 b) ). A matrix $\underline{M}$ has two free indices, therefore it is described by a box with two lines attached to its graphical representation (see Figure 2.5 c) ). We can continue this for arbitrary tensors of rank $n$, that will have $n$ lines attached to its box (see Figure 2.5 d) ). The form of the box will not have any intrinsic meaning in this work, however, we will use different shapes to distinguish tensors belonging to different quantities.

There are two types of bonds: We have *open bonds* and we have *closed bonds*. Whereas the open bonds have only one end connected to a tensor, the closed bonds

have both ends connected to tensors. Whenever a bond is closed, it represents a sum over an index. For example, the trace of a matrix can be represented by

$$tr(\underline{M}) = \sum_i M_{ii} = \boxed{M} \, i \, , \qquad (2.57)$$

where the result is a scalar, since it does not have any free bonds. In general, it does not matter how the bonds are attached to the box, they can be attached at the upper and the lower part, or at the left and the right of a box. Sometimes we give the index a name (such as in Equation 2.57), however, in most cases it is up to the reader to keep track of which bond represents which index. We can depict any linear tensor operation using this notation, for example, matrix multiplication $\underline{C} = \underline{A} \cdot \underline{B}$ is visualized as

$$C_{ij} = \sum_k A_{ik} B_{kj} = \; i \longrightarrow \boxed{A} \overset{k}{-} \boxed{B} \longrightarrow j \, , \qquad (2.58)$$

with one closed bond ($k$) and two open bonds ($i$ and $j$) since the result of the matrix multiplication is again a matrix.

The many-body state in its MPS representation as given in Equation 2.56 becomes in this graphical notation

$$|\psi_{MPS}\rangle = \sum_{n_{1\uparrow} n_{1\downarrow} \cdots n_{L\uparrow} n_{L\downarrow}} \overset{n_{1\uparrow} n_{1\downarrow} \; n_{2\uparrow} n_{2\downarrow} \qquad n_{L\uparrow} n_{L\downarrow}}{\widehat{A[1]} - \widehat{A[2]} - \cdots - \widehat{A[L]}} \; |n_{1\uparrow} n_{1\downarrow} \cdots n_{L\uparrow} n_{L\downarrow}\rangle \, , \qquad (2.59)$$

where we substituted the sequence of matrix products by its graphical representation. From this graphical representation, it can be seen easily, that for a fixed configuration $n_{1\uparrow} n_{1\downarrow} \cdots n_{L\uparrow} n_{L\downarrow}$, the very left and the very right tensor need to be rank 1 tensors (vectors) and the remaining are rank 2 tensors (matrices). When incorporating the indices $n_{i\sigma}$ which specify the configuration into the tensors, all ranks are increased by two (This is why the tensors in Equation 2.59 have three (four) bonds).

The state norm of a many-body state in the MPS representation $\langle \psi_{MPS} | \psi_{MPS} \rangle$ is calculated as (using the orthonormality of the occupation number basis and the sum rule for closed bonds)

$$\langle \psi_{MPS} | \psi_{MPS} \rangle = \sum_{n_{1\uparrow} n_{1\downarrow} \cdots n_{L\uparrow} n_{L\downarrow}} A^{*n_{1\uparrow} n_{1\downarrow}} \cdots A^{*n_{L\uparrow} n_{L\downarrow}} A^{n_{1\uparrow} n_{1\downarrow}} \cdots A^{n_{L\uparrow} n_{L\downarrow}} \qquad (2.60)$$

$$= \begin{matrix} \widehat{A[1]} - \widehat{A[2]} - \cdots - \widehat{A[L]} \\ | \qquad | \qquad \qquad | \\ \widehat{A[1]} - \widehat{A[2]} - \cdots - \widehat{A[L]} \end{matrix} \, , \qquad (2.61)$$

where we used the convention of complex conjugated matrices and vectors to have their indices at the bottom (This is just a convention that does not apply in general in tensor networks). The result of the overlap $\langle\psi_{MPS}|\psi_{MPS}\rangle$ is a scalar, therefore, its graphical representation in Equation 2.61 does not have any open bonds.

### 2.4.4 Left- and Right-Orthonormalization

Now we want to discuss a couple of properties of the MPS approach that often allow to reduce the complexity of operations on MPS. We can take advantage of the *gauge freedom* of MPS and shape the MPS to have properties that simplify following calculations.

At any closed bond $i, j = i + 1$ in the sequence of matrix products in Equation 2.61, we can insert the identity operator in form of a unitary matrix ($U^\dagger U = 1$)



$$\cdots \!-\!\!\overset{n_{i\uparrow}n_{i\downarrow}}{A[i]}\!\!-\!\!\overset{n_{j\uparrow}n_{j\downarrow}}{A[j]}\!\!-\!\cdots \;=\; \cdots \!-\!\!\overset{n_{i\uparrow}n_{i\downarrow}}{\underset{\tilde{A}[i]}{A[i]\!-\!U^\dagger}}\!\!-\!\!\underset{\tilde{A}[j]}{U\!-\!\overset{n_{j\uparrow}n_{j\downarrow}}{A[j]}}\!\!-\!\cdots \tag{2.62}$$

$$=\; \cdots \!-\!\!\overset{n_{i\uparrow}n_{i\downarrow}}{\tilde{A}[i]}\!\!-\!\!\overset{n_{j\uparrow}n_{j\downarrow}}{\tilde{A}[j]}\!\!-\!\cdots \;, \tag{2.63}$$

where $\tilde{A}[i]$ is the from the left by $U$ multiplied matrix. In these steps, the overall shape of the MPS does not change, however, the matrices $A[i]$ differ from the matrices $\tilde{A}[i]$. Therefore, the MPS representation of a many-body state is never unique. We can always introduce identities at any closed leg, which may change the elements of the MPS tensors, but leaves the expansion coefficient resulting after performing all matrix products unchanged.

Instead of inserting identities, we can also apply decomposition methods on the matrices. For example, we can QR decompose the very first tensor of the MPS

$$\overset{n_{1\uparrow}n_{1\downarrow}}{A[1]}\!\!-\!\!\overset{n_{2\uparrow}n_{2\downarrow}}{A[2]}\!\!-\; =\; \underset{\tilde{A}[1]}{Q}\!-\!\underset{\tilde{A}[2]}{R\!-\!\overset{n_{2\uparrow}n_{2\downarrow}}{A[2]}}\!\!- \tag{2.64}$$

and now, instead of multiplying $R$ back to form $A[1]$, multiplying it to the right into the following tensor $A[2]$. This leaves us again with the very same MPS, however, we know that the first tensor in the MPS in Equation 2.59 has the property

$$\underbrace{\tilde{A}[1] \atop \tilde{A}[1]}_{S[1]} = \Big[ = 1, \tag{2.65}$$

as this is a property of the QR decomposition $Q^\dagger Q = 1$. The tensor $S[1]$ is the *partial overlap* at site 1 that is in this case the identity. Then we can apply the same procedure to the second tensor in the MPS and obtain the identity

$$\underbrace{\tilde{A}[1]-\tilde{A}[2] \atop \tilde{A}[1]-\tilde{A}[2]}_{S[2]} = \Big[ = 1, \tag{2.66}$$

and continue to any arbitrary orbital $k$. If we know that this procedure has been applied to an MPS on the left of orbital $k$, we can simplify Equation 2.65 and Equation 2.66, since it is guaranteed that they will give the identity operator. For example when, calculating the norm as given in Equation 2.61, we can benefit a lot from this feature. This process is called *left-orthonormalization* of the MPS [52]. Although it seems to be of little use at this point, since it also increased the overhead of the calculation to perform the QR-decompositions, it will be very beneficial in the following. In most cases, the orthonormalization comes at no additional cost (see Section 2.4.5).

We can also bring the MPS in a *right-orthonormalized* form by applying LQ decomposition successively from the right

$$-\!\!\overset{n_{L\uparrow} n_{L\downarrow}}{A[L]} = -\!\!\underset{\tilde{A}[L]}{\overset{n_{L\uparrow} n_{L\downarrow}}{L - Q}}, \tag{2.67}$$

which then allows to simplify operations such as

$$\overset{\tilde{A}[L]}{\underset{\tilde{A}[L]}{\big\}}} = \Big] = 1. \tag{2.68}$$

Again, we can continue with the tensor $j = L - 1$

$$
\begin{array}{c}
\begin{array}{c}
\text{─}\tilde{A}[j]\text{─}\tilde{A}[L]\text{─} \\
\quad\;| \qquad\; | \\
\text{─}\tilde{A}[j]\text{─}\tilde{A}[L]\text{─}
\end{array}
= \bigg] = 1.
\end{array}
\tag{2.69}
$$

An MPS can also be in a *mixed canonical form*,

$$
\begin{array}{c}
A[1]\text{─}\cdots\text{─}A[i]\quad\text{─}A[k]\text{─}\cdots\text{─}A[L] \\
\;|\qquad\quad\;|\qquad\qquad|\qquad\qquad\; | \\
A[1]\text{─}\cdots\text{─}A[i]\text{─}A[j]\text{─}A[k]\text{─}\cdots\text{─}A[L]
\end{array}
= \;\;\text{─}A[j]\text{─}
\tag{2.70}
$$

where on the left side of the orbital $j$ the MPS tensors are left-orthonormalized and on the right side of orbital $j$ the MPS tensors are right-orthonormalized. We will discover such MPS when we are introducing the sweeping algorithm in Section 2.4.9.

## 2.4.5  Truncation and Entanglement

We have discovered various concepts of the MPS representation of the many-body state. We outlined its properties in terms of entanglement and have seen that they are not unique, but can be gauged to have special properties. However, we have not yet discussed where the reduction of complexity is applied to the many-body state. We introduced MPS in Equation 2.56 as the exact decomposition of the expansion coefficients of the many-body state, which is not related to any approximation. Therefore MPS, as described at this point, still represent the complete many-body state in Equation 2.35. Now we want to discuss how to simplify the representation of the many-body state using the MPS approach.

Earlier, we discussed that the complete representation of the many-body state is impossible to manage for medium sized basis sets due to the large number of expansion coefficients. When using the exact MPS representation of the many-body state, the number of coefficients is still growing factorially with the system size. To gain any computational benefit compared to the complete representation, we need to reduce the number of degrees of freedom of the MPS representation, which translates to a reduction of the bond dimension of the MPS tensors. For one-dimensional systems, with short-ranged interaction and a gapped ground state, we know that this reduction of dimension must be advantageous.

Next, we will discuss methods that reduce the MPS tensor dimension by using tensor decomposition based on *singular value decomposition*.

In Section 2.4.4 we have already met the first two tensor decomposition methods, namely the LQ and the QR decomposition. In line with these tensor decomposition

methods, we can decompose any of the tensors in the MPS in terms of *singular value decomposition* (SVD)



$$\ldots \quad \overset{n_{i\uparrow}n_{i\downarrow}}{-\!\!\!\!\fbox{A[i]}\!\!\!\!-} \quad \ldots \quad = \quad \ldots \quad -\!\!\!\overset{n_{i\uparrow}n_{i\downarrow}}{\bigcirc U}\!\!\!-\!\!\!\bigcirc S\!\!\!-\!\!\!\bigcirc V^\dagger\!\!\!-\quad \ldots \tag{2.71}$$

$$= \quad \ldots \quad -\!\!\!\bigcirc U\!\!\!-\!\!\!\bigcirc S\!\!\!-\!\!\!\overset{n_{i\uparrow}n_{i\downarrow}}{\bigcirc V^\dagger}\!\!\!-\quad \ldots \tag{2.72}$$

where the matrix $S$ is diagonal holding the real singular value spectrum. We are free to choose where to put the index specifying the physical state $n_{i\uparrow}n_{i\downarrow}$, either we put them at the matrix $U$ or at the matrix $V^\dagger$. The choice where to put the indices determines if the left-orthogonalization or right-orthogonalization property is implemented at this bond of the MPS, as we know $UU^\dagger = 1$ and $V^\dagger V = 1$.

The interesting feature of SVD is now that we can use it to find the optimal approximation of the tensor $A[i]$ using a reduced dimensional tensor $\tilde{A}[i]$. If we remove the singular values smaller than a certain threshold $\epsilon$ from the singular value spectrum and only keep the $D_\epsilon$ singular values that are larger then $\epsilon$, we obtain the optimal approximation of the matrix $A[i]$ [104]

$$||A[i] - \tilde{A}[i]||^2 = \sum_{\lambda_i < \epsilon} \lambda_i^2, \tag{2.73}$$

where $|| \cdot ||$ denotes the Frobenius norm and the sum is over all removed singular values. The idea is now to use SVD to truncate the tensors in Equation 2.54 to find a representation [124] of the entire MPS representation of the many-body state that is optimal with respect to some dimension $D_\epsilon$. This optimal representation is then constructed from smaller tensors $\tilde{A}[i]$

$$\ldots \quad \overset{n_{i\uparrow}n_{i\downarrow}}{-\!\!\!\!\fbox{A[i]}\!\!\!\!-} \quad \ldots \quad = \quad \ldots \quad -\!\!\!\overset{n_{i\uparrow}n_{i\downarrow}}{\bigcirc U}\!\!\!-\!\!\!\bigcirc S\!\!\!-\!\!\!\bigcirc V^\dagger\!\!\!-\quad \ldots \tag{2.74}$$

$$\approx \quad \ldots \quad -\!\!\!\overset{n_{i\uparrow}n_{i\downarrow}}{\bigcirc \tilde{U}}\!\!\!-\!\!\!\bigcirc \tilde{S}\!\!\!-\!\!\!\bigcirc \tilde{V}^\dagger\!\!\!-\quad \ldots \quad = \quad \ldots \quad -\!\!\!\overset{n_{1\uparrow}n_{1\downarrow}}{\fbox{$\tilde{A}[i]$}}\!\!\!-\quad \ldots \; , \tag{2.75}$$

where $\tilde{U}$ and $\tilde{V}^\dagger$ are the adapted transformation matrices where the lines (rows) belonging to neglected singular values have been removed. As soon as the truncated singular values are nonzero, this truncation introduces an *truncation error*, i.e. the MPS from the MPS tensors represents the many-body state approximately.
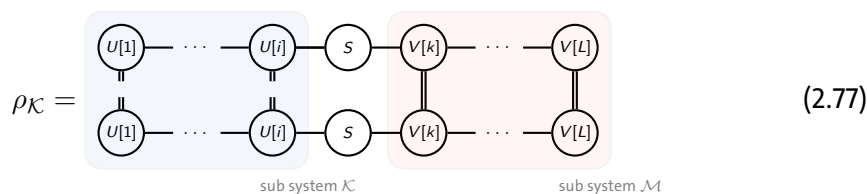
When truncating singular values from the singular value spectrum, we change the dimension of the horizontal bonds in Equation 2.56. From now on, we will distinguish

two types of bonds the tensors in the MPS have. There are bonds going vertically with the occupation number being the related quantity $n_{i\uparrow}n_{i\downarrow}$. We will call these bonds *physical bonds* as they have a direct physical meaning, namely the occupation numbers of the orbital $i$. Then there are also the bonds going horizontally in Equation 2.56 that we will call *virtual bonds*. Those are the bonds we introduced with tensor factorization of the complete coefficient tensor. The truncation based on SVD changes the dimensions of the tensors $A[i]$ with respect to virtual bonds only. The dimension of a virtual bond is called the *bond dimension*. The physical bonds remain unaffected by the SVD truncation, therefore, all configurations can contribute to the MPS representation of the many-body state. This is in strong contrast to other post-Hartree–Fock methods outlined above (see 2.3), which all cut configurations from the many-body Hilbert space, i.e. they cut the physical degrees of freedom.
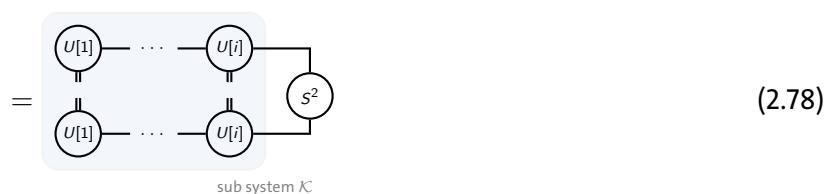
Truncating the MPS in this manner has implications on the entanglement the MPS is able to resolve. Let us divide the orbitals into two sets $\mathcal{K}$ and $\mathcal{M}$ and assume that the orbitals of the set $\mathcal{K}$ are on the left of site and include the orbital $i$ and the orbitals of the set $\mathcal{M}$ are on the right of orbital $i$. The entanglement entropy between electrons in these two orbital basis sets is given by

$$S(\rho_\mathcal{K}) = tr\{\rho_\mathcal{K} log\rho_\mathcal{K}\}, \tag{2.76}$$

where $\rho_\mathcal{K}$ is the *reduced density matrix*. In the tensor network notation it is



$$\tag{2.77}$$



$$\tag{2.78}$$

assuming that the MPS $|\Psi\rangle_{MPS}$ is in a mixed canonical form with left-normalized tensors for $\sigma \leq i$ and right-normalized tensors for $\sigma > i$. In this basis, $\rho_\mathcal{K}$ is diagonal and $S^2$ holds the eigenvalues of the reduced density matrix. If we assume a completely mixed spectrum with all eigenvalues of the reduced density being $\frac{1}{D_\epsilon}$ (this is the worst case), we can estimate the entanglement entropy as

$$S(\rho_\mathcal{K}) \propto log(D_\epsilon). \tag{2.79}$$

Therefore, the entanglement entropy that the MPS approach is able to resolve grows logarithmically with bond dimension $D$. In little entangled states, a small bond di-

mensions is sufficient to describe the state, whereas, as the entanglement grows, also the bond dimension of the MPS needs to grow to maintain precision. Depending on the many-body state, it can vary from bond dimension 1, which means no entanglement (Hartree–Fock) up to extremely large bond dimension, which means maximally entangled. When using MPS with small bond dimensions, we assume that the entanglement of the electrons is limited and the real entanglement does not exceed the entanglement the MPS are able to describe.

After the truncation to bond dimension $D$ has been performed on all tensors in the MPS, we obtain a new, approximated MPS representation of the many-body state

$$|\psi\rangle \approx |\psi_{MPS}\rangle = \sum_{n_{1\uparrow}n_{1\downarrow}\cdots n_{L\uparrow}n_{L\downarrow}} \overset{n_{1\uparrow}n_{1\downarrow}}{\underset{}{\tilde{A}[1]}}\overset{n_{2\uparrow}n_{2\downarrow}}{\underset{}{\tilde{A}[2]}}\cdots \overset{n_{L\uparrow}n_{L\downarrow}}{\underset{}{\tilde{A}[L]}} |n_{1\uparrow}n_{1\downarrow}\cdots n_{L\uparrow}n_{L\downarrow}\rangle, \quad (2.80)$$

where all MPS tensors have a maximum virtual bond dimension $D$. For a given bond dimension $D$, this is the quasi optimal approximation to the complete many-body state [124].

## 2.4.6 Level-1 Operations

Now we have a basic understanding of the concept of MPS and see how they can help us when representing many-body states. When using the MPS approach to solve the (time-dependent) Schrödinger equation, we need to perform the operations of linear algebra on MPS, such as scaling them by a factor, adding two or more MPS, and applying operators on MPS. With level 1 operations, we have operations that involve MPS only (compare to BLAS level 1 operation for vectors [175]). With level 2 operations, we have operations that involve operator applications on MPS (compare to BLAS level 2 operations for matrix-vector products).

First, and most simple operation on a many-body state in MPS representation is to scale it by a factor $\alpha$

$$\alpha |A\rangle_{MPS} = \sum_{n_{1\uparrow}n_{1\downarrow}\cdots n_{L\uparrow}n_{L\downarrow}} (\alpha A^{n_{1\uparrow}n_{1\downarrow}}[1])\cdots A^{n_{L\uparrow}n_{L\downarrow}}[L] |n_{1\uparrow}n_{1\downarrow}\cdots n_{L\uparrow}n_{L\downarrow}\rangle, \quad (2.81)$$

$$= \sum_{n_{1\uparrow}n_{1\downarrow}\cdots n_{L\uparrow}n_{L\downarrow}} (\sqrt[L]{\alpha}A^{n_{1\uparrow}n_{1\downarrow}}[1])\cdots(\sqrt[L]{\alpha}A^{n_{L\uparrow}n_{L\downarrow}}[L]) |n_{1\uparrow}n_{1\downarrow}\cdots n_{L\uparrow}n_{L\downarrow}\rangle,$$

$$(2.82)$$

where we are free to multiply the factor $\alpha$ into one of the tensors $A[i]$. Alternatively, we observed better numerical stability when multiplying each of the MPS tensors by

a factor $\sqrt[4]{\alpha}$. Then the factor is more evenly distributed, which reduces floating point errors.

Second, and still simple operation of type level 1 is a scalar product of two many-body states in MPS representation. Here again, we can formulate an optimal procedure: The scalar product of two many-body states in MPS representation is given by the tensor network (using the orthonormality of the occupation number basis)

$$\langle A_{MPS}|B_{MPS}\rangle = \begin{matrix} \boxed{A[1]} - \boxed{A[2]} - \cdots - \boxed{A[L]} \\ | \quad\quad | \quad\quad\quad\quad | \\ \boxed{B[1]} - \boxed{B[2]} - \cdots - \boxed{B[L]} \end{matrix} = S[L], \tag{2.83}$$

which is similar to the tensor network we already have seen for the MPS norm in Equation 2.61. In tensor networks such as the one shown in Equation 2.83 the order of summation is very important in terms of efficiency. In this particular tensor network, we need to perform the summations either from left to right, or from right to left. We should never perform the summation of virtual bonds first, (from bottom to top or reverse), as we then obtain the exponential scaling of the complexity we have encountered for the complete many-body state. In this example, the optimal order of summation is easy to find, however, for more complex tensor networks, it is unclear what the optimal order of summation is. Finding the optimal order of summation for a generic tensor network is NP-hard [176].

Adding two many-body states in MPS representation is more challenging, because adding is an operation that potentially changes the bond dimension of the MPS representation. Suppose we want to add the two many-body states in MPS representation $|A\rangle_{MPS}$ and $|B\rangle_{MPS}$

$$|C\rangle_{MPS} = |A\rangle_{MPS} + |B\rangle_{MPS}, \tag{2.84}$$

where $|A\rangle_{MPS}$ has the maximum bond dimension $D_A$ and $|B\rangle_{MPS}$ has the maximum bond dimension $D_B$. To form the matrix $C^{n_{i\uparrow}n_{i\downarrow}}[i]$ that form the MPS representation of the resulting state $|C\rangle_{MPS}$, we need to arrange the matrices as

$$C^{n_{i\uparrow}n_{i\downarrow}}[i] = \begin{pmatrix} A^{n_{i\uparrow}n_{i\downarrow}}[i] & 0 \\ 0 & B^{n_{i\uparrow}n_{i\downarrow}}[i] \end{pmatrix}, \tag{2.85}$$

therefore, the MPS $|C\rangle_{MPS}$ will have a maximum bond dimension of $D_C = D_A + D_B$. Next step in the addition operation is to truncate the MPS $|C\rangle_{MPS}$ by using SVD, as described in Section 2.4.5. In case that $|A\rangle_{MPS}$ and $|B\rangle_{MPS}$ are linearly dependent SVD will reduce the bond dimension to $D_A$ (or $D_B$) without introducing any error. In other situations, the MPS bond dimension need to be reduced to make sure that the MPS bond dimension does not grow with every following MPS addition.

This exact method to add MPS is too complex in most situations, and the error introduced by the extra truncation spoils the overall result. In Section 2.4.9 we will therefore introduce a variational concept to add many-body states in MPS representation that works more efficiently.

## 2.4.7 Matrix Product Operators

The same decomposition we applied to the many-body state can be applied to many-body operators [52]. Even though the operators are usually not the most challenging part in the quantum mechanical description of many-body system (most operators are extremely sparse), it is beneficial to have the MPS approach extended to operators, namely the *matrix product operator* (MPO) representation of many-body operators. The generation of MPO can be done equivalently to the MPS approach, by successive decomposition of the coefficients specifying the operator. Suppose we have the operator expressed in the occupation number basis

$$\hat{O} = \sum_{\substack{n_{1\uparrow}n_{1\downarrow}\cdots n_{L\uparrow}n_{L\downarrow} \\ n'_{1\uparrow}n'_{1\downarrow}\cdots n'_{L\uparrow}n'_{L\downarrow}}} O^{n_{1\uparrow}n_{1\downarrow}\cdots n_{L\uparrow}n_{L\downarrow}}_{n'_{1\uparrow}n'_{1\downarrow}\cdots n'_{L\uparrow}n'_{L\downarrow}} |n_{1\uparrow}n_{1\downarrow}\cdots n_{L\uparrow}n_{L\downarrow}\rangle \langle n'_{1\uparrow}n'_{1\downarrow}\cdots n'_{L\uparrow}n'_{L\downarrow}| . \qquad (2.86)$$

Then, we can express the complete tensor $O^{n_{1\uparrow}n_{1\downarrow}\cdots n_{L\uparrow}n_{L\downarrow}}_{n'_{1\uparrow}n'_{1\downarrow}\cdots n'_{L\uparrow}n'_{L\downarrow}}$ of rank $4L$ as a product of lower rank tensors. The operators in the MPO representation then reads

$$\hat{O}_{MPO} = \sum_{\substack{n_{1\uparrow}n_{1\downarrow}\cdots n_{L\uparrow}n_{L\downarrow} \\ n'_{1\uparrow}n'_{1\downarrow}\cdots n'_{L\uparrow}n'_{L\downarrow}}} O[1]^{n_{1\uparrow}n_{1\downarrow}}_{n'_{1\uparrow}n'_{1\downarrow}} \cdots O[L]^{n_{L\uparrow}n_{L\downarrow}}_{n'_{L\uparrow}n'_{L\downarrow}} |n_{1\uparrow}n_{1\downarrow}\cdots n_{L\uparrow}n_{L\downarrow}\rangle \langle n'_{1\uparrow}n'_{1\downarrow}\cdots n'_{L\uparrow}n'_{L\downarrow}| ,$$



$$(2.87)$$

where again $O[1]^{n_{1\uparrow}n_{1\downarrow}}_{n'_{1\uparrow}n'_{1\downarrow}}$ is a row vector $O[i]^{n_{i\uparrow}n_{i\downarrow}}_{n'_{i\uparrow}n'_{i\downarrow}}$ are matrices and $O[L]^{n_{L\uparrow}n_{L\downarrow}}_{n'_{L\uparrow}n'_{L\downarrow}}$ is a column vector. As for the non-truncated MPS representation of the many-body state, the MPO representation of a many-body operator is mathematically correct, and introduces no errors. The sequence of matrix products in Equation 2.87 exactly form the operator matrix elements $O^{n_{1\uparrow}n_{1\downarrow}\cdots n_{L\uparrow}n_{L\downarrow}}_{n'_{1\uparrow}n'_{1\downarrow}\cdots n'_{L\uparrow}n'_{L\downarrow}}$.

The MPO representation of a many-body operator can in most cases be found and used exactly, as the bond dimension of the virtual bonds only grows polynomially with system size [177]. Usually the many-body operators are sparse (Hamiltonian, occupation number operators, spin operators) and a large number of coefficients are

zero. This is in contrast to MPS representations of many-body states, which are in general not sparse. In quantum chemistry with the long-ranged interaction, the bond dimension of the Hamiltonian in MPO representation grows quartically with system size ($D_{MPO} \propto L^4$). That is manageable in most situations; Usually the bond dimension of the MPS representation is the limiting factor. Still the MPO representation of a many-body operator can be truncated in a similar fashion as the MPS representation of a many-body operator. This reduces the complexity of the calculation, however, it comes at the cost of dealing with an approximated Hamiltonian. Such operator truncations have been applied in quantum chemistry [177], but most studies rely on the exact MPO representation of the Hamiltonian and focus on truncation of the MPS representation of the many-body state.

## 2.4.8 Level-2 Operations

With level 2 operations, we have the application of many-body operators in MPO representation on many-body states in MPS representation. The MPO application is an operation that potentially changes the bond dimension of the MPS representation of the resulting many-body state. Here, we explain the direct method, although this method has the same issues that we already encountered for addition of many-body states in MPS representation (see Section 2.4.6). The growth of the MPS bond dimension and the necessary truncation steps spoil the result of direct application of operators in MPO representation. For this reason, we will discuss the variational operator application as a possible solution to this issue in Section 2.4.9.

If we apply a many-body operator in MPO representation directly to a many-body state in MPS representation we get

$$\hat{O}_{MPO} \ket{\psi}_{MPS} = \sum_{\substack{n_{1\uparrow} n_{1\downarrow} \cdots n_{L\uparrow} n_{L\downarrow} \\ n'_{1\uparrow} n'_{1\downarrow} \cdots n'_{L\uparrow} n'_{L\downarrow}}} O[1]^{n_{1\uparrow} n_{1\downarrow}}_{n'_{1\uparrow} n'_{1\downarrow}} \cdots O[L]^{n_{L\uparrow} n_{L\downarrow}}_{n'_{L\uparrow} n'_{L\downarrow}}$$

$$A^{n'_{1\uparrow} n'_{1\downarrow}} \cdots A^{n'_{L\uparrow} n'_{L\downarrow}} \ket{n_{1\uparrow} n_{1\downarrow} \cdots n_{L\uparrow} n_{L\downarrow}} ,$$

$$= \sum_{n_{1\uparrow} n_{1\downarrow} \cdots n_{L\uparrow} n_{L\downarrow}} \text{} \ket{n_{1\uparrow} n_{1\downarrow} \cdots n_{L\uparrow} n_{L\downarrow}} , \quad (2.88)$$

where it is again very important to choose the right order to perform the summations. The best possible order of summation is again from left to right, or from right to left, i.e. by starting with the index commonly shared by the first (last) tensors $O[1]$ ($O[L]$) and $A[1]$ ($A[L]$) and then continue sequentially to the right (left). If we want to obtain the result of this operator application in MPS representation, we skip summation

over the virtual bonds, as we need them next to recover the MPS representation as the next step.

Let us have a closer look onto one of the summations that need to be performed. The two summations over the physical bonds at site $i$ and $j = i + 1$ reads



$$\cdots - O[i] - O[j] - \cdots = \cdots - \bar{A}[i] = \bar{A}[j] - \cdots . \tag{2.89}$$

This gives a new double virtual bond connecting between the two tensors $\bar{A}[i]$ and $\bar{A}[j]$. The lower bond originates from the virtual bond in MPS representation of the many-body state $|\psi\rangle_{MPS}$, and the upper bond originates from the virtual bond in the MPO representation of the operator $\hat{O}_{MPO}$. To bring the resulting many-body state in MPS representation again, we need to unify these two virtual bonds into a single. The unified bond will have a bond dimension of $D_A \cdot D_O$, i.e. significantly larger than the previous bond dimension. This shows the problem we encountered already for addition of MPS. The bond dimension of the MPS representation of the resulting many-body state increases when performing operator applications. We need to truncate the MPS to reduce the bond dimension of the MPS representation of the resulting many-body state.

If the MPO representation of the many-body operator has a bond dimension of $D_O$, and the MPS representation of the many-body state has bond dimension of $D_A$, the computational cost for operator application scales like $\mathcal{O}(LD_O^2D_A^2)$. In our long-ranged quantum chemistry problem the bond dimension of the MPO representation of the Hamiltonian scales like $\mathcal{O}(L^2)$ with system size, we therefore obtain the costs for application of the Hamiltonian $\mathcal{O}(L^5D_A^2)$ [177].

## 2.4.9 Variational Handling of Matrix Product States

Now we want to introduce a more efficient method to add many-body states in MPS representation and to apply operators to many-body states in MPS representation. We have already seen direct methods to perform these operations in Section 2.4.6 and Section 2.4.8, however, those increase the bond dimension of the resulting many-body state in MPS representation. In this section we want to describe a procedure that variationally optimizes a many-body state in MPS representation to MPS addition or MPO application with the constraint of a previously chosen maximum bond dimension. This means we are performing the operation (addition or operator application),

while simultaneously limiting the bond dimension of the MPS representation of the resulting many-body state.

Let us start with the example of addition of two many-body states in MPS representation $|A\rangle_{MPS}$ and $|B\rangle_{MPS}$. Further, we want to obtain the resulting many-body state represented as an MPS $|C\rangle_{MPS}$ with a previously fixed bond dimension $D_C$. Instead of performing the direct addition followed by truncation (see Section 2.4.6 and Section 2.4.5 ), we vary the tensors in $|C\rangle_{MPS}$ to find the global minimum of the functional

$$\mathcal{L}[|C\rangle_{MPS}] = |||C\rangle_{MPS} - (|A\rangle_{MPS} + |B\rangle_{MPS})||^2. \tag{2.90}$$

We find the tensor $C[i]$ in $|C\rangle_{MPS}$ that minimize Equation 2.90 by taking the first derivative of the functional with respect to the tensor $C[i]^*$ in $\langle C|_{MPS}$ and set it to zero

$$0 = \frac{\partial}{\partial C[i]^*}\mathcal{L}[C] = \frac{\partial}{\partial C[i]^*} \left( {}_{MPS}\langle C|C\rangle_{MPS} - {}_{MPS}\langle C|A\rangle_{MPS} - {}_{MPS}\langle C|B\rangle_{MPS}\right).$$
$$\tag{2.91}$$

Here, we already canceled terms not depending on $C[i]^*$. Solving Equation 2.91 minimizes the value of the functional in Equation 2.90 with respect to $C[i]$ and therefore brings the MPS $|C\rangle_{MPS}$ close to the sum of the two many-body states in MPS representation $|A\rangle_{MPS}$ and $|B\rangle_{MPS}$.

At this point, the graphical representation of tensor networks is particularly handy. The derivative of Equation 2.91 reads in the graphical representation



$$\tag{2.92}$$

where the first part depicts $\langle C|C\rangle$ in Equation 2.91, the second part depicts $\langle C|A\rangle$ in Equation 2.91 and the third part depicts $\langle C|B\rangle$ in Equation 2.91. The tensor $C[i]^*$ simply vanishes when taking the derivative of Equation 2.91, since Equation 2.91 is linear in $C[i]^*$.

To solve Equation 2.92, let us remember the (left-) right-orthonormalization property of many-body states in MPS representation. In Section 2.4.4 we discussed the feature of many-body state in MPS representation to be in a special form, where parts of tensor networks such as given in Equation 2.92 form identity operators (see Equation 2.66 and Equation 2.68). At this point of the MPS addition, we can take advantage of

this property. Assume the MPS $|C\rangle_{MPS}$ happens to have its orthonormal center at orbital $i$, which means, all tensor to the left of orbital $i$ are left-orthogonalized and all tensors to the right of orbital $i$ are right-orthogonalized. Using the properties of left- and right-orthonormalization, we can simplify Equation 2.92 to

$$0 = \quad \cdots \text{—} \boxed{C[i]} \text{—} \quad - \quad \cdots \boxed{C[h]} \cdots \boxed{C[j]} \cdots \quad - \quad \cdots \boxed{C[h]} \cdots \boxed{C[j]} \cdots \quad ,$$

(2.93)

which we can rearrange to

$$\cdots \text{—} \boxed{C[i]} \text{—} \quad = \quad \cdots \boxed{C[h]} \cdots \boxed{C[j]} \cdots \quad + \quad \cdots \boxed{C[h]} \cdots \boxed{C[j]} \cdots \quad .$$

(2.94)

This is a linear equation that we can solve directly. The (left-) right-orthonormal-ization property of the many-body state in MPS representation enabled us to turn Equation 2.91 into a linear equation (Equation 2.94). By solving Equation 2.94 we find a minimum of the functional in Equation 2.90 for the particular tensor $C[i]$.

However, the minimum we found from this procedure is not necessary the global minimum of Equation 2.90. The solution of Equation 2.91 for orbital $i$ strongly depends on all tensors $C[j] \,\forall j \neq i$. To approach the global minimum, we also need to vary the other tensors in the MPS $|C\rangle_{MPS}$. We do this in the form of *sweeps* [42, 43], where we repeat the procedure we performed for orbital $i$ for the next tensor $i \to i \pm 1$ in the MPS $|C\rangle_{MPS}$, and all following. Thereby, we optimize the MPS $|C\rangle_{MPS}$ to represent the sum in Equation 2.90 variationally, until we reached convergence to the desired accuracy. Most importantly, the bond dimension of the MPS $|C\rangle_{MPS}$ remains fixed within this procedure. It is chosen for the initial guess of the MPS $|C\rangle_{MPS}$, and does not change in this procedure. The optimization happens in the fixed manifold of the many-body Hilbert space the MPS state $|C\rangle_{MPS}$ covers. This manifold is not changed within this optimization procedure, which improves efficiency compared to the direct approach outlined above in Section 2.4.6.

This procedure is also able to perform many other operations beyond the addition of two MPS. For example, we can easily use it to add more than two MPS at once. Then the Equation 2.94 is just appended by more addends on the right hand side. Further allows this procedure to truncate many-body states in MPS representation variationally [178]. Such an operation starts from the functional

$$\mathcal{L}[|C\rangle_{MPS}] = ||\,|C\rangle_{MPS} - |A\rangle_{MPS}\,||^2,$$

(2.95)

and all following steps of the variation procedure remain similar to those for MPS addition. Most importantly we can also use the variational method to apply many-body operators in MPO representation, i.e. to perform level 2 operations on many-body states in MPS representation. Here, the functional to minimize reads

$$\mathcal{L}[|C\rangle_{MPS}] = |||C\rangle_{MPS} - \hat{O}|A\rangle_{MPS}||^2, \tag{2.96}$$

but the concept of the procedure is again similar to what has been explained for MPS addition. For application of many-body operators in MPO representation the linear equation to solve reads



$$\tag{2.97}$$

which shows the additional summations that increase complexity of operator application. However, the resulting method is still more efficient than the direct approach to apply MPO to MPS (see Section 2.4.8).

Another advantage of the variational method is that we can combine various operations into one. For example, we can combine operator applications with an arbitrary large sum of other MPS. Then the functional to minimize reads

$$\mathcal{L}[|C\rangle_{MPS}] = |||C\rangle_{MPS} - \left(\hat{H}|A\rangle_{MPS} + \sum_p |p\rangle_{MPS}\right)||^2 \tag{2.98}$$

This feature will become in particular handy in the time evolution methods that we will outline in Section 2.5.

The computational cost of a variational optimization is small compared to the direct approaches explained in Section 2.4.6 and Section 2.4.8. The complexity of the variational method for the addition of two MPS with bond dimension $D$ into an MPS with bond dimension $D$ is per sweep $\mathcal{O}(LD^3)$ and therefore only grows linearly with the system size. For application of MPO in quantum chemistry to MPS, the complexity is $\mathcal{O}(L^4D^2 + L^3D^3)$, which is one order smaller in $L$ compared to the direct approach.

In this procedure to add many-body states in MPS representation, we took the derivative of a single site $C[i]^*$, which has the advantage that the MPS dimension does not change within the optimization. However, this comes at the cost that the MPS representation of the many-body state remains in a fixed manifold of the many-body Hilbert space. It is not free to adapt to a new manifold of the many-body Hilbert

space (see Section 2.4.2) by changing the virtual basis. It can adjust the coefficient in the tensors $C[i]$ only, however, without changing the virtual basis. It cannot leave the corner of the Hilbert space the initial MPS $|C\rangle_{MPS}$ was constructed to represent. For this reason, we will use a dynamic extension, that is able to adjust the corner of the Hilbert space the MPS represents. Instead of taking the derivative of a single tensor $C^*[i]$, we work with neighboring pairs of tensors

$$\frac{\partial}{\partial C[i]^*} \to \frac{\partial}{\partial C[i]^* C[j]^*}, \tag{2.99}$$



$$(2.100)$$

which allows for adaption of the virtual basis and therefore to adapt the manifold it represents in the many-body Hilbert space. $S[i,j]$ is known as the *two-site object* [51, 106] and is equivalent to the two-site DMRG algorithm [42, 43]. After the linear equation has been solved using the two-site object, it needs to be decomposed into two matrices to fit back in the resulting MPS representation of the many-body state. This can be done using the SVD introduced in Section 2.4.5. It is known that the two-site procedure of doing variational operations improves the overall MPS performance. There are existing extensions to enhance the single-site procedure as well [179], however, we will use the two-site procedure throughout this thesis.

## 2.5 Time Evolution of Matrix Product States

Now, that we have all necessary tools to operate on MPS, we can proceed by discussing how to apply these operations to solve the time-dependent Schrödinger equation (see Equation 2.1). Finally, we want to solve the time-dependent Schrödinger equation for many-body states in MPS representation

$$i\hbar\frac{\partial}{\partial t}|\Psi(t)\rangle_{MPS} = \hat{H}|\Psi(t)\rangle_{MPS}, \tag{2.101}$$

in the most efficient and precise fashion. The general solution to this differential equation is given in terms of the time evolution operator. If the state $|\Psi(t_0)\rangle_{MPS}$ is known at time $t_0$, the time evolved state at time $t - t_0$ is given by

$$|\Psi(t - t_0)\rangle_{MPS} = e^{-\frac{i}{\hbar}\hat{H}(t-t_0)}|\Psi(t_0)\rangle_{MPS}, \tag{2.102}$$

for time-independent Hamiltonians. However, finding a representation of the time evolution operator is the central challenge in time-dependent quantum mechanics. There are many methods to solve the time-dependent Schrödinger equation for many-body states in MPS representation [59], however, only a few can be applied to quantum chemical systems due to the long-ranged interaction (see Section 2.4.2).

## 2.5.1 Overview of Time Evolution Algorithms for Matrix Product States

The most prominent time evolution algorithm for many-body states in MPS representation is the *time evolving block decimation* (TEBD) method that is based on a Lie–Trotter decomposition of the time evolution operator [53]. Assume we can write the Hamiltonian in terms of a sum

$$\hat{H} = \sum_i \hat{h}_{i,i+1}, \tag{2.103}$$

where the addend to the Hamiltonian $\hat{h}_{i,i+1}$ only acts on the sites (orbital) $i$ and $i + 1$. Then we can express the time evolution operator in Equation 2.102 approximately as

$$e^{-\frac{i}{\hbar}\hat{H}t} \approx e^{-\frac{i}{\hbar}\hat{h}_{1,2}t/2} \cdots e^{-\frac{i}{\hbar}\hat{h}_{L-1,L}t/2} e^{-\frac{i}{\hbar}\hat{h}_{L-1,L}t/2} \cdots e^{-\frac{i}{\hbar}\hat{h}_{1,2}t/2} + \mathcal{O}(t^2), \tag{2.104}$$

which is also known as the Lie–Trotter decomposition and has similarities with the well known split operator method used e.g. in the bachelor theses by Wunderlich [180] and Berg [181].

With the MPO representation of the Hamiltonian in Equation 2.103, we can easily find the operators $e^{-\frac{i}{\hbar}\hat{h}_{i+1,i}t/2}$ since its is just an exponential of an operator acting on two sites (orbitals). These exponentials are successively applied to the many-body state in MPS representation according to Equation 2.104 and then generate the time evolved MPS. TEBD is likely to be the best time evolution method existing for many-body stats in MPS representation [182], however, it has a very strict limitation. The decomposition in Equation 2.103 is only possible if the Hamiltonian is short-ranged, which forbids the use of TEBD for most quantum chemical systems. For specific molecules it is possible to formulate short-ranged problems, however, in the context of ab initio quantum chemistry, the Hamiltonian is inherently long-ranged. For this reason we cannot rely on the TEBD time evolution approach.

A method that is able to treat long-ranged problems is the *time-dependent variational principle* (TDVP) applied to MPS [56, 132]. Here one solves the time-dependent Schrödinger equation for each individual tensor $\Psi[i](t)$ in the MPS representation of the many-body state $|\Psi(t - t_0)\rangle_{MPS}$. One obtains these local time-evolution equations from a projection of the time-dependent Schrödinger equation onto the tangent space of the MPS manifold. Then one solves the Schrödinger equation in this tangent space for each of the tensors in the MPS. By performing sweeps similar to the sweeps in the procedure for variational operations (see Section 2.4.9), one eventually obtains the time evolved state. The resulting procedure allows for unitary time-evolution

and can be applied to long-ranged problems, however, its performance diminishes for problems with non-local interaction [182]. With one-dimensional lineup of the different orbitals of the molecule in the MPS representation, we obtain non-uniform Coulomb integrals in the quantum chemistry Hamiltonian. This makes use of TDVP problematic in quantum chemical situations.

The two approaches outlined above are inherently designed for MPS. They use the tensor network feature and are designed to operate locally on individual tensors of the MPS representation instead of working with the total MPS. Such approaches have shown to have good efficiency [56, 58, 132, 183, 184], however, these studies included mostly systems in one-dimension, where electronic interaction and entanglement is limited. Here, with the more complex quantum chemistry situation, we will choose a different path: Instead of designing tailored time evolution algorithms for the MPS representation, we understand the MPS approach as an optimized way to represent the many-body state. With operations such as scaling, adding, and applying operators, we have everything we need to work with MPS just like we would do with the complete many-body state. Then we can use any already existing methods to solve the time-dependent Schrödinger equation. Here, we will focus on two of such methods, namely the fourth-order Runge–Kutta approach, and the Krylov space time evolution.

## 2.5.2  Fourth-Order Runge–Kutta

The first method we want to use to time evolve a many-body state in MPS representation is the *fourth-order Runge–Kutta* method [185]. For our situation with a time-independent Hamiltonian it is based on the Taylor expansion of the time evolution operator in Equation 2.102 up to the fourth order. The Runge–Kutta method starts by finding the four Runge–Kutta vectors, in our case all of them in MPS representation

$$|k_1\rangle_{MPS} := i\frac{\Delta t}{\hbar}\hat{H}|\Psi(t)\rangle_{MPS} \tag{2.105}$$

$$|k_2\rangle_{MPS} := i\frac{\Delta t}{\hbar}\hat{H}\left(|\Psi(t)\rangle_{MPS} + \frac{1}{2}|k_1\rangle_{MPS}\right) \tag{2.106}$$

$$|k_3\rangle_{MPS} := i\frac{\Delta t}{\hbar}\hat{H}\left(|\Psi(t)\rangle_{MPS} + \frac{1}{2}|k_2\rangle_{MPS}\right) \tag{2.107}$$

$$|k_4\rangle_{MPS} := i\frac{\Delta t}{\hbar}\hat{H}\left(|\Psi(t)\rangle_{MPS} + |k_3\rangle_{MPS}\right). \tag{2.108}$$

Here, we see that we just need the operations described in Section 2.4.6 and Section 2.4.8 to find the Runge–Kutta vectors. We can find these vectors by applying the variational approach as discussed in Section 2.4.9. The many-body state evolved by a

time step $\Delta t$ is then constructed from a superposition of the initial state and the four Runge–Kutta vectors

$$|\Psi(t+\Delta t)\rangle_{MPS} = |\Psi(t)\rangle_{MPS} + \frac{1}{6}\left(|k_1\rangle_{MPS} + 2\left(|k_2\rangle_{MPS} + |k_3\rangle_{MPS}\right) + |k_4\rangle_{MPS}\right)$$
$$+ \mathcal{O}(\Delta t^5), \tag{2.109}$$

which is correct up to fifth order in the discrete time step size $\Delta t$. When inserting the Runge–Kutta vectors into Equation 2.109, this exactly matches the fourth order Taylor expansion of the time evolution operator in Equation 2.102.

The Runge–Kutta method is one of the standard methods for time evolution in many studies of condensed matter theory and in numerical mathematics in general. It is easy to implement and has a very well controllable error with the time step size. There are also lower and higher order Runge–Kutta methods, however, in most studies the fourth order method provides good performance.

The Runge–Kutta method still suffers from the problem of performing the time evolution non-unitarily. As it is based on a finite expansion of the time evolution operator in Equation 2.102. The norm of the time evolved state will change with time. This error scales like $\mathcal{O}(\Delta t^5)$, which limits the size of the discrete time steps immensely. The same applies to the energy expectation value if evaluated in a state evolved using the Runge–Kutta method, which is nonphysical for time-independent Hamiltonians. Therefore a careful choice of the discrete time step size $\Delta t$ is crucial for this method.

As being a fourth order method, performing a time step from $t$ to $t + \Delta t$ using the Runge–Kutta method requires four applications of the Hamiltonian to the many-body state in MPS representation, as well as four MPS additions. We can do paired applications and additions in one variation step, however, we need to calculate the Runge–Kutta vectors sequentially, as our implementation does not allow to directly perform higher order operator applications. Therefore, we first generate the Runge–Kutta vectors as given in Equation 2.105 to Equation 2.108 and then proceed with the superposition of the time evolved state in Equation 2.109.

## 2.5.3 Orthogonalized Krylov Space Time Evolution

With the Runge–Kutta method we have seen a time evolution method that is based on the direct Taylor expansion of the time evolution operator in Equation 2.102. In contrast to this approach, we want to introduce the family of *Krylov space methods* [186, 187] that go beyond a simple expansion of the time evolution operator. The method originated by Lanczos [188] who proposed a new method to find eigenvalues

of hermitian operators based on a reduced Hilbert space that was later named the *Krylov space*. The large success of the Lanczos method makes the method popular till today, were it is still the method of choice for finding the low energy spectrum of physical problems. The idea of the Krylov space was extended to a time evolution method that performs the evaluation of the time evolution operator in the Krylov space [187]. The resulting time evolution concept is one of the most sophisticated in today's numerical mathematics. The ideas were slightly extended compared to what has been proposed initially, however, the idea of the Krylov space remains the same [189–191]. As the strengths of the Krylov space time evolution align with the needs of our requirements of a time-evolution method, we will include the Krylov space method in our analysis of time-dependent MPS. Further is the Krylov space method easily implemented given the operations on many-body states in MPS representation outlined above, therefore it fits well in the scope of our analysis of the MPS approach in quantum chemistry.

The idea of the Krylov space methods is now to, instead of solving the time-dependent Schrödinger equation in the full many-body Hilbert space, reduce the problem to a linear subspace of the many-body Hilbert space and solve the time-dependent Schrödinger equation in this smaller vector space. The smaller vector space is called the Krylov space, which is generated from successive application of the Hamiltonian to a test state. In our time-dependent situation, we choose the test state as the many-body state we want to time evolve $|\Psi(t)\rangle_{MPS}$ in the MPS representation. In this case, the Krylov space is given by

$$\mathcal{K} = span(\{|\Psi(t)\rangle_{MPS}, \hat{H}|\Psi(t)\rangle_{MPS}, \hat{H}^2|\Psi(t)\rangle_{MPS}, \hat{H}^3|\Psi(t)\rangle_{MPS} \cdots\}). \quad (2.110)$$

that can be extended to any order $N_{Kry}$. To use the Krylov space, we need to find a transformation from the complete many-body Hilbert space, to the smaller Krylov space, i.e. we need a set of basis vectors of the Krylov space expressed in the complete many-body Hilbert space.

There are different approaches to find a basis of the Krylov space, where we will discuss two concepts in detail in this thesis. A method to generate the Krylov basis vectors successively is Gram–Schmidt orthogonalization applied to the Krylov vectors in Equation 2.110

$$|\phi^{k+1}\rangle_{MPS} = \hat{H}|\phi^k\rangle_{MPS} - \sum_{j \leq k} \frac{{}_{MPS}\langle\phi^j|\hat{H}|\phi^k\rangle_{MPS}}{{}_{MPS}\langle\phi^j|\phi^j\rangle_{MPS}}|\phi^j\rangle_{MPS}, \quad (2.111)$$

where $|\phi^0\rangle_{MPS} = |\Psi(t)\rangle_{MPS}$ is the state we want to evolve. The basis generated from Equation 2.111 forms an orthogonal basis of the Krylov space using the MPS

representation of the many-body state. All operations in Equation 2.111 are efficiently performed using the variational method discussed in Section 2.4.9.

The state evolved after a time step $\Delta t$ is constructed from the Krylov basis vectors by building the superposition [59]

$$|\psi(t+\Delta t)\rangle_{MPS} = \sum_k \left[ e^{-i\frac{\Delta t}{\hbar} N^{-1} H} \right]_{k0} |\phi^k\rangle_{MPS} \qquad (2.112)$$

where the matrix $N_{ij} =_{MPS} \langle \phi^i | \phi^j \rangle_{MPS}$ represents the overlaps of the Krylov basis vectors, $H_{ij} =_{MPS} \langle \phi^i | \hat{H} | \phi^j \rangle_{MPS}$ represents the Hamiltonian in the Krylov space and $[\,\cdot\,]_{k0}$ denotes the element at the $k$-th row and the 0-th column of the exponential matrix. The overlap matrix $N$ is supposed to be an identity matrix, as the Krylov basis vectors are generated in an orthonormal way, however, we need to keep numerical errors and truncation errors of the MPS in mind. Of course, the MPS representation of the Krylov basis vectors is imperfect, which induces a loss of orthogonality of the Krylov basis vectors in MPS representation. We take this into account by including the overlap matrix in the exponential of the time evolution equation in Equation 2.112.

Let us compare the Krylov space method with the previously introduced Runge–Kutta method. As we indeed calculate the time evolution operator, including the exponential in Equation 2.112, in the Krylov space instead of in the real many-body Hilbert space, the method is now norm conserving and energy conserving. This gives the method a large advantage compared to the Runge–Kutta method. It allows for much larger time steps and longer time evolution [59]. We will observe this in the detailed analysis of the MPS approach in Section 4. Further is the Krylov space method more flexible in adapting to the physical situation. On the one hand we can try to converge the dynamics using the time step size $\Delta t$, while on the other hand, we can also change the size of the Krylov space $N_{Kry}$ and see how this effects the results.

The complexity of a time step depends on the Krylov space dimension. For a given Krylov space dimension $N_{Kry}$, we need to perform $N_{Kry} - 1$ Hamiltonian applications and $N_{Kry}$ summations. A Krylov space dimension of $N_{Kry} = 5$ is comparable with the complexity of the Runge–Kutta method.

### 2.5.4 Non-Orthogonalized Krylov Space Time Evolution

The Krylov space basis generated from the vectors in Equation 2.111 is not the only valid basis of the Krylov space. When using an MPS representation of the Krylov basis vectors, the Krylov vectors will loose orthogonality due to the MPS truncation. In the time-evolution, Equation 2.112, we handled this by introducing the inverse of the overlap matrix in the exponential. Another approach is to form the Krylov space from

non-orthonormal basis vectors in the first place. When constructing the basis in a non-orthogonalized fashion, we can use

$$|\phi^{k+1}\rangle_{MPS} = \frac{\hat{H}\,|\phi^k\rangle_{MPS}}{|\,_{MPS}\langle\phi^k|\,\hat{H}\hat{H}\,|\phi^k\rangle_{MPS}\,|^2}, \tag{2.113}$$

which spans the Krylov space just as given in the Krylov space definition in Equation 2.110. This will be the second method to form a Krylov space basis that we discuss in the following analysis of the MPS approach.

The time evolution is again done according to Equation 2.112, which already takes care of possible non-orthogonality of the basis states. The resulting time evolution is, up to a MPS truncation error, norm and energy conserving. When using the non-orthonormalized Krylov basis vectors, and forming the time evolved state from the basis vectors, the resulting equation for the time evolved state is very similar to the $N_{Kry}$-th expansion of the exact time evolution operator in Equation 2.102, however, incorporating a complex pre-factor in a way that the resulting time evolution is unitary. This is a special feature of the non-orthonormal Krylov basis vectors, that will improve the performance of the MPS time evolution approach in special circumstances (see Section 4).

However, this improved performance is limited to special problems, as time-evolution based on the non-orthogonal Krylov basis vectors is more prone to errors. Especially if the state to time evolve is close to an eigenstate of the Hamiltonian, then the non-orthonormal Krylov basis vectors tend to become linearly dependent, which causes large numerical errors, when calculating the inverse $N^{-1}$ in Equation 2.112. Therefore we have to apply the non-orthogonalized Krylov approach more carefully.

The complexity of the non-orthogonalized Krylov approach is slightly reduced compared to the orthonormalized approach. We have the $N_{Kry} - 1$ operator application and only one addition of the previous Krylov vectors, however, in most cases the application of the Hamiltonian is the most costly part of the calculation. Therefore, the formal complexity of the non-orthogonalized Krylov space method is similar compared to orthogonalized Krylov space, however, the reduction in MPS bond dimension can be significant, which allows for more efficient calculations using the non-orthogonalized Krylov method in special situations (see Section 4).

These are the time evolution algorithms we want to apply in this analysis of the MPS based time evolution for dynamics in molecules. There exist many more approaches that have been developed, ranging from Chebyshev time evolution [192], more extensions to the time-dependent variational principle [58], up to Hylleraas functions [193] to calculate dynamic Green's functions in frequency space directly. However,

for the first application of the MPS approach in time-dependent ab initio quantum chemistry presented in this thesis, we have a good variety of methods to access the performance of the MPS approach in this field.

# Competitive Implementation of the Matrix Product State Approach

<div style="text-align:right">3</div>

Many numerical implementations of the DMRG method, the MPS approach, and more complex tensor network approaches have been developed in recent years [51, 139, 141, 142, 194–197]. There are multipurpose implementations of the tensor network approach that can be adapted to many physical problems. One of such implementations is the open source ITensor package [141], where the author contributed himself. The ITensor package is able to implement any tensor network, however, most features focus on the MPS approach to represent many-body states and on the MPO approach to represent many-body operators. For this type of tensor networks, it offers procedures to perform most operations discussed in Section 2.4. Implementing the time evolution methods discussed in Section 2.5 is straight forward. For example, ITensor was the package of choice in a master project that was initiated by the author of this thesis. Kothe [198] used the ITensor package and its MPS implementation to study time-dependent transport mechanisms in tunneling junctions at finite temperature.

Highly flexible packages such as ITensor come with a significant problem when using them for calculations on a competitive level. They sacrifice performance in computation time and memory for ease of adaption. Especially in ab initio quantum chemistry there is little chance to apply non-optimized code, as the complexity of the problem is enormous for non-trivial molecules. Computational power and memory is always the bottleneck in finding results of high accuracy. The modern quantum chemistry codes have been developed and optimized for decades and they are advanced in terms of computation efficiency, memory usage, and parallelism concepts. Therefore, we need an implementation of the MPS approach specifically optimized for quantum chemistry problems when proposing MPS as a promising approach to study time-dependent effects in molecules. Only then we will be able to describe dynamics in molecules with satisfying precision and international competitive efficiency.

In the next chapter, we want to propose the Hamburg CheMPS2 extension as one of such highly optimized implementations of the MPS approach, which enables time-dependent studies in quantum chemistry. We will discuss its origins and the

properties that make it one of the state-of-the-art MPS implementations. Together with the insights in the MPS approach in context of time-dependent quantum chemistry (that we discuss in Chapter 4 and Chapter 5), the Hamburg CheMPS2 extension is the main asset developed in this Ph.D. project. The results discussed in this thesis are just the starting point of time-dependent MPS in quantum chemistry, where the Hamburg CheMPS2 extension is used in numerous ongoing and future projects.

## 3.1 Symmetry Adapted Tensor Networks

A crucial benefit in computational physics originates in the symmetries of the physical system. Symmetries allow to reduce the dimension of the considered many-body Hilbert space, which then results in a simplification of the many-body state. For example, let us suppose we have a molecule where the electrons can occupy $L = 20$ orbitals. If we span the many-body Hilbert space without using any symmetries, its dimension is given by $dim(\mathcal{H}) = 4^L \approx 1.099 \cdot 10^{12}$. To represent the many-body state computationally we need $dim(\mathcal{H}) \approx 1.099 \cdot 10^{12}$ coefficients (see Section 2.2.2), which requires $\approx 70.37\,TB$ of data when using real double precision numbers. This is computationally very challenging using today's computational resources, however, using symmetries we can reduce the problem to a subspace of the many-body Hilbert space of manageable size. If utilizing the electron number conservation and the spin conservation and focus on the many-body states with $N_\uparrow = 10$ spin-up electrons and $N_\downarrow = 10$ spin-down electrons, we can reduce the problem to a subspace of $dim\left(\mathcal{H}_{N_\uparrow=10, N_\downarrow=10}\right) = \binom{L}{N_\uparrow} \cdot \binom{L}{N_\downarrow} = 3.4134 \cdot 10^{10}$ coefficients, which only requires $0.2731\,TB$ of data to store the many-body state. Calculations for many-body Hilbert space dimensions of this magnitude have been performed successfully [93]. With the MPS we have a complementary approach to simplify the representation of the many-body state. We can combine the symmetries of the molecular system with the MPS approach to gain an additive computational advantage. In the following section, we discuss how to reduce the effective dimension of the many-body Hilbert space using symmetries and how these symmetries are implemented into the tensors of the MPS approach.

When taking advantage of symmetries, we use that the Hamiltonian is block-diagonal if written in the eigenbasis of the symmetry generating operator (see Figure 3.1). This is a consequence of

$$\left[\hat{H}, \hat{O}\right] = 0, \tag{3.1}$$

where $\hat{O}$ is the symmetry generating operator. The blocks correspond to eigenvalues of the operator $\hat{O}$, that are also good quantum numbers (for example the electron number) of the system. The many-body states with fixed quantum number form
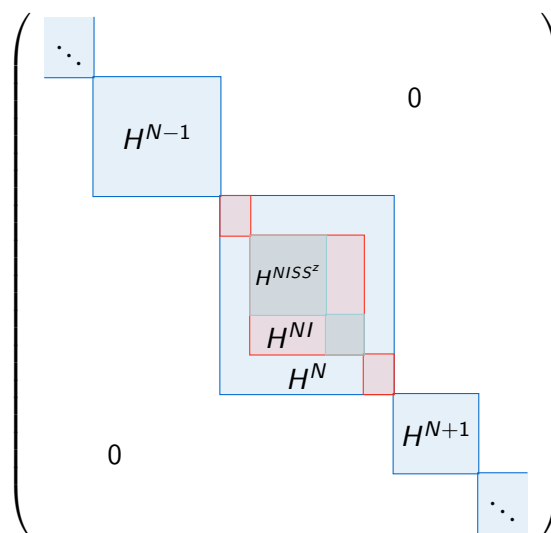
**Figure 3.1.:** Schematic factorization of the Hamiltonian into symmetry blocks. The symmetries used in this Section are particle number $N$, irreducible representation $I$, and spin quantum numbers $S$ and $S^z$.

a subspace of the many-body Hilbert space. When focussing on states with fixed quantum numbers, we can reduce the total problem onto one of the subspaces with a fixed quantum number. All other states can be neglected, since their coefficient in the many-body state are zero. Therefore, the effective Hilbert space dimension reduces and we obtain a computational advantage. This also holds for time-dependent situations, where the good quantum number is a conserved quantity of the system. As soon as the initial state is chosen from one of the subspaces, the time evolved many-body state remains part of this subspace forever.

Already the first DMRG study of chemical systems by White and Martin [105] made use of symmetries. They incorporated the abelian electron number and spin-projection symmetries to find the accurate ground state energy of water. Shortly following, studies additionally incorporating abelian point group symmetries [44, 199] were published, promoting the role of DMRG in quantum chemistry. With these symmetries implemented into the DMRG method, a rich family of quantum chemistry studies evolved with prior unmatched precise results. However, advancing the DMRG method even further by implementation of non-abelian symmetries proved more challenging. First implementation of non-abelian symmetry was done by McCulloch and Gulácsi [200–202] however, not with the aim to study quantum chemical systems. Sharma and Chan [203], as well as Wouters et al. [51] were the first to implement the non-abelian spin symmetry to study eigenstates of quantum chemical systems. Especially implementation of the non-abelian total spin symmetry enhanced the capabilities of the DMRG method and the MPS approach, enabling description of nearly degenerated states with different spin quantum numbers.

In the Hamburg CheMPS2 extension (which is an extension of the implementation by Wouters [51]) we exploit three different symmetries of the molecule. We make use of the electron number symmetry, the point group symmetry, and the spin symmetry, which we discuss in detail in the following.

### 3.1.1 Electron Number

First symmetry we want to discuss more closely is the electron number symmetry. The molecule described in Chapter 2 forms a closed system, where no electrons leave or enter the system. Neither we have any electron sources nor we consider any electron absorbing parts in the system. Then, the Hamiltonian in Equation 2.3 commutes with the total electron number operator

$$\left[\hat{H}, \hat{N}\right] = \left[\hat{H}, \sum_i \left(\hat{n}_{i\uparrow} + \hat{n}_{i\downarrow}\right)\right] = 0, \tag{3.2}$$

which attributes the conservation of the electron number in the system. Since the commutator in Equation 3.2 is zero, we can find a basis where the particle number operator $\hat{N}$ is diagonal and the Hamiltonian is (at least) block diagonal. We can choose the number of electrons (for example corresponding to a neutral molecule) and solve the Schrödinger equation for this block of the Hamiltonian without considering any other block.

In Equation 2.35 we chose to represent the complete many-body state in the occupation number basis. The Hamiltonian is already block diagonal in this basis. To utilize the electron number conservation in the complete many-body state we solely need to restrict the sum over all possible configurations in Equation 2.35 to configurations where $\sum_i n_{i\uparrow} + n_{i\downarrow} = N$ holds

$$|\Psi(t)\rangle \rightarrow |\Psi(t)\rangle_N = \sum_{\substack{n_{1\uparrow} n_{1\downarrow} \cdots n_{L\uparrow} n_{L\downarrow} \\ \sum_i n_{i\uparrow} + n_{i\downarrow} = N}} c_{n_{1\uparrow} n_{1\downarrow} \cdots n_{L\uparrow} n_{L\downarrow}}(t) |n_{1\uparrow} n_{1\downarrow} \cdots n_{L\uparrow} n_{L\downarrow}\rangle. \tag{3.3}$$

We introduced a secondary condition to the summation, as we know coefficients where $\sum_i n_{i\uparrow} + n_{i\downarrow} = N$ is violated are zero. This removes all states with electron number $\neq N$ from the many-body state and reduces the subspace of the many-body Hilbert space considered.

But also the MPS tensors can benefit from the electron number symmetry. In the MPS formulation in Equation 2.56 and Equation 2.59 the virtual basis in which the tensors $A[i]$ are expressed can be chosen arbitrarily, we did not make any statement on its form or shape. We assume the variational optimization of the MPS representation to find the optimal virtual basis and MPS tensor. However, we can support the

variational optimization of the virtual basis by writing the MPS tensors in a virtual basis of electron number eigenstates. We adapt the physical and virtual bonds of the MPS tensors to the particle number basis

$$
\begin{array}{c}
n_{i\uparrow}n_{i\downarrow} \\
\big| \\
a_{i-1} - \boxed{A[i]} - a_i
\end{array}
\quad \rightarrow \quad
\begin{array}{c}
n_i\gamma_i \\
\big| \\
N_{i-1}\alpha_{i-1} - \boxed{A[i]} - N_i\alpha_i
\end{array}
, \tag{3.4}
$$

where each bond $a_{i-1} \rightarrow N_{i-1}\alpha_{i-1}$, $a_i \rightarrow N_i\alpha_i$ and $n_{i\uparrow}n_{i\downarrow} \rightarrow n_i\gamma_i$ is a tuple of particle number $N_{i-1}$, $N_i$ and $n_i$ and remaining degrees of freedom $\alpha_{i-1}$, $\alpha_i$ and $\gamma_i$.

For example, after separation of the occupation number of the physical bond at orbital $i$, it becomes

$$
n_{i\uparrow}n_{i\downarrow} \rightarrow n_i\gamma_i \in \left\{ \begin{array}{c} |n_i = 0, \gamma_i\rangle, \\ |n_i = 1, \gamma_i\rangle, \\ |n_i = 2, \gamma_i\rangle \end{array} \right\}, \tag{3.5}
$$

where $n_i = n_{i\uparrow} + n_{i\downarrow}$ is the number of electrons in the orbital $i$ and $\gamma_i$ holds further information about the orbital (spin and the irreducible representation of the orbital, see following sections). Now the virtual basis states have well defined electron numbers. The electron number $N_i$ of the virtual bond $i$ represents the total number of electrons that are in orbitals to the left of the bond, i.e. in orbitals $\leq i$. For example, when coming across the MPS tensor element

$$
A[4]_{N_3=4\alpha_3, N_4=5\alpha_4}^{n_4=1\gamma_4} = 
\begin{array}{c}
n_4 = 1\gamma_4 \\
\big| \\
N_3 = 4\alpha_3 - \boxed{A[4]} - N_4 = 5\alpha_4
\end{array}
, \tag{3.6}
$$

we know from the virtual basis states that this element of the MPS tensors is part of an expansion coefficient $c_{n_{1\uparrow}n_{1\downarrow}\cdots n_{L\uparrow}n_{L\downarrow}}^N$ where there are 5 electrons distributed over the orbitals 1 to 3 ($5 = \sum_{i=1}^3 n_{i\uparrow} + n_{i\downarrow}$) and 6 electrons are distributed over the orbitals 1 to 4 ($6 = \sum_{i=1}^4 n_{i\uparrow} + n_{i\downarrow}$).

In naive approaches, any coefficient of the many-body state with fixed number of electrons $N$ is constructed without using the electron number symmetry via

$$
c_{n_{1\uparrow}n_{1\downarrow}\cdots n_{L\uparrow}n_{L\downarrow}}^N = \sum_{\alpha_1\cdots\alpha_L}
\begin{array}{c}
n_{1\uparrow}n_{1\downarrow} \quad n_{2\uparrow}n_{2\downarrow} \qquad n_{L\uparrow}n_{L\downarrow} \\
\big| \qquad \big| \qquad\qquad \big| \\
\boxed{A[1]} - \boxed{A[2]} \cdots - \boxed{A[L]} \\
\alpha_1 \quad\quad \alpha_2 \qquad \alpha_L
\end{array}
. \tag{3.7}
$$

$$A^{n_4=1\gamma_4}[4] = \begin{pmatrix} \tilde{A}[4]^{n_4=1\gamma_4}_{N_3=2,N_4=3} & \tilde{A}[4]^{n_4=1\gamma_4}_{N_3=2,N_4=4} \\[1em] A[4]^{n_4=1\gamma_4}_{N_3=3,N_4=3} & \tilde{A}[4]^{n_4=1\gamma_4}_{N_3=3,N_4=4} \\[1em] A[4]^{n_4=1\gamma_4}_{N_3=4,N_4=3} & A[4]^{n_4=1\gamma_4}_{N_3=4,N_4=4} \\[1em] \tilde{A}[4]^{n_4=1\gamma_4}_{N_3=5,N_4=3} & \tilde{A}[4]^{n_4=1\gamma_4}_{N_3=5,N_4=4} \end{pmatrix}$$

**Figure 3.2.:** Schematic classification of the MPS matrix $A^{n_4=1\gamma_4}[4]$ into particle number blocks. Red blocks are zero by particle number symmetry. We only store the blocks $\tilde{A}$ that conform to the electron number symmetry (blue blocks with bold font).

Here, the MPS tensors for representing the coefficient $c^N_{n_{1\uparrow}n_{1\downarrow}\cdots n_{L\uparrow}n_{L\downarrow}}$ are expressed in an arbitrary virtual basis. If physical and virtual bonds are written in the electron number basis the MPS representation turns into

$$c^N_{n_1\gamma_1\cdots n_L\gamma_L} = \sum_{N_1\alpha_1\cdots N_L\alpha_L} \quad 0 \xrightarrow{} \underset{N_1\alpha_1}{A[1]} \xrightarrow{} \underset{N_2\alpha_2}{A[2]} \cdots \xrightarrow{} A[L] \xrightarrow{} N \quad . \tag{3.8}$$

We introduced trivial bonds at the first and at the last MPS tensor. The very left virtual bond ($0$) specifies that there are no electrons on the left of orbital $1$ and the very right virtual bond ($N$) specifies that exactly $N$ electrons have to be distributed over the orbitals $1$ to $L$.

Now with the virtual bonds and physical bonds having particle number indices, we have local particle number conservation in the indices: The number of electrons to the left of orbital $i$ and the number of electrons in orbital $i$ need to sum to the number of electrons in the right bond $N_{i-1} + n_i = N_i$. We can most easily express this in terms of delta functions in the MPS tensors

$$A[i]^{n_i\gamma_i}_{N_{i-1}\alpha_{i-1},N_i\alpha_i} = \tilde{A}[i]^{n_i\gamma_i}_{N_{i-1}\alpha_{i-1},N_i\alpha_i} \, \delta_{N_{i-1}+n_i,N_i}, \tag{3.9}$$

$$N_{i-1}\alpha_{i-1} \xrightarrow{} \overset{n_i\gamma_i}{A[i]} \xrightarrow{} N_i\alpha_i \quad = \quad N_{i-1}\alpha_{i-1} \xrightarrow{} \overset{n_i\gamma_i}{\tilde{A}[i]} \xrightarrow{} N_i\alpha_i \quad \cdot \quad N_{i-1} \xrightarrow{} \overset{n_i}{\delta} \xrightarrow{} N_i \quad . \tag{3.10}$$

Only if $N_{i-1} + n_i = N_i$, the matrix element of $A[i]$ at a given bond index is different from zero and needs consideration in its computational representation. The tensor $A[i]$ is separated into blocks since it only needs to store values where the delta function evaluates to one. This simplifies the form of the MPS tensors $A[i]$, as we only store $\tilde{A}[i]$ (see Figure 3.2).

By using the particle number symmetry in this manner, we focused the MPS representation to cover states of a subspace in the many-body Hilbert space only. Instead of covering the entire many-body Hilbert space, MPS in the symmetry adapted formulation only represent states of the subspace with electron number $N$. This is why MPS implementations employing electron number symmetry have improved convergence behavior. We assisted the variational optimization (or any method that outputs an MPS) to focus on states with the occupation number we are interested in.

### 3.1.2 Irreducible Representations

Additionally to the particle number symmetry, we want to utilize the symmetry that is given by the geometry of the molecule. If the geometry is invariant under rotation or inversion, the electronic density is also invariant under these operations. We can benefit from this property and further reduce the subspace of the many-body Hilbert space that the MPS approach needs to represent.

Molecules can be attributed a point group that is formed by all operations that leave the form of the molecule invariant. Such operations are for example rotations by $2\pi/n$ of the molecule around a symmetry axis ($C_n$), reflections at a symmetry plane $\sigma$ or just the identity operation ($E$). Together with an instruction how to apply paired operations, these operations form a group which is used to characterize the symmetry of the molecule [3]. For example, the point group $C_1$ is the group of the identity alone (no symmetry at all), the point group $C_s$ is the group of the identity operation and a reflection operation at a symmetry plane, and $C_{nv}$ is the group of the identity operation, $n$-fold rotation operations around the main symmetry axis and $n$ possible reflection operations.

If the molecular geometry is invariant under operations of a given point group, also the electronic density implements these symmetry properties. Further is the electronic density surrounding the molecule constructed from the molecular orbitals. Consequently, also the molecular orbitals are invariant under the operations of the point group of the molecule, although they have the freedom to change their sign. This is most vividly demonstrated at the example of the water molecule $H_2O$. The geometry of the water molecule is invariant under operations of the $C_{2v}$ point group

$$C_{2v} = \{\{E, C_2, \sigma_{xz}, \sigma_{yz}\}, *\},$$ (3.11)

which includes the identity ($E$), rotation by $180°$ ($C_2$) around the symmetry axis, vertical mirroring at the $xz$ plane ($\sigma_v(xz)$), and vertical mirroring at the $yz$ plane ($\sigma_v(yz)$) (see Figure 3.3 a)). The symbol $*$ is the operation to multiply the symmetry operations.
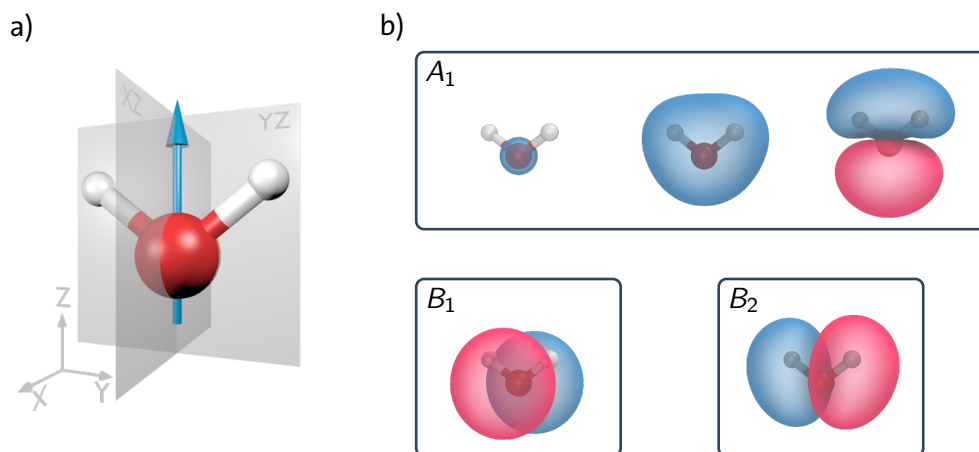
**Figure 3.3.:** Symmetry properties and molecular orbitals of the water molecule $H_2O$. a) shows the symmetry planes and the symmetry axis of the water molecule. Rotation by $\pi$ around the symmetry axis, as well as mirroring at the $xz$ plane and the $yz$ plane leaves the molecule unchanged. b) The molecular orbitals with respect to their irreducible representation. The molecular orbitals transform like the irreducible representations of the $C_{2v}$ point group. There is no occupied molecular orbital that transforms like irreducible representation $A_2$ in the water molecule.

a)

| $C_{2v}$ | $E$ | $C_2$ | $\sigma_v(xz)$ | $\sigma_v(yz)$ |
|----------|-----|-------|----------------|----------------|
| $A_1$ | 1 | 1 | 1 | 1 |
| $A_2$ | 1 | 1 | $-1$ | $-1$ |
| $B_1$ | 1 | $-1$ | 1 | $-1$ |
| $B_2$ | 1 | $-1$ | $-1$ | 1 |

b)

| $\otimes$ | $A_1$ | $A_2$ | $B_1$ | $B_2$ |
|-----------|-------|-------|-------|-------|
| $A_1$ | $A_1$ | $A_2$ | $B_1$ | $B_2$ |
| $A_2$ | $A_2$ | $A_1$ | $B_2$ | $B_1$ |
| $B_1$ | $B_1$ | $B_2$ | $A_1$ | $A_2$ |
| $B_2$ | $B_2$ | $B_1$ | $A_2$ | $A_1$ |

**Table 3.1.:** The character table a) and multiplication table b) of the $C_{2v}$ point group.

In case of $C_{2v}$ symmetry, the molecular orbitals are categorized by four *irreducible representations* (irreps) $A1$, $A2$, $B1$, and $B2$. The irreps specify under what operations of the point group a molecular orbital changes its sign. For example, the molecular orbitals of the irrep $A_1$ do not change sign if any operation of the $C_{2v}$ point group is applied (see Figure 3.3 b) (top) ). The molecular orbitals of the irrep $B_1$ change their sign if rotated by $180°$ or when mirrored at the $yz$-plane. Whether the molecular orbital changes its sign is noted in terms of *character tables*. The character table of the $C_{2v}$ symmetry is given in Table 3.1 a) where 1 symbolizes the molecular orbital remains unaffected by the operation and $-1$ symbolizes the molecular orbital changes its sign if the symmetry operation is applied. In Figure 3.3 b) we see, a sign-full representation of the molecular orbitals of the water molecule. Character tables such as the one given above for the $C_{2v}$ point group exist for all point groups [204].

In Section 2.2.2 we chose to represent the complete many-body state as a linear combination of configurations, i.e. occupation number basis states (see Equation

2.35). The configurations are not only eigenstates of the occupation number operator, but they can be attributed to a fixed irrep as well. The irrep $I$ of the configuration $|n_{1\uparrow}n_{1\downarrow}\cdots n_{L\uparrow}n_{L\downarrow}\rangle$ is

$$I = \bigotimes_{i=1}^{L} \tilde{I}_i, \qquad \tilde{I}_i = \begin{cases} \hat{I}_i, & \text{if } n_{i\uparrow} + n_{i\downarrow} = 1 \\ \hat{I}_0, & \text{otherwise} \end{cases}, \qquad (3.12)$$

where $\hat{I}_i$ is the irrep of the orbital $i$ and $\hat{I}_0$ is the trivial irrep ($A_1$ for the $C_{2\nu}$ point group example above). How the irreps are multiplied by $\otimes$ is specified in *multiplication tables* (see Table 3.1 b)). Therefore, not only the molecular orbitals correspond to one of the irreps, but we can extend this to the many-body state level by attributing the configurations a fixed irrep as well.

With the configurations embodying irreps, also the complete many-body state transforms like an irrep if constructed from configurations of one irrep only. When fixing the irrep of the many-body state prior to the calculation, the sum over all possible configurations in Equation 2.35 reduces

$$|\Psi(t)\rangle_N \rightarrow |\Psi(t)\rangle_{NI} = \sum_{\substack{n_{1\uparrow}n_{1\downarrow}\cdots n_{L\uparrow}n_{L\downarrow} \\ \sum_i n_{i\uparrow}+n_{i\downarrow}=N \\ \otimes_{i=1}^{L}\tilde{I}_i=I}} c_{n_{1\uparrow}n_{1\downarrow}\cdots n_{L\uparrow}n_{L\downarrow}}(t)\, |n_{1\uparrow}n_{1\downarrow}\cdots n_{L\uparrow}n_{L\downarrow}\rangle. \qquad (3.13)$$

Again, we construct the many-body state from a smaller subspace of the complete many-body Hilbert space just as we did for electron number symmetry.

With the newly introduced irrep of the many-body state, we can further decompose the bonds of the MPS tensors. We can again attribute the virtual bonds quantum numbers, now with respect to the irrep. Every bond gets an additional degree of freedom to specify the irrep. Together with the electron number degree of freedom the MPS tensors read



$$(3.14)$$

Also the physical bonds now carry the irrep of the orbital, or the left part of the system in all bonds. The physical bonds are now

$$n_i i_i \gamma_i \in \begin{cases} |n_i = 0, i_i = \hat{I}_0, \gamma_i\rangle \\ |n_i = 1, i_i = \hat{I}_i, \gamma_i\rangle \\ |n_i = 2, i_i = \hat{I}_0, \gamma_i\rangle \end{cases}, \qquad (3.15)$$

where empty orbitals and double occupied orbitals have the trivial irrep $\hat{I}_0$ and only single occupied orbitals contribute to the irrep of the many-body state. The index $\gamma_i$ symbolizes remaining physical degrees of freedom, which is the spin state of the electron that occupies the orbital. This degree of freedom is subject of Section 3.1.3.

In the Hamburg CheMPS2 extension we restrict ourselves to abelian point groups, i.e. to point groups where the symmetry operations commute. Non-abelian point groups are implemented in the quantum chemistry package BLOCK by Chan et al. [205], whereas the CheMPS2 package and the Hamburg CheMPS2 extension is limited to abelian symmetries.

Similar to the procedure of the particle number symmetry, we can factor the MPS tensor into a reduced tensor and a delta function. When taking advantage of the electron number symmetry and the point group symmetry of the molecule, tensors in the MPS representation read

$$A[i]^{n_i i_i \gamma_i}_{N_{i-1} I_{i-1} \alpha_{i-1}, N_i I_i \alpha_i} = \tilde{A}[i]^{n_i i_i \gamma_i}_{N_{i-1} I_{i-1} \alpha_{i-1}, N_i I_i \alpha_i} \, \delta_{N_{i-1}+n_i, N_i} \, \delta_{I_{i-1} \otimes i_i, I_i}, \qquad (3.16)$$



$$\qquad (3.17)$$



$$\qquad (3.18)$$

where the delta function $\delta_{I_{i-1} \otimes i_i, I_R}$ takes into account the contributing irreps.

The MPS representation of the expansion coefficient $c^{NI}_{n_1 i_1 \gamma_1 \cdots n_L i_L \gamma_L}$ in the complete many-body state with $N$ electrons and the irrep $I$ is again in terms of MPS tensors

$$c^{NI}_{n_1 i_1 \gamma_1 \cdots n_L i_L \gamma_L} = \sum_{\substack{N_1 \cdots N_{L-1} \\ I_1 \cdots I_{L-1} \\ \alpha_1 \cdots \alpha_{L-1}}} \quad \text{} \qquad (3.19)$$

with zero particles and the trivial irrep to the left of orbital 1. Using the fixed bonds at the very left and at the very right of the MPS and the delta functions in Equation 3.18, the MPS automatically only considers configurations with the correct irrep. Therefore, we were able to remove configurations from the sum in Equation 2.35, as their coefficients are necessarily zero. This reduces the dimension of the subspace of the many-body Hilbert space the MPS represent.

But utilizing the molecular symmetry and expressing the molecular orbitals in terms of irrep does not only simplify the representation of the complete many-body state.

Further, do some of the integrals in the quantum chemistry Hamiltonian (see Equation 2.36) evaluate to zero by symmetry [61]. The one-body integrals $t_{ij}$ and the two-body integrals $V_{ijkl}$ may be zero due to the parity of the orbital [3]. In the application of the Hamiltonian, we are able to simplify the sums, which reduces the time to apply the Hamiltonian to many-body states (either in complete representation or in MPS representation).

### 3.1.3  Spin Quantum Number

With the particle number symmetry and the symmetry of the molecular geometry we have utilized two abelian symmetries with quantum numbers that are conserved on the individual tensor level. Additionally, we want to utilize that the magnetic moment of the electrons is a conserved quantity, i.e. we want to take advantage of total spin symmetry of the molecule. The total spin symmetry is a non-abelian symmetry, which makes it more challenging to implement into the MPS approach. However, the additional reduction of the subspace of the many-body Hilbert space is significant and allows for a much more precise representation of many-body states using the MPS approach. We want to introduce the spin symmetry as implemented in CheMPS2 package by Wouters [51, 206], which is based on theory by McCulloch and Gulácsi [200].

The operators quantifying the magnetic moment of the electrons in the molecule are given in second quantization

$$\hat{S}_x = \frac{1}{2} \sum_i \left( \hat{c}_{i\uparrow}^\dagger c_{i\downarrow} + \hat{c}_{i\downarrow}^\dagger c_{i\uparrow} \right), \tag{3.20}$$

$$\hat{S}_y = \frac{1}{2i} \sum_i \left( \hat{c}_{i\uparrow}^\dagger c_{i\downarrow} - \hat{c}_{i\downarrow}^\dagger c_{i\uparrow} \right), \tag{3.21}$$

$$\hat{S}_z = \frac{1}{2} \sum_i \left( \hat{c}_{i\uparrow}^\dagger c_{i\uparrow} - \hat{c}_{i\downarrow}^\dagger c_{i\downarrow} \right), \tag{3.22}$$

$$\hat{S}^2 = \hat{S}_x \hat{S}_x + \hat{S}_y \hat{S}_y + \hat{S}_z \hat{S}_z. \tag{3.23}$$

These operators are angular momentum operators, i.e. they follow the commutation relations of the angular momentum algebra [207]. The quantum chemistry Hamiltonian in Equation 2.36 commutes with all these operators

$$\left[ \hat{H}, \hat{S}^2 \right] = 0 \text{ and } \left[ \hat{H}, \hat{S}_\alpha \right] = 0 \ \forall \alpha \in \{x, y, z\}, \tag{3.24}$$

therefore, the Hamiltonian and the spin operators share eigenstates. Further $\hat{S}^2$ and $\hat{S}_z$ commute with $\hat{N}$ and $\hat{I}$. The goal is now to find the eigenbasis of the total spin operator $S^2$ and the (for example) $S_z$ component of the spin. In this basis, the Hamiltonian is block diagonal and we can again focus on the subspace of the many-body

Hilbert space, as we did for the particle number symmetry and the molecular geometry symmetry. While $S_z$ is conserved on a local orbital level, $S^2$ involves different orbitals.

At the heart of the incorporation of the spin symmetry into MPS tensors is the *Wigner–Eckhart-Theorem* [208, 209]. It states that any tensor $T^k$ of rank $k$ expressed in the eigenbasis of the angular momentum operator $|s\, s_z\rangle$ can be decomposed as

$$\langle s\, s^z|\, T_q^k\, |s'\, s^{z'}\rangle = \langle ss^z kq|s's^{z'}\rangle\, \langle s||T^k||s'\rangle, \tag{3.25}$$

where $\langle ss^z kq|s's^{z'}\rangle$ is the *Clebsch–Gordan coefficient*, $q$ is the component of the tensor $T$, and $\langle s||T^k||s'\rangle$ is a reduced representation of the tensor, which lost its dependence on the magnetic spin quantum numbers $S_z$. The Clebsch–Gordan coefficients are mostly known from addition of angular momenta in quantum mechanics but they appear in this context as well [207].

We express the MPS tensors in the eigenbasis of the spin operators and decompose it according to the Wigner–Eckhart-Theorem. This allows us then to restrict the MPS representation to eigenstates with fixed spin $S$ and the magnetic projection $S_z$. We express all bonds, i.e. physical and virtual basis states, in the eigenbasis of the spin operators. Now, when introducing a spin-full indexing of the physical states, we have a complete set of indices specifying the physical state of the orbital $i$. We add the spin quantum numbers to the physical bonds

$$n_i i_i s_i s_i^z \in \begin{cases} |n_i = 0, i_i = I_0, s_i = 0, s_i^z = 0\rangle \\ |n_i = 1, i_i = I_i, s_i = \frac{1}{2}, s_i^z = \frac{1}{2}\rangle \\ |n_i = 1, i_i = I_i, s_i = \frac{1}{2}, s_i^z = -\frac{1}{2}\rangle \\ |n_i = 2, i_i = I_0, s_i = 0, s_i^z = 0\rangle \end{cases}, \tag{3.26}$$

and are now able to exactly characterize all four possible states of an orbital. Expressing an MPS tensor in the spin eigenbasis, we obtain



$$\tag{3.27}$$

In this basis, most strikingly, we can decompose the MPS tensors in terms of the Wigner–Eckhart-Theorem in Equation 3.25 to obtain

$$A[i]_{N_{i-1}I_{i-1}S_{i-1}S_{i-1}^z\alpha_{i-1},N_iI_iS_iS_i^z\alpha_i}^{n_i i_i s_i s_i^z} = \langle S_{i-1}S_{i-1}^z s_i s_i^z|S_iS_i^z\rangle\, \delta_{N_{i-1}+n_i,N_i}\, \delta_{I_{i-1}\otimes i_i,I_R}$$
$$\tilde{A}[i]_{N_{i-1}I_{i-1}S_{i-1}\alpha_{i-1},N_iI_iS_i\alpha_i}^{n_i i_i s_i}, \tag{3.28}$$

where it is particularly important to note that the reduced MPS tensor $\tilde{A}[i]$ does not depend on the magnetic quantum numbers $S^z_{i-1}$, $S^z_i$, and $s^z_i$. This is an immense reduction in dimension of the MPS tensors, where we use the sparsity most efficiently. The magnetic spin quantum numbers only appear in the Clebsch–Gordan coefficient, which we only evaluate if necessary.

The final MPS approach, incorporating the particle number, the geometry rotation, and the spin symmetry is then given by the reduced tensors

$$
c^{NISS^z}_{n_1 i_1 s_1 s^z_1 \cdots n_L i_L s_L s^z_L} = \sum_{\substack{N_1 \cdots N_{L-1} \\ I_1 \cdots I_{L-1} \\ S_1 \cdots S_L \\ S^z_1 \cdots S^z_L \\ \alpha_1 \cdots \alpha_{L-1}}} \quad , \qquad (3.29)
$$



where $N$ is the fixed electron number in the system, $I$ is the fixed irrep of the many-body state, $S$ is the spin quantum number of the many-body state, and $S^z$ is the magnetic spin quantum number of the many-body state. But with the reduced representations of the MPS tensors, we only need to store the reduced MPS tensors $\tilde{A}[i]$

$$
c^{NISS^z}_{n_1 i_1 s_1 s^z_1 \cdots n_L i_L s_L s^z_L} = \sum_{\substack{N_1 \cdots N_{L-1} \\ I_1 \cdots I_{L-1} \\ S_1 \cdots S_L \\ S^z_1 \cdots S^z_L \\ \alpha_1 \cdots \alpha_{L-1}}} \quad , \qquad (3.30)
$$



in the MPS representation of the complete many-body state. The remaining factors are given by the delta functions and the Clebsch–Gordan coefficients that we do not need to store as they can be evaluated on demand.

On the one hand, the spin symmetry reduces the size of the Hilbert space that the MPS is requested to span, and on the other hand reduces the rank of the individual MPS tensors. In the MPS implementation, we exclusively work with the reduced MPS tensors $\tilde{A}[i]^{N_i I_i S}_{N_L I_L S\alpha, N_R I_R S\beta}$, whereas the full tensor is never calculated. Where needed, it is multiplied with the corresponding Clebsch–Gordan coefficient and delta functions. This allows for large efficiency improvements compared to the utilizing the abelian symmetries only. It allows to reduce the size of the MPS tensors, but it also allows to resolve states that are close to degeneracy [114]. When performing ground state calculations, states may be close to degeneracy and the variational optimization is likely to be trapped in a local minimum, as it tends to mix nearly degenerate states. The use of the spin quantum number allows to distinguish between those states and

to approach the real ground state correctly (or the minimal energy state for some given *S*).

We have now achieved both, we found an efficient method to simplify the MPS structure, as well as reduced the dimension of the Hilbert space we are interested in. The particle number, the point group symmetry, and the total spin symmetry enabled us to define reduced MPS tensors with physical and virtual basis states being eigenstates of the particle number operator, a fixed irrep and the spin operator. Next, we want to discuss the Hamburg CheMPS2 extension in more detail and outline the features needed to use the MPS approach to study time-dependent situations in quantum chemistry.

## 3.2  The Hamburg CheMPS2 Extension

The program package that was developed in this work to solve the time-dependent Schrödinger equation for the quantum chemistry Hamiltonian using the MPS approach is a fork of the *CheMPS2* package written by Sebastian Wouters at Ghent University [51, 151]. CheMPS2 is considered as one of the state-of-the-art DMRG quantum chemical implementations. The CheMPS2 package is embedded in various quantum chemistry packages, such as psi4 [210, 211], pyscf [212], and molcas [213], where it serves as an efficient solver for otherwise too large active spaces. Today, it is not actively extended by the authors, however, there are maintenance updates on an irregular basis.

The CheMPS2 package is a highly optimized program tailored to find ground states and low lying excited states of molecules using the MPS approach. It incorporates particle number symmetry, point group symmetry, and spin symmetry into the MPS tensor representation (see Section 3.1). It allows to find the eigenstates using a standard two-site MPS variational method (DMRG) and to find excited states using orthogonal projection. Additionally, it implements the complete active space self consistent field method (CAS-SCF) [95, 214, 215], as well as, the complete active space second order perturbation theory method (CASPT2) [216, 217]. In these methods the full CI solver of the active space has been replaced with the DMRG solver (then it is called DMRG-SCF and DMRG-CASPT2) [108, 148, 151]. The limit for active spaces is close to 40 orbitals, holding 40 electrons. Larger active spaces require immense amounts of time and memory that are impractical in most situations. The CheMPS2 program allows for various analysis outputs of the resulting MPS, ranging from spin-spin correlation functions to $2-$, $3-$, and $4-$ particle reduced density matrices.

The CheMPS2 package, including the entire source code is published on GitHub at `https://github.com/SebWouters/CheMPS2` under the *GNU General Public License Version 2* (GPL-2.0). This license allows free use and extension of the code, given the precondition that any extensions need to be published under the GPL-2.0 or one of its successors. The Hamburg CheMPS2 extension is therefore also published on GitHub at `https://github.com/lfrahm/CheMPS2` under the license GPL-2.0 including the source code and the documentation.

In the following section we discuss the Hamburg CheMPS2 extension. We explain the necessary adaptions to solve the time-dependent Schrödinger equation and outline implementational details of the time evolution methods to improve performance.

### 3.2.1 Necessary Adaptions

Even though the CheMPS2 package is one of the most popular MPS implementation for quantum chemistry, it lacks necessary features we require in order to implement the time evolution methods described in Section 2.5. It is specifically tailored to ground and excited state optimization, rather than implementing the tensor network in a flexible way. The MPS approach is deeply integrated into the code, with most objects only present in the MPS approach. For our time-dependent MPS approach, we can reuse parts of the existing code, however, most parts needs to be adapted at least slightly.

The major adaptions include

- Development of a variational optimization algorithm to perform MPS addition and application of operators. The representation of the Hamiltonian needs to be adapted to perform variational operator application.

- Adaption of new MPS tensor objects that allow for representation of complex-valued many-body states and implementation of the complex-valued two-site objects required in the optimization scheme of complex MPS.

- Stable implementation of the time evolution methods.

### 3.2.2 Representation of the Hamiltonian

In Section 2.4.9, we describe an optimization scheme to add MPS and to apply operators (see Equation 2.97) to MPS. We optimize the virtual basis and the MPS tensors to find the MPS representation of the resulting many-body state of the performed

operation. In this optimization scheme, we replace the MPS tensor that is currently optimized with an evaluated tensor network. For example, to apply the Hamiltonian to the MPS $|B\rangle_{MPS}$, the MPS tensor $B[i]$ is replaced by (compare the tensor network in Equation 2.97)



$$\hspace{9cm} (3.31)$$

The operators $H_l$ and $H_r$ are called *renormalized operators*. The renormalized operators are the representations of the Hamiltonian in the virtual basis of the MPS tensor at orbital $i$. We need these to express the action of the Hamiltonian on the MPS tensor $C[i]$. They occur naturally in the MPS approach and are similar to the renormalized operators known from the DMRG method.

In the DMRG method, similar tensor networks as in Equation 3.31 occur, however, there the upper MPS and the lower MPS are the same. This follows from minimization of the functional

$$min = \frac{_{MPS}\langle \Psi|\hat{H}|\Psi\rangle_{MPS}}{_{MPS}\langle \Psi|\Psi\rangle_{MPS}}, \hspace{3cm} (3.32)$$

when solving for the ground state. The variational optimization is similar to what we described in Section 2.4.9, however here only one state $|\Psi\rangle_{MPS}$ appears in the functional. As the CheMPS2 package solves for eigenstates of the Hamiltonian, it is optimized to solve functionals as given in Equation 3.32, instead of the more general functional we need to solve in Equation 2.96. For the optimization in terms of operator application and MPS addition, we also need the tensor network where there are two or more states in the functional, which introduces a completely new type of tensor networks and forbids to take advantage of many useful tensor identities the original CheMPS2 packages builds upon.

For example, ground state optimization and time-dependent MPS need a renormalized representation of a product of the electron creation operator at the orbital $i$ and an electron annihilation operator at orbital $j$ ($\hat{c}_{i\sigma}^{\dagger}\hat{c}_{j\sigma}$) to represent the one-electron

integrals in the quantum chemistry Hamiltonian. Let us assume we optimize the MPS tensor at orbital $k > i, j$, then we evaluate the tensor network

$$(c_{i\sigma}^\dagger c_{j\sigma})[k] = \boxed{\begin{array}{c} \text{tensor network diagram} \end{array}}_{S[i-1]} , \qquad (3.33)$$

as part of the operator $H_I$ in Equation 3.31. The three open bonds on the right indicate that $(c_{i\sigma}^\dagger c_{j\sigma})[k]$ is an operator on the virtual bonds (rank 3 tensor). We construct such diagrams for all one-body operators in the quantum chemistry Hamiltonian and also for all two-body combinations of operators (see renormalized operators in [105] and [206] ). The object $S[i-1]$ was already introduced in Section 2.4.6, where we introduced the normalization features of the MPS representation (there $S[i]$ turned out to be the identity operator) and also in Section 2.4.4 where we described the overlap of MPS. Ground state DMRG can be formulated such that the tensor $S[i-1]$ is always the identity tensor and we do not need to evaluate it in any detail (this follows from the case $|C\rangle_{MPS} = |A\rangle_{MPS}$ and dexterous use of normalization centers). In the situation in Equation 3.31 however, we have different upper and lower MPS states, therefore we need to evaluate the tensor network for every renormalized operator.

Another helpful feature in ground state DMRG we can not utilize is the representation of conjugated operators: The renormalized operator for $\hat{c}_{j\sigma}^\dagger \hat{c}_{i\sigma}$ in the virtual basis at site $k$ is not given by the hermitian conjugation of $\hat{c}_{i\sigma}^\dagger \hat{c}_{j\sigma}$ in the virtual basis at site $k$

$$(c_{j\sigma}^\dagger c_{i\sigma})[k] \neq \left( (c_{i\sigma}^\dagger c_{j\sigma})[k] \right)^\dagger , \qquad (3.34)$$

however, we must evaluate their tensor networks independently. This is an artefact of the virtual basis of the MPS. If conjugating the renormalized operator in Equation 3.33 this would also conjugate the MPS tensors

$$\left( (c_{i\sigma}^\dagger c_{j\sigma})[k] \right)^\dagger = \boxed{\begin{array}{c} \text{tensor network diagram} \end{array}} , \qquad (3.35)$$

however, in Equation 3.31 we need the network (among many others)

$$(c_{j\sigma}^{\dagger}c_{i\sigma})[k] = \begin{array}{ccccccc} \boxed{B[1]} & \cdots & \boxed{B[i]} & \cdots & \boxed{B[j]} & \cdots & \boxed{B[k]} \\ \boxed{1[1]} & \cdots & \boxed{\hat{c}_{\sigma}[i]} & \cdots & \boxed{\hat{c}_{\sigma}^{\dagger}[j]} & \cdots & \boxed{1[k]} \\ \boxed{A[1]} & \cdots & \boxed{A[i]} & \cdots & \boxed{A[j]} & \cdots & \boxed{A[k]} \end{array}. \quad (3.36)$$

This introduces an immense number of additional tensor networks that are needed to implement and evaluate when using variational optimization to apply the Hamiltonian to an MPS.

The additional overlap tensor networks we need to consider and the missing conjugation features are just two examples where working with time-dependent MPS is more challenging than implementing ground state optimization using the MPS approach. There are more tensor networks and operators required when working with time-dependent MPS, however, we will not discuss them in more detail. Most of these adaptions originate in the examples present above: New complex networks we have to include and the absence of conjugation properties of renormalized operators.

### 3.2.3  Transition to Complex Numbers

Second major adaption in the Hamburg CheMPS2 extension is the transition to complex-valued MPS representations. The phase introduced by the time evolution gives rise to complex expansion coefficients in the complete many-body states, and therefore, we also need to represent them by complex-valued MPS representations. For ground state and excited state optimization this is not necessary, since we can find a gauge where the eigenstates of the Hamiltonian are entirely real-valued in the absence of magnetic fields. Consequently, the MPS representation as implemented in CheMPS2 uses real numbers only, which we need to adapt.

With the transition to complex numbers, the complexity of the entire MPS approach gains a factor of 4. Where the multiplication of two real numbers is usually implemented directly (on float point operation), the multiplication of two complex numbers is broken down into four multiplications of real numbers. Therefore, we need to expect at least four times the computational demand compared to ground state calculations, plus the added complexity due to the additional evaluated diagrams (see Section 3.2.2).

But with the transition to complex-valued MPS tensors further come adjustments to all computational routines. We also need to adapt the methods to operate on MPS tensors and the renormalized operators $(c_{i\sigma}^{\dagger}c_{j\sigma})[k]$, e.g. algorithms to evaluate

tensor networks using multiplication algorithms and singular value decomposition, to complex-valued MPS tensors.

## 3.2.4 Implementational Remarks

The two most important extensions of CheMPS2 program are the implementation of the variational optimization scheme for Hamiltonian application and MPS addition, as well as the implementation of the time evolution methods. In the following section we want to outline some tricks to improve convergence and increase numerical stability that are implemented in the Hamburg CheMPS2 extension.

The newly introduced class `HamiltonianOperator` handles the variational optimization, whereas the class `TimeEvolution` is responsible for everything related to time evolution. Among the added tensor networks explained in the two sections before, these two classes incorporate the most important procedures to perform time-dependent calculations. These procedures include algorithms for the three different time evolution algorithms introduced in Section 2.5.

**Implementation of Variational Optimization**

An implementational note is due on the trial MPS used for the optimization scheme. In the variational algorithm, we start by choosing an arbitrary MPS, which we then optimize to represent the desired operation. For example, when adding the MPS $|A\rangle_{MPS}$ and $|B\rangle_{MPS}$ we optimize the trial MPS $|C\rangle_{MPS}$ for the minimum of the functional (compare Equation 2.90)

$$\mathcal{L}[|C\rangle_{MPS}] = |||C\rangle_{MPS} - (|A\rangle_{MPS} + |B\rangle_{MPS})||^2. \tag{3.37}$$

The variation therefore relies on a good choice of the trial MPS $|C\rangle_{MPS}$, which needs to have overlap with the optimal MPS that minimizes the function in Equation 3.37 globally. A bad choice may let the variation finish in a local minimum instead of the global minimum. In the Hamburg CheMPS2 implementation of the variational method, we chose to reuse the virtual basis of the MPS $|A\rangle_{MPS}$ and $|B\rangle_{MPS}$ as the virtual basis of the trial MPS $|C\rangle_{MPS}$, however with random numbers filling the tensors of the MPS $|C\rangle_{MPS}$. In the examples benchmarked, this improves the convergence of the variation algorithm and it is less likely to get trapped in a local minimum.

**Implementation of Krylov Time Evolution**

Another helpful implementational adjustment is to reformulate how the time evolved states are constructed from the Krylov basis vectors in MPS representation. We already adjusted the time evolution operator in the Krylov space in Equation 2.112 by an inverted overlap matrix to account for any loss of orthogonality of the Krylov basis vectors. This is the mathematically correct method, when working with non-orthogonal bases, however, there is a more numerically stable method to do this. We will see in Section 4.3.2 that the non-orthogonalized Krylov method is prone to errors, if the state to be time evolved is close to an eigenstate of the Hamiltonian. Then the non-orthogonalized Krylov basis vectors become linearly dependent of each other and the overlap matrix $N$ approaches singularity. If the overlap matrix $N$ has eigenvalues close to zero, taking the inverse results in a significant numerical error. In the Hamburg CheMPS2 extension, we therefore adjust the time evolved state to

$$|\psi(t + \Delta t)\rangle_{MPS} = \sum_k \left[ e^{-i\frac{\Delta t}{\hbar} N^{-\frac{1}{2}} H N^{-\frac{1}{2}}} \right]_{k0} N^{-\frac{1}{2}} |\phi^k\rangle_{MPS}, \quad (3.38)$$

which is mathematically equivalent to the method in Equation 2.112, however, numerically evaluating $N^{-\frac{1}{2}}$ is more stable if $N$ is close to singularity.

**Parallelism**

Wouters additionally studied the DMRG method in terms of computational parallelism [206]. The original CheMPS2 program allows for parallelization using multi machine environments with respect to the *Message Passing Interface* (MPI), as well as parallelization using many cores on one machines using the *Open Multi-Processing* (OpenMP) protocol. He demonstrated that the CheMPS2 implementation allows for almost optimal parallelization in both frameworks. The Hamburg CheMPS2 extension right now only utilizes OpenMP parallelization. It therefore requires to run on single machines, however, it is able to make use of many cores calculating simultaneously. When running in an multi-core environment, the different symmetry sectors of MPS tensors and the renormalized operators explained in Section 3.1 are evaluated independently by different cores. The extension to multi machine environments using the MPI protocol is possible and desirable, however, it may be demanding in implementation time.

**Listing 3.1:** An example input file to perform a time-dependent MPS calculation using the Hamburg CheMPS2 extention.

```
1   FCIDUMP = h2o.fcidump
2   GROUP   = 5
3
4   MULTIPLICITY = 2
5   NELECTRONS   = 9
6   IRREP        = 0
7
8   REORDER_FIEDLER = TRUE
9
10  TIME_TYPE        = K
11  TIME_KRYSIZE     = 5
12  TIME_ORTHO       = TRUE
13  TIME_BACKWARD    = FALSE
14
15  TIME_STEP_MAJOR = 0.10
16  TIME_STEP_MINOR = 0.10
17  TIME_FINAL      = 43.0
18
19  TIME_NINIT      = 1, 2, 2, 0, 0, 0, 0, 2, 0, 2, 0, 0, 0
20
21  TIME_HDF5OUTPUT = result.hdf5
22  TIME_N_WEIGHTS  = 0
23  TIME_HF_STATE   = 2, 2, 2, 0, 0, 0, 0, 2, 0, 2, 0, 0, 0
24
25  SWEEP_STATES       = 300, 300, 300
26  SWEEP_MAX_SWEEPS   = 2, 2, 4
27  SWEEP_NOISE_PREFAC = 1e-4, 1e-6, 0
28  SWEEP_CUTOFF       = 0, 0, 0
```

## 3.2.5 Interfaces to the Hamburg CheMPS2 Extension

The Hamburg CheMPS2 extension offers two interfaces to interact with users. First, it offers a C++ interface for compiled applications that make use of the Hamburg CheMPS2 library. Here all necessary classes and features can be used and controlled from external applications. Second, it has build-in executables for the most common tasks, such as:

- The `chemps2dyn` executable for time-dependent calculations using MPS.

- The `chemps2fci` executable for time-dependent calculations using the complete many-body state.

- The `chemps2conv` executable to convert a real-valued MPS to a complex-valued MPS.

- The `chemps2ion` executable for removing an electron from an orbital in a complex-valued MPS.

These executables come with every installed version of the Hamburg CheMPS2 extension. They show a complete documentation of input parameters by calling them using the help command `./chemps2xxx --help`. All of the executables can be controlled by *input* files that allow the user to specify the task. This is an adaption of the original CheMPS2 package that also offers an interface via input files, however, we extended the interface for time-dependent MPS calculations.

Listing 3.1 shows an example input file to perform a time-dependent MPS calculation using the `chemps2dyn` executable. It starts with the definition of the system, for example, giving the file of integrals for the many-body Hamiltonian (FCIDUMP), a symmetry group identifier, the number of electrons in the system (lines 1 to 8) and the order of orbitals used (here reordering based on the Fiedler minimization of the Hamiltonian band with [151]). It then continues with parameters to specify the time evolution in lines 10 to 22, such as an identifier for the time evolution method (here Krylov), parameters as time step size and the time to propagate to, and the form of the initial state. It ends with the definition of parameters for the optimization algorithm, giving the number of sweeps and the bond dimension of the MPS tensors.

The `chemps2dyn` executable allows for input of three different types of initial states. First and most basic option is to give the initial state in terms of occupation numbers of the orbitals, such as given in line 19 of Listing 3.1. The program then forms an uncorrelated state using the given occupation numbers. Of course, the sum of the occupation numbers need to match to the number of electrons in the system that is given in line 5 of Listing 3.1. Second option is to define a superposition of uncorrelated states as the initial state. This is done by writing

```
1    TIME_NINIT      = 2, 2, 2, 2, 0, 0, 0, 0, 0, 2, 1, 0, 0, 0, 0, 2, 2, 0, 0, 0, 0
2    TIME_2_NINIT    = 2, 2, 2, 2, 0, 0, 0, 0, 0, 1, 2, 0, 0, 0, 0, 2, 2, 0, 0, 0, 0
3    TIME_PREFACS    = 0.7071067811865475, 0.0, 0.7071067811865475, 0.0
```

in the input file. The program then forms a superposition of the two uncorrelated states with similar prefactors. The initial state is constructed as

$$|\psi(t_0)\rangle_{MPS} = \frac{1}{\sqrt{2}} |1\rangle_{MPS} + \frac{1}{\sqrt{2}} |2\rangle_{MPS}, \tag{3.39}$$

where the states $|1\rangle_{MPS}$ and $|2\rangle_{MPS}$ are the uncorrelated states given in line 1 and line 2. Such an initial state has been used in Section 5. Third option to specify the initial state is to give an MPS that has to match to the system and the chosen symmetry (size of the system, number of electrons, multiplicity). Here any MPS stored in the HDF5 format can be used by giving

```
1    TIME_INIT       = CheMPS2_CMPS_ION.h5
```

in the input file.

The Hamburg CheMPS2 extension offers two ways of providing the results. Some of the result are printed to the console. This includes quantities that serve more for debugging purposes such as the energy at any point in time (which is supposed to be constant in ideal situations), the norm of the time-evolved state (which should stay close to 1). But also the occupation number of the molecular orbitals, CI weights, as

well as, the projection onto the initial state, which is a one-particle Green's function are printed at every time step.

For more complex output parameters the Hamburg CheMPS2 extension also creates a binary output in the version 5 of the Hierarchical Data Format (HDF5). In this binary file the results are stored in a simple to parse format. Here the user also gets the one-particle reduced density matrix, the two-particle reduced density matrix if requested, full CI coefficients and more calculation depending numbers such as the size of the MPS tensors and the time since start of the calculation. The HDF5 file can be easily extend by arbitrary observables and correlators.

The Hamburg CheMPS2 extension is published under the GNU General License version 2 and can be freely copied and extended, however, with the condition that modified versions are published under the GPL2-2.0 or one of its successors.

# Analysis of the Matrix Product State Approach to Study Ultrafast Dynamics in Molecules

<span style="float:right; font-size:3em; color:#1a6fc4;">4</span>

At this point, we established the concepts to operate with many-body states in MPS representation and discussed the Hamburg CheMPS2 extension to perform numerical calculations on time-dependent problems in quantum chemical systems. However, the MPS representation has never been used to describe electron dynamics in molecules before, therefore, a profound analysis of the performance of this novel method is due. In this chapter, we focus on simple systems that are represented by small orbital sets, such that the complete many-body state from Equation 2.35 is still manageable using our computing facilities. This gives us the opportunity to challenge the MPS representation with the complete many-body state. We can directly observe the impact of convergence parameters (MPS bond dimension, time evolution method, time step size) on the validity of the results and conclude regularities to operate with the MPS approach in the context of time-dependent quantum chemistry.

We begin the analysis by studying different types of hydrogen chains, starting from the simple hydrogen molecule $H_2$ and continuing with longer chains $H_{10}$. For these molecules, we compare time-dependent reduced density matrices obtained from the different representations of the many-body state. Further, we study the one-body Green's function in both, the time domain, as well as, in the frequency domain. Next, we continue with higher-dimensional molecules in extended basis sets. In particular, we study electron dynamics following a sudden (double) ionization of the molecules hydrogen fluoride FH, water $H_2O$, ammonia $NH_3$, and methane $CH_4$ in the 6-31G Gaussian basis set [218]. To rate the accuracy of the MPS representation, we discuss the relative error of the one-body reduced density matrix originating from the MPS truncation. In the last part, we analyze different methods to perform time evolution of many-body states in MPS representation, which reveals an entanglement between the MPS approach and the time evolution method. A correctly chosen time evolution method allows us to improve the performance of the MPS representation in special situations.

Parts of this Chapter have been published in the *Journal of Chemical Theory and Computation* [219] and in the *European Physical Journal Web of Conferences* [220].

Especially the analysis of the hydrogen chain, as well as, the results on the time evolution methods have found consideration in these journals.

# 4.1  Hydrogen Based Molecules

We start the analysis of the MPS representation by describing electron dynamics in one-dimensional chains of hydrogen atoms. In Section 2.4.2, we highlighted the optimal performance of the MPS approach when representing gapped ground states of short-ranged one-dimensional systems. This optimal performance is a consequence of the limited electron entanglement in this type of states (remember the area law). Therefore, MPS have an intrinsic benefit when representing states of one-dimensional systems (this is due to the factorization of the coefficient tensor in a one-dimensional chain of matrix products), which we rely upon to start the analysis of time-dependent MPS representation defensively.

The hydrogen molecule and the hydrogen chain have received much interest by physicists and chemists from the beginning of quantum mechanics [221]. The cationic hydrogen molecule $H_2^+$ is exactly solvable in the Born–Oppenheimer approximation, which started the field of molecular orbital theory a hundred years ago [222] . This model is still at the heart of our current understanding of electrons in molecules (see Chapter 2). In recent years, hydrogen chains have been extensively used as simplified model systems for complex molecular chains [223–227]. Its actual simple structure in combination with the long-ranged Coulomb interaction allows the hydrogen chain to be simple, while representing most features of more complex systems. The hydrogen chain has also been subject to numerous benchmark studies of many-body methods. For example, it was the system of interest for the benchmark studies of *density matrix renormalization group* [205, 228–230] and *density-matrix embedding theory* [231–233], and in an outstanding review benchmarking almost all latest many-body methods by Motta et al. [24]. The distance between the atoms here serves as a handle to tune the electronic correlation, which enables to measure how stable a particular many-body method handles correlations.

## 4.1.1  The Hydrogen Molecule

Let us start the analysis with the most simple molecule existing, the hydrogen molecule. It consists of two hydrogen atoms placed at a distance $d$, namely the bond distance. Both hydrogen atoms bring one electron, therefore there are two electrons in the system, which is a simple realistic many-electron system. For the case of the cationic hydrogen molecule, the exact solutions within the Born–Oppenheimer approximation has been found by Burrau in 1929 [222], which is the only molecular
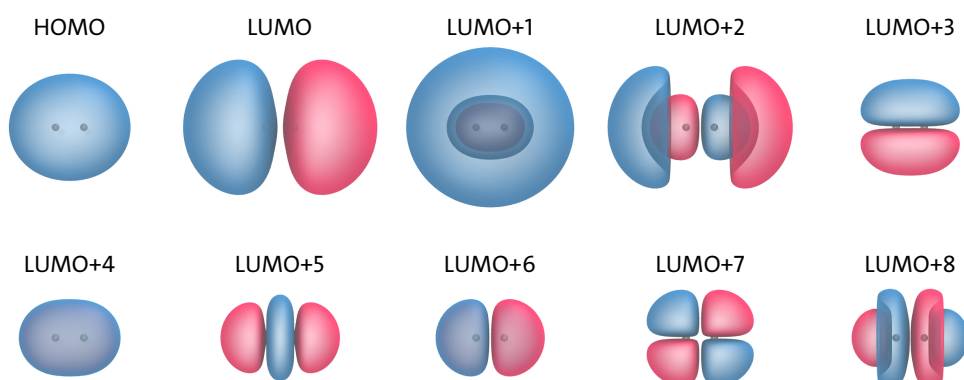
**Figure 4.1.:** Isosurfaces to molecular orbitals of the hydrogen molecule from a closed-shell Hartree–Fock calculation using the cc-pVDZ Gaussian basis set. The two hydrogen atoms are separated by the equilibrium distance $0.75$Å. The orbital contours show the surface of $\phi_i(\mathbf{r}) = \pm 0.03$.

system we know the exact solution for. Already for the neutral molecule, we need approximate methods to describe the quantum state.

In our analysis, we describe the hydrogen molecule using a Gaussian basis set, as introduced in Section 2.2.1. We use the basis set *cc-pVDZ* [234], which is an extended basis set that is adapted for correlated post-Hartree–Fock methods. The cc-pVDZ considers five orbitals per atom ($1s,2s,2p_x,2p_y$, and $2p_z$,), therefore in total we have a system of two electrons occupying ten different orbitals. This is a system size, where it is possible to treat the complete many-body state in Equation 2.35. This allows us to perform calculations using the complete many-body state for direct comparison with calculations using the MPS representation.

From a Hartree–Fock calculation we obtain molecular orbitals that are optimized on the single body level (see Figure 4.1). The distance between the two hydrogen atoms is the equilibrium distance for this basis set $d = 0.747954335$Å. The hybridization of the atomic orbitals can be observed, where for example the energetically lowest orbital is constructed from the two hybridized $1s$ orbitals. In the Hartree–Fock ground state, the two electrons occupy the energetically lowest orbital, which is already the highest occupied molecular orbital (HOMO).

The many-body state can be now expressed using the set of molecular orbitals. When taking advantage of the electron number symmetry, as well as the molecular rotation symmetry ($C_{2\nu}$), this results in a many-body Hilbert space dimension of 44, i.e. a size

that is easily manageable using desktop computers. The MPS representation of the complete many-body state is given by MPS tensors with the bond dimensions

$$
\underset{A[1]}{} \overset{3}{-} \underset{A[2]}{} \overset{4}{-} \underset{A[3]}{} \overset{5}{-} \underset{A[4]}{} \overset{4}{-} \underset{A[5]}{} \overset{3}{-} \underset{A[6]}{} \overset{2}{-} \underset{A[7]}{} \overset{3}{-} \underset{A[8]}{} \overset{2}{-} \underset{A[9]}{} \overset{3}{-} \underset{A[10]}{} , \qquad (4.1)
$$

where the numbers above the virtual bonds denote the dimension of the bond. The largest bond dimension is $D_{FCI} = 5$, i.e. no challenge for regular desktop computers either.

This discussion of the hydrogen molecule serves to introduce the time-dependent MPS representation at the simplest molecule possible. Situations with more challenging many-body Hilbert space dimensions will follow after we have seen how the MPS representation performs at this minimal example.

In the following analysis of the dynamics of the hydrogen molecule, we use the Hartree–Fock ground state as the initial state for time evolution. Although the Hartree–Fock ground state is the ground state of the effective single body problem, it is not an eigenstate of the Hamiltonian acting on in the many-body Hilbert space. The system in the Hartree–Fock ground state will therefore evolve electron dynamics. However, at this point, it is less of the question what the dynamics look like, but the focus of this discussion is on the performance of the MPS representation. We omit all discussions of the actual dynamics and related physics, but focus exclusively on the capabilities of the MPS approach to represent the complete many-body state.

First quantity we utilize for comparison between the MPS representation and the complete many-body state is the spin summed *two-body reduced density matrix* (TBRDM) [61]. The TBRDM is given by

$$
\Gamma^{\alpha}_{ij;kl}(t) = \sum_{\sigma\tau} \langle \Psi(t) | \hat{c}^{\dagger}_{i\sigma} \hat{c}^{\dagger}_{j\tau} \hat{c}_{l\tau} \hat{c}_{k\sigma} | \Psi(t) \rangle_{\alpha} , \qquad (4.2)
$$

with $\alpha \in \{\text{MPS, FCI}\}$ indexing whether the TBRDM has been calculated from the state in MPS representation, or from the complete many-body state (the full CI state). The TBRDM holds both, a variety of two-body correlators, as well as one-body quantities. For example, the *one-body reduced density matrix* (OBRDM) (see Equation 2.47) can be extracted from the TBRDM via

$$
\gamma^{\alpha}_{ij}(t) = \frac{1}{N-1} \sum_{k} \Gamma^{\alpha}_{ik;jk}(t), \qquad (4.3)
$$

which holds information on coherences the electrons develop and the occupation numbers of the molecular orbitals. Also the particle number and the energy expecta-
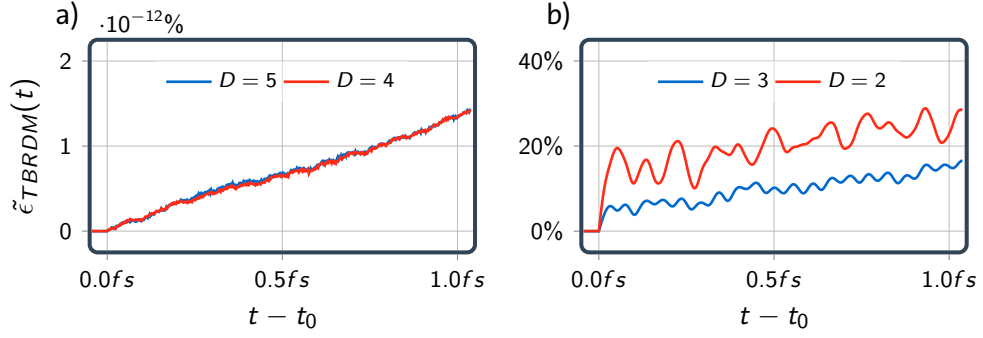
**Figure 4.2.:** Relative error of the two-body reduced density matrix of the hydrogen molecule for various MPS bond dimensions. The initial state is the Hartree–Fock ground state for the cc-pVDZ Gaussian basis set. In all calculations (full CI based representation and MPS based representation) the state is time-evolved using the orthogonalized Krylov space method with Krylov space dimension $N_{Kry} = 6$ and time step size $\Delta t = 2.42 as$.

tion value can be calculated from the TBRDM (compare second quantized Hamiltonian in Equation 2.36)

$$N^\alpha(t) = \sum_{i\sigma} {}_\alpha\langle \Psi(t)|\hat{n}_{i\sigma}|\Psi(t)\rangle_\alpha = \sum_{ij} \Gamma^\alpha_{ij;ij}(t) = N^\alpha, \tag{4.4}$$

$$E^\alpha(t) = {}_\alpha\langle \Psi(t)|\hat{H}|\Psi(t)\rangle_\alpha = \sum_{ij\sigma} t_{ij}\gamma_{ij}(t) + \frac{1}{2}\sum_{ijkl} V_{ij;kl}\Gamma^\alpha_{ij;kl}(t) + E_0 = E^\alpha, \tag{4.5}$$

where both are supposed to be constants of motion in the systems discussed here (up to errors due to MPS truncation). Hence, the TBRDM is an object with extensive physical content that describes the system's state beyond the single electron picture. In this particular situation of only two electrons, it holds an equivalent amount of information as the complete many-body state. It will be a good quantity to quantify the quality of the time-dependent MPS representation.

For each of the two representations of the many-body state we obtain the time-dependent TBRDM. Where we consider the TBRDM extracted from the complete many-body state to be the exact result, the TBRDM extracted from the MPS representation experiences an error due to MPS truncation. We can quantify the absolute error of the MPS truncation on the TBRDM by

$$\epsilon_{TBRDM}(t) = ||\Gamma^{FCI}(t) - \Gamma^{MPS}(t)||, \tag{4.6}$$

where $|| \cdot ||$ denotes the Frobenius norm [235]. From the absolute error, we get the relative error via

$$\tilde{\epsilon}_{TBRDM}(t) = \frac{||\Gamma^{FCI}(t) - \Gamma^{MPS}(t)||}{||\Gamma^{FCI}(t)||}, \tag{4.7}$$

which is shown in Figure 4.2 for various MPS bond dimensions. In Figure 4.2, all calculations use orthogonalized Krylov space time evolution as described in Section 2.5.3 with a Krylov space dimension of $N_{Kry} = 6$ and a time step size of $2.42as$.

At time $t = 0.0fs$, the TBRDM extracted from the complete many-body state and the TBRDM extracted from the MPS representation completely match. The truncation error of the MPS representation at time $t = 0.0fs$ is zero for all MPS bond dimensions, since no truncation has been applied at this point. However, from the first discrete time step, the complete many-body state and the MPS representation differ due to MPS truncation. We observe this truncation error in the growth of the error of the TBRDM. This errors growths linearly, since the MPS representation suffers an error with every discrete time step. In Figure 4.2 we see the form of the error growth and how it depends on the bond dimension of the MPS representation. The bond dimension, as a measure for MPS truncation, directly controls the slope of the error of the TBRDM. Where the error induced by the MPS representation is negligible for bond dimension $D = 5$ and $D = 4$ (see Figure 4.2 a) ), it grows to 30% within a period of $1fs$ for an MPS bond dimension of $D = 2$ (see Figure 4.2 b) ).

From the negligible error in case of bond dimension $D_{FCI} = 5$, we can conclude that the MPS approach is able to find an accurate representation of the many-body state. For this large bond dimension limit, the MPS is able to hold as much information as the complete many-body state, i.e. the MPS approach of the complete many-body state could only differ due to problems in the time evolution algorithm. Apparently, this is not the case and the MPS representation matches the complete many-body state with numerical precision within the first $1fs$ time range.

But the error of the TBRDM is not only for the maximum MPS bond dimension negligible. Also if the bond dimension of the MPS is limited to $D = 4$, the MPS approach represents the complete many-body state with numeric precision (see Figure 4.2 a) ). In contrast to the case with bond dimension $D_{FCI} = 5$ described above, with a bond dimension of $D = 4$ the MPS is indeed truncated, however, the induced truncation error appears to be vanishing. Already in this most basic situation, the electron entanglement is limited and we can cut parts of the many-body Hilbert space with no error. This demonstrates the power of the MPS approach, as we can conclude that there are unimportant parts of the many-body Hilbert space that can be omitted, without applying any a-priori approximations to the system. This further demonstrates, that assumption of small entanglement we applied to justify the MPS approach is valid for this example, and we can truncate with respect to entanglement, even in time-dependent situations.

The precision of the MPS representation drastically changes when limiting the MPS bond dimension to $D = 3$ or $D = 2$ (see Figure 4.2 b) ). Again, the error of the TBRDM
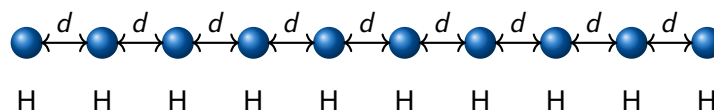
**Figure 4.3.:** One-dimensional chain of ten hydrogen atoms placed at a bond distance $d$.

grows linearly, however the slope is significantly larger than what we have observed for bond dimensions $D = 4$ and $D_{FCI} = 5$. This shows that, by limiting the MPS bond dimension, now we remove important parts of the many-body Hilbert space and the resulting MPS representation is unable to reproduce the correct TBRDM. Still, the error of the TBRDM is reasonable for the MPS representation with bond dimension $D = 3$ (up to $18\%$ within the first $1 fs$), however, the MPS representation is limited in the time range it is able to find the TBRDM approximately.

This very first analysis already exposed important properties of the MPS approach. First, in the large bond dimension limit, it was able to represent the complete many-body state with numeric precision in the time range of $1 fs$. Second, we observed that already in this simple situation, the entanglement of the electrons is limited and we can remove parts of the many-body Hilbert space without inducing an error to the MPS representation. Third, when cutting significant parts from the many-body Hilbert space using the MPS representation is still a reasonable approximation, however, the time range where the MPS representation is accurate is limited. We need to keep these properties in mind when continuing to more interesting, more challenging systems in the following.

## 4.1.2  The Hydrogen Chain

Next molecule we want to discuss in the analysis of the time-dependent MPS approach is the chain of hydrogen atoms that are equally spaced on a one-dimensional line (see Figure 4.3). Isolated from the environment, this molecule is not stable for open boundary conditions; It will dissociate in a series of $H_2$ molecules. This mechanism makes it difficult to study the system in experimental situations directly, however, in our theoretical model we fix the distance between the atoms.

In recent years, the interest of the solid state and quantum chemistry community in the hydrogen chain enhanced [225, 229, 236–238]. It is understood as an ab initio extension of the Hubbard model, including a much more profound representation of the long-ranged Coulomb interaction [24]. When changing the distance between the atoms $d$, the hydrogen chain undergoes a phase transition in the thermodynamic limit, being metallic at small bond distances and becoming Mott-insulating as the distance between the atoms is increased. Here we will use a bond distance of $d = 0.95$Å, which corresponds to metallic phase[60] and is close to the equilibrium
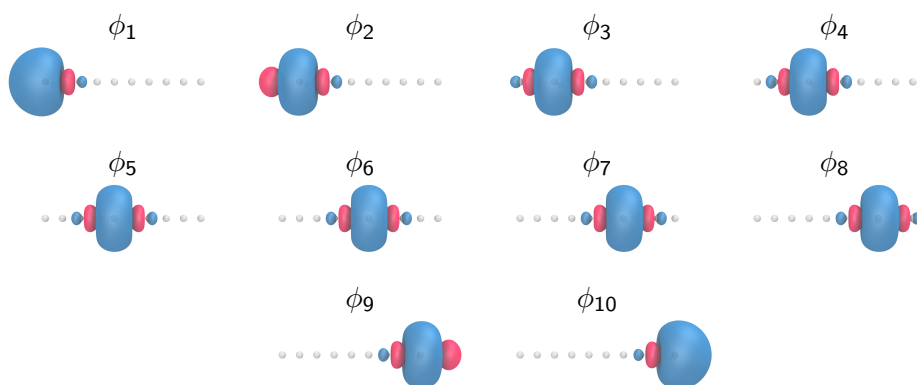
**Figure 4.4.:** Isosurfaces of the orthogonalized atomic orbitals for hydrogen chain of 10 atoms. The atomic orbitals are formed by the minimal STO-6G Gaussian basis set and then orthogonalized using Löwdin orthogonalization. The orbital contours show the surface of $\psi_i(\mathbf{r}) = \pm 0.01$. The distance between the atoms is $d = 0.95$Å.

bond distance for periodic boundary conditions [24, 229]. But the hydrogen chain is also interesting from a methodological point of view, as it is a molecule where the Hartree–Fock method and many other post-Hartree–Fock methods fail [24, 60]. With the directly tunable correlation parameter, it is the molecule used in numerous benchmark studies to analyze solid state and ab initio methods [24, 229, 239]. It has been used to study the performance of DMRG [60, 205, 228–230], density matrix embedding theory [231], auxiliary-field quantum Monte Carlo [236] and many other methods [24].

In line with this prominent history, we choose the hydrogen chain to challenge the time-dependent MPS representation and see how it can handle the physics of this molecule. As the complexity of the calculations scales with the length of the hydrogen chain, we can easily adjust the size of the molecule to a size where we can perform calculations using the complete many-body state in reasonable time. Then we can directly compare between results based on the MPS representation and the quasi exact results based on the complete many-body state.

We restrict the size of the hydrogen chain to 10 atoms and use the minimal Gaussian basis set STO-6G [218]. This translates to a system of one electron and one orbital for each of the hydrogen atoms. In total, the systems consists of 10 electrons occupying 10 orbitals. When using the particle number symmetry and spin projection symmetry $\hat{S}_z$, this leaves us with a total number of 63504 configurations, a dimension that is manageable by using desktop computers. Therefore, for this system, we can compare the MPS representation with the complete many-body state.

The shape and the ordering of the orbitals in the MPS representation is crucial for its performance. We know from the area law that the MPS approach performs best if the problem is short-ranged, therefore, we want to minimize the long-ranged interaction

as much as possible. If using a random order of the orbitals, or if using completely delocalized orbitals such as molecular orbitals from a Hartree–Fock calculation, we exaggerate the non-local property of the system artificially. Therefore, if possible, we use localized basis sets and order the orbitals with respect to the physical situation. Of course, the Coulomb-interaction is still long-ranged in this system and the MPS representation still accounts for this, however, when connecting the orbitals with MPS tensors in the MPS representation, an elegant order of the orbitals reduces this artificial added long-range property. The ordering of the orbitals in the MPS representation is subject to various studies [44, 122, 146, 167, 203, 205, 240, 241], although, apart from using physical intuition where possible, no universal method to find the optimal order has been proposed yet.

For this study, we will use atomic orbitals that have been orthogonalized using the Löwdin orthogonalization method (see Figure 4.4). The Löwdin orthogonalization finds the orbitals that are orthogonal to each other

$$\langle \phi_i | \phi_j \rangle = \int d^3 r \phi_i^*(\mathbf{r}) \phi_j(\mathbf{r}) = \delta_{ij}, \tag{4.8}$$

while the overlap with the initial atomic orbital is maximized in a least square manner [61]. This gives the orbitals in Figure 4.4 the helpful property of being localized at the atomic positions and being orthogonal to each other. This simplifies the choice of the orbital ordering. We order the orbitals with respect to their localization in the molecule from left to right in the MPS representation.

The situation we will analyse is a hydrogen chain that has been singly ionized at the 5th orbital of the molecule, i.e. in the center of the chain. Prior the time evolution calculation, we prepare the system in its neutral ground state $|\Psi_0\rangle$. To find the ground state in the complete many-body representation, we use the parent program package of our time-dependent MPS implementation, namely the CheMPS2 program [51]. It has a build-in full CI solver, which is based on the full CI method described by Knowles and Handy [242]. To find the ground state in MPS representation we use the DMRG implementation of CheMPS2 by Wouters [51]. We perform a regular DMRG calculation in the large bond dimension limit, i.e. the MPS representation of the ground state covers the entire many-body Hilbert space (maximum bond dimension $D = 516$). Then we apply an annihilation operator at the fifth orbital, suddenly removing one electron from the system and thereby driving the system "out of equilibrium". After normalizing, the initial state is

$$|\Psi(t_0)\rangle_\alpha = \frac{1}{{}_\alpha \langle \Psi_0 | \hat{c}_{5\sigma}^\dagger \hat{c}_{5\sigma} | \Psi_0 \rangle_\alpha} \, \hat{c}_{5\sigma} | \Psi_0 \rangle_\alpha \,, \tag{4.9}$$

where $|\cdot\rangle_\alpha$, $\alpha \in \{MPS, FCI\}$ is either the MPS representation or the complete many-body state, and $\sigma \in \{\uparrow, \downarrow\}$ can be chosen arbitrarily since we have spin symmetry.

The initial state we are looking at is therefore a state with 9 electrons and multiplicity $2S + 1 = 2$.

The complete many-body state for this symmetry sector is a linear combination of up to 52920 possible configurations, which allows for fast quasi exact calculations and to compare to the MPS approach. The MPS representation of the complete many-body state, which covers the entire many-body Hilbert space, has the bond dimensions

$$
\text{(} A[1] \text{)} \xrightarrow{3} \text{(} A[2] \text{)} \xrightarrow{10} \text{(} A[3] \text{)} \xrightarrow{35} \text{(} A[4] \text{)} \xrightarrow{126} \text{(} A[5] \text{)} \xrightarrow{417} \text{(} A[6] \text{)} \xrightarrow{210} \text{(} A[7] \text{)} \xrightarrow{56} \text{(} A[8] \text{)} \xrightarrow{15} \text{(} A[9] \text{)} \xrightarrow{4} \text{(} A[10] \text{)}, \tag{4.10}
$$

with the maximum bond dimension of $D_{FCI} = 417$ between the the fifth and the sixth MPS tensor. This is the MPS representation where the complete many-body Hilbert-Space is considered, i.e. it is the MPS representation in the large bond dimension limit. In the following, we will see, how efficient the MPS approach behaves when this bond dimension is limited to smaller numbers and therefore parts of the many-body Hilbert space are truncated from the MPS representation.

**Reduced Density Matrices**

Similar to the analysis of the hydrogen molecule above, we start the analysis of the hydrogen chain with a discussion of the TBRDM as given in Equation 4.2 and the (relative) residuum as given in Equation 4.6. This enables access to the two-body correlators of the many-body state, but also is a good measure for the coherences arising in the system (see Equation 4.3). Additionally to the TBRDM, we will analyze the accuracy of the one-body reduced density matrix (OBRDM) from now on, as it is the quantity to obtain the electron density from. The absolute and relative error of the OBRDM due to MPS truncation is

$$
\epsilon_{OBRDM}(t) = ||\gamma^{FCI}(t) - \gamma^{MPS}(t)||, \tag{4.11}
$$

$$
\tilde{\epsilon}_{OBRDM}(t) = \frac{||\gamma^{FCI}(t) - \gamma^{MPS}(t)||}{||\gamma^{FCI}(t)||^2}, \tag{4.12}
$$

(compare to Equation 4.6 and Equation 4.7).

Using the initial state in Equation 4.9, we perform the time evolution by applying the Krylov space method as described in Section 2.5.3. We use the orthogonalized formulation with a Krylov space dimension of $N_{Kry} = 5$ and a time step size of $\Delta t = 1.21 as$ for both many-body state representations. These are conservative time evolution parameters, where we have seen from convergence tests on the complete many-body state that a Krylov space dimension of $N_{Kry} = 5$ is stable for time steps of up to $\Delta t = 2 as$ (see Appendix A.1). Any discrepancies in the TBRDM or the OBRDM
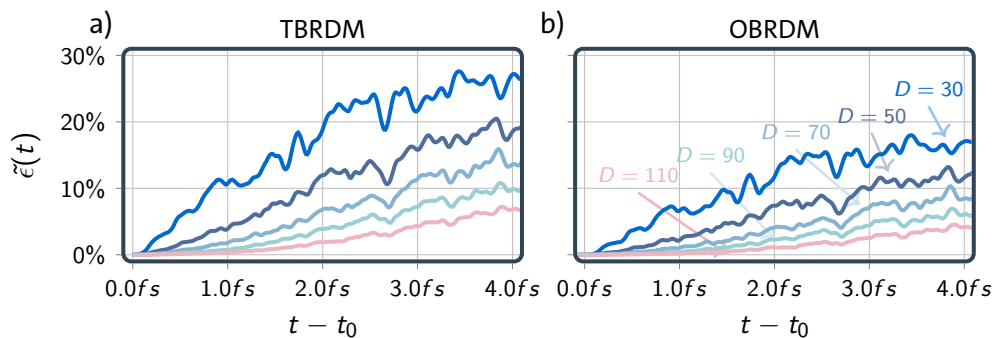
**Figure 4.5.:** Relative error of the one-body reduced density matrix and the two-electron reduced density matrix of the hydrogen molecule for various MPS bond dimensions. The initial state is the correlated ground state after a suddenly ionization of the fifth atomic orbital $\phi_5$. For both representations (complete many-body state and its MPS based representation) the many-body state is propagated using the orthogonalized Krylov space method with Krylov space dimension $N_{Kry} = 5$ and time step size $\Delta t = 1.21as$.

extracted from the two many-body state representations are a result of the truncation of the MPS representation and not consequence of poorly converged time evolution parameters.

The truncation error of the MPS representation directly depends on the bond dimension of the MPS representation. We observe this in the relative error of the TBRDM (see Figure 4.5 a) ) and in the error of the OBRDM (see Figure 4.5 b) ). For all bond dimensions shown, the error grows linearly within the period of $4fs$ after the sudden ionization of the hydrogen chain. We already have observed and discussed this linear growth at the example of the hydrogen molecule (see Figure 4.2). Again, the slope of the errors can be controlled by adjusting the bond dimension of the MPS representation.

Already for medium sized MPS bond dimensions, the TBRDM and the OBRDM extracted from the many-body state in MPS representation resembles the result of the complete many-body state. Working with an MPS bond dimension of $D = 110$ refers to a truncation of the many-body state, but still the MPS approach finds the OBRDM with an error of less than 5%. This demonstrates that the MPS approach is able to find the relevant domain of the many-body Hilbert space and truncates remaining parts from the representation of the many-body state. The highly entangled states truncated from the MPS representation need time to emerge, which manifests in the time-dependent growth of the truncation errors.

For small bond dimensions, the truncation error of the MPS representation grows faster. This is the already mentioned *runaway* error (see Section 2.4.2) of the MPS approach, where we can only control the slop of the error growth, however, we cannot prevent the error from happening at all. The slope increases when using

smaller bond dimensions. The OBRDM error stays reasonably small within the first two femtoseconds for MPS bond dimensions $D = 30$, however, it rises beyond 10% afterwards.

We therefore conclude that the MPS bond dimension has to be chosen with respect to the time period of interest. Where dynamics on short periods can be described using small MPS bond dimensions, for longer periods the bond dimension must be larger. This mechanisms will eventually limit the time period we are able to describe using the MPS approach.

In Figure 4.5 we also note that the error of the OBRDM is proportional to the error of the TBRDM. This reveals that the MPS approach performs equally well in representing correlation as it does in representing coherences. This is also an important observation, as problems with coherences might be reduced by changing the orbital basis time-dependently [243]. Such an extension of our time- dependent MPS method is planed for future projects but goes beyond what is discussed in this thesis.

**Time-Dependent Green's function**

To gain a more profound understanding of the performance of the MPS approach for the hydrogen chain, we continue the analysis with the one-body Green's function. This allows us to further quantify the performance of the MPS representation, however using a quantity that is closer to experimental observables compared to the more theoretically driven reduced density matrices. Seeing the performance in Green's function calculations, we can estimate what the truncation errors we have seen previously actually mean for observables. We will study both, the Green's function in the time domain, as well as its Fourier transformed partner in the frequency domain. Again, we will directly compare results using the complete many-body state and its truncated MPS representation.

The one-body Green's function in the time domain is given by

$$G_{ij}^{\sigma\alpha}(t - t') = -i\Theta(t - t')_\alpha \langle \Psi_0 | \hat{c}_{i\sigma}^\dagger e^{i(\hat{H} - E_0)(t - t')} \hat{c}_{j\sigma} | \Psi_0 \rangle_\alpha , \qquad (4.13)$$

with $\alpha \in \{MPS, FCI\}$ again being the index identifying whether the Green's function has been calculated using the MPS representation or using the complete many body state. The state $|\Psi_0\rangle_\alpha$ denotes the correlated ground state of the neutral molecule in its $\alpha$ representation with the ground state energy $E_0$. The one-body Green's function is a measure for how a system responds to excitation. In our molecular situation, we understand it as the response of the hydrogen chain to ionization in orbital $j$ with spin $\sigma$ at time $t'$. It describes the component that the electron hole has moved to
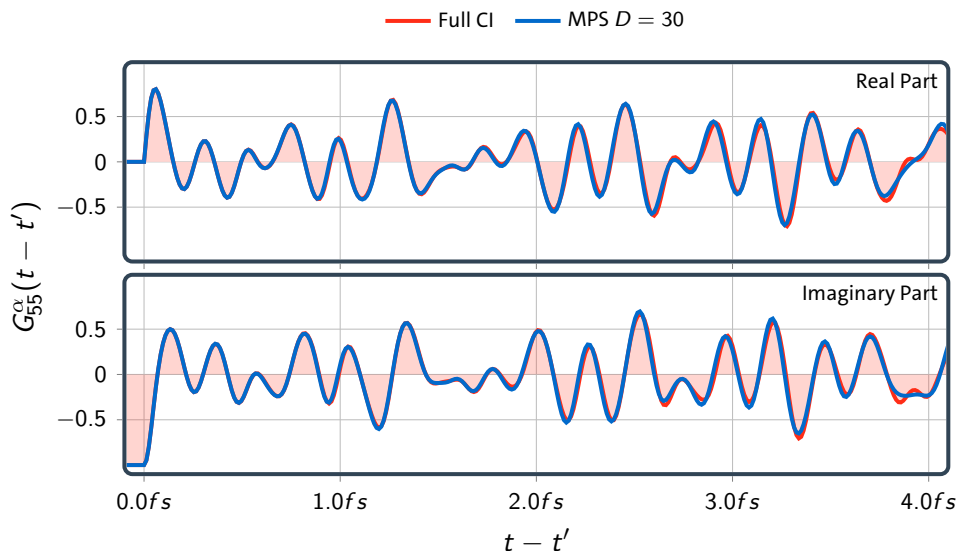
**Figure 4.6.:** Real part (upper) and imaginary part (lower) of the time-dependent Green's function as defined in Equation 4.13 calculated using the complete many-body state (full CI) and calculated using the MPS representation of the many-body state with a bond dimension $D = 30$. For both representations the many-body state is propagated using the orthogonalized Krylov space method with Krylov space dimension $N_{Kry} = 5$ and time step size $\Delta t = 1.21 as$.

orbital $i$ following the ionization. The Green's function is a very popular quantity discussed, as it allows to calculate ionization probabilities of correlated systems (such as our ab initio model of the hydrogen chain) [60, 61]. The ionization potentials have been discussed in a study by Ronca et al. [60] using the MPS approach. This allows us not only to compare to the quasi exact results using the complete many-body state, but also enables a comparison of the implementations of the MPS approach.

We have all necessary tools to calculate the Green's function in Equation 4.13 using the MPS approach. First, we find the ground state of the neutral hydrogen chain, and describe it in the complete many-body state representation and in the MPS representation. Then we apply the annihilation operator at orbitals $j$, reducing the total electron number by one and thereby ionizing the system. As the next step, we understand $\hat{c}_{j\sigma} |\Psi_0\rangle_\alpha$ as the initial state for time evolution and start a backwards time evolution calculation using the methods explained in Section 2.5. At this point, we use again the orthogonalized Krylov space method for both representations of the many-body state. After the time evolution has been performed, we project the time evolved state onto the ground state with an ionization at orbital $i$. This then leaves us with the time-dependent one-body Green's function calculated using either the MPS ($G_{ij}^{\sigma MPS}(t - t')$) or the full CI approach ($G_{ij}^{\sigma FCI}(t - t')$).

Even for significantly truncated MPS, the one-body Green's function calculated using the MPS representation agrees with the one-body Green's function calculated using
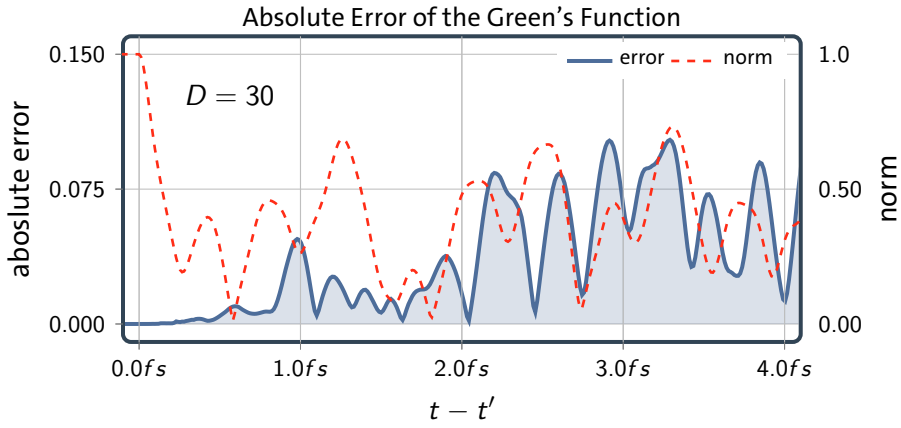
**Figure 4.7.:** Absolute error of the time-dependent one-body Green's function (blue, left axis) and the total norm of the time-dependent Green's function (red, right axis). The time-dependent Green's function, as given in Equation 4.13, is calculated using the MPS approach with bond dimension $D = 30$ to represent the state and then compared to the respective full CI Green's function. Both representations of the many-body state are propagated using the orthogonalized Krylov space method with Krylov space dimension $N_{Kry} = 5$ and time step size $\Delta t = 1.21as$.

the complete many-body state. We observe this in Figure 4.6, where we show the spin summed and normalized Green's functions

$$G_{ij}^{\alpha}(t - t') = \frac{\sum_\sigma G_{ij}^{\alpha\sigma}(t - t')}{\left|\sum_\sigma G_{ij}^{\alpha\sigma}(0)\right|}, \tag{4.14}$$

calculated using the two representations of the many-body state. Here, the bond dimension of the MPS representation is limited to $D = 30$. In the period of $4fs$, it is difficult to recognize any differences between both representations. The real and the imaginary part of the Green's function almost exactly match to the completely correlated results (Full CI) with just small deviations starting after $\approx 2fs$. However, these deviations are minor and does not affect the very well qualitative correspondence of the two approaches. These calculation were done using the Krylov space dimension of $N_{Kry} = 5$ with a time step size of $\Delta t = 1.21as$ and orthogonalized Krylov basis vectors.

We observe a qualitatively perfect result although we have observed a relative error of about 15% when we compared the OBRDM in Figure 4.5. This tells us that the relative errors of the reduced density matrix is a sensitive measure of the accuracy of the many-body state. The quality of observables is much better than an estimate from the error of the reduced density matrices would suggest. This is a consequence of $G_{ij}^{\alpha}(t - t')$ can be understood as one matrix element of the OBRDM. Nevertheless, we continue the benchmark using the reduced density matrices in Section 4.2, as it is a generic quantity and especially since the OBRDM is the main quantity when interested in electronic densities (see Chapter 5 5).

When looking at the absolute error of the time-dependent Green's function ($\epsilon = |G_{55}^{FCI}(t-t') - G_{55}^{MPS}(t-t')|$) in Figure 4.7, we again see the error growing with time, however, with very small slope. The errors in the first four femtoseconds stays below an absolute value of $0.1$, which means the correspondence of the two approaches is better than two digits in average . This behavior is independent of the norm of the Green's function (see dashed red line in Figure 4.7). This shows, even in this correlated situation, the main features of the Green's function are governed by little entangled states, as those are the only ones covered by the MPS representation with bond dimension $D = 30$.

**Frequency dependent Green's function**

We finish the analysis of the hydrogen chain, by discussing the performance of the MPS representation to find the Green's function in the frequency domain. On the one hand, the frequency-dependent Green's function can be obtained via Fourier transformation of the time-dependent Green's function

$$G_{ij}^{\alpha}(\omega) = \int_{-\infty}^{\infty} d(t-t') e^{i\omega(t-t') - \eta(t-t')} G_{ij}^{\alpha}(t-t'), \qquad (4.15)$$

where we also include a broadening $\eta$ that helps to identify major peaks. For this approach, the time-dependent Green's function calculated from the MPS representation needs to be correct over an extended period of time. From the accurate results we have seen in Figure 4.6, we can expect our time-dependent MPS representation to give reasonable result on the frequency-dependent Green's function as well. On the other hand, the frequency-dependent Green's function can also be directly calculated using the MPS representation either from a Krylov-space approach [244] or by minimizing a Hylleraas-like functional [60]. Ronca et al. showed that a direct evaluation is advantageous if only a specific frequency region is of interest. However, as we are mostly interested in the performance of time-dependent MPS, we choose to Fourier transform the results of Figure 4.6.

In Figure 4.8 we see the frequency dependent Green's function derived from the complete many-body state and derived from the MPS representation with bond dimension $D$. For $\hbar\omega > -20.0eV$, the MPS representation is able to present all major peaks with respect to peak position, peak height, and peak width. For smaller frequencies, we observe that the Green's function from the MPS representation is slightly shifted to smaller frequencies (see insets Figure 4.8).

In our implementation of the time-dependent MPS representation, we do not observe any nonphysical results in the imaginary part of the Green's function. Ronca et al.
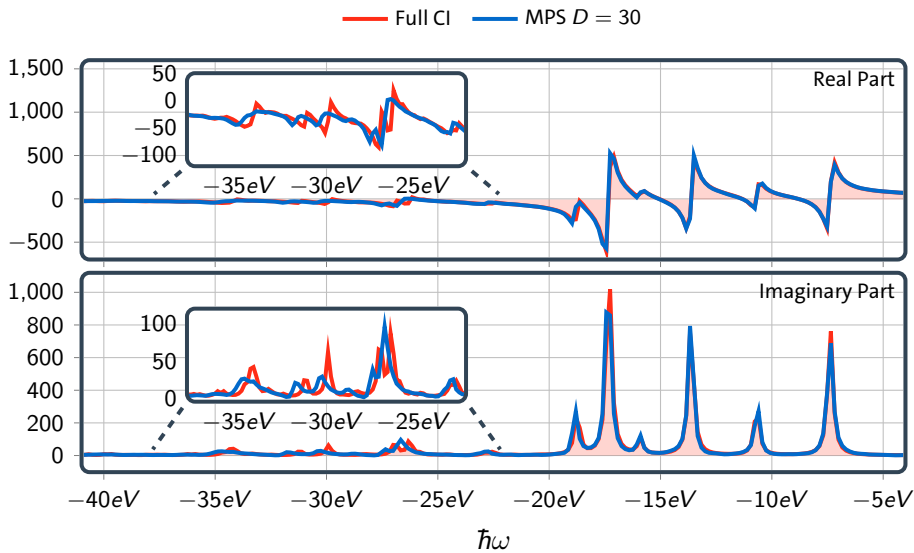
**Figure 4.8.:** Frequency dependent Green's function derived from the complete many-body state, as well as from the MPS approach with a bond dimension of $D = 30$. (Upper) shows the real part and (lower) shows the imaginary part. All curves have been obtained from calculations using the orthogonalized Krylov space approach with $N_{Kry} = 5$ and a time step size of $\Delta t = 1.21 as$. Further, a broadening of $\eta = 0.14 eV$ has been applied to the Fourier transform (see Equation 4.15).

[60] concluded in previous work, that extracting the frequency dependent Green's function from the time-dependent Green's function is very prone to errors if the time-dependent Green's function was calculated using the MPS representation. They observed noisy Green's functions and unexpected zero-crossings. We cannot confirm this based on our Krylov space based implementation of the time-dependent MPS representation. We think this is due to our very general approach, where every Krylov vector is represented by its own MPS with its own optimized virtual basis. This allows for versatile adaption of the MPS compared to methods that act on local MPS tensors inducing an averaged virtual basis for all Krylov vectors utilized by Ronca et al. [60].

## 4.1.3  Conclusion

We have seen in this section that the MPS approach is able to represent the time-dependent many-body state efficiently. It is able to resolve quantities holding electronic correlations (TBRDM), quantities holding electronic coherences (OBRDM), as well as the Green's function. The accuracy of the MPS representation is directly correlated to the period of time we are interested in and the MPS bond dimension. For longer time periods, we need to employ larger MPS bond dimensions. We performed this analysis in a rather artificial situation of the one-dimensional hydrogen chain, described by a minimal basis set. This model usually does not allow for quantitative predictions as the electrons are too confined in the small orbital set. How the MPS

approach performs when the basis set is non-local is still an open question, which we address in the next section.

## 4.2  Multi-Dimensional Molecules

In the following we want to extend the analysis of the MPS representation to molecules that stretch in all three dimensions. Further, will we go beyond the minimal basis set approach (STO-6G) we used in Section 4.1.2 and utilize the extended basis set *6-31G* [218]. This basis set additionally adds orbitals to the basis set that are unoccupied in the single atom picture (for example 2s orbitals for hydrogen). On the one hand, the extended basis set increases the complexity due to the enlarged single-body basis, and on the other hand the complexity is increased due to the additional non-locality induced by the artificial one-dimensional orbital ordering in the MPS representation. It is completely unknown how the time-dependent MPS approach can represent the time-dependent many-body state, since the MPS representation has never been used for this type of problems.

### 4.2.1  Single Ionization

We study the time-dependent response of the electrons in the molecule following a single ionization. This is a situation directly accessible in experiments, where a single electron is removed from the molecule on an ultrafast time scale [98, 245–247]. For example such a process can be initiated by attosecond light pulses [248]. This ionization process can be considered to happen suddenly, i.e. all other particles (nuclei as well as electrons) remain at their positions during the ionization process. Then, following the ionization process, the electrons start to respond to the excitation first in a process called *charge migration*, which is then followed by nuclear motion leading to *charge transfer*. Describing the nuclear motion goes beyond our model that is based on the Born–Oppenheimer approximation, therefore, we will focus on time scales where the nuclei remain still. This is usually a period of ten femtoseconds after the ionization process depending on the nuclei masses [21].

We analyze the performance of the MPS approach in describing four distinct molecules: hydrogen fluoride HF, water $H_2O$, ammonia $NH_3$, and methane $CH_4$. These four molecules cover most common elements that are the major building blocks in nature. Also, these molecules were already subject of several full CI studies [105, 249–252], showing that the electrons indeed enter correlated states. Therefore, we assume correlation driven electron dynamics following ionization to be crucial in these systems. But the molecules and the chosen basis set are still simple enough to perform calculations using the complete many-body state. Thus, we can continue the direct

| FH | H$_2$O | NH$_3$ | CH$_4$ |
|---|---|---|---|
| $\phi_{CG}^{H,1s}(\mathbf{r}-\mathbf{R}_H)$ | $\phi_{CG}^{H,1s}(\mathbf{r}-\mathbf{R}_{H_1})$ | $\phi_{CG}^{H,1s}(\mathbf{r}-\mathbf{R}_{H_1})$ | $\phi_{CG}^{H,1s}(\mathbf{r}-\mathbf{R}_{H_1})$ |
| $\phi_{CG}^{H,2s}(\mathbf{r}-\mathbf{R}_H)$ | $\phi_{CG}^{H,2s}(\mathbf{r}-\mathbf{R}_{H_1})$ | $\phi_{CG}^{H,2s}(\mathbf{r}-\mathbf{R}_{H_1})$ | $\phi_{CG}^{H,2s}(\mathbf{r}-\mathbf{R}_{H_1})$ |
| | $\phi_{CG}^{H,1s}(\mathbf{r}-\mathbf{R}_{H_2})$ | $\phi_{CG}^{H,1s}(\mathbf{r}-\mathbf{R}_{H_2})$ | $\phi_{CG}^{H,1s}(\mathbf{r}-\mathbf{R}_{H_2})$ |
| | $\phi_{CG}^{H,2s}(\mathbf{r}-\mathbf{R}_{H_2})$ | $\phi_{CG}^{H,2s}(\mathbf{r}-\mathbf{R}_{H_2})$ | $\phi_{CG}^{H,2s}(\mathbf{r}-\mathbf{R}_{H_2})$ |
| | | $\phi_{CG}^{H,1s}(\mathbf{r}-\mathbf{R}_{H_3})$ | $\phi_{CG}^{H,1s}(\mathbf{r}-\mathbf{R}_{H_3})$ |
| | | $\phi_{CG}^{H,2s}(\mathbf{r}-\mathbf{R}_{H_3})$ | $\phi_{CG}^{H,2s}(\mathbf{r}-\mathbf{R}_{H_3})$ |
| | | | $\phi_{CG}^{H,1s}(\mathbf{r}-\mathbf{R}_{H_4})$ |
| | | | $\phi_{CG}^{H,2s}(\mathbf{r}-\mathbf{R}_{H_4})$ |
| $\phi_{CG}^{F,1s}(\mathbf{r}-\mathbf{R}_F)$ | $\phi_{CG}^{O,1s}(\mathbf{r}-\mathbf{R}_O)$ | $\phi_{CG}^{N,1s}(\mathbf{r}-\mathbf{R}_N)$ | $\phi_{CG}^{C,1s}(\mathbf{r}-\mathbf{R}_C)$ |
| $\phi_{CG}^{F,2s}(\mathbf{r}-\mathbf{R}_F)$ | $\phi_{CG}^{O,2s}(\mathbf{r}-\mathbf{R}_O)$ | $\phi_{CG}^{N,2s}(\mathbf{r}-\mathbf{R}_N)$ | $\phi_{CG}^{C,2s}(\mathbf{r}-\mathbf{R}_C)$ |
| $\phi_{CG}^{F,2p_x}(\mathbf{r}-\mathbf{R}_F)$ | $\phi_{CG}^{O,2p_x}(\mathbf{r}-\mathbf{R}_O)$ | $\phi_{CG}^{N,2p_x}(\mathbf{r}-\mathbf{R}_N)$ | $\phi_{CG}^{C,2p_x}(\mathbf{r}-\mathbf{R}_C)$ |
| $\phi_{CG}^{F,2p_y}(\mathbf{r}-\mathbf{R}_F)$ | $\phi_{CG}^{O,2p_y}(\mathbf{r}-\mathbf{R}_O)$ | $\phi_{CG}^{N,2p_y}(\mathbf{r}-\mathbf{R}_N)$ | $\phi_{CG}^{C,2p_y}(\mathbf{r}-\mathbf{R}_C)$ |
| $\phi_{CG}^{F,2p_z}(\mathbf{r}-\mathbf{R}_F)$ | $\phi_{CG}^{O,2p_z}(\mathbf{r}-\mathbf{R}_O)$ | $\phi_{CG}^{N,2p_z}(\mathbf{r}-\mathbf{R}_N)$ | $\phi_{CG}^{C,2p_z}(\mathbf{r}-\mathbf{R}_C)$ |
| $\phi_{CG}^{F,3s}(\mathbf{r}-\mathbf{R}_F)$ | $\phi_{CG}^{O,3s}(\mathbf{r}-\mathbf{R}_O)$ | $\phi_{CG}^{H,3s}(\mathbf{r}-\mathbf{R}_N)$ | $\phi_{CG}^{C,3s}(\mathbf{r}-\mathbf{R}_C)$ |
| $\phi_{CG}^{F,3p_x}(\mathbf{r}-\mathbf{R}_F)$ | $\phi_{CG}^{O,3p_x}(\mathbf{r}-\mathbf{R}_O)$ | $\phi_{CG}^{N,3p_x}(\mathbf{r}-\mathbf{R}_N)$ | $\phi_{CG}^{C,3p_x}(\mathbf{r}-\mathbf{R}_C)$ |
| $\phi_{CG}^{F,3p_y}(\mathbf{r}-\mathbf{R}_F)$ | $\phi_{CG}^{O,3p_y}(\mathbf{r}-\mathbf{R}_O)$ | $\phi_{CG}^{N,3p_y}(\mathbf{r}-\mathbf{R}_N)$ | $\phi_{CG}^{C,3p_y}(\mathbf{r}-\mathbf{R}_C)$ |
| $\phi_{CG}^{F,3p_z}(\mathbf{r}-\mathbf{R}_F)$ | $\phi_{CG}^{O,3p_z}(\mathbf{r}-\mathbf{R}_O)$ | $\phi_{CG}^{N,3p_z}(\mathbf{r}-\mathbf{R}_N)$ | $\phi_{CG}^{C,3p_z}(\mathbf{r}-\mathbf{R}_C)$ |
| 11 orbitals | 13 orbitals | 15 orbitals | 17 orbitals |

**Table 4.1.:** Orbital basis sets for discussed molecules formed from contracted Gaussian orbitals (see Section 2.2.1).

comparison between the MPS representation and the quasi exact representation of the many-body state.

In this analysis, we start again from atomic orbitals that we represent by Gaussian orbitals (see Section 2.2.1). Precisely, in the employed 6-31G Gaussian basis set, the orbitals include (see Table 4.1):

- hydrogen fluoride HF: For the fluoride atom the orbitals $\{1s, 2s, 2p_x, 2p_y, 2p_z, 3s, 3p_x, 3p_y, 3p_z\}$ and for the hydrogen atom the orbitals $\{1s, 2s\}$ are taken into account, i.e. in total 10 electrons in 11 atomic orbitals.

- water H$_2$O: For the oxygen atom the orbitals $\{1s, 2s, 2p_x, 2p_y, 2p_z, 3s, 3p_x, 3p_y, 3p_z\}$ and for each of the hydrogen atoms the orbitals $\{1s, 2s\}$ are taken into account, i.e. in total 10 electrons in 13 atomic orbitals.

- ammonia $NH_3$: For the nitrogen atom the orbitals $\{1s, 2s, 2p_x, 2p_y, 2p_z, 3s, 3p_x, 3p_y, 3p_z\}$ and for the each of the hydrogen atoms the orbitals $\{1s, 2s\}$ are taken into account, i.e. in total 10 electrons in 15 atomic orbitals.

- methane $CH_4$: For the carbon atom the orbitals $\{1s, 2s, 2p_x, 2p_y, 2p_z, 3s, 3p_x, 3p_y, 3p_z\}$ and for each of the hydrogen atoms the orbitals $\{1s, 2s\}$ are taken into account, i.e. in total 10 electrons in 17 atomic orbitals.

In the following discussion, we use molecular orbitals that were optimized on the Hartree–Fock level. The Hartree–Fock calculation provides both, the equilibrium geometry of the molecule, as well as the molecular orbitals optimized on the single-body level. We used the molpro quantum chemistry program package [80] to perform the Hartree–Fock calculations. The molecular orbitals are then used as the one-body basis to expand the many-body state. In the MPS representation of the many-body state, we choose an order according to the orbital symmetry and the orbital energy. First the orbitals are ordered with respect to their irreducible representation and within these symmetry sectors they are ordered with respect to the orbital energy. The ordering in symmetry sectors allows to minimize (long-range) coherences, as matrix element of the OBRDM are zero for orbitals with different irreducible representation [3].

By preparing the initial state, we try to simulate experimental situations, however, without being too fixed on the actual experimental realization. Prior the ionization process, we assume the molecule to be in its neutral Hartree–Fock ground state $|\Psi_0\rangle$ , i.e. it can be described by a single configuration of our molecular orbital occupation number basis. The five molecular orbitals lowest in energy are doubly occupied, whereas all remaining molecular orbitals stay completely empty. At time $t_0$ we suddenly remove an electron from one of the orbitals (single-channel sudden ionization)

$$|\Psi(t_0)\rangle_\alpha = \hat{c}_{i\sigma} |\Psi_0\rangle_\alpha \,, \qquad (4.16)$$

leaving the molecule singly ionized. The ionized state $|\Psi(t_0)\rangle$ is again described by a single configuration. In the uncorrelated one-body picture, this state is still an eigenstate of the Hamiltonian. In an uncorrelated universe, the system would not experience any dynamics, as we brought the molecule from its neutral ground state into one of the cationic eigenstates (Koopmans' theorem) [61, 253]. However, in our description the electrons start moving, as the state $|\Psi(t_0)\rangle$ is not an eigenstate of the Hamiltonian including many-body effects. All dynamics we observe are therefore completely driven by the presence of electronic correlations [245].

Even though the electrons start moving and this motion is correlation driven, the dynamics are not subject of this study. The remaining electrons will try to fill the newly created hole in a motion that depends on the localization of the hole. These dynamics are indeed challenging for the MPS representation of the time-dependent state, however, we focus on the capabilities of the MPS representation to handle the correlated state and do not discuss the occurring dynamics in any detail. The dynamics following ionization are subject to further studies, such as the bachelor thesis by Schaub [254].

As the measure of accuracy of the MPS representation, we utilize reduced density matrices as we did in the analysis of the hydrogen based molecules in Section 4.1. While we discussed there the TBRDM as well as the OBRDM, we will focus now on the OBRDM. We have seen, in Figure 4.5 that the errors of the TBRDM and the error of the OBRDM are almost proportional to each other, which allows us to estimate the error of the MPS representation from the rather easy to calculate OBRDM.

**MPS Representation Error**

We determine the error of the MPS representation for all molecules outlined above. For a given molecule, we prepare the molecule in an initial state as described and let the system time-evolve. After the system evolved for about one femtosecond, we calculate the OBRDM. This procedure is performed once using the complete representation of many-body state, and once again using the MPS representation of the many-body state. At time $t = 1fs$, we compare the two resulting OBRDM by calculating the relative error (see Equation 4.12). From the relative error of the OBRDM, we estimate the error the MPS representation acquired in the time period of $1fs$. We repeat this practice for all possible singly ionized states of the molecule (see Figure 4.9).

In almost all situations shown, the relative error of the OBRDM is below 15%, even if the MPS bond dimension is as small as $D = 30$. Already for the smallest MPS bond dimension shown, the MPS representation resolves the OBRDM with little error. Here the error is between 5% and 15%, however it decreases when the bond dimension is increased. Most situations are well approximated by a MPS representation with bond dimension $D = 70$, which refers to a significant reduction of the size of the represented many-body Hilbert space. Especially dynamics following ionization in the valence orbitals (HOMO to HOMO-3) are described well by the MPS representation with bond dimension $D = 70$, where the relative error is below 5%. This feature is apparent for all molecules tested. The small errors of the calculation with $D = 70$ is in particular striking, as the large bond dimension limits the different molecules
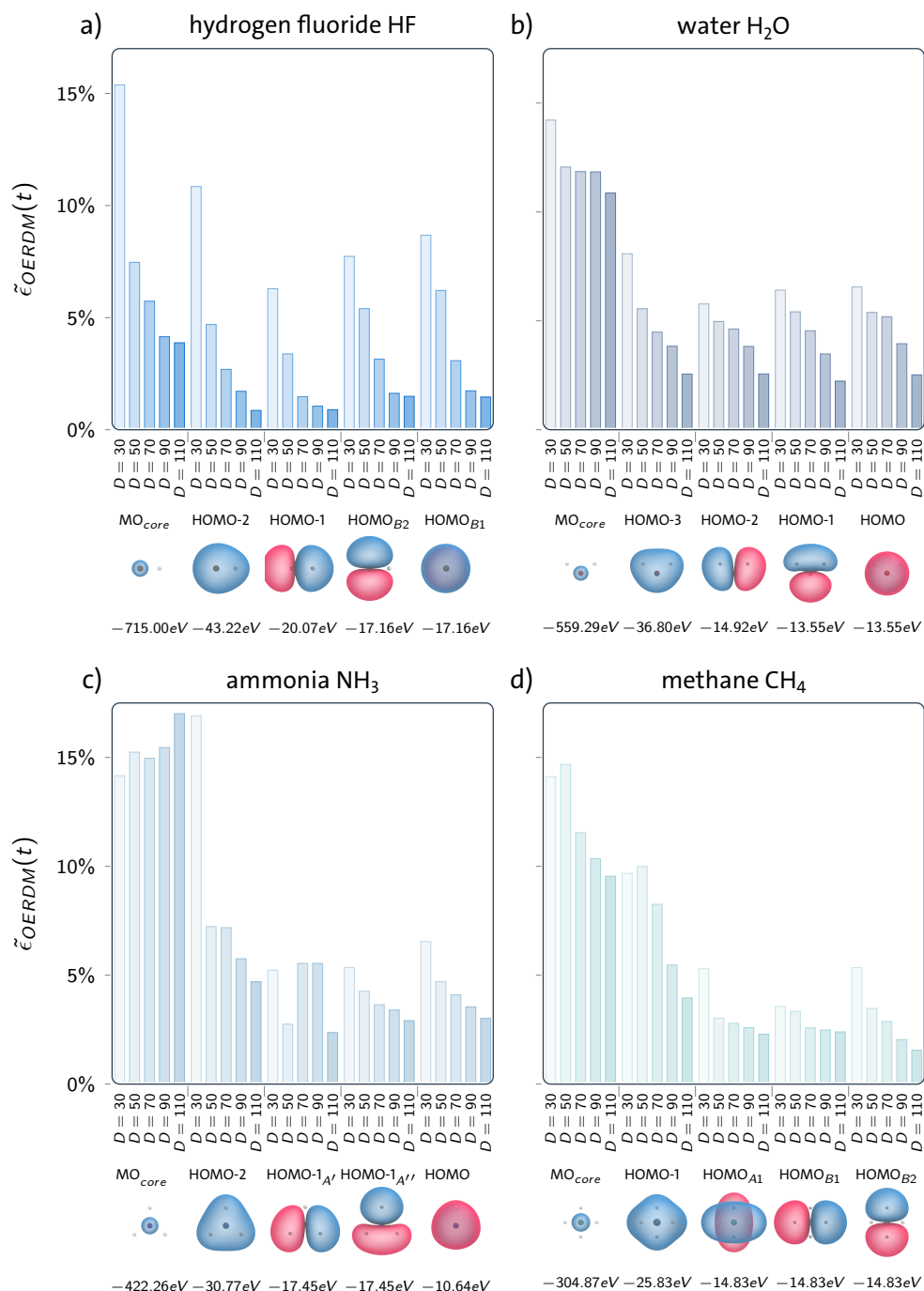
**Figure 4.9.:** Relative errors of the OBRDM at $t = 1\,fs$ calculated using the MPS representation for various molecules (hydrogen fluoride, water, ammonia and methane), initial states ( single ionization in HOMO, HOMO-1, HOMO-2, HOMO-3 and $MO_{core}$) and bond dimensions ($D = 30$, $D = 50$, $D = 70$, $D = 90$, and $D = 110$). In all calculations (using the complete many-body representation and using the MPS representation) the state is propagated using the orthogonalized Krylov space method with Krylov space dimension $N_{Kry} = 6$ and time step size $\Delta t = 1.0\,as$. The error of the OBRDM is averaged over a period of $\pm 50\,as$ at time $t = 1\,fs$. Additionally, the orbital shape and its ionization potential is given.

|          | FH      | $H_2O$   | $NH_3$   | $CH_4$    |
|----------|---------|----------|----------|-----------|
| $D = 30$ | 2433.8s | 3533.7s  | 5559.6s  | 7056.6s   |
| $D = 50$ | 3204.1s | 5625.9s  | 8112.7s  | 11375.1s  |
| $D = 70$ | 4160.5s | 6380.6s  | 11110.1s | 13662.7s  |
| $D = 90$ | 4984.9s | 8626.2s  | 15287.3s | 19831.1s  |
| $D = 110$| 5578.5s | 10679.4s | 17262.3s | 24897.1s  |
| FCI      | **893.2s** | **4767.3s** | **71548.9s** | **149042.4s** |

**Table 4.2.:** Run times of the Hamburg CheMPS2 extension in seconds. The initial state is the Hartree–Fock ground state with a hole in the HOMO. The time evolution for all calculations were performed by the orthogonalized Krylov space method with a Krylov space dimension of $N_{Kry} = 6$, a time step size of $\Delta = 1as$, and the final time $t = 1fs$. The calculation was performed on an Intel(R) Xeon(R) CPU E5-2680 v3 @ 2.50GHz processor with a 20 cores running in parallel. Neither of the calculations required significant amounts of memory.

differ significantly. The large bond dimension limit for the orbital set of hydrogen fluoride is $D_{FCI}^{HF} = 318$, while the largest possible bond dimension for the methane is $D_{FCI}^{CH_4} = 1885$. Apparently, for dynamics following ionization in the valence orbitals, all these molecules can be described appropriately by an MPS approach with bond dimension $D = 70$, which is a manifestation of Koopmans theorem.

Therefore, the area of the many-body Hilbert space required to describe the ionized molecule is small and it does not grow with the size of the complete many-body Hilbert space. The dynamics in molecules with a large many-body Hilbert space can be described by the MPS approach with small bond dimensions. This demonstrates that the shown cations do not develope correlations that exceed the capabilities of the MPS approach in this time frame. Even though the molecules are high-dimensional, include long-ranged Coulomb interaction, and the artificial orbital order exaggerates the non-locality of the description, the entanglement in the systems spreads slowly and the MPS approach is able to represent the state with a small bond dimension.

The large area of the many-body Hilbert-space that is neglected in the MPS representation also manifests in the computation times of these examples (see Table 4.2). For the molecules $NH_3$ and $CH_4$, computations using the MPS representation runs significantly faster than its quasi exact counterpart (denoted as FCI in the table). While the complexity of the calculation using the complete many-body state grows factorially with number of electrons and number of orbitals, the MPS representation only scales polynomially. This gives the MPS representation an advantage in computation time, that further amplifies when going to larger systems. In systems with small orbital sets (hydrogen fluoride), the overhead added by the MPS approach reduces the benefit of using a truncated many-body state, where the quasi exact calculation is faster than the MPS based calculations.

Beyond the trend of smaller errors when the bond dimension is increased, the errors in Figure 4.9 show, that the MPS approach struggles with ionization in core orbitals ($MO_{core}$). Compared to ionization in valence orbitals, the error of the MPS approach almost doubles if the ionization takes place at the $MO_{core}$ (the $1s$ orbital at the heavy atom F, O, N, or C). A deeper ionization corresponds to a stronger excitation, which leads to faster emerging correlations. Therefore, the MPS approach will be able to handle excitation close to the HOMO better than excitations that are close to or in core orbitals. Nevertheless, also in situations with an electron hole in a core orbital, the accuracy can be controlled by the bond dimension of the MPS, however, they need to be larger compared to a hole in valence orbitals.

A comment is due on the different truncation errors of degenerated orbitals. For example, the $HOMO_{B1}$ and the $HOMO_{B2}$ of the hydrogen fluoride molecule have the same shape and the same orbital energy; they differ in symmetry only. Following ionization, we expect for both orbitals the same form of entanglement to emerge, which then may be cut by the truncated MPS representation of the many-body state. But the truncation error of the MPS representation differs for ionization in these two orbitals, meaning that we cut different amounts of entanglement. In some sense, this is an unphysical result, which clearly demonstrates the importance of the order of the molecular orbitals in the MPS representation. Although the two orbitals are physically similar, they are considered at different positions in the artificially one-dimensional MPS representation. For one of the orbitals, the interaction with the remaining system is effectively on a longer (orbital) distance, which leads to more long-ranged entanglement that is cut more rigorously.

**CI Weights**

Let us now try to understand how the MPS approach is able to reproduce the complete many-body state with this precision. The errors given in Figure 4.9 show that the MPS is able to represent the complete many-body state, but to use the MPS representation in situations where we cannot provide quasi exact results for comparison, we need criteria to decide whether the MPS representation is valid. With the convergence of the bond dimension, we already have one criterion to validate the MPS approach. However, to go beyond simple bond dimension convergence, we also want to discuss *configuration interaction weights* (CI weights) to understand how the MPS compare to CI expansions.

We can quantify the importance of the different CI excitation classes (see Section 2.3 for details) by calculating the CI weights. The CI weights tell us how the MPS state is constructed in terms of configurations in the occupation number basis and how

important different types of excitations are. Let $|\Psi_0\rangle$ be the Hartree–Fock ground state, then, for example, the weight of states where there is one hole in one of the initially occupied Hartree–Fock states (the *one-hole-zero-particle* weight) is given by

$$P_\alpha^{1h0p}(t) = \sum_{i\sigma} |_\alpha \langle \Psi(t)|\hat{c}_{i\sigma}|\Psi_0\rangle_\alpha|^2, \tag{4.17}$$

with $|\Psi(t)\rangle_\alpha$ being the time dependent state in its $\alpha \in \{FCI, MPS\}$ representation. The one-hole-zero-particle weight is one at the initial time $P_\alpha^{1h0p}(t_0) = 1$, as we chose our initial state to be a one-hole-zero-particle configuration. However, following the dynamics, also other CI configuration classes can be populated, which eventually reduces the one-hole-zero-particle weight.

The weight of states with two holes in core or valence molecular orbitals and one electron excited to a virtual orbital, i.e. the *two-hole-one-particle weight* is given by

$$P_\alpha^{2h1p}(t) = \sum_{ijk\sigma\tau} |_\alpha \langle \Psi(t)|\hat{c}_{i\sigma}^\dagger \hat{c}_{j\sigma} \hat{c}_{k\tau}|\Psi_0\rangle_\alpha|^2. \tag{4.18}$$

This can be extended to arbitrary excitations, where all configurations belong to one of such CI classes. All weights added give the norm of the many-body state

$$P_\alpha^{1h0p}(t) + P_\alpha^{2h1p}(t) + \cdots = |_\alpha \langle \psi(t)|\psi(t)\rangle_\alpha|^2. \tag{4.19}$$

This allows to extract the weight of higher excitation classes by reordering Equation 4.19 to $P_\alpha^{high}(t) = |_\alpha \langle \psi(t)|\psi(t)\rangle_\alpha|^2 - P_\alpha^{1h0p}(t) - P_\alpha^{2h1p}(t)$, as it is usually difficult to calculate all weights. There are too many coefficients to be calculated (see curse of dimensionality in Section 2). For $\alpha = FCI$, the norm of the state is $|_{FCI} \langle \psi(t)|\psi(t)\rangle_{FCI}|^2 = 1$, however, this is not necessarily the case for the truncated MPS representation, although it should stay close to one.

In Figure 4.10 we see the time-dependent CI weights together with the truncation error of the MPS approach for electron dynamics in the water molecule. We prepare similar initial states as discussed before, i.e. all possible single ionizations of the water molecule, ranging from the HOMO to $MO_{core}$ (see Figure 4.9 for graphical depiction of the orbitals). Additionally the CI weights of the complete many-body state calculation (FCI) are shown in light colors in the background to allow for comparison with the quasi exact results. From these we can estimate the importance of highly excited configurations to the many-body state representation and validate if the MPS representation is able to cover highly excited configurations states appropriately. In almost all situations, the MPS representation shows the correct CI weights, which indicates it is able to incorporate the correct configurations dynamically.
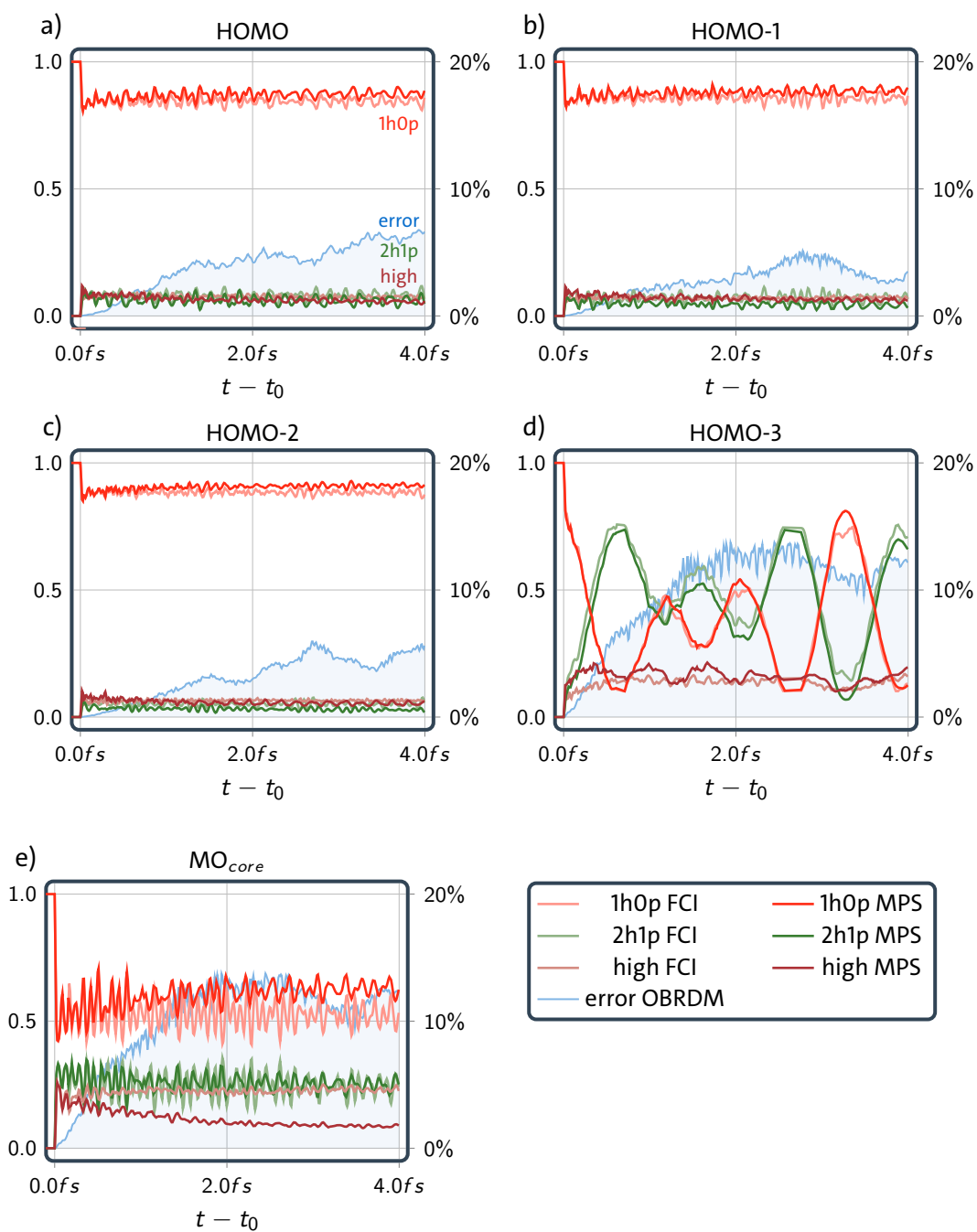
**Figure 4.10.:** CI weights of the time-dependent many-body state of the ionized water molecule (left y-axis) and errors of the one-body reduced density matrix (right y-axis). The error is shown for MPS calculations with bond dimension $D = 70$. The shown CI weights are the *one-hole-zero-particle* weight (1h0p), the *two-hole-one-body* weight (2h1p) and contributions of higher CI classes (high). In all calculations (based on the complete many-body state and MPS based representation) the state is propagated using the orthogonalized Krylov space method with Krylov space dimension $N_{Kry} = 6$ and time step size $\Delta t = 1.0as$.

An interesting feature shown in Figure 4.10 is the dependence of the weights on the position of the created hole. Following ionization in the HOMO, the HOMO-1, and the HOMO-2, the system stays in states that are well represented by configurations of type $1h0p$ and $2h1p$. These types of configurations account for 92% of the entire many-body state. A CISD expansion of the many-body state would be able to describe the electron dynamics in these situations correctly. However, the physics changes if the system is prepared in an initial state with an ionization in the HOMO-3 or the $MO_{core}$ orbital. For these two initial states, the following electron dynamics show significant population of excited configurations. Here, the higher excited configurations account for about 25% of the total many-body state. A simple CISD representation of the many-body state would be unable to resolve this behavior, as it restricts the many-body state representation to low excited configurations.

The CI weights are adjusted dynamically in the MPS representation of the time-dependent many-body state. In contrast to the CI expansions, with the MPS approach we do not need to choose a specific type of configuration in our representation prior the calculation. The MPS approach is able to adapted the configurations dynamically and it includes higher excited configurations when needed. This already happens at very small bond dimensions (bond dimension of $D = 70$ in Figure 4.10), showing that higher excitation classes are not necessarily tied to strong entanglement in the state. By limiting the bond dimension, we effectively reduce the amount of entanglement the MPS is able to represent. Apparently, this does not mean, that the MPS representation is limited to low excitation CI classes, as we still see large weights of excited configurations in MPS with small bond dimension. Therefore, the approach does go beyond the typical CI expansion of the many-body state.

**Conclusion**

In this section we have seen that the MPS approach also allows to treat the dynamics of realistic molecules that have been singly ionized. We demonstrated this using the hydrogen fluoride molecule, the water molecule, the ammonia molecule, as well as the methane molecule in the extended basis set 6-31G. In all these examples, the MPS results converged quickly when increasing the bond dimension, which shows their stable behavior, even if the molecule spreads over all three dimension and the molecular orbitals are delocalized. Next we analyse how the MPS representation performs in case of the doubly ionized initial states.

## 4.2.2 Double Ionization

To complete the analysis of the MPS representation, we now discuss their performance in case the molecule has been doubly ionized. Multiple (including double) ionization processes of molecules are widespread in nature that either happen as an ionization following previous ones (*sequential ionization*), but also involve processes where multiple electrons are liberated from the molecule at once (*non-sequential ionization*). Experimentally, molecules can be brought into a doubly ionized state by strong-field ionization [180, 255] and by using ultra short laser pulses [256, 257]. It is therefore interesting how the MPS representation performs when applied in modeling these situations. As benchmark systems, we utilize the same molecules as described above, namely hydrogen fluoride CF, water $H_2O$, ammonia $NH_4$, and methane $CH_4$.

Again, double ionization processes can happen suddenly, i.e. they occur on time scales faster than all electronic response. We will therefore continue in a similar fashion as our study on single ionization. We prepare the initial state in the Hartree–Fock ground state, but now remove two electrons from a given orbital at time $t = 0$. This leaves the molecule with $8$ electrons, which will react onto the newly prepared situation on the time scale of a few femtoseconds.

Electron dynamics following double ionization has been studied by Hollstein et. al. using the CI approach [94]. Their CI approach was limited to the two-hole-zero-particle configurations (2h0p), i.e. configurations where there are two holes in the state compared to the Hartree–Fock ground state, as well as the three-hole-one-particle configurations (3h1p), i.e. states with three holes in the Hartree–Fock ground state and one electron promoted to one of the virtual orbitals. These studies demonstrated the impact of the 3h1p configuration class, which are absolutely important in describing the electron dynamics in $C_2H_4BrI^{2+}$. As the MPS representation is particularly suited for describing dynamics that are driven by highly excited configurations, it is interesting to see how the MPS approach is able to handle doubly ionized situations and what important CI weights occur in the MPS representation.

**MPS Representation Error**

The MPS representation is also capable of handling situations where the molecule has been doubly ionized, especially if the double ionization took place in an outer-valence orbital. We conclude this from the relative error of the OBRDM after $1fs$ of time evolution, shown in Figure 4.11. In all outer-shell (HOMO, HOMO-1, and HOMO-2) examples, the MPS representation is able to find the correct OBRDM within an error
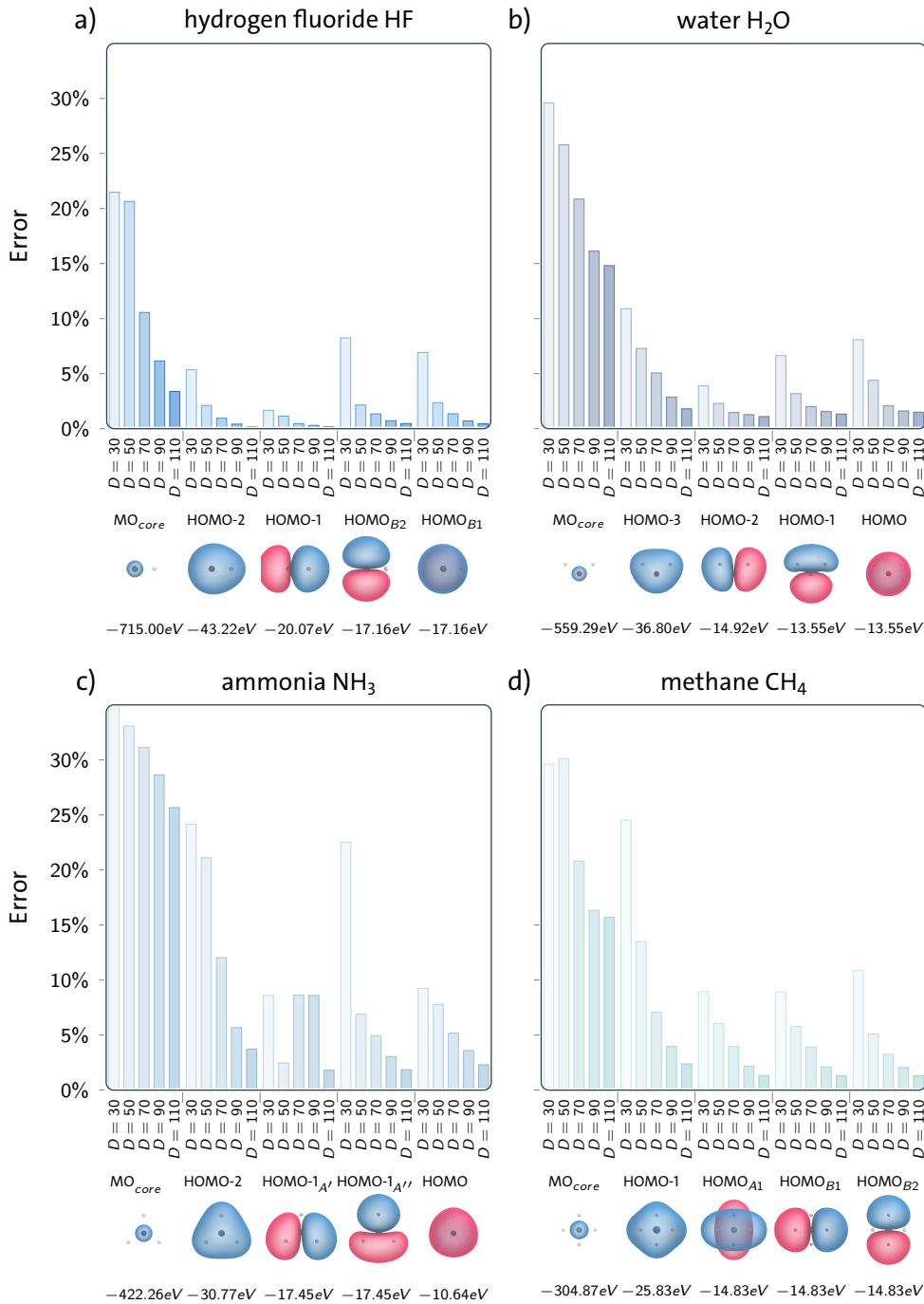
**Figure 4.11.:** Relative errors of the OBRDM at $t = 1fs$ calculated using the MPS representation for various molecules (hydrogen fluoride, water, ammonia and methane), initial states ( double ionization in HOMO, HOMO-1, HOMO-2, HOMO-3 and $MO_{core}$) and bond dimensions ($D = 30$, $D = 50$, $D = 70$, $D = 90$, and $D = 110$). In all calculations (using the complete many-body representation and using the MPS representation) the state is propagated using the orthogonalized Krylov space method with Krylov space dimension $N_{Kry} = 6$ and time step size $\Delta t = 1.0as$. The error of the OBRDM is averaged over a period of $\pm 50as$ at time $t = 1fs$.

of 5% when using a MPS bond dimension $D = 70$. The error reduces to $< 2\%$ when using a MPS bond dimension of $D = 110$. We observe the rapid convergence of the MPS results with growing bond dimension that we have already seen for the singly ionized molecules. This convergence is independent of the actual dimension of the complete many-body Hilbert space. The dimension of the complete many-body state for the smallest example hydrogen fluoride molecule is 27252 ($D_{FCI} = 175$), where it is for the largest example methane 1416368 ($D_{FCI} = 808$). Although these dimensions differ in size, we do not observe the larger Hilbert space requiring significantly larger MPS bond dimensions to find the OBRDM within an error of 5%.

The situation changes when discussing inner-valence double ionization (HOMO-3) and double ionization of the core orbital (HOMO-4). Here the MPS approach struggles to represent the many-body states correctly, which we observe in errors of the OBRDM in the range of 15% to 30%. Increasing the MPS bond dimension reduces the error of the OBRDM in case the molecule was prepared in a state with a double hole in the HOMO-3 orbital. Here we find for an MPS bond dimension of $D = 110$ an error of the OBRDM in the range of 2% to 5%. In case the water molecule was prepared in a state with a double hole located in the HOMO-4, a bond dimension of $D = 110$ is still not sufficient. We need to increase the bond dimension further, which reduces the computational advantage of the MPS approach in comparison to the calculation using the complete many-body state.

The fact that double ionization in core orbitals are difficult to describe using MPS tells us that in these situations the entanglement grows comparably fast. This makes a MPS description of such situations difficult. We need to be careful when describing situations with deeply ionized molecules in the system. This might also be a consequence of the used orbital ordering that placed the core orbital at the very left of the MPS representation, leaving it with a large (MPS)distance to energetically large orbitals on the right of the MPS representation. Further studies on the orbital ordering in this situation possibly allow to improve the MPS performance for this situation.

**CI Weights**

Figure 4.12 shows the CI weights of the time-dependent many-body state for dicationic water $H_2O^{2+}$. The initial state is doubly ionized Hartree–Fock ground state, with the double hole located at the HOMO (Figure 4.12 a) ), located at the HOMO-1 (Figure 4.12 b) ), located at the HOMO-2 (Figure 4.12 c) ), located at the HOMO-3 (Figure 4.12 d) ), and located at the MO$_{core}$ (Figure 4.12 e) ).
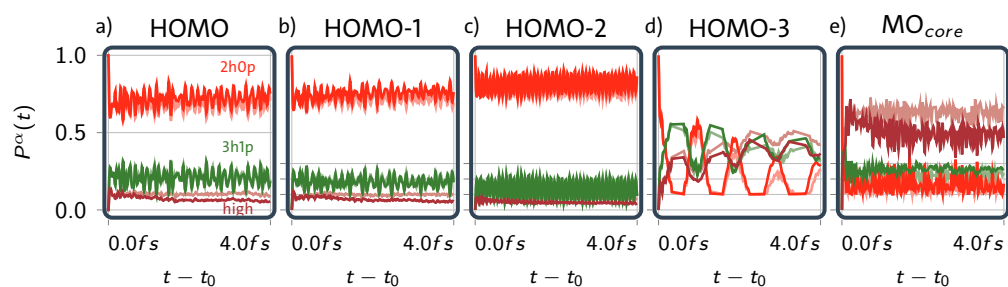
**Figure 4.12.:** Time-dependent CI weights of the many-body state of dicationic water ($H_2O^{2+}$). The initial state is a double ionization in the molecular orbital as given in the titles of the plots. The shown CI weights are the *two-hole-zero-particle* weight (2h0p), the *three-hole-one-body* weight (2h1p) and contributions of higher CI classes (high). In all calculations (based on the complete many-body state and MPS based representation) the state is propagated using the orthogonalized Krylov space method with Krylov space dimension $N_{Kry} = 6$ and time step size $\Delta t = 1.0 as$.

The many-body state for outer-valence double ionization has a particular high 2h0p and 3h1p weight (see Figure 4.12 a) to c) ). In these situations a CI expansion is justified and the system remains in states related to few particle-hole excited configurations. The settings with a double excitation in the outer-valence orbitals are those we observed good convergence of the MPS representation for (see Figure 4.11).

In case of inner-valence double ionization and core orbital double ionization, higher excited configurations become rather important. If the initial state of the water molecule is prepared as doubly ionized HOMO-3, or doubly ionized $MO_{core}$ Hartree–Fock state, the weights of the 2h0p and 3h1p configurations reduce. Then the importance of the higher excited configurations increases. A simple CI expansion of the many-body state is unable to describe these situations, as multiple particle-hole excitations contribute significantly. This confirms to observations we made for the singly ionized systems already, where ionization of deeper orbitals responds to higher excitations of the molecule. As a consequence of the higher excited initial state, also the dynamics involves higher excited configurations, which we notice in the form of a large $P_{high}(t)$ weight.

However, the MPS approach is able to include the weights of the higher CI expansion correctly. The CI weight of the MPS representation (bold colors in Figure 4.12) correspond in all situations to the CI weights of the complete many-body state (light colors in Figure 4.12). Even in situations where the MPS approach looses precision in the OBRDM, the CI classes are accurately found in the MPS representation. This underlines its capabilities to adjusting the representation of the many-body state dynamically.

**Conclusion**

We conclude that the MPS approach enables to represent the many-body state with minor truncation errors in case the molecule has been doubly ionized. However, the convergence needs to be monitored more carefully, as we have observed larger relative errors of the OBRDM if the double hole is located in inner-valence or core orbitals. Here, the MPS bond dimension needs to be increased compared to the singly ionized situations studied above, which we attribute to the enlarged excitation energy of the initial state, but also the orbital ordering can be responsible for this behavior. For outer-valence orbitals, we have observed similar convergence performance compared to the single ionization situations, where it was easy to reduce the relative error to $5\%$ by using bond dimensions of $D = 70$. The necessary bond dimension is independent of the dimension of the complete many-body Hilbert space of the problem. This shows that we can gain computational advantages compared to the CI expansions, especially in situations where more electrons and orbitals are involved. In case of double ionization, the importance of highly excited configurations seems to be increased in comparison to the singly ionized situations.

### 4.2.3  Conclusion

Eventually, we can tell with certainty that the MPS approach performs well for the more realistic molecules discussed here. We have demonstrated this discussing both, singly ionized, as well as doubly ionized molecules. Strikingly, the necessary bond dimension to describe a system is independent of the dimension of the complete many-body Hilbert space. Therefore, we can converge the MPS representation with respect to MPS bond dimension and obtain a quasi exact representation of the complete many-body state. With the exception of double holes in core orbitals, this convergence was fast and the MPS result agreed with the full CI results upon an error of less than $10\%$ at bond dimensions close to $D = 70$. Therefore, we are positive, the MPS does simplify the calculation of electron dynamics in molecules, however, being much more dynamic than, for example, the CI expansion of the many-body state. We proved this specifically by discussing the CI weights and comparing to results of a full CI calculation. The MPS approach is able to incorporate highly excited configurations dynamically.

# 4.3 Comparison of Time Evolution Algorithms for Matrix Product States

From the beginning of this chapter, we analyzed the MPS approach to understand if it is able to handle dynamically emerging entanglement. In these studies, we mostly utilized the orthogonalized Krylov space time evolution method (see Section 2.5) with a Krylov space dimension $N_{Kry} = 6$ and a time step size of $\Delta t = 1as$. For this particular time evolution method, we noticed that the MPS results converged correctly to the quasi exact results when increasing the MPS bond dimension. Thus, the MPS approach was able to handle the entanglement appropriately. However, from a technical point of view, is the orthogonalized Krylov space method the optimal choice to time-evolve an MPS in quantum chemistry? How does it compare to the more prominent fourth-order Runge–Kutta method and is there any option to improve the performance of the Krylov space method? We address these questions in the following section.

We continue the analysis of the MPS approach, however, now with respect to the time evolution method rather than focussing on the MPS performance only. The MPS representation of a many-body state is not unique, i.e. the exact same many-body state can be equally well represented by MPS with different bond dimensions. As we interact with the MPS purely variationally, it is possible that the MPS with fixed bond dimensions show different performance for different time evolution methods. We will find, the choice of the time evolution method does have an effect on the MPS representation, where the optimal method can reduce the size of the MPS bond dimension. This reduction then follows a computational advantage, since we can either reduce the MPS bond dimension and maintain accuracy, or we can keep the MPS bond dimension and improve accuracy.

It is important to remark that we still discuss the MPS approach, however, now with focus on its interplay with the time evolution method. This section is not about analyzing the time evolution methods themselves. For this, a rich family of studies exists [258–260].

## 4.3.1 Non-Unitary vs. Unitary Time Evolution

In Section 2.5 we discussed two different types of time evolution algorithms. On the one hand, we have the family of non-unitary time evolution methods, that expand the time evolution operator in Equation 2.102 in a manner that violates the unitarity, i.e. the time reversal symmetry is broken and the norm of the time-evolved state may change. For example, the Runge–Kutta methods belongs to this family. On the
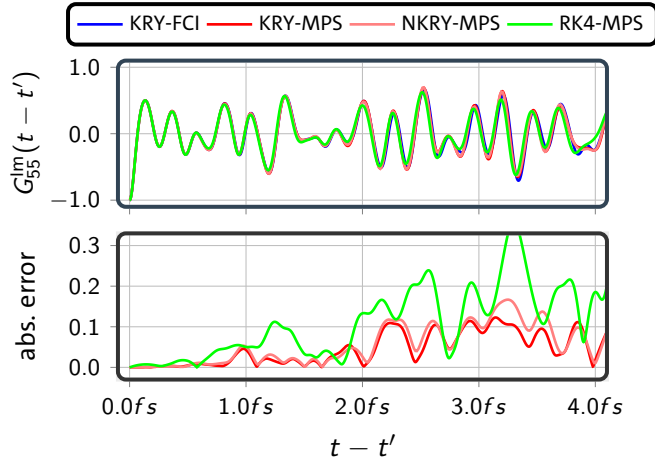
**Figure 4.13.:** (top) Time-dependent one-body Green's function of the hydrogen chain calculated using the complete many-body state and the MPS representation with bond dimension $D = 30$. For the complete many-body state the time evolution (KRY-FCI) was performed using the orthogonalized Krylov space method with a Krylov space dimension of $N_{Kry} = 5$ and a time step size of $\Delta t = 1.21 as$. For the MPS representation of the many-body state, the time-evaluation was performed using the orthogonalized Krylov space method (KRY-MPS), the non-orthogonalized Krylov space method (NKRY-MPS), and the fourth-order Runge–Kutta method (RK4-MPS). (bottom) The absolute error of the one-body Green's function with respect to the calculation using the complete many-body state (KRY-FCI).

other hand, we have unitary time evolution methods, which also expand the time evolution operator from Equation 2.102, however, in a fashion that conserves the feature of unitarity. The Krylov space methods belong to this family. In the following section, we want to compare these methods and see if the missing unitarity of the Runge–Kutta method matters to the truncated MPS representation. As the MPS representation of the many-body state is truncated time-dependently, it looses norm and its energy expectation value changes anyway. The additional impact of the time evolution method is yet unclear.

For this comparison, we draw our attention to the chain of 10 hydrogen atoms again, which we already discussed in Section 4.1.2. It is a very well behaved system, and it is the single system where the MPS approach has been applied before [60] to study frequency dependent Green's functions and ionization potentials. To allow comparison with these studies, we analyze the time evolution methods using this system, although, we already know the MPS approach can handle more complex, respectively multi-dimensional, systems. As the quantity for comparison, we utilize the time-dependent one-body Green's function as already given in Equation 4.13 and in Equation 4.15. We have seen the good convergence of the MPS approach for these calculations, however, whether the results can be improved by changing the time evolution method is open.

Figure 4.13 shows the time evolution of the imaginary part of the time-dependent Green's function $G_{55}(t - t')$ in a period of $4fs$. The Green's function was obtained from four independent calculations:

- (KRY-FCI) A calculation that uses the complete many-body state. The time evolution was performed using the orthogonalized Krylov space method with a Krylov space dimension of $N_{Kry} = 5$ and a time step size of $\Delta t = 1.21as$. We consider this calculation as *quasi exact* with respect to the many-body Hilbert space and with respect to the time evolution parameters. Using larger Krylov space dimensions, or reducing the time step size does not affect the result of the one-body Green's function shown (see Appendix A.1).

- (KRY-MPS) A calculation that uses the MPS representation of the many-body state that is fixed to MPS bond dimension $D = 30$. The time evolution was performed using the orthogonalized Krylov space method (see Section 2.5.3) with a Krylov space dimension of $N_{Kry} = 5$ and a time step size of $\Delta t = 1.21as$.

- (NKRY-MPS) A calculation that uses the MPS representation of the many-body state that is fixed to MPS bond dimension $D = 30$. The time evolution was performed using the non-orthogonalized Krylov space method (see Section 2.5.4) with a Krylov space dimension of $N_{Kry} = 5$ and a time step size of $\Delta t = 1.21as$.

- (RK4-MPS) A calculation that uses the MPS representation of the many-body state that is fixed to MPS bond dimension $D = 30$. The time evolution was performed using the fourth-order Runge–Kutta method (see Section 2.5.2) with a time step size of $\Delta t = 1.21as$.

All above methods require four applications of the Hamiltonian, therefore, they are similar in computational demand and we should expect similar accuracy. Further, all MPS based calculations require comparable amounts of memory.

From the imaginary part of the one-body Green's function (see 4.13 (top) ), we observe good accuracy for all three calculations using the MPS representation. All calculations show qualitatively the same behavior, and the oscillation frequencies appear to be close to the quasi exact frequencies. The performance of the different methods only manifests in the absolute error of the one-body Green's function

$$\epsilon_{ij}^{\alpha}(t - t') = |G_{ij}^{FCI}(t - t') - G_{ij}^{\alpha}(t - t')|, \tag{4.20}$$

with $\alpha \in \{\text{KRY-MPS, NKRY-MPS, RK4-MPS}\}$. While the two Krylov space based methods have no problem in describing the one-body Green's function within an absolute
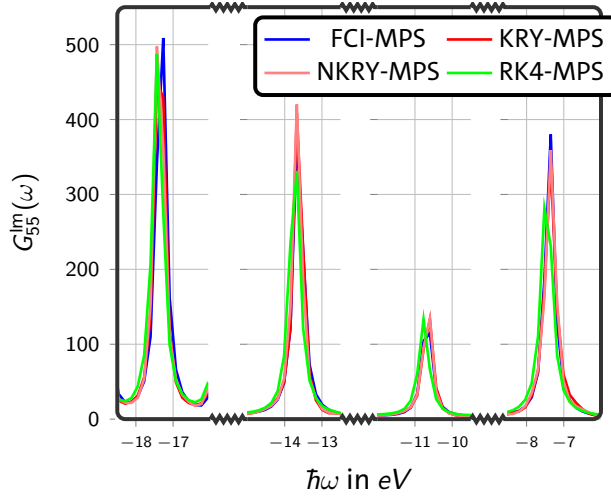
**Figure 4.14.:** Major peaks of the frequency dependent one-body Green's function for a chain of 10 hydrogen atoms. Peaks are obtained from the Fourier transform of the results in Figure 4.13, using the same labels. To extract the major peaks, a broadening of $\eta = 0.14eV$ has been applied to the Fourier transform (see Equation 4.15). This figure is published in Frahm [219].

error of $0.1$ (real and imaginary part combined), the Runge–Kutta method already acquires an error larger than $0.3$ in the period of $3.3fs$. This is an unexpected result, given all calculations use the MPS representation with the same number of degrees of freedom and all expand the time evolution operator with four Hamiltonian applications. Solely the method to express the time evolved state has changed. Again, this is not a consequence of poorly converged time evolution parameters, but can be accounted to the non-linear entanglement of the time evolution method and the MPS representation. The time step size is chosen reasonably small such that all time-evolution methods (fourth-order Runge–Kutta and Krylov) should show the same dynamics (see Appendix A.1). This demonstrates, choosing the optimal time evolution method is relevant for finding the optimal MPS representation of the time evolved state, where in this example, the two unitary Krylov methods are superior to the non-unitary Runge–Kutta expansion. The form of the Krylov space method (orthogonalized and non-orthogonalized) has no significant impact on the accuracy of the many-body Green's function. In this example, we see similar absolute errors with respect to the complete many-body state for both methods.

These two features of the Runge–Kutta method and the Krylov method also display in the frequencies dependent one-body Green's function (see Figure 4.14). For the major peaks of the imaginary part (compare Figure 4.8) we see improved accuracy of the two Krylov methods compared to the Runge–Kutta method. The peaks from the Runge–Kutta method are close to the full CI peaks, however, they are slightly shifted towards frequencies larger in magnitude. The two Krylov space methods perform well in peak position and height, where the orthogonalized approach is almost indistinguishable from the quasi exact results.

With this we can conclude the Krylov space time evolution method to be well suited for the time-dependent MPS and we should not rely on the too simple Runge–Kutta approach longer. In this example, the results obtained by using the Krylov space methods are significantly more accurate, while requiring the same amount of computational resources. We account this to the conservation of unitarity of the Krylov space methods. We continue by analyzing the Krylov space method in the following.

## 4.3.2 Krylov Space Methods

Now we want to discuss the different options for the Krylov space method in more detail. In the previous section, we have already seen that the Krylov space methods perform better on MPS than its non-unitary competitor, i.e. the fourth-order Runge–Kutta method. In this section, we want to analyze the various convergence parameters of the Krylov space methods in detail. We focus on the size of the Krylov space $N_{Kry}$, the time step size $\Delta t$, and on the option of using orthogonal or non-orthogonal Krylov basis vectors.

We perform this comparison at the example of the water molecule, which we already discussed in Section 4.2.1 and Section 4.2.2. We describe it on the 6-31G basis set level, which gives us, after the Hartree–Fock calculation, a set of 13 molecular orbitals. This orbital set is within the dimension where we can perform calculations using the complete many-body state.

**Single Ionization**

As the initial state, we use the Hartree–Fock ground state, with a sudden ionization at the core orbital ($MO_{core}$), i.e. the 1s orbital of the oxygen atom (see Figure 4.9 b)). In the analysis of the MPS representation performed previously in Section 4.2.1, this was the most difficult situation for the MPS approach we have encountered. The large excitation energy a core hole brings along challenges the MPS representation most. The time evolution method used there (orthogonalized Krylov with $N_{Kry} = 6$ and $\Delta t = 1as$) was able to find the correct OBRDM within an error of $\approx 12\%$ for single ionization, however, showing only little improvement with respect to MPS bond dimension. We want to pick this initial state, as we see in this situation the largest opportunity for improvement of the MPS approach.

In Figure 4.15, we see the relative error of the OBRDM increasing with time. The OBRDM was first calculated using the complete many-body state with the orthogonalized Krylov method with Krylov space dimension $N_{Kry} = 6$ and a time step size of $\Delta t = 0.484as$. Then we calculated the OBRDM using the MPS representation with
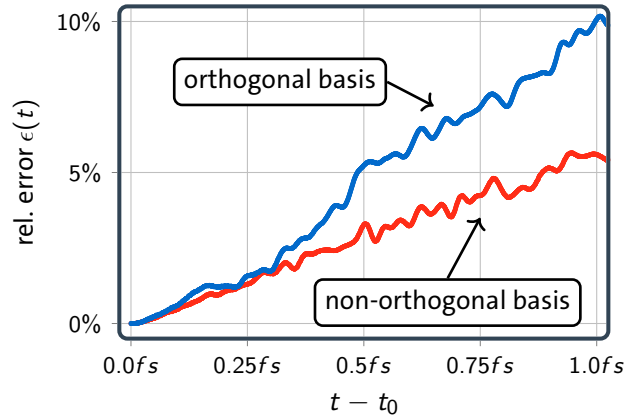
**Figure 4.15.:** Error of the one-body reduced density matrix for two Krylov space time evo-
lution methods. The corresponding quasi exact calculation employs a Krylov
space dimension of $N_{Kry} = 6$ and a time step size of $\Delta t = 0.484as$. This figure
is published in Frahm [219].

a maximum bond dimension $D = 60$, but once with orthogonalized Krylov space
method and once with the non-orthogonalized. Figure 4.15 shows the relative er-
rors of these two calculations with respect to the quasi exact calculation using the
complete many-body state.

We observe the linearly growing error of the OBRDM we have seen before for the
hydrogen chain (see Figure 4.5), however, with slopes depending on the time evolution
method. Using the non-orthogonalized Krylov method the error grows to 5% after $1fs$,
whereas when using the orthogonalized Krylov method the error grows almost twice
as fast to 10% in the same period. In this example, the non-orthogonalized Krylov
method allows to reduce the error significantly. Therefore, tweaking the Krylov space
properties does affect the accuracy of the MPS approach, which eventually reduces
the necessary bond dimension to achieve a given precision. A detailed analysis of the
Krylov time evolution method may allow us to find the optimal parameters for time
evolution using MPS and tells us what intrinsic mechanisms in the MPS limit the time
evolution.

We observe improvements when using the non-orthogonal approach, which allows
to reduce the relative error of the OBRDM by 50%. Waiving the orthogonalization
improves the MPS representation of the many-body state. Using MPS with limited
bond dimension inevitably reduces their flexibility to represent the time evolved state
correctly. An efficient use of the remaining coefficients is therefore essential when
optimizing the MPS to represent the correct time evolved state. When constructing
the orthogonalized Krylov vectors in MPS representation however, the MPS sacrifice
their Krylov space property to the additional constraint of being orthogonal to other
Krylov vectors. This additional constraint makes them leave the Krylov space (due to
truncation errors in the variational procedure) and the Krylov space is not spanned

properly anymore. This constraint is absent when using non-orthogonal Krylov space vectors in the first place. When using the non-orthogonal Krylov vectors, the Krylov vectors are already much closer to the different orders of the Taylor expansion of the time evolution operator

$$\hat{U}(\Delta t)\,|\Psi(t_0)\rangle = \underbrace{|\Psi(t_0)\rangle}_{|\psi^0\rangle} - i\hbar\Delta t\,\underbrace{\hat{H}\,|\Psi(t_0)\rangle}_{|\psi^1\rangle} + \frac{1}{2}\hbar^2\Delta t^2\,\underbrace{\hat{H}^2\,|\Psi(t_0)\rangle}_{|\psi^2\rangle} + \cdots, \qquad (4.21)$$

with $|\psi_i\rangle$ being the $i$-th non-orthogonalized Krylov vector. Although the construction of the time evolved state goes beyond the expansion in Equation 4.21 in the Krylov space method, it is a good picture to understand why the non-orthonormalized Krylov method performs better than its orthogonalized counterpart.

We now discuss the convergence of the Krylov method based time evolution using MPS by varying the MPS bond dimension, the Krylov space dimension $N_{Kry}$, the time step size $\Delta t$, and the Krylov basis vector type. In Figure 4.16 we see the color mapped relative error after a period of $1fs$, but averaged in an interval of $50as$. The calculations using the complete many-body state uses the orthogonalized Krylov method and a Krylov space dimension of $N_{Kry} = 6$. Further, the calculation compared to uses the same time step size as the MPS approach, such that time points for comparison match exactly. The Krylov parameters are well converged, even for the largest shown time step size $2.25as$. For the calculation using the complete many-body state, the results are independent whether we use a time step size of $\Delta t = 2.25as$ (maximum shown) or $\Delta t = 0.25as$ (minimum shown). The relative difference of the respective OBRDM is $|\gamma_{FCI}^{\Delta t=0.25as} - \gamma_{FCI}^{\Delta t=2.35as}| \sim 0.4\%$, i.e. negligible on the color scale of Figure 4.16.

We see that all calculations converge to a minimal error when increasing the MPS bond dimension $D$. This happens especially systematically when using the orthogonalized Krylov space method (upper row of Figure 4.16). While the full CI decomposition of the MPS approach is $D_{FCI} = 608$, already at bond dimension of $D = 80$ for the orthogonalized Krylov method the resulting OBRDM is calculated within an relative error of 10%. The necessary bond dimension to achieve an error of 10% with the non-orthogonalized Krylov space method is even lower (lower row of Figure 4.16). Here it ranges between $D = 40$ and $D = 50$ depending on the time step size $\Delta t$ and the dimension of the Krylov space $N_{Kry}$. This is an essential reduction of the MPS bond dimension, leading to a significant computation advantage. Remember: The complexity of the MPS representation scales with $D^3$, therefore decreasing the bond dimension by 50% corresponds to a reduction of the computation time to an eighth.
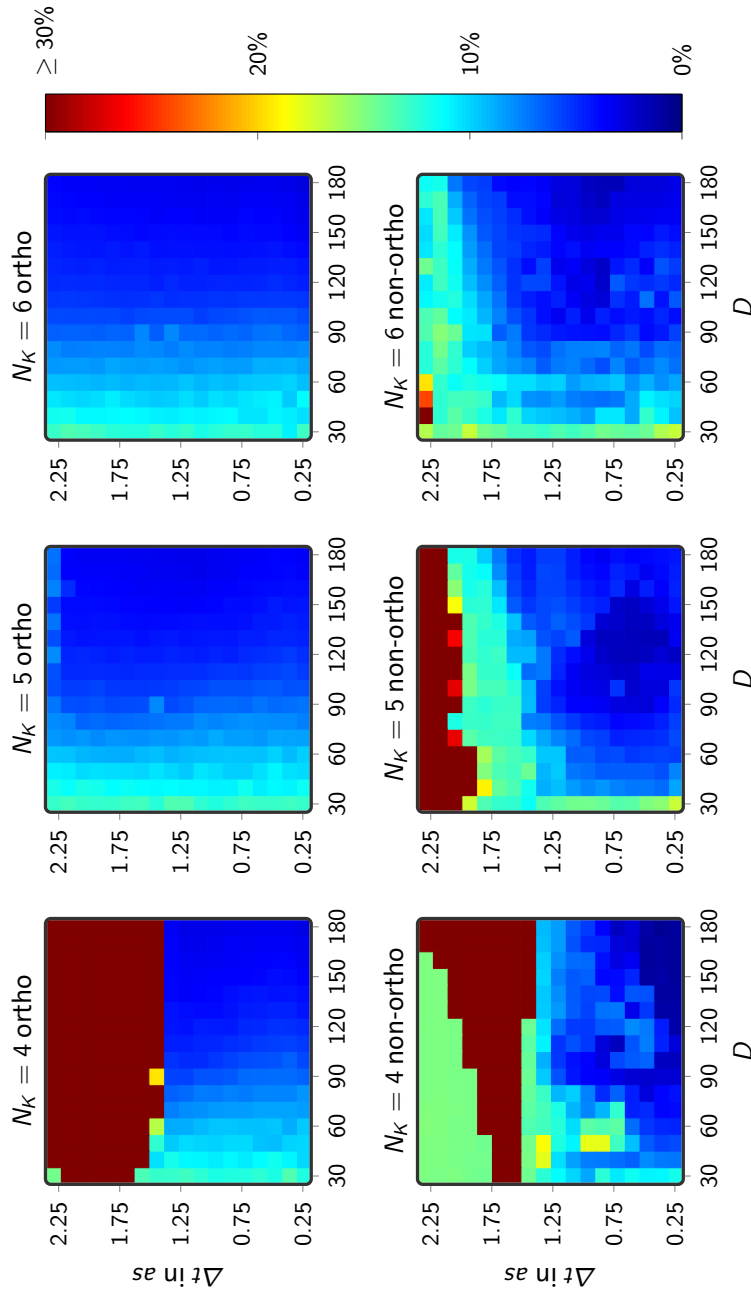
**Figure 4.16.:** Relative error of the OBRDM for various settings of the Krylov space time evolution method. The error is evaluated at $t = 1\,fs$ after the water molecule was ionized at the $1s$ core orbital of the oxygen. The calculation compared to employs the complete many-body state and the orthogonalized Krylov space method with Krylov space dimension $N_{Kry} = 6$. The time step size $\Delta t$ of the MPS calculation always matches the time step-size of the calculation using the complete many-body state. The relative difference of the OBRDM from the completely many-body state is $|\gamma_{FCI}^{\Delta t=0.25as} - \gamma_{FCI}^{\Delta t=2.35as}| \sim 0.4\%$. This figure is published in Frahm [219].

This reduction of the MPS bond dimension comes at the cost of smaller time step sizes $\Delta t$ needed for the non-orthogonalized Krylov space method. For example when using the Krylov space dimension $N_{Kry} = 5$, the time step for the non-orthogonalized Krylov method needs to be close to $\Delta t = 1.125 as$ to achieve an error of 10%, whereas the orthogonalized Krylov method is already stable at a time step of $\Delta t = 2.25 as$. This is a disadvantage of the non-orthogonalized Krylov space method: It requires shorter time steps and therefore requires more time steps to propagate to some fixed point in time. The increased number of time steps reduces the computational advantage we gained due to the smaller bond dimensions. However, since the number of time steps only grows reciprocally with decreasing time step size, it is still beneficial to use the non-orthogonalized method in this situation. The orthogonalized Krylov method with a Krylov space dimension of $N_{Kry} = 5$, a time step size of $\Delta t = 2.25 as$ and an MPS bond dimension of $D = 80$, gives the OBRDM within an error of 10%. To achieve the same accuracy with the non-orthogonalized Krylov space method with $N_{Kry} = 5$, we need to reduce the time step size to $\Delta t = 1.25 as$, but can also decrease MPS bond dimension to $D = 40$. Eventually, if using these settings, the calculation using the non-orthogonalized Krylov space method will finish twice as fast as the calculation using the orthogonalized Krylov space method.

However, we also observe an issue with the non-orthogonalized Krylov space approach. When using MPS with small bond dimensions, the non-orthogonalized Krylov basis vectors tend to become linear dependent very quickly. This happens in particular if the state to be time-evolved is close to an energy eigenstate, i.e. $\hat{H} |\psi^0\rangle \approx E |\psi^0\rangle$. Then, the first Krylov vector $|\psi^0\rangle_{MPS}$, the second Krylov vector $\hat{H} |\psi^0\rangle_{MPS}$, and all following Krylov vectors $\hat{H}^n |\psi_0\rangle_{MPS}$ are close to being linearly dependent. The overlap matrix as given in Equation 3.38 approaches singularity and numerically calculating its inverse becomes unstable. The initial state in our study, i.e. a single $1s$ hole in Hartree–Fock ground state, is such a state close to an eigenstate according to Koopmans' theorem. Therefore, linearly dependent Krylov basis vectors clutter the expansion of the time evolved state in Equation 3.38, which then results in noisy results when performing convergence analysis. Further, does in such situations a larger Krylov space dimension not guarantee better results, as the issue with linear dependent Krylov basis vectors enhances in lager Krylov spaces (see dependence on $N_{Kry}$ in Figure 4.16 ). This effect needs to be balanced by reducing the Krylov space dimension and by reducing the time step size of the time evolution. Therefore, the non-orthogonalization Krylov method requires smaller time steps than its orthogonalized counterpart.

The non-orthogonalized Krylov approach must not be applied if the initial state is close to an eigenstate. Coincidentally, the orthogonalized Krylov method allows for efficient treatment here, as it orthogonalizes the Krylov vectors and the overlap matrix is close to a diagonal matrix.

Our implementation of the Krylov space time evolution does not suffer from the effect that the quality of the results declines if using small time steps. In work by Ronca et al. [60] they encountered an issue if the time steps were chosen small. In their implementation of fourth-order Runge–Kutta method, that works on local MPS tensors instead of the global MPS object, the increased number of truncation steps pollutes the MPS representation and the resulting dynamics emerge erroneous. They had to choose the time step size first to be large, such that the number of MPS truncations can be reduced and second to be small to reduce the error of the Runge–Kutta method (see Supporting Information of [60]). These contradicting demands limits applicability. In our Krylov space method, where every Krylov vector is represented by its own MPS, we do not see any issues with small time steps. Contrarily, we see the error of the MPS representation to decrease for the non-orthogonalized Krylov space method and small time steps.

**Double Ionization**

Previously in Section 4.2.2, we noticed that the MPS approach struggles when representing dynamics resulting from double ionization of a core orbital. We accounted this to the large excitation energy a double ionization introduces to the system, which induces heavily entangled states. Let us now analyse, if the MPS representation is able to cover the entanglement more effectively when propagated using the non-orthogonalized Krylov space method. As initial state, we again choose the most challenging situations found in Section 4.2.2, i.e. a double hole located at the $1s$ orbital of the oxygen atom of the water molecule.

Figure 4.17 shows for the orthogonalized Krylov space method (upper row), that we need very large MPS bond dimensions $D$ and very short time steps $\Delta t$ in order to describe the doubly ionized situation within an error of less than 10%. Only in the limit of $D = 150$ and $\Delta t = 0.3as$ it is able to approach the OBRDM calculated from the complete many-body state, whereas the results are independent of the Krylov space dimension $N_{Kry}$. This bad performance of the orthogonalized Krylov space method was already discussed in Section 4.2.2.

When turning to the non-orthogonalized Krylov space method, the results drastically improve with respect to both, MPS bond dimension $D$ and time step size $\Delta t$ (see lower row in Figure 4.17). We see for all Krylov space dimensions an improved convergence, where the Krylov space dimension of $N_{Kry} = 5$ appears to be optimal. Here, only an MPS bond dimension of $D = 90$ and a time step size of $1.25as$ is required to find the OBRDM within an error of less than 10%. Again, for the calculation using the complete many-body state, it does not matter if we use a time step size of

**Figure 4.17.:** Relative error of the OBRDM for various settings of the Krylov space time evolution method. The error is evaluated at $t = 1\,fs$ after the water molecule was doubly ionized at the 1s core orbital of the oxygen. The calculation compared to employs the complete many-body state and the orthogonalized Krylov space method with Krylov space dimension $N_{Kry} = 6$. The time step size $\Delta t$ of the MPS calculation always matches the time step-size of the calculation using the complete many-body state. For the complete many-body state, the OBRDM is independent of the time step size. The relative difference of the OBRDM from the completely many-body state is $\left| \gamma_{FCI}^{\Delta t=0.25as} - \gamma_{FCI}^{\Delta t=2.35as} \right| \sim 2.1\%$.
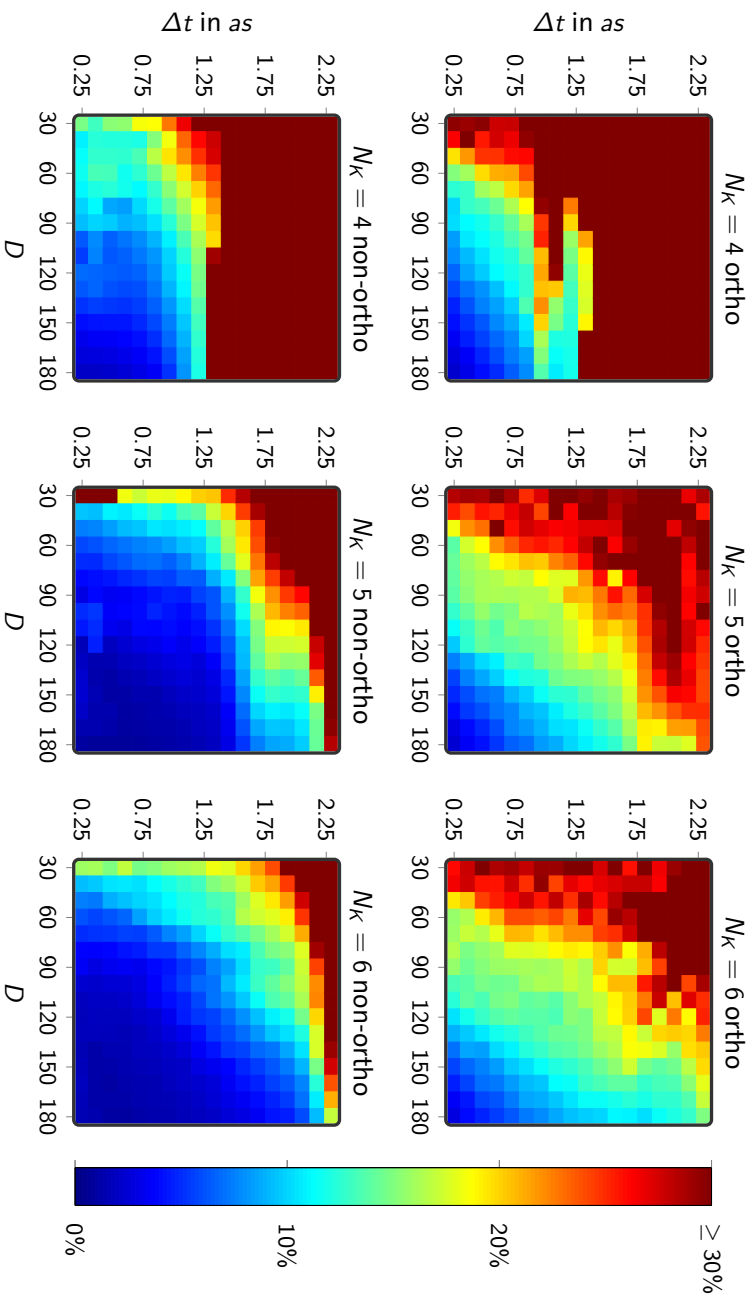
$\Delta t = 2.25 as$ (maximum shown) or $\Delta t = 0.25 as$ (minimum shown) as both are small enough for the chosen Krylov space dimension $N_{Kry}$. The relative difference of the respective OBRDM is $|\gamma_{FCI}^{\Delta t=0.25as} - \gamma_{FCI}^{\Delta t=2.35as}| \sim 2.1\%$, i.e. minor on the color scale of Figure 4.17.

This confirms the conclusions drawn from the singly ionized situation. First, the MPS approach is able to handle more entanglement when using the non-orthogonalized Krylov space method. Previously, we explained the improved performance of the non-orthogonal Krylov space method by the more efficient usage of the reduced number of degree of freedom. In the orthogonalized Krylov space method some of them are wasted with respect to keep the Krylov vectors orthogonal. However, in the non-orthogonalized Krylov space method, the MPS is directly optimized to represent the time-evolved many-body state. This enables the non-orthogonal MPS representation to embed entanglement more accurately, which is in particular important in highly excited states, such as the double hole ionization discussed here. Second, the non-orthogonal Krylov space method may not be applied when discussing states close to eigenstates of the Hamiltonian. For the single ionization, we noticed noisy convergence with respect to the time step size, which we accounted to a problem if states are close to eigenstates. In the doubly ionized situation discussed now, Koopmans' theorem does not apply and we can assume that the initial state is far from being an eigenstate of the Hamiltonian. With the initial state being not an eigenstate, also the noise vanishes in the convergence of the time step size $\Delta t$. Now, the results of the calculation using the non-orthogonalized Krylov space method converges smoothly and it should be easy to achieve convergence if there are not quasi exact results to compare to.

### 4.3.3 Conclusion

In this section, we discussed three different methods to time-evolve a many-body state in MPS representation. We observed a strong dependence on the MPS representation and the time evolution method. This proves that at least some degree of entanglement in the MPS representation is artificial and can be removed by choosing the time evolution method wisely. We can conclude, the Krylov space time evolution methods are superior to the fourth-order Runge–Kutta method, due to unitarity properties. The Krylov method is able to reduce the absolute error of the time-dependent Green's function, as well as the relative error of the OBRDM. We displayed this at the example of the hydrogen chain.

For the Krylov method, we see an additional advantage of the non-orthogonalized Krylov space method in comparison to the orthogonalized Krylov space method. We related this benefit to intrinsic properties of the truncated MPS representation of

the many-body state, where the reduced number of degrees of freedom are used more efficiently when using the non-orthogonalized Krylov space method. However, this advantage is not universal, as there are situations where the Krylov basis vectors need to be orthogonalized to achieve accurate results. We demonstrated this at the example of an initial state that is close to an eigenstate of the Hamiltonian.

## 4.4 Conclusions

In this chapter, we analyzed the performance of the MPS approach in describing time-dependent problems for different families of molecules. Starting from the hydrogen molecule, we showed how truncated MPS are able to describe the dynamics on a quasi exact level. Continuing to the chain of hydrogen atoms, we described the large potential of the MPS representation in reducing the number of degrees of freedom dynamically. We demonstrated this by discussing the relative error of the two-body reduced density matrix, as well as the relative error of the one-body density matrix. Further, we demonstrated the accuracy of the MPS method at the example of the one-body Green's function, in both, the time domain, as well as in the frequency domain.

Discussing more realistic molecules, we showed the good performance of the MPS approach in describing the dynamics of the OBRDM after the molecule has been singly or doubly ionized. In the direct comparison with full CI results, we chose the hydrogen fluoride molecule, the water molecule, the ammonia molecular, and the methane molecule. For all these molecules the relative error of the OBRDM converged with increasing MPS bond dimension.

In a comparison of the time evolution methods, we analyzed the fourth-order Runge–Kutta method, the orthogonalized Krylov method, as well as the non-orthogonalized Krylov method. We see the two Krylov methods to work particularly well with the MPS approach, where the non-orthogonalized Krylov method allows to further reduce the necessary MPS bond dimension in special circumstances. With this, we know about the capabilities of the MPS representation and can proceed by applying it to situations where quasi exact results from the complete many-body state are beyond today's computational means.

# 5

# Role of Correlation to Electron Migration in Iodoacetylene

After we have analyzed the performance of the MPS representation in Chapter 4, we are now in the position to employ the MPS representation to molecules, where a description using the complete many-body state is beyond modern computational means. Although the systems discussed in the previous chapter included realistic models of stable molecules, the 6-31G Gaussian orbital set for characterization of the one-body states is considered basic in quantum chemistry community. To allow for a quantitative description of the electron dynamics in the molecule we need a more elaborate orbital basis set, which inevitably enlarges the dimension of the many-body Hilbert space. The larger orbital sets increase the complexity of the calculations and an efficient representation of the many-body state is necessary to numerically solve the time-dependent Schrödinger equation of the electrons in the molecule.

In the following chapter, we employ the MPS representation to study charge migration effects in iodoacetylene $C_2HI$ on a quantitative level that allows for direct comparison to experiments. We study iodoacetylene that has been single ionized at the iodine atom and discuss the resulting dynamics with respect to a recent experiment by Kraus et al. [5]. Using the MPS representation, we find migration frequencies in direct agreement with the experiment, outrunning previous studies performed on this system. To understand the origin of the migration frequencies, we analyze the dynamics and find that considering electronic correlation is essential in this situation. We support this conclusion by examining the role of correlations in the time-dependent MPS state and compare to calculations of uncorrelated and correlated eigenstates. Finally, we discuss the impact of nuclear geometry to preclude that the dynamics are subject to nuclear induced dephasing that was reported elsewhere [84].

Parts of this chapter have found consideration in the *Journal of Chemical Theory and Computation* [219].

**Figure 5.1.:** The iodoacetylene molecule at its equilibrium geometry. The geometry was optimized on the Hartree–Fock level, using Stuttgart/Cologne ECP46MDF and ECP2MWB effective core potentials and the associated Gaussian basis sets. The hydrogen atom is included on the 6-31G Gaussian basis set level.

1.05Å  1.20Å    2.00Å
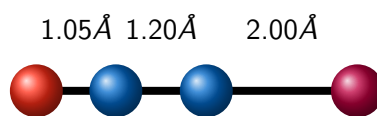
## 5.1  Charge Migration in Iodoacetylene

The following study was motivated by an experiment performed by Kraus et al., who were able to resolve ultrafast electron dynamics in the iodoacetylene molecule by using high-harmonic spectroscopy [5]. They showed considerable control over the entire processes while achieving a temporal resolution of $\approx 100as$. In collaboration with theory, they tracked charge migration following strong-field ionization spatially and temporally. Further, a time-dependent density functional theory (DFT) study by Wörner et al. [261] was able to describe the electron dynamics quantitatively, however the major frequency differed from the experimental result by 17%, indicating that DFT is missing important aspects of the situation.

In this section, we use the MPS approach to understand the processes that are the fundamental reason behind charge migration on the femtosecond scale. Furthermore, we study how the MPS approach is able to resemble the experimental setting and extract the role of electronic correlations in this situation.

The molecule discussed is iodoacetylene $C_2HI$, which expands in one dimension having the two carbon nuclei at its center surrounded by one hydrogen atom and one iodine atom (see Figure 5.1). Being a linear molecule, iodoacetylene exhibits a $C_{\infty v}$ point group symmetry, which is a non-abelian symmetry group (see Section 3.1). The Hamburg CheMPS2 extension is only able to handle abelian point groups, we therefore describe the molecule with respect to the closest point group $C_{2v}$. In the experiment, iodoacetylene was chosen due to its special characteristics with respect to strong-field ionization. Strong-field ionization is able to leave the molecule with multiple populated electronic states of the cationic molecule, whose coupling depends on the relative orientation of the molecular axis and the polarization direction of the laser. In case of perpendicular molecular axis and field polarization direction, which they controlled using a much slower alignment pulse, the molecule evolves field-free dynamics.

We model the experimental situation on an ab initio level, however, we describe electrons in core orbitals using effective core potentials. This is a popular method to reduce the number of active electrons considered directly in the model, which especially simplifies the study of heavy atoms such as iodine [262–264]. For heavy elements, most chemical bonds involve electrons that are located in higher orbitals, therefore we can remove electrons in core orbitals from the calculation with little error. In this study, we employ the Stuttgart/Cologne pseudopotentials [72, 265] , where we remove 46 electrons from the iodine atom, leaving it with 7 active electrons only. The used *ECP46MDF* [72] effective core potentials were obtained from a multi-electron fit of the atomic valence energy spectra and it encompasses relativistic effects in the iodine atom. Furthermore, we remove 2 electrons from each of the carbon atoms using the *ECP2MWB* [265] effective core potential, leaving it with 6 electrons. For the carbon atom we do not employ any relativistic corrections. We use the accompanied Gaussian basis set for the iodine atom and the carbon atoms that were specifically optimized for the given effective core potentials. The hydrogen atom in iodoacetylene is included using the 6-31G Gaussian basis set. In total, we describe the iodoacetylene molecule using 16 electrons in a set of 34 orbitals.

Prior ionization, we assume the iodoacetylene molecule to be in its uncorrelated (Hartree–Fock) ground state $|\Psi_0\rangle$ and at its equilibrium (Hartree–Fock) geometry. Using the quantum chemistry program package Molpro, we find the geometry as given in Figure 5.1, that only differs slightly to the geometry given by Kraus et al. [5], who used more elaborate methods than our Hartree–Fock approach to find the equilibrium geometry. After the Hartree–Fock calculation, we not only have the equilibrium geometry, but we also obtain molecular orbitals, which serve as a one-body orbital basis for the many-body state (see Section 2.2.1, analogous to what we performed in Chapter 4).

Figure 5.2 shows the valence orbitals of the iodoacetylene molecule, as well as, its lowest four virtual orbitals (more are included in the calculation but not shown in the figure). The orbitals are separated by the irreducible representations of the $C_{2\nu}$ symmetry of the iodoacetylene molecule. The molecule does not have any orbitals belonging to the $B_2$ symmetry in our model.

In our study, we focus on the field-free time evolution after the ionization process. We completely waive the ionization process in our model, but consider the ionization to happen suddenly at $t_0$. Considering the electric field of the ionization pulse is possible and has been studied by Weißler [266], however, here we neglect it and assume the electron to be suddenly removed at time $t_0$ and no external fields perturb the molecule in the period $t > t_0$. In time-dependent DFT calculations preceding the experiment (see Supplemental Information of [5]), it was shown that the interaction with the laser pulse dominantly couples the neutral ground state to the cationic
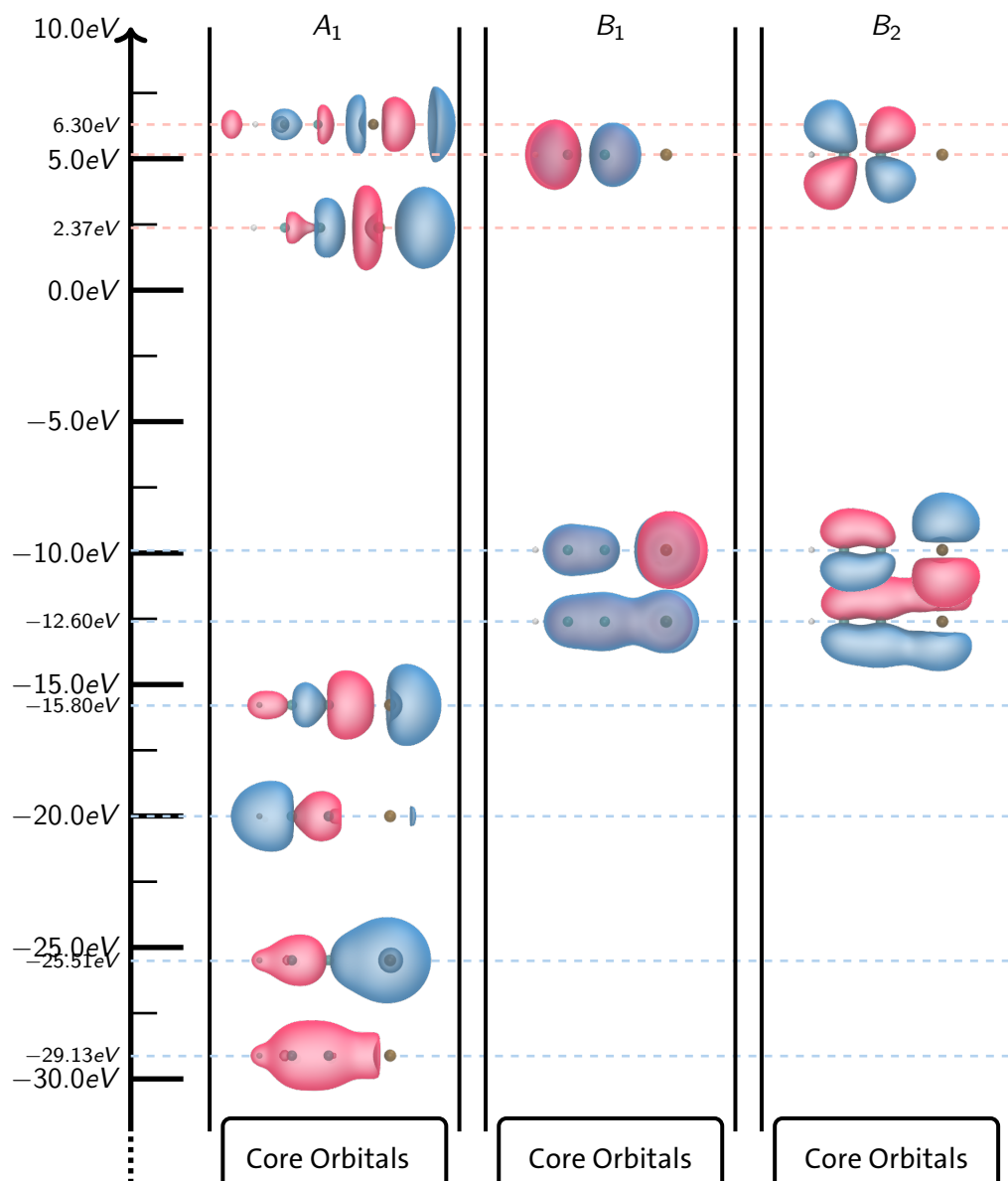
**Figure 5.2.:** Energy diagram of the molecular orbitals of the iodoacetylene molecule. The molecular orbitals are obtained on the Hartree–Fock level using Stuttgart/-Cologne effective core potential and the associated basis sets. The orbitals are categorized by the irreducible representations of the $C_{2\nu}$ point group.
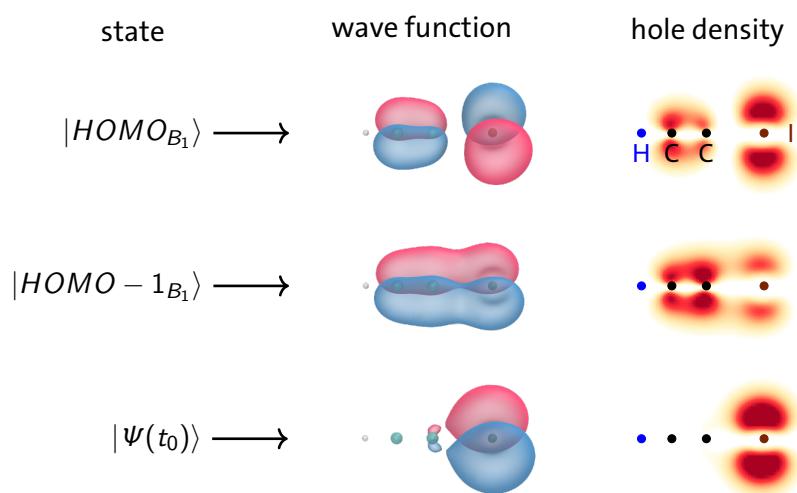
**Figure 5.3.:** Molecular orbitals and hole densities used to construct the initial state discussed observed in the experiment.

state with an ionization in the HOMO ($|\text{HOMO}\rangle = \hat{c}_{\text{HOMO}} |\Psi_0\rangle$) and to the state with ionization at the HOMO-1 ($|\text{HOMO-1}\rangle = \hat{c}_{\text{HOMO-1}} |\Psi_0\rangle$). Excitation to cationic states with an ionization at the HOMO-2 ($|\text{HOMO-2}\rangle = \hat{c}_{\text{HOMO-2}} |\Psi_0\rangle$) and higher is negligible. Based on this result, we construct our initial state as linear combination of the state $|\text{HOMO}\rangle$ and the state $|\text{HOMO-1}\rangle$.

Further, in the experiment Kraus et al. were able to obtain the phase relation of the state $|\text{HOMO}\rangle$ and the state $|\text{HOMO-1}\rangle$ at the time of the ionization. They found a small phase difference between the two states ($\phi = -0.34 \pm 0.37$). Here, we assume no phase difference to be present in the initial state and construct the state at time $t_0$ (see Figure 5.3)

$$|\Psi(t_0)\rangle = \frac{1}{\sqrt{2}} \left( |\text{HOMO}_{B_1}\rangle + |\text{HOMO-1}_{B_1}\rangle \right), \tag{5.1}$$

where we chose the hole to be created in molecular orbitals of irreducible representation $B_1$. Creating the hole in the degenerated orbitals of irreducible representation $B_2$ is physically equivalent.

### Hole Migration

The time-dependent electron density of the molecule can be calculated from the one-body reduced density matrix (OBRDM) and the single electron orbitals. The electron density at time $t$ and position $\mathbf{r}$ is given by

$$\rho(\mathbf{r}, t) = \sum_{ij} \gamma_{ij}(t)\phi_i(\mathbf{r})\phi_j^*(\mathbf{r}), \tag{5.2}$$

where $\gamma_{ij}(t)$ is the time-dependent OBRDM as defined in Equation 2.47 and $\phi_i(\mathbf{r})$ are the molecular orbitals obtained from the Hartree–Fock calculation. Using this quantity, we can find the hole density by comparing the electron density of the cation to the electron density of the neutral Hartree–Fock ground state. The time-dependent hole density is then given by

$$\rho^{1h}(\mathbf{r}, t) = \rho^{HF}(\mathbf{r}) - \rho(\mathbf{r}, t), \tag{5.3}$$

where $\rho^{HF}(\mathbf{r})$ is the electron density of the molecular orbitals obtained from the Hartree–Fock calculation.

The linear combination of cationic states as given in Equation 5.1 prepares the system with strong hole localization at the iodine atom. In Figure 5.3, we see the signful representation of the molecular orbitals, as well as the corresponding hole densities when preparing a hole in the respective state. Where both states, $|\text{HOMO}_{B_1}\rangle$ and $|\text{HOMO-1}_{B_1}\rangle$, show a rather delocalized hole at the iodine and at the two carbon atom, the linear combination as given in Equation 5.3 has strong hole localization at the iodine atom, just as described in the experiment. This leaves us with an initial state with dominant hole population at the iodine atom. If we choose the relative phase between the states $|\text{HOMO}_{B_1}\rangle$ and $|\text{HOMO-1}_{B_1}\rangle$ as $\pi$, the hole localizes at the acetylene, which is a state we will encounter within the dynamics.

Now, we study the electron dynamics following a sudden preparation of the initial state as given in Equation 5.1. This initial state is neither an eigenstate of the one-body Hamiltonian used in Hartree–Fock, nor is it an eigenstate of the Hamiltonian living on the many-body Hilbert space. Therefore, the system will evolve dynamics, expectedly on an atto- to femtosecond time scale. Describing these dynamics is difficult however, as we have now 15 electrons occupying a set of 34 molecular orbitals. Treating this using the complete many-body state is beyond today's computational capabilities. Therefore, we are going to use the MPS approach, since we have seen in Chapter 4 it is able to represent the many-body state accurately depending on the MPS bond dimension and the period of time we are interested in. To simplify the convergence analysis, we use the orthogonalized Krylov space method to propagate the MPS in
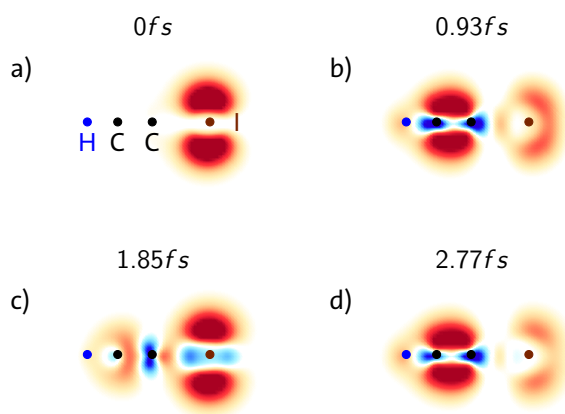
**Figure 5.4.:** Snapshots of the time-dependent hole density. The used MPS bond dimension is $D = 200$. For time-evolution we use the orthogonalized Krylov space method with a Krylov space dimension $N_{Kry} = 5$ with time step size $\Delta t = 1as$. (a) in the initial state, most of the hole is located at the iodine atom; (b) the hole migrates to the acetylene leaving the iodine neutral; (c) after $1.85$ the hole migrated back to the iodine atom again; (d) the hole moved to the acetylene part of the molecule again.

time, although, we discussed in Section 4.3.2, that the non-orthogonalized Krylov space method can be computational beneficial in special circumstances. However, the non-orthogonalized method requires additional convergence analysis with respect to the time step size $\Delta t$ and the Krylov space dimension $N_{Kry}$. To limit the extend of this analysis, we use the orthogonalized approach with conservative Krylov space parameters. In the following calculations, we use a Krylov space dimension of $N_{Kry} = 5$ and a time step size of $\Delta t = 1as$. When comparing these parameters with the performance analysis we conducted in Section 4.3.2 on the water molecular (see Figure 4.15), we can expect these parameters to give stable time evolution parameters. The open question is how large the bond dimension of the MPS approach needs to be to describe the time-evolution in this physical situation. We will therefore vary the bond dimension in the following, to make sure the dynamics are stable with respect to the part of the many-body Hilbert space covered by the MPS representation.

In Figure 5.4 we see snapshots of the time-dependent hole density for four distinct points in time. The initial state shows the strong hole localization at the iodide atom, with the remaining molecule being unaffected by the ionization pulse. Following the sudden ionization at time $t_0$, the hole starts to migrate nearly completely to the acetylene part of the molecule, leaving a neutral iodine atom behind after $0.93fs$. At time $1.85fs$, the hole has migrated to the iodine atom again, by showing electron dynamics very similar to that in the initial state. This oscillation between the iodine atom and the acetylene continues, as we observe, the hole is again at the acetylene part after $2.77fs$ in a state very similar to what we have seen at time $0.93fs$ already. For times $t > 2.77fs$ this oscillation continues, although, the MPS representation of the many-body state becomes prone to errors for periods $> 3fs$, therefore dynamics

need to be considered carefully in this period. These results were obtained from a calculation using MPS bond dimension $D = 200$ and 26 orbitals, which is well converged (see Appendix A.2 for analysis of the MPS bond dimension and the number of included orbitals).

The snapshots in Figure 5.4, show the hole density at the measured transition points in the experiment [5, 267]. There, they see a similar oscillatory motion of the hole between the iodine atom and the acetylene with an oscillation period of $1.85 fs$. The shown densities in Figure 5.4 compare nicely to previous results, although, we encounter some additional features in the hole densities that are absent in earlier reports. These are a consequence of our extensive model of the situation. Where the study by Kraus et al. considered the system as effective two-level system ($|\text{HOMO}\rangle$ and $|\text{HOMO-1}\rangle$, or its correlated partners), we included the entire many-body Hilbert space, although represented in its truncated MPS representation. Therefore, we model the system much more fundamentally, which then induces additional features into the hole density. Nevertheless, the major features of the charge motion agree in both studies. Describing the period of migration has been proven challenging in previous studies using the time-dependent DFT method with a Perdew-Burke-Ernzerhof functional. In previous work by Wörner et al. [261], they found the migration to occur with an oscillation period of $2.13 fs$, which deviates from the experimental value of $1.85 fs$ [267] by 17%. Especially when considering the time resolution of $\approx 100 as$ in the experiment.

**Population Analysis**

To quantify the oscillation we need an appropriate observable indicating the location of the hole. In the previous work by Wörner et al., they discussed the time-dependent electric dipole moment of the molecule, which relates to the displacement of the electron in the molecule. In contrast to their work, we are going to assign the electrons in the molecules to specific atoms by using *Löwdin population analysis* [61]. Using Löwdin population analysis, we will be able to quantify how the hole spreads over the individual atoms of the molecules. Using the populations, we are then able to extract the oscillation period of the hole migration that we have seen in Figure 5.4 precisely.

Löwdin population analysis allows us to assign each electron in the molecule to an atom. We are able to observe, how many electrons are in orbitals located at the iodine atom, how many electron are in orbitals located at the two carbon atoms and how many electrons are located in orbitals located at the hydrogen atom. To achieve this, we project the electron density onto orthogonalized atomic orbitals that are centered

at the nuclei. Let us start from the integrated electron density given in Equation 5.2 and expand it in terms of molecular orbitals

$$N = \int \rho(\mathbf{r}, t) d\mathbf{r} \tag{5.4}$$

$$= \sum_{ij} \gamma_{ij}(t) \int \psi_i(\mathbf{r})\psi_j^*(\mathbf{r}) d\mathbf{r}, \tag{5.5}$$

where $\gamma_{ij}(t)$ is the time-dependent OBRDM as given in Equation 2.47 and $\psi_i(\mathbf{r})$ are the molecular orbitals we used to construct the many-body state. The molecular orbitals are themselves linear combinations of atomic orbitals. Expanding the molecular orbitals in terms of atomic orbitals gives

$$N(t) = \sum_{\alpha\beta} \underbrace{\left( \sum_{ij} \gamma_{ij} c_{i\alpha} c_{j\beta}^* \right)}_{\tilde{\gamma}_{\beta\alpha}} \underbrace{\int \phi_\alpha(\mathbf{r})\phi_\beta^*(\mathbf{r}) d\mathbf{r}}_{S_{\alpha\beta}} = \sum_\beta (\tilde{\gamma}S)_{\beta\beta} = tr(\tilde{\gamma}S), \tag{5.6}$$

where we now understand the matrix element $(\tilde{\gamma}S)_{\beta\beta}$ as occupation numbers of atomic orbital $\phi_\beta$. $S$ is the overlap matrix we already came across in Equation 2.15. Assuming that each atomic orbital is centered at one of the nuclei, we can account the total number of electrons in orbitals located at that nuclei. This procedure is called *Mulliken population analysis* [61]. However, Mulliken population analysis has the disadvantage that atomic orbitals can be occupied by more than two electrons. This is a consequence of the non-orthogonality of the atomic orbitals, which makes interpretation of the results difficult. However, this can be fixed easily by orthogonalizing the atomic orbitals. By using the permutation rule in the trace operation we obtain

$$N(t) = tr(\gamma S) = tr(S^{\frac{1}{2}}\tilde{\gamma}S^{\frac{1}{2}}) = \sum_\beta \left( S^{\frac{1}{2}}\tilde{\gamma}S^{\frac{1}{2}} \right)_{\beta\beta}, \tag{5.7}$$

where now $\left( S^{\frac{1}{2}}\tilde{\gamma}S^{\frac{1}{2}} \right)_{\beta\beta}$ is the occupation number of the orthogonalized atomic orbital $\phi_\beta^{Orth}$ which is upper bounded at occupation number 2 but is still centered at one of the nuclei. Using these occupation numbers, we can attribute a given number of electrons to each atom, which then helps us to quantify the time-dependent location of the hole in the iodoacetylene molecule.

We see the results of this hole population analysis in Figure 5.5, which shows the partial hole charge at the iodine atom and at the acetylene part of the molecule for the first $3fs$ after a sudden ionization at time $t_0$. Initially, at time $t = t_0$, the hole is almost entirely located in orbitals associated with the the iodine atom. The following dynamics show the behavior we already observed in Figure 5.4, however, now revealing the oscillation period. For comparison with the experiment, we highlighted
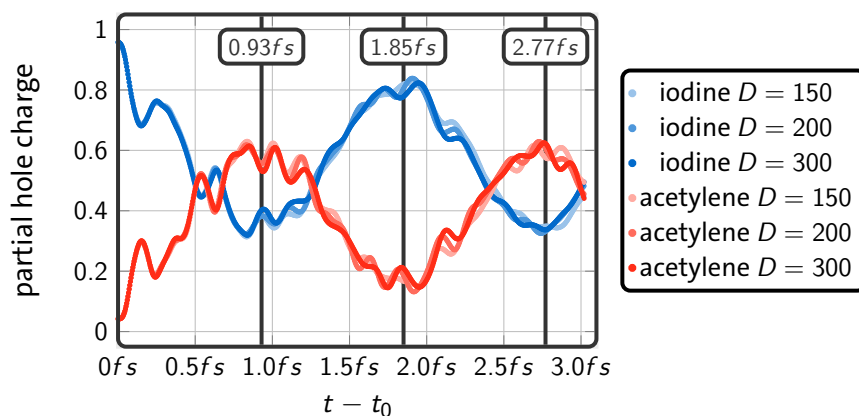
**Figure 5.5.:** Time-dependent partial hole charge at the iodine atom and at the acetylene part of the iodoacetylene molecule. The many-body state was represented using the MPS approach with different bond dimensions $D$ to demonstrate convergence. The time-evolution was done using the orthogonalized Krylov space method with Krylov space dimension $N_{Kry} = 5$ and the time step size $\Delta t = 1as$. For reference, transition points of the experimental oscillation [267] are indicating using vertical lines. The vertical line at $2.77fs$ was added for completeness. This figure is published in Frahm [219].

transition points in the dynamics measured, namely the vertical bars at $0.93fs$, $1.85fs$, and $2.77fs$. They fit correctly to the revival points of the dynamics in our MPS based calculation with an error below the temporal resolution of the experiment.

Figure 5.5 additionally shows the hole population for various bond dimension parameters of the MPS approach. From the calculations with MPS bond dimensions within the range of $D = 150$ and $D = 300$, we see no significant dependence of the qualitative behavior of the dynamics. For all these bond dimensions, the resulting dynamics are converged and we can assume that the results resolve the dynamics accurately. This is the largest system we have discussed using the MPS approach so far, where full CI bond dimension as large as $D_{FCI} = 6077943$. Still, we see no significant increase of the necessary bond dimension to obtain properly converged results. Again, MPS with bond dimension of $D = \mathcal{O}(100)$ are sufficient to resolve the dynamics, which shows even in this physical situation the electron entanglement is limited and can be represented with MPS of small bond dimension.

This raises the question if the dynamics are correlated at all, given the situation of MPS with really small bond dimension being able to reproduce the experimental results. Although the DFT calculations performed for this situation suggest that at least some correlations are present and required, maybe a simple model to the situation is able to reproduce the dynamics equally well.
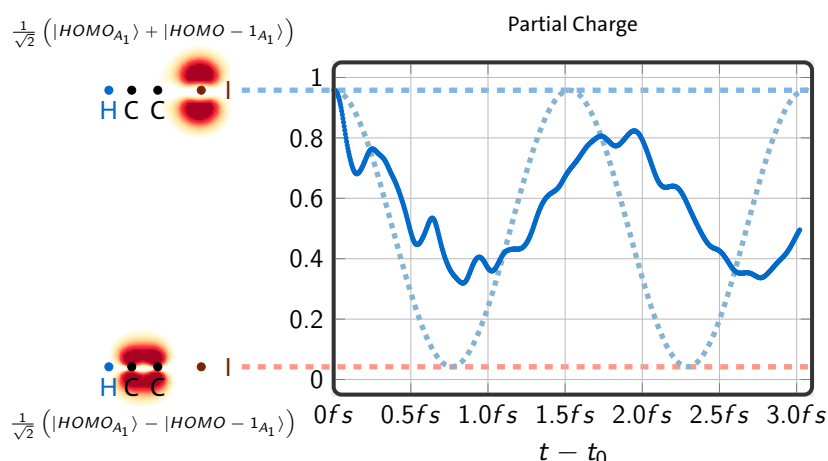
$$\frac{1}{\sqrt{2}}\left(|HOMO_{A_1}\rangle + |HOMO-1_{A_1}\rangle\right)$$

$$\frac{1}{\sqrt{2}}\left(|HOMO_{A_1}\rangle - |HOMO-1_{A_1}\rangle\right)$$

**Figure 5.6.:** Partial hole charge of the iodine obtained from the MPS representation with bond dimension $D = 300$ (solid) and from a simplified two-level model using the Hartree–Fock orbitals (dotted).

**Two-Level Model Based on Hartree-Fock Orbitals**

We will try to describe the physical situation with an uncorrelated model and see if this allows to find the same oscillation period of $1.85\,fs$ that we see in the MPS calculation and in the experiment. When neglecting correlations, the states $|HOMO_{B_1}\rangle$ and $|HOMO\text{-}1_{B_1}\rangle$ are eigenstates of the many-body Hamiltonian (Koopmans' theorem). Our initial state is the same superposition as we discussed before (see in the upper left of Figure 5.6) with most hole location at the iodine atom. If the states $|HOMO_{B_1}\rangle$ and $|HOMO\text{-}1_{B_1}\rangle$ are eigenstates, we can consider the molecule as an effective two-level system and neglect all other states. Changing the phase relation between the states by $\pi$ gives a state that has most of the hole population located at the acetylene part of the molecule, just as it was observed in the experiment (see in the lower left of Figure 5.6).

Now, in the effective two-level model, the dynamics are directly described by the energies of the two cationic states $|HOMO_{B_1}\rangle$ and $|HOMO\text{-}1_{B_1}\rangle$. The energies can be accessed by the *ionization potential* (IP) coming with every Hartree–Fock calculation

$$E_i = E_0 + IP_i, \tag{5.8}$$

where $E_0$ is the Hartree–Fock energy of the neutral molecule and $IP_i$ is the IP of the orbital $i$. The IP is the energy necessary to ionize the neutral molecule from its (Hartree–Fock) ground state $|\Psi_0\rangle$ to the cationic state with an electron removed in orbital $i$. For example, the energy $IP_{HOMO_{B_1}}$ is necessary to ionize the molecule via the channel $|\Psi_0\rangle \rightarrow |HOMO_{B_1}\rangle$. From the IP, we get the energy gap $\Delta E = IP_{HOMO_{B_1}} - IP_{HOMO\text{-}1_{B_1}}$ between the two states, which ultimately determines the
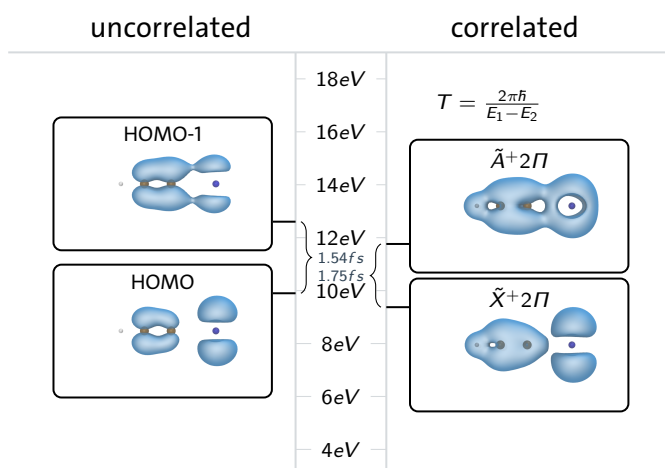
**Figure 5.7.:** Energy level scheme including hole densities for the cation comparing uncorrelated eigenstates with correlated eigenstates. (left) the uncorrelated eigenstates of the cationic molecule and corresponding energy levels. The uncorrelated orbitals indicate a oscillation period of $1.53fs$, which underestimates the observed migration period. (right) Correlated eigenstates of the cationic orbitals as obtained by the DMRG method. The MPS bond dimension to represent the correlated state was $D = 100$. With $1.75fs$, the oscillation period is now close to the observed migration oscillation and within the resolution of the experiment.

oscillation period in our two-level system. The time-dependent state in this model evolves like

$$|\Psi(t)\rangle = \frac{1}{\sqrt{2}} \left( e^{\frac{-i}{\hbar} E_{\text{HOMO}_{B_1}} t} |\text{HOMO}_{B_1}\rangle + e^{\frac{-i}{\hbar} E_{\text{HOMO-1}_{B_1}} t} |\text{HOMO-1}_{B_1}\rangle \right) \qquad (5.9)$$

$$= \frac{1}{\sqrt{2}} e^{\frac{-i}{\hbar} E_{\text{HOMO}_{B_1}} t} \left( |\text{HOMO}_{B_1}\rangle + e^{\frac{-i}{\hbar} \Delta E t} |\text{HOMO-1}_{B_1}\rangle \right), \qquad (5.10)$$

where $e^{\frac{-i}{\hbar} E_{\text{HOMO}_{B_1}} t}$ is a global phase that is unaccessible experimentally. Only the relative phase $e^{\frac{-i}{\hbar} \Delta E t}$ determines the electron dynamics. From the Hartree–Fock calculation, the molecular orbital $|\text{HOMO}_{B_1}\rangle$ has an ionization potential of $IP_{\text{HOMO}_{B_1}} = 9.8995eV$ and the molecular orbital $|\text{HOMO}_{B_1}\rangle$ has an ionization potential of $IP_{\text{HOMO-1}_{B_1}} = 12.604eV$ (see Figure 5.2), resulting in an energy gap of $\Delta E = -2.705eV$. This energy gap belongs to an oscillation period of $T = 1.53fs$, which is too short in comparison to the experiment and the correlated result using the MPS approach (see Figure 5.6).

The reason for this lies in the missing electronic correlation in the model based on two Hartree–Fock molecular orbitals. When constructing the uncorrelated eigenstates of the ion by using Koopmans' theorem, we reuse the uncorrelated molecular orbitals of the neutral molecule also for the cationic molecule. It is therefore immediately clear, that the ionization potentials based on Koopmans' theorem have to be considered as upper bounds. Performing an additional Hartree–Fock calculation of the cationic molecule would allow the molecular orbitals to relax to the ionized situation. The

newly relaxed molecular orbitals of the cationic molecule will have smaller orbital energies since they are optimized to the cationic situation. Therefore, already in the one-body picture of the Hartree–Fock method, we know that Koopmans' theorem overestimates ionization potentials and experimental ionization potentials will be smaller [61].

Further, when adding correlations to the representation of the many-body states, the eigenstate will acquire an additional energy shift which is called *correlation energy*. The correlation energy describes the amount of energy the electrons save by entering correlated many-body states. Both ionized states discussed here ($|\text{HOMO}_{B_1}\rangle$ and $|\text{HOMO-1}_{B_1}\rangle$) acquire such an energy shift (see Figure 5.7 right). The newly correlated eigenstates of the cation further have adjusted densities, but they maintain the character of the cationic states based on Koopmans' theorem. The cationic state with an electron hole in the HOMO becomes in the correlated notation $|\text{HOMO}_{B_1}\rangle \rightarrow |\tilde{X}^+ 2\Pi\rangle$ with an correlation energy of $E^{corr}_{\tilde{X}^+ 2\Pi} = -5.820 eV$ and the cationic state with an electron hole in the HOMO-1 becomes in the correlated notation $|\text{HOMO}_{B_1}\rangle \rightarrow |\tilde{A}^+ 2\Pi\rangle$ with a correlation energy $E^{corr}_{\tilde{A}^+ 2\Pi} = -6.134 eV$. We obtained the correlation energies by an independent DMRG calculation of the correlated cationic states. We use the ground state optimization algorithm for MPS as implemented in CheMPS2 [106] with a bond dimension of $D = 100$. Both cationic states obtain an energy shift ($E^{corr}_{\tilde{X}^+ 2\Pi}$ and $E^{corr}_{\tilde{A}^+ 2\Pi}$) due to the electronic correlations. The amount of correlation energy however differs for these states, which eventually changes the gap between the two lowest cationic eigenstates (see Table 5.1 for a summary of energies).

Previously in Chapter 4, we have seen that states with deeper holes experience a more dominant effect by correlations, which manifested in an enlarged MPS bond dimension necessary to describe the correlated electron motion following ionization. From these results, we can expect that correlations in the state $|\text{HOMO-1}_{B_1}\rangle \rightarrow |\tilde{A}^+ 2\Pi\rangle$ to be more important than correlations in the state $|\text{HOMO}_{B_1}\rangle \rightarrow |\tilde{X}^+ 2\Pi\rangle$. The correlation energy of the state $|\text{HOMO-1}_{B_1}\rangle \rightarrow |\tilde{A}^+ 2\Pi\rangle$ is therefore larger, which eventually reduces the energy gap between the two cationic states (see Figure 5.7). With the reduced energy gap between the states $|\text{HOMO}_{B_1}\rangle$ and $|\text{HOMO-1}_{B_1}\rangle$, the migration of the hole slows down. This is the reason, why our Hartree–Fock model underestimates the oscillation period. The stronger correlations in states with a deeper hole brings the cationic states closer together in energy and ultimately slows down the charge migration dynamics with respect to the Hartree–Fock model.

This demonstrates that methods beyond Hartree–Fock are required to find the accurate oscillation period. Both, the simple Hartree–Fock model outlined above, and the time-dependent DFT study by Wörner et al. [261] fail to describe the dynamics quantitatively. Where the uncorrelated model based on Hartree–Fock orbitals underestimates the oscillation period, modelling the system as two-level system of

|  | HOMO$_{B_1}$ | HOMO-1$_{B_1}$ | $\tilde{X}^+2\Pi$ | $\tilde{A}^+2\Pi$ |
|---|---|---|---|---|
| $IP$ | $9.8995eV$ | $12.604eV$ | $9.373eV$ | $11.762eV$ |
| $E^{corr}$ | | | $5.820eV$ | $6.134eV$ |
| $\Delta E$ | $-2.705eV$ | | $-2.388eV$ | |
| $\Delta t$ | $1.53fs$ | | $1.732fs$ | |

**Table 5.1.:** Summary of uncorrelated and correlated eigenstates together with the corresponding ionization potentials ($IP$), correlation energies ($E^{corr}$) and energy gaps ($\Delta E$ and $\Delta t$) discussed in this section.

correlated states approaches the oscillation period more accurately. Also the MPS approach forecasts the oscillation period within the resolution of the experiment, which lets us conclude that the electronic correlations are reasonably included in our MPS representation of the many-body state.

### Green's Function

That the correlated eigenstates are correctly included in the MPS based calculation becomes apparent when looking at the one-body Green's function for this situation

$$G(t) = \langle \Psi(t_0)|e^{-\frac{i}{\hbar}\hat{H}(t-t_0)}|\Psi(t_0)\rangle\,, \tag{5.11}$$

where $|\Psi(t_0)\rangle$ is the initial state as defined in Equation 5.1. By Fourier transformation of the Green's function into the frequency domain $G(\omega)$, see Equation 4.15, we can derive the IP of correlated states that have some overlap with the initial state $|\Psi(t_0)\rangle$.

In Figure 5.8, we see the frequency dependent Green's function extracted from an MPS based calculation with bond dimension $D = 300$. The frequency dependent Green's function has two major peaks, each corresponding to a correlated eigenstate of the cationic molecule. We can assign the peaks the two correlated eigenstates $\tilde{X}^+2\Pi$ and $\tilde{A}^+2\Pi$ introduced above. We can attribute these two correlated states, since we know from Koopmans' theorem that our initial state, which is a superposition of two uncorrelated eigenstates, needs to be close to two correlated eigenstates of the cationic molecule. Previously, we assigned the state $|\text{HOMO}-1_{B_1}\rangle \rightarrow |\tilde{A}^+2\Pi\rangle$ and the state $|\text{HOMO}_{B_1}\rangle \rightarrow |\tilde{X}^+2\Pi\rangle$. These are the two states observed in Figure 5.8. They fit in energy directly to the energies obtained from an independent DMRG calculation specifically targeting the cationic ground state $|\tilde{X}^+2\Pi\rangle$ and the first excited cationic state $|\tilde{A}^+2\Pi\rangle$.
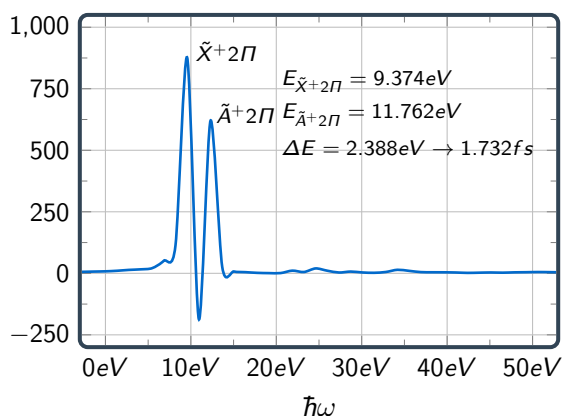
**Figure 5.8.:** Frequency dependent imaginary part of the Green's function for the case the molecule was prepared in the initial state as give in Equation 5.1. The time-evolution was using the orthogonalized Krylov space method with a Krylov space dimension $N_{Kry} = 5$ and a time step size of $\Delta t = 1as$. The final time was $3fs$ and a broadening of $0.14eV$ was applied to resolve the major peaks. The peaks were assigned correlated eigenstates of the cationic molecule with assigned energies from a complementary calculations using the DMRG method to determine eigenstates.

From this we can conclude that the dynamics are intrinsically correlated and that the MPS approach is able to capture the necessary amount of correlations to describe the situation quantitatively. We demonstrated this at the simplified model based on Koopmans' theorem and Hartree–Fock molecular orbitals, which fails to find the correct oscillation period of the hole migration in iodoacetylene. With the MPS approach, we accounted the underestimation of the simplified model directly to the missing correlations, which are correctly included in the MPS representation. Independent calculations to find the cationic eigenstates done for the cationic molecule support this conclusion, where we see the eigenenergies perfectly aligned with the spectrum obtained from the time-dependent MPS based calculation.

## 5.1.1 Impact of Nuclear Geometry

To finalize the discussion of iodoacetylene, we want to study how sensitive the charge migration discussed above is to displacement of the nuclei. Until now, we have described the iodoacetylene molecule using a fixed molecular geometry that remains static during the entire period investigated. This is usually satisfied by the heavy weight of the nuclei in comparison to the weight of the electrons (see Born–Oppenheimer Approximation in Section 2.1.2). However, previous studies have reported dephasing induced by the finite width of the wave packet of the nuclei that damps the electronic charge migration. This can lead to dephasing of the electronic dynamics in tens of femtoseconds [268–271], which is usually studied by sampling the nuclear positions by Gaussians. But this can also occur within a few femtoseconds [84], if additionally considering the nuclear motion on potential energy surfaces of
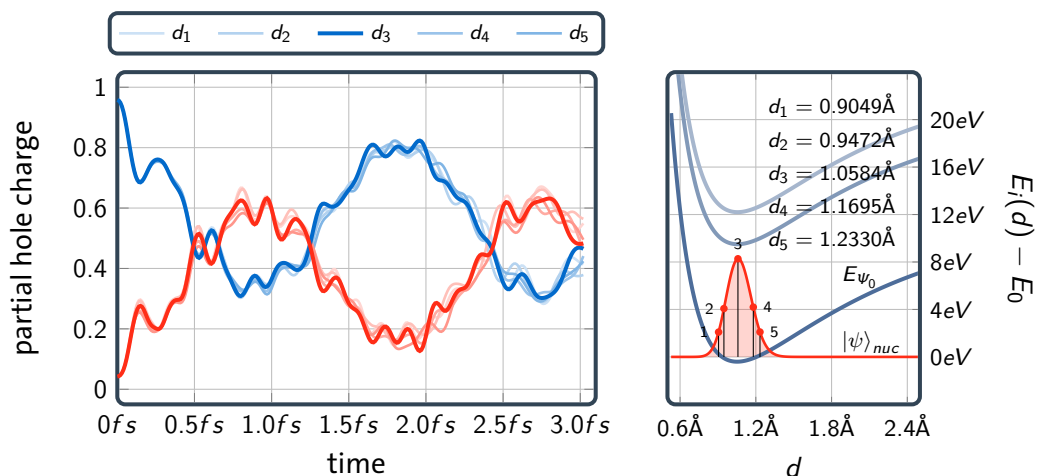
**Figure 5.9.:** Dependence of the hole migration on the length of the hydrogen-carbon bond. (left) partial hole charge at the iodine atom (blue) and at the acetylene part (red) for five different hydrogen-carbon bond lengths. (right) Potential energy surface of the Hartree–Fock ground state with respect to the hydrogen-carbon bond length (blue). In this energy surface, the hydrogen nucleus forms a nuclear wave function (red) with a finite width. Five distances are chosen to account for the zero-point motion of the hydrogen nucleus (see left).

the cationic states. It is interesting whether the charge migration discussed above is also subject to this nuclear induced dephasing on the time-range we are interested in, as it may affect the migration dynamics substantially.

In the discussion above we focused on the dynamics within period of $3fs$ after the sudden ionization of the molecule. We are restricted to this very short period by the limited amount of entanglement the MPS representation is able to handle (see Chapter 4). In the discussion we assumed the nuclei to remain still due to their heavy weight; Only the electrons respond to the newly ionized situation. Now, when releasing the approximation of fixed nuclei, we consider the light atoms in iodoacetylene only as these are the nuclei that move the fastest. Only the light nuclei have a wave function broad enough to affect the charge migration dynamics, whereas the heavy nuclei have a wave function so sharply localized that the assumption of fixed positions is still valid. The lightest nucleus in iodoacetylene is the nucleus of the hydrogen atom. We therefore concentrate on the impact of the hydrogen displacement on the charge migration dynamics, and proceed to consider the remaining atoms as fixed in the period of $3fs$.

Let $d$ be the bond distance between the carbon atom away from the iodine atom and the hydrogen atom in iodoacetylene (see Figure 5.1). When varying this bond distance, the ground state energy of the molecule changes, which then forms a potential energy surface (see Figure 5.9 (right)) for iodoacetylene, see Figure 2.1 for the nitrogen dimer $N_2$). The form of this potential energy surface determines how strong the hydrogen is bound to the molecule, which consequently determines the width of the

nuclear wave function. The potential energy surface of the hydrogen-carbon bond in iodoacetylene is shown in 5.9 (right) for the Hartree-Fock ground state $|\Psi_0\rangle$ (bold blue curve) and the first two ionized states $|HOMO_{B_1}\rangle$ and $|HOMO-1_{B_1}\rangle$ (light blue curves). We now consider the nuclei in an external potential which is given by the potential energy surface. In this external potential the nucleus extends its nuclear wave function with a finite width. We solve the one-body Schrödinger equation for the nucleus and use the resulting wave function as approximation for the hydrogen nucleus (see red line in Figure 5.9 (right)).

From the nuclear wave function we can read the spacial distribution of the hydrogen atom in the neutral iodoacetylene molecule. We see from Figure 5.9 (right), the hydrogen is delocalized in an area of $0.2$Å. To account for the sensitivity of the charge migration dynamics to the hydrogen delocalization, we choose five distinct hydrogen bond distances to sample the finite width of the nuclear wave function. For these five distinct bond distances, we perform a charge migration calculation using the MPS approach and see if the dynamics depend on the bond distance (see Figure 5.9 (left)).

We observe a partial hole population independent of the bond distance of the hydrogen atom. For the five sampled bond distances, the hole population only shows minor deviations with the equilibrium bond distance used in the Section 5.1. Therefore, we deduce that the finite width of the hydrogen nuclei does not affect any of the conclusions drawn when we used the equilibrium bond distance.

Further, we do not need to expect this conclusion to be affected by the potential energy surfaces of the cationic states (see light blue curves in Figure 5.9 (right)). In [84] they observed femtosecond dephasing only in cases the equilibrium bond distance (the *Franck-Condon-Point*) is located at a point, where the cationic potential energy surfaces have different slopes. The nuclear wave function moves with different speeds or even in different directions, which significantly reduces the dephasing time. As in our situation all potential energy surfaces have their minimum close to each other, the nuclear wave function is unable to change drastically in the period of $3fs$.

## 5.2 Conclusions

In this chapter, we applied to MPS representation of the many-body state to study charge migration in iodoacetylene to model a recent experiment by Kraus et al. [5]. We assumed the iodoacetylene to be suddenly ionized by a light pulse, creating a rather localized hole at the iodine atom of the molecule. This localized hole starts to migrate between the iodine atom and the acetylene part of the molecule on a time

scale of $1.8 fs$. The results obtained from the MPS representation agreed with experimental results qualitatively and quantitatively. We demonstrated the important role of electron correlations in this system by comparing to an uncorrelated model based on Hartree–Fock molecular orbitals. This uncorrelated model is unable to describe the charge migration quantitatively, because it underestimates the oscillation period of the hole migration. We broke down this issue in terms of uncorrelated and correlated eigenstates of the cationic molecule; attributing the correlation energy to reduce the gap between the cationic states and thereby changing the frequency of migration. Further we demonstrated that the MPS representation includes the correct correlated states of the cation by discussing the frequency-depending Green's function. This reveals that the correlated states are represented in the time-dependent MPS representation, which ultimately is the reason for their improved agreement with the experiment. Lastly, we discussed the impact of the geometry of the molecule on the charge migration dynamics, specifically accounting for the finite width of the wave function of the hydrogen atom. The charge migration dynamics is unaffected by displacing the hydrogen with respect to the remaining molecule and it is therefore not subject to dephasing driven by the finite width of nuclear wave function.

# Conclusions

6

In this thesis, we explored the *matrix product state* (MPS) approach as an efficient representation of time-dependent many-body states from a quantum chemical perspective. Specifically, we employed it to study the ultrafast response of electrons in molecules to sudden ionization. The MPS approach is able to describe the resulting electron dynamics for a few femtoseconds on a full quantum level. The following chapter summarizes how we justify this conclusion and proposes directions to continue based on the findings of this thesis.

**Summary**

We started by highlighting the versatile interest in ultrafast dynamics of molecular systems in Chapter 1. Molecules are understood as intrinsically driven by quantum mechanical effects, that are controllable by their interaction with light. When interacting with an incoming light pulse, the electrons and nuclei in the molecule respond on the attosecond ($10^{-18}s$) to femtosecond $10^{-15}s$ time scale. We outlined several approaches to describe such processes theoretically, particularly highlighting the *density matrix renormalization group* (DMRG) method and the closely related *matrix product state* (MPS) approach to represent the many-body state of the molecule. The MPS approach has obtained large attention in quantum chemistry, however, its performance in describing time-dependent molecular systems is unknown. Obtaining such an understanding marks the fundamental objective of this thesis.

In order for this thesis to be comprehensible for a broad audience, we introduce the basic concepts of *ab initio quantum chemistry* in Chapter 2. To reduce the number of active particles, we simplified the model by describing the nuclei as classic particles at fixed positions. This is known as the *Born–Oppenheimer approximation* for electrons. Further, as the starting point of the now exclusive electronic system, we introduced the *Hartree–Fock* method that describes the molecule in an uncorrelated fashion using orbitals. Eventually, the Hartree–Fock method provides *molecular orbitals* that are optimal with respect to the ground state of the uncorrelated picture.

We discussed the *post-Hartree–Fock* methods, *configurational interaction* and the *complete active space* with respect to the expansion of many-body state in the ba-

sis of *configurations* (*Slater determinants*). As a more general representation of the many-body state, we introduced the *matrix product state* (MPS) approach. Based on the assumption that the entanglement in the molecule is limited, we factorize the expansion coefficients of the complete many-body state into matrices with *bond dimension D*. By operating on these matrices, instead of the complete many-body state, we save significant amounts of computation time and memory. Further, we propose a variational method to add MPS and to apply operators to MPS, that performs efficiently and implements the necessary operations for the time-evolution method introduced next. For time-evolution of many-body states in MPS representation, we introduced two methods that operate globally on MPS. The *fourth-order Runge–Kutta* method Taylor expands the time evolution operator up to the fourth order and constructs the time evolved state as the sum of the expansion terms. In contrast to this expansion, the *Krylov space time evolution* method transforms the time-evolution operator into a small subspace of the many-body Hilbert space, the *Krylov space*, and finds the exact time-evolution operator in this small space.

After the general introduction of the MPS approach in Chapter 2, we discussed the MPS approach more explicitly in Chapter 3 in terms of symmetries and implementational details. We started by outlining how the MPS approach can be adapted to symmetries of the molecule. First, we introduced the particle number symmetry of the molecule, that is a result of the closed model of the molecule. Second, we introduced the point group symmetry of the molecule, that allows to identify many-body states with respect to *irreducible representations*. Third, we introduced the spin symmetry of the molecule, that is a result of magnetic momentum conservation of the molecule. Writing the MPS tensors in the eigenbasis of these quantities improves convergence of the MPS approach. In the second part of Chapter 3, we discussed the Hamburg CheMPS2 extension that was developed in this study. The Hamburg CheMPS2 extension, our implementation of the MPS representation, is based on the CheMPS2 program package developed by Wouters [51]. We highlighted necessary adaptions to extend the package to time-dependent problems, including the representation of the Hamiltonian in the renormalized basis and the transition to complex-valued many-body states. We finished this chapter with implementational remarks that demonstrated the improved convergence of the MPS approach and presented major features of the Hamburg CheMPS2 extension to facilitate future application.

As this study is the first to use the MPS approach to study electron dynamics in molecules, a profound analysis is due to assure its validity in this context. This analysis was conducted in Chapter 4, where we started with simple molecules consisting of hydrogen only. We demonstrated that the MPS approach is able to describe the *one-body reduced density matrix* (OBRDM), the *two-body reduced density matrix* (TBRDM), and the *one-body Green's function* within a period of a few femtosecond

after ionization, by directly comparing to calculations using the completely correlated many-body state. Depending on the bond dimension $D$, the MPS approach reproduces the correct observables with minor truncation errors. For longer time periods, we need to choose a larger bond dimension, which diminishes the computational advantage when using the MPS approach. We therefore focus on short time periods, i.e. the response of the molecule within a time frame of $3fs$. This is no restriction as the nuclear motions alters the dynamics for longer time periods.

Next in Chapter 4, we analyzed the time-dependent MPS approach for common molecules in nature. We discussed the MPS approach to resolve charge migration in the hydrogen fluoride molecule, the water molecule, the ammonia molecule, as well as in the methane molecule. For each of the examples, we prepared the molecule in the Hartree–Fock ground state and applied a sudden ionization at time $t_0$. The OBRDM obtained from the MPS approach was compared with the OBRDM obtained from the completely correlated many-body state after $1fs$. This reveals that the MPS is able to describe the OBRDM within an error of 10%, already for a small bond dimension of $D = 70$. This performance is almost independent of the size of the orbital basis set (here orbital sets of 11 to 17 orbitals were used). This enables an extensive computational advantage compared to the completely correlated many-body state, where we the MPS approach allows to reduce the number of degrees of freedom by several orders of magnitude. This conclusion holds for both, single and double ionization at $t_0$, where only double ionization in core orbitals appeared to challenge the MPS approach.

Knowing that the MPS approach is able to represent the ultrafast dynamics in molecules, we analyzed its compatibility with the different time-evolution methods introduced in the end of Chapter 2. First, we demonstrated that the fourth-order Runge–Kutta method is able to resolve the correct one-body Green's function of a hydrogen chain, however, a description using the Krylov space method is advantageous. The Krylov space method is able to reproduce the completely correlated results with smaller errors, using the same time step size as the Runge–Kutta method. We traced back this behavior to its unitary property. Further, in our analysis for the single and double ionized water molecule, we showed the particularly good compatibility of the MPS with the Krylov space method with non-orthogonalized Krylov space vectors. The use of non-orthogonalized Krylov space vectors was able to reduce truncation errors observed by up to 50%. This exhibits that some of the entanglement in the MPS representation is introduced artificially by the orthogonality requirement and can be removed by using an elegantly chosen time evolution method and optimal time evolution parameters.

In Chapter 5 we extended the analysis of the MPS approach to a situation that cannot be crosschecked by comparing to completely correlated calculations. Here,

we used the MPS approach to resolve ultrafast charge migration in single ionized iodoacetylene $C_2HI^+$. Such a situation was studied experimentally by Kraus et al. [5], who measured migration dynamics between the iodine and the acetylene part of the molecule. We utilized the MPS approach to model the situation studied in the experiment and to evaluate the role of correlation in this situation.

First, we noticed that the MPS results are stable with respect to the bond dimension $D$. Already at a bond dimension of $D = 150$, which is tiny compared to the full CI limit, the migration dynamics resolved from the MPS approach are in accordance with the experiment quantitatively. Second, we compared to an uncorrelated Hartree–Fock model to estimate the importance of correlations in this situation. We demonstrated that the correlations indeed stretch the oscillation period, by comparing correlated and uncorrelated eigenstates of the molecule. The correct dynamics can only be resolved when accounting for correlations, which the MPS approach does automatically. Third, we investigated the impact of the hydrogen atom position, as already the width of the nuclear wave function has reportedly caused dephasing on the femtosecond time scale [84]. We find that the studied migration dynamics is not subject to this nuclei induced dephasing and the migration dynamics is independent on the hydrogen position in the molecule.

**Outlook**

With the findings of this thesis, a wide range of avenues opens to proceed the study of ultrafast dynamics using the MPS approach. We want to outline ideas for future developments, where some are already subject to ongoing research projects.

The role of Auger processes [272] induced migration following core-ionization can now be described. Where we mostly discussed molecules with charge holes in valence orbitals, x-ray photons also enable to excite electrons in core orbitals. This leaves the molecule with a highly localized charge hole, that usually decays involving delocalized electrons in valence orbitals. The decay time of these core-hole states is in the area of hundreds of attosecond to femtoseconds, therefore being exactly in the time frame, the MPS approach is able to resolve quasi exactly. Such *Auger induced charge migration* processes have been reported experimentally [273–275] and theoretically [276], where this type of process is expected to occur in all molecules involving light elements. With the MPS approach, we are now able to model such situations theoretically, without relying on fixed configuration spaces.

Another interesting direction to proceed is to incorporate the light pulse causing the ionization. In this thesis, the molecule was always ionized suddenly at time $t_0$,
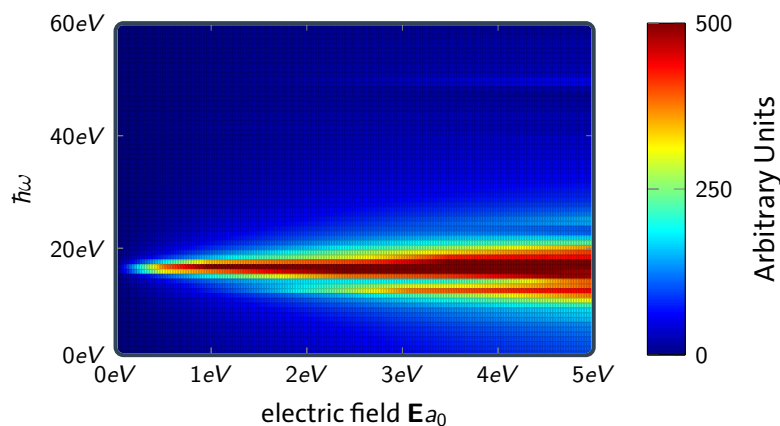
**Figure 6.1.:** Fourier spectrum of the dipole moment of the one-dimensional chain of hydrogen atoms with bond distance $0.53\text{Å}$. At time $< t_0$ the hydrogen chain is in its correlated ground state. At time $t_0$ an electric field is suddenly switched on for a period of $50as$ and suddenly switched off afterwards. The calculation was performed using the Hamburg CheMPS2 extension with a MPS bond dimension of $D = 100$ and the Krylov space time evolution with a Krylov space dimension of $N_{Kry} = 8$ and time step size of $\Delta t = 1.21as$. Data from Weißler [266].

however, this is a simplification that can be dropped easily. When including the ionization pump, the photoelectron can be tracked during the ionization process. Experimentally, this has been recently demonstrated using *strong-field photoelectron holography* [277]. Incorporating the light pulse into the Hamburg CheMPS2 extension has already been done by Weißler [266], who studies the impact of light pulses on the one-dimensional hydrogen chain using the MPS approach. The light pulse drives the hydrogen chain into a state with several excited states populated. The weights of the excited eigenstates in the molecular state after the pulse, as well as their energies can be directly extracted from the Fourier transform of the time-dependent dipole moment (see Figure 6.1). The dipole moment of the chain directly resembles the electronic structure of the molecule. A simplified model by using the non-interacting Hubbard model allowed to decrypt the process triggering the excitation of the hydrogen chain.

Further, we think the MPS approach commands about unused potential to describe electron dynamics in longer time ranges. We noticed in this study a very strict barrier for the time frame of approximately $3fs$, where the MPS bond dimension has to be chosen considerably lager to extend this period. We accounted this issue to the emerging electron entanglement. However, the entanglement in the MPS representation is basis set depending. We assume, that the time range can be extended by optimizing the single-electron orbitals time-dependently. In our study, the single-electron basis was fixed throughout the entire time evolution. Adapting the molecular orbitals time-dependently, for example to natural orbitals at the given point in time, extends the time period significantly. Using time-dependent optimized orbitals, coherences are removed from the MPS representation and the MPS can focus on representing cor-

relations correctly. Such an optimization has been performed for ground states using Gaussian transformation at the variational optimization step [243]. A similar simultaneous optimization of the orbital basis set for time-dependent MPS would allow to study electron dynamics happening on time scales of tens of femtoseconds.

At the point, where we are able to describe the molecule at time scales beyond $3fs$, it is especially interesting to take into account the nuclear motion. The nuclei start moving as a response to the electronic excitation. The nature of this charge transfer process and the role of the electronic correlation is mainly undiscovered [278]. We know, that after a couple of femtoseconds the molecule will enter a little correlated state, however, how it gets there and how the finial product depends on the correlated state at the beginning of this dephasing is unknown and challenging to study. A joint procedure of the MPS approach and the (classically) moving nuclei could allow to study this type of entangled electron-nucleus processes.

# Convergence Analysis

<div style="text-align:right">

**A**

</div>

## A.1 Convergence of the Time Step Size for Propagation of the Green's Function for the Hydrogen Chain
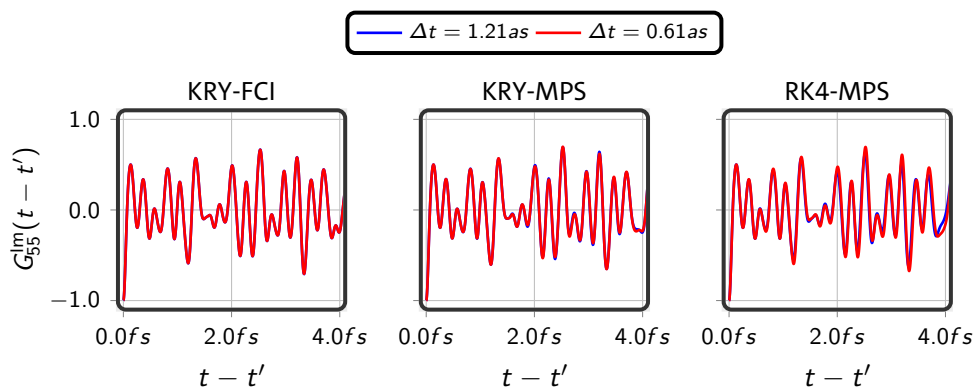


**Figure A.1.:** (left) The imaginary part of the one-particle Green's function calculated using the quasi exact full CI approach for the many-electron state representation and the Krylov time evolution method to solve the time-dependent Schrödinger equation. The Krylov space is spanned from five $N_K = 5$ orthonormal basis vectors and the time step size is $\Delta t = 1.21 as$ (blue) and $\Delta t = 0.61 as$ (red). (middle) The imaginary part of the one-particle Green's function calculated using the MPS approach for the many-electron state representation and the Krylov time evolution method to solve the time-dependent Schrödinger equation. The Krylov space is spanned from five $N_K = 5$ orthonormal basis vectors and the time step size is $\Delta t = 1.21 as$ (blue) and $\Delta t = 0.61 as$ (red). (right) The imaginary part of the one-particle Green's function calculated using the MPS approach for the many-electron state representation and the fourth-order Runge-Kutta method to solve the time-dependent Schrödinger equation. The the time step size is $\Delta t = 1.21 as$ (blue) and $\Delta t = 0.61 as$ (red). Figure and caption is published in Frahm [219].

# A.2 Convergence of the Partial Hole Charge with the Number of Included Orbitals
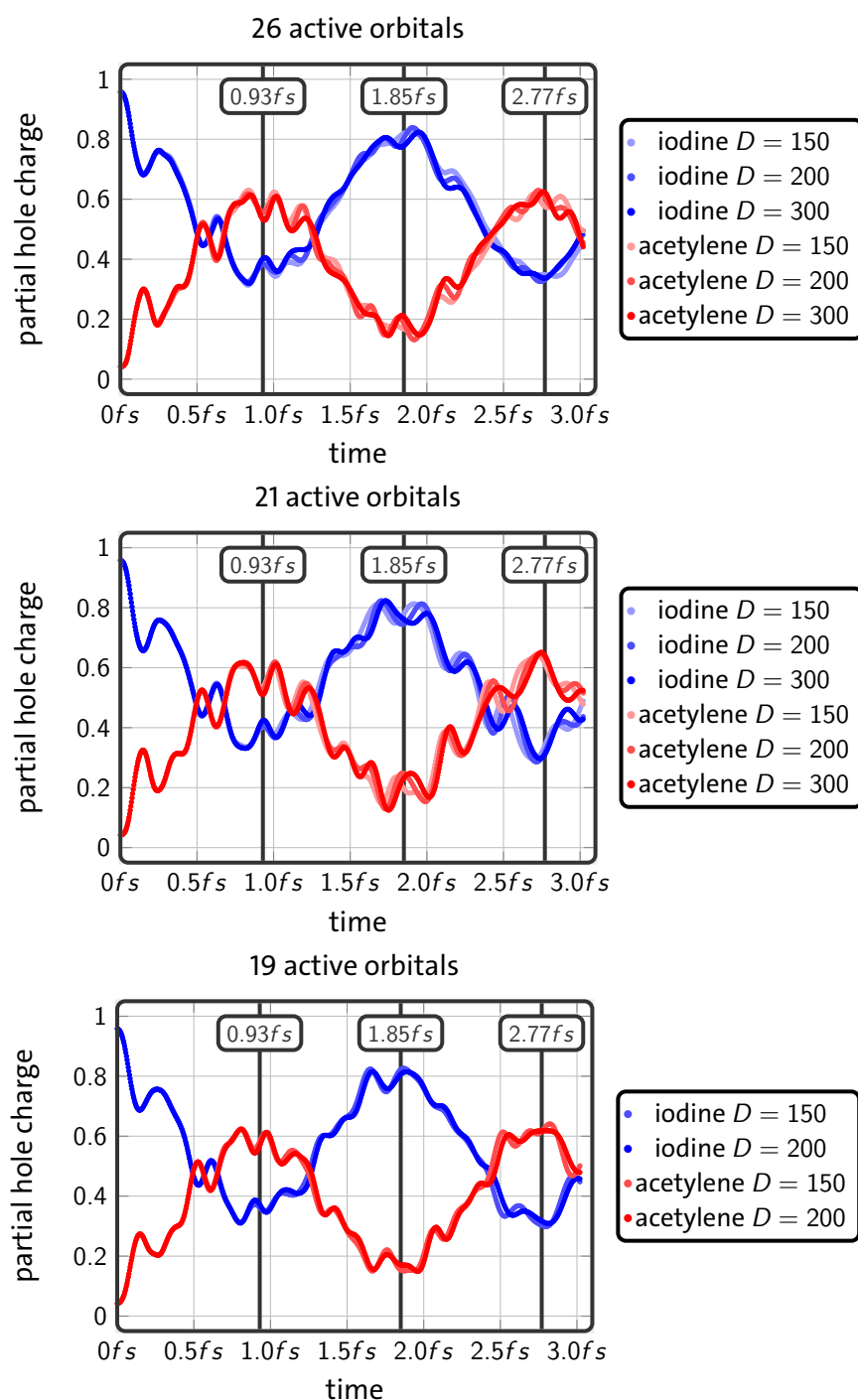


**Figure A.2.:** Convergence of the partial hole charge with the number of active orbitals and the MPS bond dimension for the ionized iodoacetylene molecule. The Krylov space dimension is $N_K = 5$ for all calculations and the time step size is $1 as$. Special points from the experiment by Kraus et al. [5] are highlighted for reference. Figure and caption is published in Frahm [219].

# Bibliography

[1] David J. Griffiths and Darrell F. Schroeter. *Introduction to Quantum Mechanics*. 3rd ed. Cambridge University Press, **2018**.

[2] Arnaldo Donoso and Craig C. Martens. *Simulation of Coherent Nonadiabatic Dynamics Using Classical Trajectories*. The Journal of Physical Chemistry A, **1998**, 102, 4291–4300.

[3] P.W. Atkins and R.S. Friedman. *Molecular Quantum Mechanics*. OUP Oxford, **2011**.

[4] K. Klünder, J. M. Dahlström, M. Gisselbrecht, et al. *Probing Single-Photon Ionization on the Attosecond Time Scale*. Physical Review Letters, **2011**, 106, 143002.

[5] P. M. Kraus, B. Mignolet, D. Baykusheva, et al. *Measurement and laser control of attosecond charge migration in ionized iodoacetylene*. Science, **2015**, 350, 790–795.

[6] S. Baker, J. S. Robinson, C. A. Haworth, et al. *Probing Proton Dynamics in Molecules on an Attosecond Time Scale*. Science, **2006**, 312, 424–427.

[7] Benjamin Erk, Rebecca Boll, Sebastian Trippel, et al. *Imaging charge transfer in iodomethane upon x-ray photoabsorption*. Science, **2014**, 345, 288–291.

[8] H. M. Dhammika Bandara and Shawn C. Burdette. *Photoisomerization in different classes of azobenzene*. Chemical Society Reviews, **2012**, 41, 1809–1825.

[9] Chaozhi Wan, Torsten Fiebig, Shana O. Kelley, et al. *Femtosecond dynamics of DNA-mediated electron transfer*. Proceedings of the National Academy of Sciences, **1999**, 96, 6014–6019.

[10] Heleen Meuzelaar, Kristen A. Marino, Adriana Huerta-Viga, et al. *Folding Dynamics of the Trp-Cage Miniprotein: Evidence for a Native-Like Intermediate from Combined Time-Resolved Vibrational Spectroscopy and Molecular Dynamics Simulations*. The Journal of Physical Chemistry B, **2013**, 117, 11490–11501.

[11] Shruti Koulgi, Uddhavesh Sonavane, and Rajendra Joshi. *Insights into the folding pathway of the Engrailed Homeodomain protein using replica exchange molecular dynamics simulations*. Journal of Molecular Graphics and Modelling, **2010**, 29, 481 –491.

[12] Rufin VanRullen and Simon J. Thorpe. *The Time Course of Visual Processing: From Early Perception to Decision-Making*. Journal of Cognitive Neuroscience, **2001**, 13, 454–461.

[13] N. S. Sariciftci, L. Smilowitz, A. J. Heeger, and F. Wudl. *Photoinduced Electron Transfer from a Conducting Polymer to Buckminsterfullerene*. Science, **1992**, 258, 1474–1476.

[14] Ksenija Glusac. *What has light ever done for chemistry?* Nature Chemistry, **2016**, 8, 734 EP –.

[15] Derren J. Heyes, Samantha J. O. Hardman, Martin N. Pedersen, et al. *Light-induced structural changes in a full-length cyanobacterial phytochrome probed by time-resolved X-ray scattering*. Communications Biology, **2019**, 2, 1.

[16] Paul Brumer. *Shedding (Incoherent) Light on Quantum Effects in Light-Induced Biological Processes*. The Journal of Physical Chemistry Letters, **2018**, 9, 2946–2955.

[17] Sarah Maria Falke, Carlo Andrea Rozzi, Daniele Brida, et al. *Coherent ultrafast charge transfer in an organic photovoltaic blend*. Science, **2014**, 344, 1001–1005.

[18] Arianna Marchioro, Joël Teuscher, Dennis Friedrich, et al. *Unravelling the mechanism of photoinduced charge transfer processes in lead iodide perovskite solar cells*. Nature Photonics, **2014**, 8, 250 EP –.

[19] Torsten R Dunkern, Gerhard Fritz, and Bernd Kaina. *Ultraviolet light-induced DNA damage triggers apoptosis in nucleotide excision repair-deficient cells via Bcl-2 decline and caspase-3/-8 activation*. Oncogene, **2001**, 20, 6026–6038.

[20] R.E. Blankenship. *Molecular Mechanisms of Photosynthesis*. Wiley, **2014**.

[21] Mauro Nisoli, Piero Decleva, Francesca Calegari, Alicia Palacios, and Fernando Martin. *Attosecond Electron Dynamics in Molecules*. Chemical Reviews, **2017**, 117, 10760–10825.

[22] Benjamin J. Sussman, Dave Townsend, Misha Yu. Ivanov, and Albert Stolow. *Dynamic Stark Control of Photochemical Processes*. Science, **2006**, 314, 278–281.

[23] Matthias F. Kling, Philipp von den Hoff, Irina Znakovskaya, and Regina de Vivie-Riedle. *(Sub-)femtosecond control of molecular reactions via tailoring the electric field of light*. Physical Chemistry Chemical Physics, **2013**, 15, 9448–9467.

[24] Mario Motta, David M. Ceperley, Garnet Kin-Lic Chan, et al. *Towards the Solution of the Many-Electron Problem in Real Materials: Equation of State of the Hydrogen Chain with State-of-the-Art Many-Body Methods*. Physical Review X, **2017**, 7, 031059.

[25] D. R. Hartree. *The Wave Mechanics of an Atom with a Non-Coulomb Central Field. Part I. Theory and Methods*. Mathematical Proceedings of the Cambridge Philosophical Society, **1928**, 24, 89–110.

[26] J. C. Slater. *The Self Consistent Field and the Structure of Atoms*. Physical Review, **1928**, 32, 339–348.

[27] P. Hohenberg and W. Kohn. *Inhomogeneous Electron Gas*. Physical Review, **1964**, 136, B864–B871.

[28] W. Kohn and L. J. Sham. *Self-Consistent Equations Including Exchange and Correlation Effects*. Physical Review, **1965**, 140, A1133–A1138.

[29] Anthony P. Scott and Leo Radom. *Harmonic Vibrational Frequencies: An Evaluation of Hartree–Fock, Møller–Plesset, Quadratic Configuration Interaction, Density Functional Theory, and Semiempirical Scale Factors*. The Journal of Physical Chemistry, **1996**, 100, 16502–16513.

[30] David Maurice and Martin Head-Gordon. *Analytical second derivatives for excited electronic states using the single excitation configuration interaction method: theory and application to benzo[a]pyrene and chalcone*. Molecular Physics, **1999**, 96, 1533–1541.

[31] Martin Head-Gordon, Rudolph J. Rico, Manabu Oumi, and Timothy J. Lee. *A doubles correction to electronic excited states from configuration interaction in the space of single substitutions*. Chemical Physics Letters, **1994**, 219, 21 –29.

[32] George D. Purvis and Rodney J. Bartlett. *A full coupled-cluster singles and doubles model: The inclusion of disconnected triples*. The Journal of Chemical Physics, **1982**, 76, 1910–1918.

[33] Krishnan Raghavachari, Gary W. Trucks, John A. Pople, and Martin Head-Gordon. *A fifth-order perturbation comparison of electron correlation theories*. Chemical Physics Letters, **1989**, 157, 479 –483.

[34] Troy Van Voorhis and Martin Head-Gordon. *Two-body coupled cluster expansions*. The Journal of Chemical Physics, **2001**, 115, 5033–5040.

[35] H.-D. Meyer, U. Manthe, and L.S. Cederbaum. *The multi-configurational time-dependent Hartree approach*. Chemical Physics Letters, **1990**, 165, 73 –78.

[36] Chr. Møller and M. S. Plesset. *Note on an Approximation Treatment for Many-Electron Systems*. Physical Review, **1934**, 46, 618–622.

[37] John A. Pople, Martin Head-Gordon, and Krishnan Raghavachari. *Quadratic configuration interaction. A general technique for determining electron correlation energies*. The Journal of Chemical Physics, **1987**, 87, 5968–5975.

[38] Kieron Burke and Lucas O. Wagner. *DFT in a nutshell*. International Journal of Quantum Chemistry, **2013**, 113, 96–101.

[39] Kieron Burke and Lucas O. Wagner. *Erratum: DFT in a nutshell*. International Journal of Quantum Chemistry, **2013**, 113, 1601–1601.

[40] J.M. Thijssen and J.M. Thijssen. *Computational Physics*. Cat Who mysteries. Cambridge University Press, **1999**.

[41] Deidre Cleland, George H. Booth, and Ali Alavi. *Communications: Survival of the fittest: Accelerating convergence in full configuration-interaction quantum Monte Carlo*. The Journal of Chemical Physics, **2010**, 132, 041103.

[42] Steven R. White. *Density matrix formulation for quantum renormalization groups*. Physical Review Letters, **1992**, 69, 2863–2866.

[43] Steven R. White. *Density-matrix algorithms for quantum renormalization groups*. Physical Review B, **1993**, 48, 10345–10356.

[44] Ö. Legeza and J. Sólyom. *Optimizing the density-matrix renormalization group method using quantum information entropy*. Physical Review B, **2003**, 68, 195116.

[45] Christian Stemmle, Beate Paulus, and Örs Legeza. *Analysis of electron-correlation effects in strongly correlated systems ($N_2$ and $N_2^+$) by applying the density-matrix renormalization-group method and quantum information theory*. Physical Review A, **2018**, 97, 022505.

[46] Fabian M. Faulstich, Mihály Máté, Andre Laestadius, et al. *Numerical and Theoretical Aspects of the DMRG-TCC Method Exemplified by the Nitrogen Dimer*. Journal of Chemical Theory and Computation, **2019**, 15, 2206–2220.

[47] Garnet Kin-Lic Chan, Mihály Kállay, and Jürgen Gauss. *State-of-the-art density matrix renormalization group and coupled cluster theory studies of the nitrogen binding curve*. The Journal of Chemical Physics, **2004**, 121, 6110–6116.

[48] Ö. Legeza, J. Röder, and B. A. Hess. *QC-DMRG study of the ionic-neutral curve crossing of LiF*. Molecular Physics, **2003**, 101, 2019–2028.

[49] Gerrit Moritz, Alexander Wolf, and Markus Reiher. *Relativistic DMRG calculations on the curve crossing of cesium hydride*. The Journal of Chemical Physics, **2005**, 123, 184105.

[50] Yuki Kurashige and Takeshi Yanai. *Second-order perturbation theory with a density matrix renormalization group self-consistent field reference function: Theory and application to the study of chromium dimer*. The Journal of Chemical Physics, **2011**, 135, 094104.

[51] Sebastian Wouters, Ward Poelmans, Paul W. Ayers, and Dimitri Van Neck. *CheMPS2: A free open-source spin-adapted implementation of the density matrix renormalization group for ab initio quantum chemistry*. Computer Physics Communications, **2014**, 185, 1501 –1514.

[52] Ulrich Schollwöck. *The density-matrix renormalization group in the age of matrix product states*. Annals of Physics, **2011**, 326, 96 –192.

[53] Guifré Vidal. *Efficient Simulation of One-Dimensional Quantum Many-Body Systems*. Physical Review Letters, **2004**, 93, 040502.

[54] Steven R. White and Adrian E. Feiguin. *Real-Time Evolution Using the Density Matrix Renormalization Group*. Physical Review Letters, **2004**, 93, 076401.

[55] A J Daley, C Kollath, U Schollwöck, and G Vidal. *Time-dependent density-matrix renormalization-group using adaptive effective Hilbert spaces*. Journal of Statistical Mechanics: Theory and Experiment, **2004**, 2004, P04005.

[56] Jutho Haegeman, Christian Lubich, Ivan Oseledets, Bart Vandereycken, and Frank Verstraete. *Unifying time evolution and optimization with matrix product states*. Physical Review B, **2016**, 94, 165116.

[57] Michael P. Zaletel, Roger S. K. Mong, Christoph Karrasch, Joel E. Moore, and Frank Pollmann. *Time-evolving a matrix product state with long-ranged interactions*. Physical Review B, **2015**, 91, 165112.

[58] Benedikt Kloss, Yevgeny Bar Lev, and David Reichman. *Time-dependent variational principle in matrix-product state manifolds: Pitfalls and potential*. Physical Review B, **2018**, 97, 024307.

[59] Juan José García-Ripoll. *Time evolution of Matrix Product States*. New Journal of Physics, **2006**, 8, 305–305.

[60] Enrico Ronca, Zhendong Li, Carlos A. Jimenez-Hoyos, and Garnet Kin-Lic Chan. *Time-Step Targeting Time-Dependent and Dynamical Density Matrix Renormalization Group Algorithms with ab Initio Hamiltonians*. Journal of Chemical Theory and Computation, **2017**, 13, 5560–5571.

[61] Attila Szabo and Neil S. Ostlund. *Modern Quantum Chemistry: Introduction to Advanced Electronic Structure Theory*. First. Mineola: Dover Publications, Inc., **1996**.

[62] Erich Hückel. *Quantentheoretische Beiträge zum Benzolproblem*. Zeitschrift für Physik, **1931**, 70, 204–286.

[63] Michael J. S. Dewar, Eve G. Zoebisch, Eamonn F. Healy, and James J. P. Stewart. *Development and use of quantum mechanical molecular models. 76. AM1: a new general purpose quantum mechanical molecular model*. Journal of the American Chemical Society, **1985**, 107, 3902–3909.

[64] Michael J. S. Dewar and Walter Thiel. *Ground states of molecules. 38. The MNDO method. Approximations and parameters*. Journal of the American Chemical Society, **1977**, 99, 4899–4907.

[65] James J. P. Stewart. *Optimization of parameters for semiempirical methods I. Method*. Journal of Computational Chemistry, **1989**, 10, 209–220.

[66] S Saebo and P Pulay. *Local Treatment of Electron Correlation*. Annual Review of Physical Chemistry, **1993**, 44, 213–236.

[67] Michael Lau. *Grundzustands-Berechnungen des Stickstoff-Moleküls mittels DMRG*. **2018**,

[68] Naoki Nakatani and Sheng Guo. *Density matrix renormalization group (DMRG) method as a common tool for large active-space CASSCF/CASPT2 calculations*. The Journal of Chemical Physics, **2017**, 146, 094102.

[69] Hanneli R. Hudock, Benjamin G. Levine, Alexis L. Thompson, et al. *Ab Initio Molecular Dynamics and Time-Resolved Photoelectron Spectroscopy of Electronically Excited Uracil and Thymine*. The Journal of Physical Chemistry A, **2007**, 111, 8500–8508.

[70] Jeremy P. Coe, Daniel J. Taylor, and Martin J. Paterson. *Calculations of potential energy surfaces using Monte Carlo configuration interaction*. The Journal of Chemical Physics, **2012**, 137, 194111.

[71] I.P. Grant. *Relativistic Quantum Theory of Atoms and Molecules: Theory and Computation*. Springer Series on Atomic, Optical, and Plasma Physics. Springer, **2007**.

[72] Hermann Stoll, Bernhard Metz, and Michael Dolg. *Relativistic energy-consistent pseudopotentials—Recent developments*. Journal of Computational Chemistry, **2002**, 23, 767–778.

[73] Zhanli Cao, Zhendong Li, Fan Wang, and Wenjian Liu. *Combining the spin-separated exact two-component relativistic Hamiltonian with the equation-of-motion coupled-cluster method for the treatment of spin–orbit splittings of light and heavy elements*. Physical Chemistry Chemical Physics, **2017**, 19, 3713–3721.

[74] Paul Adrien Maurice Dirac and Ralph Howard Fowler. *The quantum theory of the electron*. Proceedings of the Royal Society of London. Series A, Containing Papers of a Mathematical and Physical Character, **1928**, 117, 610–624.

[75] Kenny Lipkowitz. *A handbook of computational chemistry: A practical guide to chemical structure and energy calculations, by Tim Clark, John Wiley, New York, 332 pp. Price: $35.00 (1985)*. Journal of Computational Chemistry, **1986**, 7, 379–380.

[76] Frank Jensen. *Introduction to Computational Chemistry*. USA: John Wiley & Sons, Inc., **2006**.

[77] C. David Sherrill and Henry F. Schaefer. *The Configuration Interaction Method: Advances in Highly Correlated Approaches*. Ed. by Per-Olov Löwdin, John R. Sabin, Michael C. Zerner, and Erkki Brändas. Vol. 34. Advances in Quantum Chemistry. Academic Press, **1999**, 143 –269.

[78] C.J. Cramer. *Essentials of Computational Chemistry: Theories and Models*. Wiley, **2005**.

[79] Hermann G. Kümmel. *A Biography of the Coupled Cluster Method*. International Journal of Modern Physics B, **2003**, 17, 5311–5325.

[80] H.-J. Werner, P. J. Knowles, G. Knizia, F. R. Manby, M. Schütz, et al. *MOLPRO, version 2019.1, a package of ab initio programs*. **2019**.

[81] W. J. Hehre, R. F. Stewart, and J. A. Pople. *Self-Consistent Molecular-Orbital Methods. I. Use of Gaussian Expansions of Slater-Type Atomic Orbitals*. The Journal of Chemical Physics, **1969**, 51, 2657–2664.

[82] J. Franck and E. G. Dymond. *Elementary processes of photochemical reactions*. Transactions of the Faraday Society, **1926**, 21, 536–542.

[83] L. S. Cederbaum. *Born–Oppenheimer approximation and beyond for time-dependent electronic processes*. The Journal of Chemical Physics, **2008**, 128, 124101.

[84] Caroline Arnold, Oriol Vendrell, and Robin Santra. *Electronic decoherence following photoionization: Full quantum-dynamical treatment of the influence of nuclear motion*. Physical Review A, **2017**, 95, 033425.

[85] B H Bransden and Charles Joachain. *Physics of Atoms and Molecules*. **2014**.

[86] J. C. Slater. *Atomic Shielding Constants*. Physical Review, **1930**, 36, 57–64.

[87] Jos Thijssen. *Computational Physics*. 2nd ed. Cambridge University Press, **2007**.

[88] S. F. Boys and Alfred Charles Egerton. *Electronic wave functions - I. A general method of calculation for the stationary states of any molecular system*. Proceedings of the Royal Society of London. Series A. Mathematical and Physical Sciences, **1950**, 200, 542–554.

[89] Peter M.W. Gill. *Molecular integrals Over Gaussian Basis Functions*. Vol. 25. Academic Press, **1994**, 141 –205.

[90] E. F. Valeev. *Libint: A library for the evaluation of molecular integrals of many-body operators over Gaussian functions*. http://libint.valeyev.net/. **2018**.

[91] Qiming Sun, Timothy C. Berkelbach, Nick S. Blunt, et al. *PySCF: the Python-based simulations of chemistry framework*. **2017**.

[92] Karen L. Schuchardt, Brett T. Didier, Todd Elsethagen, et al. *Basis Set Exchange: A Community Database for Computational Sciences*. Journal of Chemical Information and Modeling, **2007**, 47, 1045–1052.

[93] Konstantinos D. Vogiatzis, Dongxia Ma, Jeppe Olsen, Laura Gagliardi, and Wibe A. de Jong. *Pushing configuration-interaction to the limit: Towards massively parallel MCSCF calculations*. The Journal of Chemical Physics, **2017**, 147, 184111.

[94] Maximilian Hollstein and Daniela Pfannkuche. *Multielectron dynamics in the tunneling ionization of correlated quantum systems*. Physical Review A, **2015**, 92, 053421.

[95] Per E. M. Siegbahn, Jan Almlöf, Anders Heiberg, and Björn O. Roos. *The complete active space SCF (CASSCF) method in a Newton–Raphson formulation with application to the HNO molecule*. The Journal of Chemical Physics, **1981**, 74, 2384–2396.

[96] Takeshi Sato and Kenichi L. Ishikawa. *Time-dependent complete-active-space self-consistent-field method for multielectron dynamics in intense laser fields*. Physical Review A, **2013**, 88, 023402.

[97] Stephen R. Langhoff and Ernest R. Davidson. *Configuration interaction calculations on the nitrogen molecule*. International Journal of Quantum Chemistry, **1974**, 8, 61–72.

[98] Maximilian Hollstein, Robin Santra, and Daniela Pfannkuche. *Correlation-driven charge migration following double ionization and attosecond transient absorption spectroscopy*. Physical Review A, **2017**, 95, 053411.

[99] U. Schollwöck. *The density-matrix renormalization group*. Reviews of Modern Physics, **2005**, 77, 259–315.

[100] D. Perez-Garcia, F. Verstraete, M. M. Wolf, and J. I. Cirac. *Matrix Product State Representations*. Quantum Information and Computation, **2007**, 7, 401–430.

[101] Román Orús. *A practical introduction to tensor networks: Matrix product states and projected entangled pair states*. Annals of Physics, **2014**, 349, 117 –158.

[102] Romuald A. Janik. *Exact bosonic Matrix Product States (and holography)*. Journal of High Energy Physics, **2019**, 2019, 225.

[103] Edwin Stoudenmire and David J Schwab. *Supervised Learning with Tensor Networks*. Advances in Neural Information Processing Systems 29. Ed. by D. D. Lee, M. Sugiyama, U. V. Luxburg, I. Guyon, and R. Garnett. Curran Associates, Inc., **2016**, 4799–4807.

[104] Biswa Nath Datta. *Numerical Linear Algebra and Applications, Second Edition*. 2nd. Philadelphia, PA, USA: Society for Industrial and Applied Mathematics, **2010**.

[105] Steven R. White and Richard L. Martin. *Ab initio quantum chemistry using the density matrix renormalization group*. The Journal of Chemical Physics, **1999**, 110, 4127–4130.

[106] Sebastian Wouters and Dimitri Van Neck. *The density matrix renormalization group for ab initio quantum chemistry*. The European Physical Journal D, **2014**, 68, 272.

[107] Roberto Olivares-Amaya, Weifeng Hu, Naoki Nakatani, et al. *The ab-initio density matrix renormalization group in practice*. The Journal of Chemical Physics, **2015**, 142, 034102.

[108] Soichi Shirai, Yuki Kurashige, and Takeshi Yanai. *Computational Evidence of Inversion of 1La and 1Lb-Derived Excited States in Naphthalene Excimer Formation from ab Initio Multireference Theory with Large Active Space: DMRG-CASPT2 Study*. Journal of Chemical Theory and Computation, **2016**, 12, 2366–2372.

[109] Wataru Mizukami, Yuki Kurashige, and Takeshi Yanai. *More Pi Electrons Make a Difference: Emergence of Many Radicals on Graphene Nanoribbons Studied by Ab Initio DMRG Theory*. Journal of Chemical Theory and Computation, **2013**, 9, 401–407.

[110] Vedika Khemani, Frank Pollmann, and S. L. Sondhi. *Obtaining Highly Excited Eigenstates of Many-Body Localized Hamiltonians by the Density Matrix Renormalization Group Approach*. Physical Review Letters, **2016**, 116, 247204.

[111] E. Miles Stoudenmire and Steven R. White. *Sliced Basis Density Matrix Renormalization Group for Electronic Structure*. Physical Review Letters, **2017**, 119, 046401.

[112] Mohammad Sayad, Roman Rausch, and Michael Potthoff. *Relaxation of a Classical Spin Coupled to a Strongly Correlated Electron System*. Physical Review Letters, **2016**, 117, 127201.

[113] Roman Rausch and Michael Potthoff. *Filling-dependent doublon dynamics in the one-dimensional Hubbard model*. Physical Review B, **2017**, 95, 045152.

[114] Matthias Peschke, Lena-Marie Woelk, and Michael Potthoff. *Phase diagram of the Kondo model on the zigzag ladder*. Physical Review B, **2019**, 99, 085140.

[115] Matthias Peschke, Roman Rausch, and Michael Potthoff. *Frustrated quantum magnetism in the Kondo lattice on the zigzag ladder*. Physical Review B, **2018**, 97, 115124.

[116] Mari Carmen Bañuls, Krzysztof Cichy, J. Ignacio Cirac, Karl Jansen, and Stefan Kühn. *Tensor Networks and their use for Lattice Gauge Theories*. 36th International Symposium on Lattice Field Theory, East Lansing (United States), 22 Jul 2018 - 28 Jul 2018. **2018**, 15.

[117] T. Pichler, M. Dalmonte, E. Rico, P. Zoller, and S. Montangero. *Real-Time Dynamics in U(1) Lattice Gauge Theories with Tensor Networks*. Physical Review X, **2016**, 6, 011023.

[118] Arpan Bhattacharyya, Zhe-Shen Gao, Ling-Yan Hung, and Si-Nong Liu. *Exploring the tensor networks/AdS correspondence*. Journal of High Energy Physics, **2016**, 2016, 86.

[119] E. Rico, T. Pichler, M. Dalmonte, P. Zoller, and S. Montangero. *Tensor Networks for Lattice Gauge Theories and Atomic Quantum Simulation*. Physical Review Letters, **2014**, 112, 201601.

[120] Pasquale Calabrese and John Cardy. *Entanglement Enetropy and Quantum Field Theory: A Nono-Technical Introduction*. International Journal of Quantum Information, **2006**, 04, 429–438.

[121] M. Dalmonte and S. Montangero. *Lattice gauge theory simulations in the quantum information era*. Contemporary Physics, **2016**, 57, 388–412.

[122] G. Barcza, Ö. Legeza, K. H. Marti, and M. Reiher. *Quantum-information analysis of electronic states of different molecular structures*. Physical Review A, **2011**, 83, 012508.

[123] Stellan Östlund and Stefan Rommer. *Thermodynamic Limit of Density Matrix Renormalization*. Physical Review Letters, **1995**, 75, 3537–3540.

[124] I. Oseledets. *Tensor-Train Decomposition*. SIAM Journal on Scientific Computing, **2011**, 33, 2295–2317.

[125] D. V. Savostyanov, S. V. Dolgov, J. M. Werner, and Ilya Kuprov. *Exact NMR simulation of protein-size spin systems using tensor train formalism*. Physical Review B, **2014**, 90, 085139.

[126] Tomotoshi Nishino and Andrej Gendiar. *Origin of Matrix Product State in Statistical Mechanics*. International Workshop on Density Matrix Renormalization Group and Other Advances in Numerical Renormalization Group Methods, **2010**,

[127] H. A. Kramers and G. H. Wannier. *Statistics of the Two-Dimensional Ferromagnet. Part II*. Physical Review, **1941**, 60, 263–276.

[128] R. J. Baxter. *Dimers on a Rectangular Lattice*. Journal of Mathematical Physics, **1968**, 9, 650–654.

[129] M. Chandross and J. C. Hicks. *Density-matrix renormalization-group method for excited states*. Physical Review B, **1999**, 59, 9699–9702.

[130] Weifeng Hu and Garnet Kin-Lic Chan. *Excited-State Geometry Optimization with the Density Matrix Renormalization Group, as Applied to Polyenes*. Journal of Chemical Theory and Computation, **2015**, 11, 3000–3009.

[131] Jonathan J. Dorando, Johannes Hachmann, and Garnet Kin-Lic Chan. *Targeted excited state algorithms*. The Journal of Chemical Physics, **2007**, 127, 084109.

[132] Jutho Haegeman, J. Ignacio Cirac, Tobias J. Osborne, et al. *Time-Dependent Variational Principle for Quantum Lattices*. Physical Review Letters, **2011**, 107, 070601.

[133] Ulrich Schollwöck. *Time-dependent Density-Matrix Renormalization-Group Methods*. Journal of the Physical Society of Japan, **2005**, 74, 246–255.

[134] Eric Jeckelmann. *Dynamical density-matrix renormalization-group method*. Physical Review B, **2002**, 66, 045114.

[135] Naokazu Shibata. *Thermodynamics of the Anisotropic Heisenberg Chain Calculated by the Density Matrix Renormalization Group Method*. Journal of the Physical Society of Japan, **1997**, 66, 2221–2223.

[136] R J Bursill, T Xiang, and G A Gehring. *The density matrix renormalization group for a quantum spin chain at non-zero temperature*. Journal of Physics: Condensed Matter, **1996**, 8, L583–L590.

[137] Adrian E. Feiguin and Steven R. White. *Finite-temperature density matrix renormalization using an enlarged Hilbert space*. Physical Review B, **2005**, 72, 220401.

[138] G. Alvarez. *The Density Matrix Renormalization Group for Strongly Correlated Electron Systems: A Generic Implementation*. Computer Physics Communications, **2009**, 180, 1572–1578.

[139] B Bauer, L D Carr, H G Evertz, et al. *The ALPS project release 2.0: open source software for strongly correlated systems*. Journal of Statistical Mechanics: Theory and Experiment, **2011**, 2011, P05001.

[140] Cheng Guo, Andreas Weichselbaum, Stefan Kehrein, Tao Xiang, and Jan von Delft. *Density matrix renormalization group study of a quantum impurity model with Landau-Zener time-dependent Hamiltonian*. Physical Review B, **2009**, 79, 115137.

[141] ITensor Library (version 2.0.11) http://itensor.org,

[142] Ying-Jer Kao, Yun-Da Hsieh, and Pochung Chen. *Uni10: an open-source library for tensor network algorithms*. Journal of Physics: Conference Series, **2015**, 640, 012040.

[143] M B Hastings. *An area law for one-dimensional quantum systems*. Journal of Statistical Mechanics: Theory and Experiment, **2007**, 2007, P08024–P08024.

[144] J. Eisert, M. Cramer, and M. B. Plenio. *Colloquium: Area laws for the entanglement entropy*. Reviews of Modern Physics, **2010**, 82, 277–306.

[145] Eduardo Sánchez Burillo, David Zueco Láinez, and Luis Martín Moreno. **2017**,

[146] Ö. Legeza, J. Röder, and B. A. Hess. *Controlling the accuracy of the density-matrix renormalization-group method: The dynamical block state selection approach*. Physical Review B, **2003**, 67, 125114.

[147] Debashree Ghosh, Johannes Hachmann, Takeshi Yanai, and Garnet Kin-Lic Chan. *Orbital optimization in the density matrix renormalization group, with applications to polyenes and beta-carotene*. The Journal of Chemical Physics, **2008**, 128, 144117.

[148] Fengyi Liu, Yuki Kurashige, Takeshi Yanai, and Keiji Morokuma. *Multireference Ab Initio Density Matrix Renormalization Group (DMRG)-CASSCF and DMRG-CASPT2 Study on the Photochromic Ring Opening of Spiropyran*. Journal of Chemical Theory and Computation, **2013**, 9, 4462–4469.

[149] Tran Nguyen Lan, Yuki Kurashige, and Takeshi Yanai. *Toward Reliable Prediction of Hyperfine Coupling Constants Using Ab Initio Density Matrix Renormalization Group Method: Diatomic 2 Sigma and Vinyl Radicals as Test Cases*. Journal of Chemical Theory and Computation, **2014**, 10, 1953–1967.

[150] V. Murg, F. Verstraete, R. Schneider, P. R. Nagy, and Ö. Legeza. *Tree Tensor Network State with Variable Tensor Order: An Efficient Multireference Method for Strongly Correlated Systems*. Journal of Chemical Theory and Computation, **2015**, 11, 1027–1036.

[151] Sebastian Wouters, Ward Poelmans, Stijn De Baerdemacker, Paul W. Ayers, and Dimitri Van Neck. *CheMPS2: Improved DMRG-SCF routine and correlation functions*. Computer Physics Communications, **2015**, 191, 235 –237.

[152] Johannes Hachmann, Jonathan J. Dorando, Michael Avilés, and Garnet Kin-Lic Chan. *The radical character of the acenes: A density matrix renormalization group study*. The Journal of Chemical Physics, **2007**, 127, 134309.

[153] Ö. Legeza and J. Sólyom. *Quantum data compression, quantum information generation, and the density-matrix renormalization-group method*. Physical Review B, **2004**, 70, 205118.

[154] Takeshi Yanai, Yuki Kurashige, Eric Neuscamman, and Garnet Kin-Lic Chan. *Multireference quantum chemistry through a joint density matrix renormalization group and canonical transformation theory*. The Journal of Chemical Physics, **2010**, 132, 024105.

[155] Paweł Tecmer, Katharina Boguslawski, Örs Legeza, and Markus Reiher. *Unravelling the quantum-entanglement effect of noble gas coordination on the spin ground state of CUO*. Physical Chemistry Chemical Physics, **2014**, 16, 719–727.

[156] Dominique Gobert, Corinna Kollath, Ulrich Schollwöck, and Gunter Schütz. *Real-time dynamics in spin-$\frac{1}{2}$ chains with adaptive time-dependent density matrix renormalization group*. Physical Review E, **2005**, 71, 036102.

[157] C. Kollath, U. Schollwöck, and W. Zwerger. *Spin-Charge Separation in Cold Fermi Gases: A Real Time Analysis*. Physical Review Letters, **2005**, 95, 176401.

[158] C. Karrasch, J. H. Bardarson, and J. E. Moore. *Finite-Temperature Dynamical Density Matrix Renormalization Group and the Drude Weight of Spin-$1/2$ Chains*. Physical Review Letters, **2012**, 108, 227206.

[159] Adrian E. Feiguin and Gregory A. Fiete. *Spectral properties of a spin-incoherent Luttinger liquid*. Physical Review B, **2010**, 81, 075108.

[160] F. Heidrich-Meisner, A. E. Feiguin, and E. Dagotto. *Real-time simulations of nonequilibrium transport in the single-impurity Anderson model*. Physical Review B, **2009**, 79, 235336.

[161] Peter Schmitteckert. *Nonequilibrium electron transport using the density matrix renormalization group method*. Physical Review B, **2004**, 70, 121302.

[162] C. Karrasch, D. M. Kennes, and J. E. Moore. *Transport properties of the one-dimensional Hubbard model at finite temperature*. Physical Review B, **2014**, 90, 155104.

[163] A. Branschädel, G. Schneider, and P. Schmitteckert. *Conductance of inhomogeneous systems: Real-time dynamics*. Annalen der Physik, **2010**, 522, 657–678.

[164] Z. Shuai, S.K. Pati, J.L. Brédas, and S. Ramasesha. *DMRG studies of the 1B exciton binding energy and 1B/2A crossover in an extended Hubbard-Peierls model*. Synthetic Metals, **1997**, 85, 1011 –1014.

[165] V. Murg, F. Verstraete, Ö. Legeza, and R. M. Noack. *Simulating strongly correlated quantum systems with tree tensor networks*. Physical Review B, **2010**, 82, 205105.

[166] Y.-Y. Shi, L.-M. Duan, and G. Vidal. *Classical simulation of quantum many-body systems with a tree tensor network*. Physical Review A, **2006**, 74, 022320.

[167] Naoki Nakatani and Garnet Kin-Lic Chan. *Efficient tree tensor network states (TTNS) for quantum chemistry: Generalizations of the density matrix renormalization group algorithm*. The Journal of Chemical Physics, **2013**, 138, 134113.

[168] G. Evenbly and G. Vidal. *Tensor Network Renormalization Yields the Multiscale Entanglement Renormalization Ansatz*. Physical Review Letters, **2015**, 115, 200401.

[169] Bartlomiej Czech, Lampros Lamprou, Samuel McCandlish, and James Sully. *Tensor networks from kinematic space*. Journal of High Energy Physics, **2016**, 2016, 100.

[170] Andrew J. Ferris and David Poulin. *Tensor Networks and Quantum Error Correction*. Physical Review Letters, **2014**, 113, 030501.

[171] Norbert Schuch, Didier Poilblanc, J. Ignacio Cirac, and David Pérez-García. *Resonating valence bond states in the PEPS formalism*. Physical Review B, **2012**, 86, 115108.

[172] Norbert Schuch, Ignacio Cirac, and David Pérez-García. *PEPS as ground states: Degeneracy and topology*. Annals of Physics, **2010**, 325, 2153 –2192.

[173] Román Orús and Guifré Vidal. *Simulation of two-dimensional quantum systems on an infinite lattice revisited: Corner transfer matrix for tensor contraction*. Physical Review B, **2009**, 80, 094403.

[174] Norbert Schuch, Michael M. Wolf, Frank Verstraete, and J. Ignacio Cirac. *Computational Complexity of Projected Entangled Pair States*. Physical Review Letters, **2007**, 98, 140506.

[175] Robert van de Geijn and Kazushige Goto. *BLAS (Basic Linear Algebra Subprograms). Encyclopedia of Parallel Computing*. Ed. by David Padua. Boston, MA: Springer US, **2011**, 157–164.

[176] Robert N. C. Pfeifer, Jutho Haegeman, and Frank Verstraete. *Faster identification of optimal contraction sequences for tensor networks*. Physical Review E, **2014**, 90, 033315.

[177] Garnet Kin-Lic Chan, Anna Keselman, Naoki Nakatani, Zhendong Li, and Steven R. White. *Matrix product operators, matrix product states, and ab initio density matrix renormalization group algorithms*. The Journal of Chemical Physics, **2016**, 145, 014102.

[178] E M Stoudenmire and Steven R White. *Minimally entangled typical thermal state algorithms*. New Journal of Physics, **2010**, 12, 055026.

[179] C. Hubig, I. P. McCulloch, U. Schollwöck, and F. A. Wolf. *Strictly single-site DMRG algorithm with subspace expansion*. Physical Review B, **2015**, 91, 155115.

[180] Zsuzsa Wunderlich. *Non-sequential double ionization of a quantum dot = : nicht-sequentielle Doppelionisation eines Quantenpunkts*. **2018**,

[181] Ole Berg. *Non-sequential double ionization of an artificial atom = Nicht sequentielle Doppelionisation eines künstlichen Atoms*. **2016**,

[182] Claudius Hubig. *Symmetry-protected tensor networks*. **2017**,

[183] Michael Zwolak and Guifré Vidal. *Mixed-State Dynamics in One-Dimensional Quantum Lattice Systems: A Time-Dependent Superoperator Renormalization Algorithm*. Physical Review Letters, **2004**, 93, 207205.

[184] M. C. Bañuls, M. B. Hastings, F. Verstraete, and J. I. Cirac. *Matrix Product States for Dynamical Simulation of Infinite Chains*. Physical Review Letters, **2009**, 102, 240603.

[185] C. Runge. *Ueber die numerische Auflösung von Differentialgleichungen*. Mathematische Annalen, **1895**, 46, 167–178.

[186] M. Hochbruck and C. Lubich. *On Krylov Subspace Approximations to the Matrix Exponential Operator*. SIAM Journal on Numerical Analysis, **1997**, 34, 1911–1925.

[187] Tae Jun Park and J. C. Light. *Unitary quantum time evolution by iterative Lanczos reduction*. The Journal of Chemical Physics, **1986**, 85, 5870–5876.

[188] Cornelius Lanczos. *An iteration method for the solution of the eigenvalue problem of linear differential and integral operators*. Journal of Research of the National Bureau of Standards B, **1950**, 45, 255–282.

[189] D.A. Knoll and D.E. Keyes. *Jacobian-free Newton–Krylov methods: a survey of approaches and applications*. Journal of Computational Physics, **2004**, 193, 357–397.

[190] Y. Saad. *Krylov Subspace Methods on Supercomputers*. SIAM Journal on Scientific and Statistical Computing, **1989**, 10, 1200–1232.

[191] Andrew Chapman and Yousef Saad. *Deflated and Augmented Krylov Subspace Techniques*. Numerical Linear Algebra with Applications, **1997**, 4, 43–66.

[192] Jad C. Halimeh, Fabian Kolley, and Ian P. McCulloch. *Chebyshev matrix product state approach for time evolution*. Physical Review B, **2015**, 92, 115130.

[193] Sandeep Sharma and Garnet Kin-Lic Chan. *Communication: A flexible multireference perturbation theory by minimizing the Hylleraas functional with matrix product states*. The Journal of Chemical Physics, **2014**, 141, 111101.

[194] Gabriele De Chiara, Matteo Rizzi, Davide Rossini, and Simone Montangero. *Density Matrix Renormalization Group for Dummies*. Journal of Computational and Theoretical Nanoscience, **2008**, 5, 1277–1288.

[195] G. Alvarez, L. G. G. V. Dias da Silva, E. Ponce, and E. Dagotto. *Time Evolution with the DMRG Algorithm: A Generic Implementation for Strongly Correlated Electronic Systems*. Physical Review E, **2011**, 84, 056706.

[196] M L Wall and Lincoln D Carr. *Out-of-equilibrium dynamics with matrix product states*. New Journal of Physics, **2012**, 14, 125015.

[197] Sheng Guo, Mark A. Watson, Weifeng Hu, Qiming Sun, and Garnet Kin-Lic Chan. *N-Electron Valence State Perturbation Theory Based on a Density Matrix Renormalization Group Reference Function, with Applications to the Chromium Dimer and a Trimer Model of Poly(p-Phenylenevinylene)*. Journal of Chemical Theory and Computation, **2016**, 12, 1583–1591.

[198] Simon Kothe. *Time-Dependent Transport Using Matrix Product States*. **2019**,

[199] Garnet Kin-Lic Chan. *An algorithm for large scale density matrix renormalization group calculations*. The Journal of Chemical Physics, **2004**, 120, 3172–3178.

[200] I. P McCulloch and M Gulácsi. *The non-Abelian density matrix renormalization group algorithm*. Europhysics Letters (EPL), **2002**, 57, 852–858.

[201] Ian P. McCulloch and Miklos Gulácsi. *Density Matrix Renormalisation Group Method and Symmetries of the Hamiltonian*. Australian Journal of Physics, **2001**, 53, 597–612.

[202] Ian P. Mcculloch and Miklós Gulácsi. *Total spin in the density matrix renormalization group algorithm*. Philosophical Magazine Letters, **2001**, 81, 447–453.

[203] Sandeep Sharma and Garnet Kin-Lic Chan. *Spin-adapted density matrix renormalization group algorithms for quantum chemistry*. The Journal of Chemical Physics, **2012**, 136, 124121.

[204] G.F. Koster. *Properties of the thirty-two point groups*. Massachusetts institute of technology press research monograph. M.I.T. Press, **1963**.

[205] Garnet Kin-Lic Chan and Martin Head-Gordon. *Highly correlated calculations with a polynomial cost algorithm: A study of the density matrix renormalization group*. The Journal of Chemical Physics, **2002**, 116, 4462–4476.

[206] Sebastian Wouters. *Accurate variational electronic structure calculations with the density matrix renormalization group*. eng. PhD thesis. Ghent University, **2014**, IX, 209.

[207] R. Shankar. *Principles of Quantum Mechanics*. Springer US, **1995**.

[208] Jun John Sakurai. *Modern quantum mechanics; rev. ed*. Reading, MA: Addison-Wesley, **1994**.

[209] D. A. Varshalovich, A. N. Moskalev, and V. K. Khersonskii. *Quantum Theory of Angular Momentum*. Singapore: World Scientific, **1988**.

[210] Robert M. Parrish, Lori A. Burns, Daniel G. A. Smith, et al. *Psi4 1.1: An Open-Source Electronic Structure Program Emphasizing Automation, Advanced Libraries, and Interoperability*. Journal of Chemical Theory and Computation, **2017**, 13, 3185–3197.

[211] Justin M. Turney, Andrew C. Simmonett, Robert M. Parrish, et al. *Psi4: an open-source ab initio electronic structure program*. Wiley Interdisciplinary Reviews: Computational Molecular Science, **2012**, 2, 556–565.

[212] Qiming Sun, Timothy C. Berkelbach, Nick S. Blunt, et al. *PySCF: the Python-based simulations of chemistry framework*. Wiley Interdisciplinary Reviews: Computational Molecular Science, **2018**, 8, e1340.

[213] Francesco Aquilante, Jochen Autschbach, Rebecca K. Carlson, et al. *Molcas 8: New capabilities for multiconfigurational quantum chemical calculations across the periodic table*. Journal of Computational Chemistry, **2016**, 37, 506–541.

[214] Björn O. Roos, Peter R. Taylor, and Per E.M. Sigbahn. *A complete active space SCF method (CASSCF) using a density matrix formulated super-CI approach*. Chemical Physics, **1980**, 48, 157 –173.

[215] Björn O. Roos. *The Complete Active Space Self-Consistent Field Method and its Applications in Electronic Structure Calculations. Advances in Chemical Physics*. John Wiley and Sons, Ltd, **2007**, 399–445.

[216] Kerstin. Andersson, Per Aake. Malmqvist, Bjoern O. Roos, Andrzej J. Sadlej, and Krzysztof. Wolinski. *Second-order perturbation theory with a CASSCF reference function*. The Journal of Physical Chemistry, **1990**, 94, 5483–5488.

[217] Kerstin Andersson, Per-Ake Malmqvist, and Björn O. Roos. *Second-order perturbation theory with a complete active space self-consistent field reference function*. The Journal of Chemical Physics, **1992**, 96, 1218–1226.

[218] W. J. Hehre, R. Ditchfield, and J. A. Pople. *Self—Consistent Molecular Orbital Methods. XII. Further Extensions of Gaussian—Type Basis Sets for Use in Molecular Orbital Studies of Organic Molecules*. The Journal of Chemical Physics, **1972**, 56, 2257–2261.

[219] Lars-Hendrik Frahm and Daniela Pfannkuche. *Ultrafast ab Initio Quantum Chemistry Using Matrix Product States*. Journal of Chemical Theory and Computation, **2019**, 15, 2154–2165.

[220] Frahm, Lars-Hendrik and Pfannkuche, Daniela. *A new method to calculate ultrafast electron dynamics in molecules based on matrix product states*. EPJ Web Conf. **2019**, 205, 03009.

[221] Robert Brooks. *The Fundamentals of Atomic and Molecular Physics*. **2013**.

[222] Øjvind Burrau. *Berechnung des Energiewertes des Wasserstoffmolekel-Ions (H2+) im Normalzustand*. Naturwissenschaften, **1927**, 15, 16–17.

[223] Muammar El Khatib, Oriana Brea, Edoardo Fertitta, et al. *Spin delocalization in hydrogen chains described with the spin-partitioned total position-spread tensor*. 9th Congress on Electronic Structure: Principles and Applications (ESPA 2014): A Conference Selection from Theoretical Chemistry Accounts. Ed. by Manuel F. Ruiz-Lopez and Francisco J. Olivares del Valle. Berlin, Heidelberg: Springer Berlin Heidelberg, **2016**, 33–40.

[224] Guglielmo Mazzola, Seiji Yunoki, and Sandro Sorella. *Unexpectedly high pressure for molecular dissociation in liquid hydrogen by electronic simulation*. Nature Communications, **2014**, 5, 3487 EP –.

[225] Lorenzo Stella, Claudio Attaccalite, Sandro Sorella, and Angel Rubio. *Strong electronic correlation in the hydrogen chain: A variational Monte Carlo study*. Physical Review B, **2011**, 84, 245117.

[226] Ion Mitxelena, Mauricio Rodriguez-Mayorga, and Mario Piris. *Phase dilemma in natural orbital functional theory from the N-representability perspective*. The European Physical Journal B, **2018**, 91, 109.

[227] Huihuo Zheng, Hitesh J. Changlani, Kiel T. Williams, Brian Busemeyer, and Lucas K. Wagner. *From Real Materials to Model Hamiltonians With Density Matrix Downfolding*. Frontiers in Physics, **2018**, 6, 43.

[228] Sebastian Wouters, Peter A. Limacher, Dimitri Van Neck, and Paul W. Ayers. *Longitudinal static optical properties of hydrogen chains: Finite field extrapolations of matrix product state calculations*. The Journal of Chemical Physics, **2012**, 136, 134110.

[229] Johannes Hachmann, Wim Cardoen, and Garnet Kin-Lic Chan. *Multireference correlation in long molecules with the quadratic scaling density matrix renormalization group*. The Journal of Chemical Physics, **2006**, 125, 144101.

[230] Yingjin Ma and Haibo Ma. *Assessment of various natural orbitals as the basis of large active space density-matrix renormalization group calculations*. The Journal of Chemical Physics, **2013**, 138, 224105.

[231] Sebastian Wouters, Carlos A. Jiménez-Hoyos, Qiming Sun, and Garnet K.-L. Chan. *A Practical Guide to Density Matrix Embedding Theory in Quantum Chemistry*. Journal of Chemical Theory and Computation, **2016**, 12, 2706–2719.

[232] Gerald Knizia and Garnet Kin-Lic Chan. *Density Matrix Embedding: A Strong-Coupling Quantum Embedding Theory*. Journal of Chemical Theory and Computation, **2013**, 9, 1428–1432.

[233] Chen Huang, Michele Pavone, and Emily A. Carter. *Quantum mechanical embedding theory based on a unique embedding potential*. The Journal of Chemical Physics, **2011**, 134, 154110.

[234] Thom H. Dunning. *Gaussian basis sets for use in correlated molecular calculations. I. The atoms boron through neon and hydrogen*. The Journal of Chemical Physics, **1989**, 90, 1007–1023.

[235] Roger A. Horn and Charles R. Johnson. *Matrix Analysis*. 2nd. New York, NY, USA: Cambridge University Press, **2012**.

[236] W. A. Al-Saidi, Shiwei Zhang, and Henry Krakauer. *Bond breaking with auxiliary-field quantum Monte Carlo*. The Journal of Chemical Physics, **2007**, 127, 144101.

[237] Takashi Tsuchimochi and Gustavo E. Scuseria. *Strong correlations via constrained-pairing mean-field theory*. The Journal of Chemical Physics, **2009**, 131, 121102.

[238] Anton V. Sinitskiy, Loren Greenman, and David A. Mazziotti. *Strong correlation in hydrogen chains and lattices using the variational two-electron reduced density matrix method*. The Journal of Chemical Physics, **2010**, 133, 014104.

[239] Nan Lin, C. A. Marianetti, Andrew J. Millis, and David R. Reichman. *Dynamical Mean-Field Theory for Quantum Chemistry*. Physical Review Letters, **2011**, 106, 096402.

[240] E. Fertitta, B. Paulus, G. Barcza, and Ö. Legeza. *Investigation of metal–insulator-like transition through the ab initio density matrix renormalization group approach*. Physical Review B, **2014**, 90, 245129.

[241] A. O. Mitrushenkov, Roberto Linguerri, Paolo Palmieri, and Guido Fano. *Quantum chemistry using the density matrix renormalization group II*. The Journal of Chemical Physics, **2003**, 119, 4148–4158.

[242] P.J. Knowles and N.C. Handy. *A new determinant-based full configuration interaction method*. Chemical Physics Letters, **1984**, 111, 315 –321.

[243] C. Krumnow, L. Veis, Ö. Legeza, and J. Eisert. *Fermionic Orbital Optimization in Tensor Network States*. Physical Review Letters, **2016**, 117, 210402.

[244] Matthias Balzer, Nadine Gdaniec, and Michael Potthoff. *Krylov-space approach to the equilibrium and nonequilibrium single-particle Green's function*. Journal of Physics: Condensed Matter, **2011**, 24, 035603.

[245] L.S. Cederbaum and J. Zobeley. *Ultrafast charge migration by electron correlation*. Chemical Physics Letters, **1999**, 307, 205 –210.

[246] Siegfried Lünnemann, Alexander I. Kuleff, and Lorenz S. Cederbaum. *Ultrafast charge migration in 2-phenylethyl-N,N-dimethylamine*. Chemical Physics Letters, **2008**, 450, 232 –235.

[247] Holger Hennig, Jörg Breidbach, and Lorenz S. Cederbaum. *Electron Correlation as the Driving Force for Charge Transfer: Charge Migration Following Ionization in N-Methyl Acetamide*. The Journal of Physical Chemistry A, **2005**, 109, 409–414.

[248] P. B. Corkum and Ferenc Krausz. *Attosecond science*. Nature Physics, **2007**, 3, 381 EP –.

[249] M Ehara, M Nakata, H Kou, K Yasuda, and H Nakatsuji. *Direct determination of the density matrix using the density equation: potential energy curves of HF, CH4, BH3, NH3, and H2O*. Chemical Physics Letters, **1999**, 305, 483 –488.

[250] R.J. Harrison and N.C. Handy. *Full CI calculations on BH, H2O, NH3, and HF*. Chemical Physics Letters, **1983**, 95, 386 –391.

[251] Wenjian Liu and Mark R. Hoffmann. *iCI: Iterative CI toward full CI*. Journal of Chemical Theory and Computation, **2016**, 12, 1169–1178.

[252] Joani Mato and Mark S. Gordon. *A general spin-complete spin-flip configuration interaction method*. Physical Chemistry Chemical Physics, **2018**, 20, 2615–2626.

[253] Michael Deleuze, Barry Pickup, and Joseph Delhalle. *Plane wave and orthogonalized plane wave many-body Green's function calculations of photoionization intensities*. Molecular Physics - MOL PHYS, **1994**, 83, 655–686.

[254] Darius Schaub. *Charge migration dynamics in the water ion*. **2018**,

[255] Stefan Pabst, Manfred Lein, and Hans Jakob Wörner. *Preparing attosecond coherences by strong-field ionization*. Physical Review A, **2016**, 93, 023412.

[256] A. Wirth, R. Santra, and E. Goulielmakis. *Real time tracing of valence-shell electronic coherences with attosecond transient absorption spectroscopy*. Chemical Physics, **2013**, 414, 149 –159.

[257] E. M.-L. Ohrendorf, F. Tarantelli, and L. S. Cederbaum. *Dicationic states of hydrocarbons and a statistical approach to their Auger spectra*. The Journal of Chemical Physics, **1990**, 92, 2984–2999.

[258] J. C. Schulze, P. J. Schmid, and J. L. Sesterhenn. *Exponential time integration using Krylov subspaces*. International Journal for Numerical Methods in Fluids, **2009**, 60, 591–609.

[259] C. Moler and C. Van Loan. *Nineteen Dubious Ways to Compute the Exponential of a Matrix*. SIAM Review, **1978**, 20, 801–836.

[260] C. Moler and C. Van Loan. *Nineteen Dubious Ways to Compute the Exponential of a Matrix, Twenty-Five Years Later*. SIAM Review, **2003**, 45, 3–49.

[261] Hans Jakob Wörner, Christopher A. Arrell, Natalie Banerji, et al. *Charge migration and charge transfer in molecular systems*. Structural Dynamics, **2017**, 4, 061508.

[262] P. Jeffrey Hay and Willard R. Wadt. *Ab initio effective core potentials for molecular calculations. Potentials for K to Au including the outermost core orbitals*. The Journal of Chemical Physics, **1985**, 82, 299–310.

[263] P. Jeffrey Hay and Willard R. Wadt. *Ab initio effective core potentials for molecular calculations. Potentials for the transition metal atoms Sc to Hg*. The Journal of Chemical Physics, **1985**, 82, 270–283.

[264] Willard R. Wadt and P. Jeffrey Hay. *Ab initio effective core potentials for molecular calculations. Potentials for main group elements Na to Bi*. The Journal of Chemical Physics, **1985**, 82, 284–298.

[265] Andreas Bergner, Michael Dolg, Wolfgang Küchle, Hermann Stoll, and Heinzwerner Preuß. *Ab initio energy-adjusted pseudopotentials for elements of groups 13–17*. Molecular Physics, **1993**, 80, 1431–1441.

[266] Frederik Weißler. *Zeitabhängige ab initio Quantenchemie*. **2019**,

[267] Michael Allan, Else Kloster-Jensen, and John P. Maier. *Emission spectra of Cl-C=C-H+, Br-C=C-H+ and I-C=C-H+ radical cations: A2P->X2P band systems and the decay of the A2P states*. J. Chem. Soc., Faraday Trans. 2, **1977**, 73, 1406–1416.

[268] Morgane Vacher, David Mendive-Tapia, Michael J. Bearpark, and Michael A. Robb. *Electron dynamics upon ionization: Control of the timescale through chemical substitution and effect of nuclear motion*. The Journal of Chemical Physics, **2015**, 142, 094105.

[269] Morgane Vacher, Lee Steinberg, Andrew J. Jenkins, Michael J. Bearpark, and Michael A. Robb. *Electron dynamics following photoionization: Decoherence due to the nuclear-wave-packet width*. Physical Review A, **2015**, 92, 040502.

[270] Andrew J. Jenkins, Morgane Vacher, Michael J. Bearpark, and Michael A. Robb. *Nuclear spatial delocalization silences electron density oscillations in 2-phenylethyl-amine (PEA) and 2-phenylethyl-N,N-dimethylamine (PENNA) cations*. The Journal of Chemical Physics, **2016**, 144, 104110.

[271] Andrew J. Jenkins, Morgane Vacher, Rebecca M. Twidale, Michael J. Bearpark, and Michael A. Robb. *Charge migration in polycyclic norbornadiene cations: Winning the race against decoherence*. The Journal of Chemical Physics, **2016**, 145, 164103.

[272] WALTER BAMBYNEK, BERND CRASEMANN, R. W. FINK, et al. *X-Ray Fluorescence Yields, Auger, and Coster-Kronig Transition Probabilities*. Reviews of Modern Physics, **1972**, 44, 716–813.

[273] F. Trinter, M. S. Schöffler, H. K. Kim, et al. *Resonant Auger decay driving intermolecular Coulombic decay in molecular dimers*. Nature, **2013**, 505, 664 EP –.

[274] A. C. F. Santos, D. N. Vasconcelos, M. A. MacDonald, et al. *Atomic versus molecular Auger decay in CH2Cl2 and CD2Cl2 molecules*. The Journal of Chemical Physics, **2018**, 149, 054303.

[275] Helena Aksela and Seppo Aksela. *Photoionization and Auger decay in free atoms, molecules and small clusters*. Radiation Physics and Chemistry, **2007**, 76, 370 –374.

[276] A. Picón, C. Bostedt, C. Hernández-García, and L. Plaja. *Auger-induced charge migration*. Physical Review A, **2018**, 98, 043433.

[277] Jia Tan, Yueming Zhou, Mingrui He, et al. *Time-resolving tunneling ionization via strong-field photoelectron holography*. Physical Review A, **2019**, 99, 033402.

[278] B. Wolter, M. G. Pullen, A.-T. Le, et al. *Ultrafast electron diffraction imaging of bond breaking in di-ionized acetylene*. Science, **2016**, 354, 308–312.

# Eidesstattliche Versicherung

Hiermit versichere ich an Eides statt, die vorliegende Dissertationsschrift selbst verfasst und keine anderen als die angegebenen Hilfsmittel und Quellen benutzt zu haben.

Die eingereichte schriftliche Fassung entspricht der auf dem elektronischen Speichermedium.

Die Dissertation wurde in der vorgelegten oder einer ähnlichen Form nicht schon einmal in einem früheren Promotionsverfahren angenommen oder als ungenügend beurteilt.

*Hamburg, den 28. Juni 2019*

_____

Lars-Hendrik Frahm